Electron photoemission from sodium and carbon clusters

Philipp Wopperer

THÈSE

En vue de l'obtention du

DOCTORAT DE L'UNIVERSITÉ DE TOULOUSE

Délivré par l'Université Toulouse III – Paul Sabatier
en cotutelle avec l'université
Friedrich-Alexander-Universität Erlangen-Nürnberg

Discipline ou spécialité: Physique de la matière

Présentée et soutenue par:

Philipp WOPPERER

Le 7 juin 2013

Titre:

Electron photoemission from sodium and carbon clusters

Jury:

M^{me}	Phuong Mai DINH	Examinateur
M.	Daniel DUNDAS	Membre invité
M.	Jorge KOHANOFF	Rapporteur
M.	Franck LÉPINE	Membre invité
M.	Christoph MEIER	Président du jury
M.	Karl-Heinz MEIWES-BROER	Examinateur
M.	Paul-Gerhard REINHARD	Directeur de thèse
M.	Jan-Michael ROST	Examinateur
M.	Eric SURAUD	Directeur de thèse
M^{me}	Valérie VÉNIARD	Rapporteur
M.	Günter ZWICKNAGEL	Membre invité

Ecole doctorale: Sciences de la matière
Unité de recherche: Laboratoire de Physique Théorique de Toulouse
Directeurs de thèse: Paul-Gerhard REINHARD/Eric SURAUD

Thanks to...

...my two advisors, Paul-Gerhard Reinhard at the University of Erlangen-Nürnberg, Germany, and Eric Suraud at the University of Toulouse, France. They made great efforts to find funding for my stay in Toulouse and provided me the unique opportunity to make my PhD under joint-supervision. I could so benefit from their longstanding, close and fruitful cooperation, an enormous wealth of ideas, knowledge and experience. I am grateful to them for encouraging, supporting and inspiring me with patience and humanity.

...Mai Dinh for many ideas and suggestions concerning this work, inspiring discussions about and beside physics, the help in administration matters, for making my arrival in France as much comfortable as possible, and for the warm-hearted and convenient environment in the office.

...the members, whether students, post-docs, permanents, or visitors of the Laboratoire de Physique Théorique in Toulouse for the friendly, welcoming and international working climate in the lab.

...the current and former group members of the Lehrstuhl für Theoretische Physik II in Erlangen where I could start my PhD work before my relocation to France.

...the Regional Computing Center Erlangen (RRZE), Germany, providing and maintaining the high performance computing resources which were indispensable for many calculations.

...my parents, my sister and my brother for the moral support throughout the course of my studies.

List of publications

Parts of this thesis have already been published or submitted for publication in international peer-reviewed journals:

- P. Wopperer, B. Faber, P. M. Dinh, P.-G. Reinhard, and E. Suraud, *Orientation averaged angular distributions of photo-electrons from free Na clusters*, Physics Letters A, **375**, 39 (2010).
- P. Wopperer, B. Faber, P. M. Dinh, P.-G. Reinhard, and E. Suraud, *Angular distributions of photoelectrons from free Na clusters*, Physical Review A, **82**, 063416 (2010).
- P. Wopperer, P. M. Dinh, E. Suraud, and P.-G. Reinhard, *Frequency dependence of photoelectron angular distributions in small Na clusters*, Physical Review A, **85**, 015402 (2012).
- P. Wopperer, P. M. Dinh, P.-G. Reinhard, and E. Suraud, *Laser excitation of clusters: observables from electron emission*, Journal of Physics: Conference Series, **393**, 012001 (2012).
- P. Wopperer, P. M. Dinh, P.-G. Reinhard, and E. Suraud, *Dynamics of irradiation: from molecules to nano-objects and from material science to biology*, Journal of Physics: Conference Series, **410**, 012158 (2013).
- P. Wopperer, P.-G. Reinhard, and E. Suraud, *On photo-electron angular distributions from clusters*, published online in Annalen der Physik (Berlin), DOI: 10.1002/andp.201200280 (2013).
- P. Wopperer, P. M. Dinh, P.-G. Reinhard, and E. Suraud, *On the role of resonances in photoionization of metal clusters*, submitted to Journal of Physics: Conference Series.

Toulouse and Erlangen,
April 2013 **Philipp Wopperer**

Résumé substantiel

La première partie de ce texte présente l'approche théorique et les méthodes numériques utilisées tout au long des travaux. Le fondement théorique, basé sur la théorie de la fonctionnelle de la densité dépendante du temps (dans l'approximation de la densité locale dépendante du temps avec correction d'auto-interaction), fournit un outil convenable et efficace pour décrire l'état fondamental ainsi que les propriétés dynamiques des systèmes à N corps finis. Dans cette approche, la dynamique éléctronique de petits agrégats de sodium, de chaînes de carbone, et de buckminsterfullerènes C_{60} sont étudiés, en se concentrant notamment sur les distributions angulaires (PAD) et les spectres (PES) de photoélectrons émis par les systèmes considérés sous l'action d'un laser à impulsions femtosecondes linéairement polarisées ou sous l'action d'une impulsion instantanée. Des conditions aux limites absorbantes et des points de mesure permettent de déterminer la PAD et le PES. Alors qu'en théorie, l'agrégat/la molécule est fixe dans l'espace (la boîte de simulation) avec une orientation donnée par rapport à l'axe de polarisation du laser, les expériences se déroulent plutôt avec un ensemble d'agrégats orientés de façon aléatoire. Il s'avère que la PAD moyennée sur les orientations différentes (OA-PAD) se réduit en coordonnées sphériques à une forme très simple $\sim 1 + \beta_2 P_2(\cos\vartheta) + \beta_4 P_4(\cos\vartheta) + \ldots$, où P_{2l} sont les polynômes de Legendre, ϑ est l'angle d'émission des électrons mesuré par rapport à l'axe de polarisation du laser, et β_{2l} sont les paramètres d'anisotropie. L'ordre maximal d'un β_{2l} non nul est lié à l'ordre du processus de photons. Dans le régime à un photon, un seul paramètre d'anisotropie permet de décrire l'OA-PAD : $d\overline{\sigma}/d\Omega = \overline{\sigma}/(4\pi)(1+\beta_2 P_2)$, avec β_2 variant de -1 à 2. Ainsi, l'OA-PAD montre une dépendance anisotrope de la forme $\cos^2\vartheta$ pour $\beta_2 = 2$, tandis que pour $\beta_2 = -1$ une dépendance $\sin^2\vartheta$ est observée. Pour $\beta_2 = 0$ la distribution est isotrope. La valeur de β_2 n'est pas seulement liée à l'ordre du processus de photons, mais aussi au moment angulaire de l'état initial et de l'état final. Pour un état initial s parfaitement sphérique, par exemple, β_2 est toujours égal à 2.

Afin de compenser l'écart entre théorie et expérience, des procédures de calcul de l'OA-PAD ont été mis au point. Le premier schéma de calcul de la moyenne est basé sur la théorie des perturbations au premier ordre et est dérivé par des rotations d'Euler. Ici, trois calculs linéairement indépendants sont nécessaires pour déterminer la section efficace $\overline{\sigma}$ moyennée sur les orientations et six pour l'anisotropie β_2. Dans la pratique, l'agrégat reste fixé dans la boîte de simulation,

mais la polarisation du laser est modifiée. En revanche, le second schéma fait varier l'orientation de l'agrégat, mais fixe l'axe de polarisation. L'OA-PAD est donc calculée par sommation sur un ensemble fini d'orientations différentes. Cette procédure conceptuellement plus simple est plus générale car elle peut être appliquée aussi dans le régime multiphotonique ou non-linéaire. Toutefois, le nombre d'orientations différentes nécessaires pour la convergence est, en principe, inconnu au détriment éventuel d'un coût de calcul élevé.

Dans la deuxième partie de cet ouvrage, les procédures développées sont d'abord appliquées à une sélection de petits agrégats de $Na_N^{(+)}$ neutres ou positivement chargés avec $N = 3 - 19$. Deux modèles différents pour la description du fond ionique sont comparés : les pseudopotentiels locaux et le modèle du jellium sphérique/déformé. Le premier modèle tient compte explicitement de la structure ionique de l'agrégat alors que dans le second modèle les cœurs ioniques sont considérés comme uniformes. Les différences dans le calcul de l'OA-PAD dans ces deux modèles sont frappantes. Alors que dans le modèle du jellium les paramètres d'anisotropie prennent pour la plupart des agrégats une valeur proche du maximum de deux, le fond ionique les réduit substantiellement. La déformation des fonctions d'onde des états initiaux et finaux imposée par les pseudopotentiels, introduit un mélange de composantes à haut moment angulaire qui contient toujours quelques éléments provoquant une émission latérale.

Des analyses détaillées ont été effectuées pour une meilleure compréhension du comportement de β_2 en fonction des paramètres du laser, en particulier, en fonction de la fréquence du laser ω_{las}. Un modèle de jellium sphérique pour Na_8 sert ici de point de départ. Dans ce cas une comparaison directe de la théorie des perturbations stationaires et les résultats de la théorie de la fonctionnelle de la densité dépendante du temps est possible. Dans le modèle stationaire plusieurs hypothèses pour les états initiaux et finaux ont été proposées et insérées dans la formule de Bethe-Cooper-Zare. Dans tous les cas, l'anisotropie monoéléctronique $\beta_2^{(i)}(\omega_{\text{las}})$ dépend du contenu de moment angulaire de l'état initial i considéré. Par exemple, le modèle d'ondes planes montre une baisse caractéristique de l'anisotropie de l'état p près du potentiel d'ionisation. Des chutes abruptes vers des valeurs négatives qui sont associées aux passages par zéro des éléments de la matrice de transition, suivent aux plus grandes énergies cinétiques. Cependant, de petites variations des deux fonctions d'onde ont des effets généralement énormes sur $\beta_2^{(i)}(\omega_{\text{las}})$, ce qui est en accord avec la comparaison précédente du fond ionique explicite et du modèle de jellium. Par conséquent, la prise en compte de la structure ionique semble rebattre les cartes. Les tendances de l'anisotropie en fonction de la fréquence du laser sont maintenant très lisses avec une émission de préférentielle le long de la polarisation du laser, plus un certain fond isotrope. Une exception apparaît dans les agrégats négativement chargés, ici Na_7^-, où l'hypothèse onde plane

pour l'onde sortante est légitime en raison du faible potentiel de liaison. Du coup, la tendance générale pour une émission latérale prévaut aux fréquences proches du seuil. Néanmoins, les modèles statiques ne peuvent pas décrire intégralement le processus d'ionisation, car ils ne tiennent pas compte des effets dynamiques tels que la polarisation et le réarrangement de l'agrégat résiduel.

Les résultats sur les agrégats de sodium montrent que la distribution angulaire est très sensible à tous les détails de la modélisation. Cela exige une description théorique sans compromis. Ainsi, l'approche dynamique la plus sophistiquée avec des potentiels non-locaux de type Goedecker pour le fond ionique est utilisée pour le buckminsterfullerène C_{60} et pour les chaînes de carbone linéaires C_3, C_5, et C_7. Pour C_{60}, l'application des pseudopotentiels est d'autant plus important qu'une surface sphérique de type jellium ne peut même pas donner l'état fondamental correct avec une fermeture de couche éléctronique à 240 électrons de valence. L'utilisation des pseudopotentiels cependant rompt la sphéricité, met en oeuvre la symétrie icosaédrique de la molécule, et une fermeture de couche est obtenue pour $N_{\mathrm{val}} = 240$ électrons. Le spectre d'états monoélectroniques occupés se réduit de façon significative à un nombre de bandes beaucoup plus bas, ce qui est lié à la symétrie et à la dégénérescence de haut niveau. Egalement, la symétrie du fullerène se révèle utile pour trouver un procédé direct de calcul de la distribution moyenne et des paramètres d'anisotropie β_2, β_4, ... Ainsi régimes différents sont considérés : le régime à un photon employant des fréquences du laser comme généralement utilisées au synchrotron, et le régime multiphotonique avec des fréquences bien inférieures au seuil d'ionisation. Il s'avère que ces deux régimes donnent des PAD et des PES complètement différents. Dans le régime à un photon, le PES reflète le spectre monoélectronique ressemblant à un spectre moléculaire. La PAD montre la dépendance attendue de la forme $1 + \beta_2 P_2$. Par contre, dans le domaine multiphotonique le PES décroit exponentiellement et est superposés avec des oscillations importantes alors que la PAD possède des anisotropies non nulles β_{2l} d'ordres supérieurs. Les deux comportements différents, en particulier du PES, sont liés à la déplétion des niveaux monoéléctroniques.

La thèse s'achève sur une brève étude de petites chaînes de carbone linéaires C_3, C_5, et C_7. Contrairement à C_{60}, ces petites molécules possèdent une résonance distincte de plasmon longitudinal ω_{pl} qui peut être excitée par une impulsion forte et instantanée simulant un ion rapide passant l'agrégat. L'énergie déposée est d'abord stockée dans le plasmon et plus tard transféré aux particules individuelles. Comme la fréquence de plasmon ω_{pl} est inférieure au potentiel d'ionisation, deux ou plusieurs modes doivent être absorbés pour ioniser le système. Le PES reflète donc le spectre monoéléctronique doublement ou triplement excité. Les composantes du moment angulaire du PAD augmentent toujours par une unité lors de l'absorption d'un mode dipôle supplémentaire.

Contents

1 Introduction **15**

2 Many-body theory in cluster physics **19**
2.1 Ionic background 20
2.2 Electron dynamics: Density-functional theory 23
2.2.1 Stationary density-functional theory 23
2.2.2 Local-density approximation 26
2.2.3 Self-interaction correction 27
2.2.4 Time-dependent density-functional theory 28
2.3 Summary 29

3 Excitation and analysis tools **31**
3.1 Gauges and dipole approximation 31
3.2 Pulse profile 33
3.3 Determination of the emitted density 34
3.4 Determination of photoangular distributions 36
3.5 Determination of photoelectron spectra 37
3.6 Integrated photoelectron spectra 39
3.7 Combined determination of PES and PAD 40

4 Averaging methods **43**
4.1 The anisotropy parameter 43
4.2 The analytical averaging scheme 45
4.2.1 The Euler angles 45
4.2.2 Notation 46
4.2.3 Derivation in first-order perturbation theory 48
4.2.4 Transformation into Cartesian coordinates 50
4.2.5 Procedure 51
4.3 Direct averaging schemes 52

5 First results **55**
5.1 Example: Na_8 spherical jellium 55
5.2 One-photon processes in small sodium clusters 58

5.3 Ionization beyond the linear regime . . . 64
5.3.1 Resonant emission below the ionization threshold . . . 64
5.3.2 Convergence tests of the direct averaging scheme . . . 69
5.4 Summary . . . 72

6 Frequency dependence of PAD in small sodium clusters 75
6.1 Perturbative approaches . . . 76
6.1.1 Bethe-Cooper-Zare formula . . . 76
6.1.2 Approximations for the outgoing wave . . . 77
6.2 Static results for Na_8 spherical jellium . . . 79
6.2.1 Harmonic oscillator model . . . 79
6.2.2 Static results with self-consistent wavefunctions . . . 80
6.3 Time-dependent spherical jellium calculations . . . 90
6.4 Role of deformation . . . 90
6.4.1 Trends in static plane wave approximation . . . 90
6.4.2 Time-dependent calculations . . . 93
6.5 Static and time-dependent results for Na_7^- . . . 95
6.6 Summary . . . 98

7 Buckminsterfullerene 101
7.1 Basic properties . . . 103
7.1.1 Ionic structure . . . 103
7.1.2 Electronic structure, ionization potential, and gaps . . . 103
7.1.3 Dipole response . . . 106
7.2 Averaging and integration scheme . . . 110
7.3 Photoemission in one-photon domain . . . 111
7.3.1 First results – Velocity maps . . . 111
7.3.2 Systematics with frequency . . . 116
7.4 Multiphoton domain . . . 117
7.4.1 Systematics with intensity . . . 117
7.4.2 Systematics with frequency . . . 121
7.5 Comparison with experiment . . . 122
7.6 Summary . . . 124

8 Carbon chains 127
8.1 Ionic and electronic structure . . . 128
8.2 Dipole response . . . 130
8.3 Plasmon-enhanced photoemission . . . 131

9 Conclusion 137

Appendix

A Angular momentum and rotations **145**
A.1 Euler angles and rotation operators 145
A.1.1 Wigner 3j-symbols 146
A.1.2 Transformation of 1st-order tensors 147
A.2 Legendre polynomials and spherical harmonics 149

B Radial Schrödinger equation **151**
B.1 Introduction 151
B.2 Continuum solutions 152
B.2.1 Free solution 152
B.2.2 Solution in short-range potentials 152
B.2.3 Solution in long-range potentials 153
B.3 Integrals for the harmonic oscillator model 154
B.4 Spherical Bessel and Coulomb functions 155
B.4.1 Spherical Bessel and Neumann functions 155
B.5 Spherical Coulomb functions 156
B.6 Numerical solution 156
B.6.1 The Numerov algorithm 156
B.6.2 Application of the Numerov algorithm 157

Bibliography **159**

1 Introduction

Electrons emitted from clusters contain rich information. Hence, photoelectron spectroscopy (PES) has been used since long in cluster physics. First experiments were performed on iron and cobalt clusters in 1986 [1], a few years later also on sodium clusters [2] and C_{60} [3, 4]. PES helps to distinguish ionization mechanisms (e.g., direct vs. thermal emission [5]). For direct emission processes, molecular-like spectra reflecting the single-particle and excited-state spectrum, can be observed up to cluster sizes of several hundreds of atoms. Shell closings and openings are clearly seen and estimations about the relative degeneracy of the single-particle states can be made. Furthermore, PES measurements as a function of photon energy give insight into spatial matrix elements of initial and final states. But PES is not only used to elucidate the electronic structure. In combination with theoretical predictions it also allows to make assumptions about the ionic structure of the investigated species [6, 7].

Information can also be gathered when resolving the direction of the outgoing electrons, thus measuring photoangular distributions (PAD), see, e.g., [8] on C_{60}. The PAD depends on the angular momentum coupling of initial and final state and is, in a direct process, strongly anisotropic. Similar to the PES, the behaviour of the PAD as a function of excitation parameters can indicate different ionization mechanisms. However, spectroscopic experiments are often performed in gas phase, i.e., on an ensemble of randomly orientated clusters. Measured PAD and PES are so orientation-averaged observables which complicates comparison with theory. One of the purposes of this work is therefore to provide efficient averaging procedures.

The achievements obtained in experimental techniques in the last decades boosted the progress is cluster physics anew. The velocity map imaging technique developed in 1997 by Eppink and Parker [9] enables a combined measurement of PES and PAD [10–14]. One may thus determine the order of the photon process and assign main angular momentum components to each feature seen in the PES [15]. One can also conclude about the general shape of the cluster. Deformation splits single-particle shells into several subshells of same angular momentum exhibiting thus similar PAD. Combined PES/PAD is nowadays applied even in a time-resolved manner [16]. Several competing ionization mechanisms acting on different time scales can so be discriminated fully in time, energy and space.

Also recent advances in attosecond physics [17–19] are expected to give an

important contribution to cluster physics. Benefitting from the effect of high-harmonic generation, one is now able to produce ultrashort laser pulses in the sub-femtosecond regime consisting of only a few cycles of the electromagnetic field, and so to resolve electron dynamics taking place on this time scale. Research in this currently strongly evolving field is still in its infancy.

From the theoretical perspective, the description of quantum many-body systems has experienced major changes, too. Starting with phenomenological shell models like the Clemenger-Nilsson model [20] for simple metal clusters, static many-body [21] and time-dependent perturbative approaches [22], full time-dependent many-body calculations [23, 24] determining the dynamical response of clusters are commonly performed today. This was, of course, made possible only by the enormous evolution of computing facilities in the past decades. A theoretical tool of choice is the time-dependent density-functional theory (TDDFT). The method derived in 1964 by Hohenberg and Kohn [25], is nowadays widely used to describe the electronic structure and dynamics in atoms, molecules, clusters and bulk material. This thesis deals with the calculation of PES and PAD from sodium and carbon clusters using TDDFT. It is outlined as follows:

- Chapter 2 gives an introduction into the theoretical framework: the many-body Schrödinger equation is separated into an ionic and electronic part. Several models for the ions (jellium, pseudo-potentials) and main features of density-functional theory for the description of electron dynamics are presented.

- Chapter 3 introduces tools and theory behind for numerical implementation of a laser field and for an efficient calculation of PAD and PES.

- Two procedures for determination of the orientation-averaged angular distribution are worked out in Chapter 4. The first analytical method is based on first-order perturbation theory. Euler rotations are needed.

- In Chapter 5 the developed methods are tested and first results are presented. Calculations in the one-photon regime using the jellium model and pseudo-potentials are directly compared for a variety of small sodium clusters. Moreover, emission observables are studied when laser frequencies below the ionization threshold are applied.

- Detailed analysis of the behaviour of the PAD as a function of the laser frequency is carried out in Chapter 6. The dependence of the PAD on initial and final state wavefunctions is studied within a spherical jellium model for Na_8 described by stationary perturbation theory. Increasingly refined levels

of theory are then considered up to the full time-dependent TDLDA using pseudo-potentials. Comparison with experimental results is performed for the negatively charged cluster Na_7^-.

- In the following Chapters 7 and 8 the fully fledged approach is finally applied to the buckminsterfullerene C_{60} and carbon chains. Basic properties like dipole response and electronic structure of these systems are studied. PES and PAD of C_{60} are calculated systematically as a function of laser intensity and frequency in one- as well as multiphoton regime. The chains are excited by an instantaneous boost.

2 Many-body theory in cluster physics

A single-element cluster X_N is a complex, quantum mechanical many-body system consisting of N nuclei of mass M and of charge $Z{\cdot}e$ each and $W = N{\cdot}Z$ electrons. The Schrödinger equation of the given system reads

$$\mathrm{i}\hbar\partial_t\Psi(\mathbf{R}_1,\ldots,\mathbf{R}_N,\mathbf{r}_1,\ldots,\mathbf{r}_W,t) = \hat{H}\Psi(\mathbf{R}_1,\ldots,\mathbf{R}_N,\mathbf{r}_1,\ldots,\mathbf{r}_W,t)\,, \qquad (2.1)$$

where $\mathbf{R}_1,\ldots,\mathbf{R}_N$ and $\mathbf{r}_1,\ldots,\mathbf{r}_W$ are the coordinates of the nuclei and the electrons, respectively. The Hamiltonian is given by:

$$\begin{aligned}\hat{H} = &\sum_{i=1}^{W}\frac{\hat{\mathbf{p}}_i^2}{2m_e} + \frac{1}{2}\sum_{i\neq j}^{W}\frac{e^2}{|\mathbf{r}_i-\mathbf{r}_j|} - \sum_{i=1}^{W}\sum_{I=1}^{N}\frac{Ze^2}{|\mathbf{r}_i-\mathbf{R}_I|}\\ &+\sum_{I=1}^{N}\frac{\hat{\mathbf{P}}_I^2}{2M} + \frac{1}{2}\sum_{I\neq J}^{N}\frac{Z^2e^2}{|\mathbf{R}_I-\mathbf{R}_J|}\,.\end{aligned}$$

The exact solution of the $3{\cdot}(N{+}W)$-dimensional equation (2.1) is already for small particle numbers only numerically possible and computational highly demanding. This is all the more so as soon as an external potential $\hat{V}_{\mathrm{ext}}(t)$ is applied to the system and the Hamiltonian and its solution become time-dependent. In practice, the external potential may be, e.g., a laser pulse, in theory it is usually a time-dependent, one-particle potential: $\hat{V}_{\mathrm{ext}} = \sum_{l=i,I}\hat{v}_l$. For the description of dynamical processes, it is therefore unavoidable to undergo approximations. Depending on the physical property of interest, two basic approximations can usually be applied without losing too much accuracy, but crucially simplify the problem:

- The decoupling of ionic and electronic motion:
  The mass of a nucleus is much larger than the electron mass, $M \gg m_e$. As a consequence, when forces are applied to the many-body system, electrons can react on a scale of attoseconds (10^{-18} s) while the ionic motion is much slower on the picosecond time scale (10^{-12} s). It is therefore justified to treat electronic and ionic motion separately. For electrons quantum mechanics is still used. The treatment of the ions, however, may differ from problem to problem. In many cases, in particular when dynamical processes within femtoseconds are considered, it is sufficient to treat the nuclei as point charges

fixed in space or – at the next level of accuracy – following the classical equations of motion.

- The valence electron approximation:
  Covalent and metallic clusters exhibit an electronic structure which permits to clearly divide the bound electrons into two groups, the core and the valence electrons. The core electrons are deep lying, localized electronic states while the valence electrons are less bound and, in particular in metallic clusters, strongly delocalized and shared among all nuclei. In these clusters the valence electrons establish the chemical bonding and determine the dynamical response after excitation, while the core electrons remain rather inert and insensitive to the molecular environment. It is therefore legitimate to treat the core electrons of each nucleus together with the latter as one inert core. This assumption applies of course only as long as the excitation energy/laser frequency remains below a certain threshold.

The above two assumptions simplify the original equation (2.1) to the $3 \cdot N_{\mathrm{val}}$-dimensional problem with the electronic (time-dependent) Hamiltonian

$$\hat{H}_{\mathrm{el}} = \sum_{i=1}^{N_{\mathrm{val}}} \frac{\hat{\mathbf{p}}_i^2}{2m_e} + \frac{1}{2} \sum_{i \neq j}^{N_{\mathrm{val}}} \frac{e^2}{|\mathbf{r}_i - \mathbf{r}_j|} + \hat{V}_{\mathrm{ext}}(t) + \hat{V}_{\mathrm{back}}(t) \; ,$$

where the background potential $\hat{V}_{\mathrm{back}}$ represents the positively charged cores. The quantum mechanical treatment is restricted to the valence electrons, for instance, in sodium to the $3s$ electrons and in carbon to the $2s$ and $2p$ electrons. The eliminated $2p$ state in Na lies at about $-2\,\mathrm{Ry}$, the $1s$ state in C at about $-20\,\mathrm{Ry}$ [26]. Below these excitation thresholds, ionization out of the core states may be neglected.

2.1 Ionic background

The potential which is generated by each core is not a simple, attractive Coulomb potential $-N_{\mathrm{val}} \cdot e^2/r$ since the core electrons induce also a repulsive force (Pauli repulsion) to the valence electrons. Moreover, even if the Pauli repulsion might be neglectable like in hydrogen, e.g., where it even vanishes completely, the singularity of the Coulomb-like core potential is still numerically hard to handle. Core pseudo-potentials represent here a helpful tool for accounting for both aspects, 1) considering the effect of the core electrons and ionic structure, and 2) providing an expression which is suitable for implementation on a three-dimensional numerical grid. Many realizations for pseudo-potentials already exist. They all

depend on the element X in question. Since this work also intends to study the impact of the ionic structure on electron dynamics, different approaches have been used.

Woods-Saxon potential In simple metals like alkali metals, valence electrons are very weakly bound. The ionic background which is seen by the valence electrons can then be considered as a smooth function, i.e., the point charges of the cores are smeared out and the charge distribution becomes homogeneous and time-independent. This kind of background model is called "jellium". The most simple jellium approach is to assume a homogeneously charged sphere of a certain width R_{jel} (spherical potential well). A more refined jellium model which is widely used in this work, is the so-called Woods-Saxon profile for the charge distribution [23]:

$$\rho_{\text{jel}}(\mathbf{r}) = \frac{3}{4\pi r_s^3}\left[1+\exp\left(\frac{r-\varrho(\vartheta,\varphi)}{\sigma_{\text{jel}}}\right)\right]^{-1} ,$$

with

$$\varrho(\vartheta,\varphi) = R_{\text{jel}}\left(1+\sum_{lm}\alpha_{lm}Y_{lm}(\vartheta,\varphi)\right) .$$

The only material quantities in this model are r_s and σ_{jel}. The parameter σ_{jel} gives the steepness of the charge distribution at $|\mathbf{r}| = R_{\text{jel}}$, e.g., the limit $\sigma_{\text{jel}} \to 0$ yields the step function. r_s is the Wigner-Seitz radius. The parameters α_{lm} allow also for a deformed distribution. Axial (prolate and oblate) systems are described by a non-zero parameter α_{20}, triaxial clusters by modification of α_{20} and α_{22}. The potential $\hat{V}_{\text{back}} = \hat{V}_{\text{jel}}$ is determined by solving the Poisson equation.

Although a very rough approximation, the jellium model was widely used for sodium clusters [21] and is still in use, nowadays even for more complex clusters like C_{60}. In this case, ions are smeared out over a spherical shell with a certain outer and inner radius [27]. In this specific case, however, the jellium model does not deliver the correct shell closings[1]. Hence, it has been applied throughout this work only for the sodium clusters with $r_s \approx 4\,a_0$ and $\sigma_{\text{jel}} \approx 1\,a_0$ (depending on size and shape of the cluster).

Local soft pseudo-potentials The Woods-Saxon potential neglects most of the effects which are caused by the explicit ionic structure. Therefore, a more sophisticated model has been developed by Kümmel *et al.* [28]. Here, the charge distribution of the cationic cores are described by two Gaussians, one representing

[1] Within the jellium model by Bauer *et al.* [27], a closed electron shell is obtained for a system of 250 valence electrons.

the attractive force of the positive charge of the cores, the other one representing the Pauli repulsion of the core electrons. The potential has then the form:

$$V_{\text{back}} = V_{\text{sps}}(r) = -\frac{Ze^2}{r} \sum_{i=1}^{2} c_i \operatorname{erf}\left(\frac{r}{\sqrt{2}\sigma_i}\right) ,$$

with

$$\operatorname{erf}(x) = \frac{2}{\sqrt{\pi}} \int_0^x dy \, \exp(-y^2) .$$

The advantage of this approach is that on the one hand it considerably improves agreement with experiments, on the other hand it is still numerically efficient due the locality of the potential. Moreover, it is now possible to propagate the cores. The ionic motion is described classically by molecular-dynamical methods. The short time spans studied in this work, however, allow to neglect dynamic effects due to the ions. Thus, the cores are always considered as fixed in space.

For sodium, the following parameters have been used: $Z = 1$, $c_1 = -2.292$, $c_2 = 3.292$, $\sigma_1 = 0.681\, a_0$, and $\sigma_2 = 1.163\, a_0$.

Goedecker-Teter-Hutter potentials Even more accurate pseudo-potentials have been provided by Goedecker *et al.* [29], here for all elements of the first two rows of the periodic table. The Goedecker potentials consist of a local and a non-local part:

$$V_{\text{back}} = V_{\text{goe}}(\mathbf{r}, \mathbf{r}') = V_{\text{loc}}(r) + V_{\text{nloc}}(\mathbf{r}, \mathbf{r}') ,$$

with

$$V_{\text{loc}}(r) = -\frac{Z}{r} \operatorname{erf}\left(\frac{r}{\sqrt{2} r_{\text{loc}}}\right) + \Gamma \exp\left(-\frac{r^2}{2 r_{\text{loc}}^2}\right) ,$$

and

$$\Gamma = C_1 + C_2 \left(\frac{r}{r_{\text{loc}}}\right)^2 + C_3 \left(\frac{r}{r_{\text{loc}}}\right)^4 + \left(\frac{r}{r_{\text{loc}}}\right)^6 ,$$

for the local part, and

$$V_{\text{nloc}}(\mathbf{r}, \mathbf{r}') = \sum_{i=1}^{2} Y_{00}(\Omega_r) p_i^{(0)}(r) h_i^{(0)} p_i^{(0)}(r') Y_{00}^*(\Omega_{r'}) - \sum_{m=-1}^{1} Y_{1m}(\Omega_r) p_1^{(1)}(r) h_1^{(1)} p_1^{(1)}(r') Y_{1m}^*(\Omega_{r'}) .$$

for the non-local part. The functions $p_1^{(0)}$, $p_2^{(0)}$, and $p_1^{(1)}$ are basically Gaussians of width $r^{(0)}$ and $r^{(1)}$, respectively. This gives ten parameters: r_{loc}, C_1, C_2, C_3,

C_4, $r^{(0)}$, $r^{(1)}$, $h_1^{(0)}$, $h_2^{(0)}$, and $h_1^{(1)}$. However, at most, seven free coefficients are necessary to specify the entire analytical form (in many cases even less are needed). Goedecker potentials fully realized with two s-projectors and one p-projector are in very good agreement with results obtained by all-electron calculations. Errors arising from the pseudo-potential approximation are often much lower than errors arising from DFT assumptions (e.g., from the local-density approximation). Nevertheless, the potential is non-local and reduces the speed of the calculation significantly. They are thus used only for calculations on carbon clusters where high precision is inquired.

So, the following values have been chosen: $Z = 4$, $r_{\mathrm{loc}} = 0.7\,a_0$, $C_1 = 0.0628$, $C_2 = -0.7079$, $r^{(0)} = 0.7\,a_0$, and $h_1^{(0)} = 0.7380\,\mathrm{Ry}$. The remaining coefficients are zero or obsolete, so that only one projector with $l = 0$ has been used here.

2.2 Electron dynamics: Density-functional theory

Since its development in 1964 by Hohenberg and Kohn[2] density-functional theory (DFT) has become a multi-disciplinary key tool for the theoretical description of electronic structure and dynamics in atoms and molecules, clusters and bulk material. As there exist many textbooks dealing with DFT in detail [30–33], this chapter provides only a basic introduction to the theoretical framework. For the sake of simplicity, the following considerations are at first restricted to the stationary problem.

2.2.1 Stationary density-functional theory

The stationary Schrödinger equation of any system of N interacting electrons[3] is given by:

$$\left\{\hat{T} + \hat{W} + \hat{V}\right\} |\Psi\rangle = E|\Psi\rangle\,, \tag{2.2}$$

with

$$\hat{T} = -\sum_{i=1}^{N} \frac{\hbar^2}{2m_e}\Delta_i \quad = \quad \text{kinetic energy and}$$

$$\hat{W} = \frac{1}{2}\sum_{i\neq j}^{N} \frac{e^2}{|\hat{\mathbf{r}}_i - \hat{\mathbf{r}}_j|} \quad = \quad \text{Coulomb interaction (2-particle interaction).}$$

[2] 1998 Nobel Prize in Chemistry for W. Kohn and J. A. Pople [30].

[3] The discussion is furthermore restricted to Coulomb-interacting many-electron systems. Actually, the formalism can also be developed for different interacting as well as bosonic systems.

$\hat{V}$ is an external (one-particle) potential representing for example the interaction of the valence electrons with the cores, and $\langle \mathbf{r}|\Psi\rangle = \Psi(\mathbf{r}_1, \ldots, \mathbf{r}_N)$ is the many-body wavefunction. The Schrödinger equation (2.2) constitutes a $3N$-dimensional differential equation. Its numerical solution becomes highly sophisticated even for small N. An alternative approach is therefore provided by the Hohenberg-Kohn theorem [25] which is the basis of DFT. The main statements of this theorem are:

1. The ground-state (g.s.) expectation value of any observable is a *unique* functional of the density, in particular,

$$E = E[n] = \underbrace{\langle \Psi[n]|\hat{T} + \hat{W}|\Psi[n]\rangle}_{=F_{\mathrm{HK}}[n]} + \int d^3r\, V(\mathbf{r}) n(\mathbf{r})\,.$$

   For a non-degenerate ground-state, also the wavefunction $|\Psi\rangle$ is determined by the density n, i.e., $|\Psi\rangle = |\Psi[n]\rangle$. For a degenerate ground-state this map does not exist, obviously. In this case, however, one can show that E is still a functional of n and $|\Psi[n]\rangle$ denote any of the possible g.s. wavefunctions related to the density n.

2. If the kinetic energy $\hat{T}$ and the two-particle interaction $\hat{W}$ are specified, the g.s. density n determines the external, local potential $\hat{V}$, thus the full Hamiltonian.

From the first statement one could, in principle, find the ground-state of a given system by variation of the energy functional with respect to the density.[4] The problem is that the functional F_{HK} is not known, in general. One therefore goes further by combining the two statements:

3. For any interacting system there exists an auxiliary system of non-interacting particles moving in an effective, local *single-particle* potential (mean-field potential):[5]

$$E_s[n] = T_s[n] + \int d^3r\, V_s(\mathbf{r}) n(\mathbf{r})\,,$$

   with

$$T_s[n] = \langle \Psi_s[n]|\hat{T}|\Psi_s[n]\rangle\,, \quad \text{and} \quad W_s \equiv 0\,.$$

   The auxiliary many-body wavefunction $|\Psi_s\rangle$ delivers the exact g.s. density $n = \Psi^\dagger\Psi = \Psi_s^\dagger\Psi_s$ and the exact energy $E = E_s$.

[4] By construction, the Hohenberg-Kohn theorem is only valid for g.s. densities which are solutions of the Hamiltonian in Eq. (2.2) with a local, external potential V. In order to derive a variational principle, one has to ascertain that V exists for each trial density, i.e., the trial density is V-representable. For details, see [31].

[5] This implies V-representability of the g.s. density in both systems.

Assuming furthermore that the electronic density $n(\mathbf{r})$ can be written in terms of single-particle orbitals (i.e., the density is N-representable),

$$n(\mathbf{r}) = \sum_{\alpha} \varphi_{\alpha}^{\dagger}\varphi_{\alpha} \,, \quad \langle\varphi_{\alpha}|\varphi_{\beta}\rangle = \delta_{\alpha\beta} \,,$$

which is possible for any non-negative density [34], one can derive a variational scheme in the auxiliary system with respect to the single-particle orbitals (under condition of ortho-normalization of the φ_{α}), the so-called Kohn-Sham scheme [35]. The Kohn-Sham scheme decouples the $3N$-dimensional differential equation (2.2) into N three-dimensional equations and the kinetic energy functional can be given exactly:

$$\left\{-\frac{\hbar^2}{2m_e}\Delta + V_{\text{K.S.}}[n](\mathbf{r})\right\}\varphi_{\alpha}[n](\mathbf{r}) = \epsilon_{\alpha}\varphi_{\alpha}[n](\mathbf{r}) \,, \quad \forall\alpha \in \{1,\ldots,N\} \,.$$

The potential $V_{\text{K.S.}} = V_s$ is conventionally decomposed into a Hartree term, i.e., the mean Coulomb interaction between the particles, an external potential and an exchange-correlation term which accounts for the exchange energy and the two-particle character of the Coulomb interaction,

$$\hat{V}_{\text{K.S.}} = \hat{V}_{\text{ext}} + \hat{V}_{\text{H}} + \hat{V}_{\text{xc}} \,,$$

with

$$V_{\text{xc}}[n](\mathbf{r}) = \left.\frac{\delta E_{\text{xc}}[n']}{\delta n'(\mathbf{r})}\right|_{n'=n} \,, \quad \text{and} \quad V_{\text{H}}[n](\mathbf{r}) = \int d^3r' \frac{e^2}{|\mathbf{r}-\mathbf{r}'|} n(\mathbf{r}') \,.$$

Unfortunately, an analytical expression for $\hat{V}_{\text{xc}}$ is not known up to present times. The development of suitable, approximate exchange-correlation functionals/potentials remains as the main task in DFT.

A word on the physical meaning of the Kohn-Sham orbitals: from the above derivation of the Kohn-Sham (K.S.) equations, it is clear that the K.S. orbitals and eigenvalues are just constructed auxiliary quantities which have, in general, little physical meaning. Nevertheless, it can be shown (in case that $\hat{V}_{\text{xc}}$ is exact) that the highest occupied eigenvalue ϵ_{HOMO} of the N-particle K.S. system corresponds to the exact ionization potential (Koopmans' theorem [36]):[6]

$$\text{IP} = E_N[n_N] - E_{N-1}[n_{N-1}] \simeq -\epsilon_{\text{HOMO}} \,, \tag{2.3}$$

[6] The ionization potential of the non-interacting K.S. system is by definition $\text{IP}_{\text{K.S.}} = -\epsilon_{\text{HOMO}}$. However, for any finite system the density decays exponentially as $n_{\text{K.S.}} \to \exp(-\alpha\sqrt{\text{IP}_{\text{K.S.}}}r)$ for large r [37, 38]. Since $n_{\text{K.S.}} = n$, real and auxiliary system have the same ionization potentials $\text{IP} = \text{IP}_{\text{K.S.}}$.

where n_N and n_{N-1} are the g.s. densities of the systems with N or $N-1$ electrons, respectively. Moreover, the deeper lying eigenvalues can be interpreted as approximate vertical ionization potentials [39–41] (if the exchange-correlation functional is accurate enough), eigenvalue differences as approximations for excitation energies. Anyway, the static K.S. eigenvalues cannot account for dynamic and collective effects in the course of photoionization. These effects require time-dependent calculations.

The energy functional is also defined for fractional particle numbers [42]. If E_{xc} is exact, the ground-state energy E_N as a function of fractional particle numbers N consists of a straight line between integers, and possible derivative discontinuities at integers [31]. Hence, following Koopmans' theorem the gradient of the energy functional E_N between N and $N-1$ corresponds then to the IP.

2.2.2 Local-density approximation

Since the exact exchange-correlation functional is not known, it has to be approximated. $V_{\mathrm{xc}}[n](\mathbf{r})$ is local in space, but in general highly non-local in the density,

$$V_{\mathrm{xc}}[n](\mathbf{r}) = V_{\mathrm{xc}}(n(\mathbf{r}), \nabla n(\mathbf{r}), \ldots; \mathbf{r}) \,,$$

as it depends on the density at all coordinates $\mathbf{r} \in \mathbb{R}^3$. The most common used approximation is therefore to truncate this dependence, i.e.,

$$V_{\mathrm{xc}}^{(\mathrm{LDA})}[n](\mathbf{r}) = V_{\mathrm{xc}}(n(\mathbf{r}); \mathbf{r}) \,, \quad \text{and} \quad E_{\mathrm{xc}}^{(\mathrm{LDA})}[n] = \int d^3r \, n(\mathbf{r}) V_{\mathrm{xc}}(n(\mathbf{r}); \mathbf{r}) \,.$$

This approximation is called the local-density approximation (LDA), since the potential depends only on the density at the coordinate where it is evaluated. Obviously, the approximation is legitimate for weakly varying n. Nevertheless, it is also often used for strongly inhomogeneous systems like atoms and molecules where it produces remarkable good results.

The LDA exchange-correlation potential is conventionally separated into an exchange term v_{x} and the correlation v_{c}. Within the LDA approximation v_{x} can be given exactly (Slater-Dirac exchange). Since v_{x} depends only on the density n at $\mathbf{r}$, it can be considered as piecewise function defined on infinite small intervals in which the density remains constant, i.e., homogeneous. The exchange energy per particle of an homogeneous electron gas has the simple, analytical form [43, 44]:

$$v_{\mathrm{x}}(n) = -\frac{3e^2}{4} \left(\frac{3}{\pi} \right)^{1/3} n^{1/3} \,.$$

Analytical expressions for v_c are not known, thus plenty of different correlation functionals are available nowadays. In this work the (local) representation by Perdew and Wang [45] (PW92) is used consistently.

2.2.3 Self-interaction correction

One major problem of LDA is that the mean-field falls off exponentially at large r and not like $1/r$ is it should be, in short is does not produce a physical potential. As a consequence, the ionization potential is always underestimated and Koopmans' theorem is violated (E_N as a function of fractional particle numbers is usually convex) [33]. However, especially for ionization processes, a correct long-range description is all the more important, since outgoing electrons surely feel the Coulomb tail of the potential.

In contrast, the Hartree-Fock theory (HF) shows the right asymptotic behaviour. The reason for this is that HF accounts for the fact that an electron cannot interact with itself. The self-interaction in the Hartree energy,

$$E^{\mathrm{SI}} = \sum_\alpha \int d^3r \int d^3r'\, n_\alpha(\mathbf{r}) \frac{e^2}{|\mathbf{r}-\mathbf{r}'|} n_\alpha(\mathbf{r}') \;, \quad n_\alpha = \varphi_\alpha^\dagger \varphi_\alpha \;,$$

is cancelled by the Fock term. In order to overcome this problem in LDA self-interaction corrections (SIC) has been developed over the years. An obvious scheme has been proposed by Perdew and Zunger [46] by simply subtracting the contribution produced by a single electron:

$$E_{\mathrm{xc}}^{\mathrm{SIC}} = E_{\mathrm{xc}}^{(\mathrm{LDA})}[n] - \sum_\alpha E_{\mathrm{H}}[n_\alpha] - \sum_\alpha E_{\mathrm{xc}}^{(\mathrm{LDA})}[n_\alpha] \;.$$

The problem is now that the exchange-correlation functional depends not only on the full density n, but also on n_α. Variation under the condition of ortho-normality of the φ_α leads to a set of coupled equations [47],

$$\hat{h}_{\mathrm{K.S.}}^{(\alpha)} |\varphi_\alpha) = \sum_\beta \lambda_{\alpha\beta} |\varphi_\beta) \;,$$

which again is computationally expensive to solve.

Perdew and Zunger [46] also referred to an alternative, much simpler SIC, the average density SIC (ADSIC) [48]. The single-orbital density n_α is here approximated by n/N and the same for all orbitals,

$$E_{\mathrm{xc}}^{\mathrm{ADSIC}}[n](\mathbf{r}) = E_{\mathrm{xc}}^{(\mathrm{LDA})}[n] - N \cdot E_{\mathrm{H}}\left[\frac{n}{N}\right] - N \cdot E_{\mathrm{xc}}^{(\mathrm{LDA})}\left[\frac{n}{N}\right] \;.$$

The exchange-correlation functional depends then on the density only, consequently the variational principle yields again decoupled differential equations like for bare LDA. It turned out that this SIC is especially suited for systems in which the considered electrons occupy the same spatial and energetic range, e.g., in simple metal clusters [49]. On the other hand, it does not correctly describe phenomena in inhomogeneous systems, e.g., dissociation and polarization, and in large systems where $n/N \to 0$. Nevertheless, ADSIC restores the correct asymptotic behaviour of the exchange-correlation potential and Koopmans' theorem [46]. The single-particle energies are downshifted compared to LDA and calculated IPs agree better with experiments.

All in all, ADSIC appears favorable compared to other correction schemes for the description of the photoionization processes considered here. In combination with LDA it provides a reasonable and efficient approximation of the exchange-correlation functional. It has been used throughout this work.

2.2.4 Time-dependent density-functional theory

In 1984, Runge and Gross [50] extended the stationary DFT to time-dependent problems. The proof of the time-dependent analogous to the Hohenberg-Kohn theorem is more involved. The reason for this is that the total energy is not conserved in time-dependent systems. Thus, there is no variational principle on the basis of the total energy functional. On the other hand, the time-dependent Schrödinger equation can be derived through the calculation of the stationary points of the action:

$$S = \int dt \, \langle \Psi(t) | \hat{H} - \mathrm{i}\hbar\partial_t | \Psi(t) \rangle \; .$$

Runge and Gross [50] showed now that S is a unique functional of the time-dependent density $n(\mathbf{r}, t)$ and derived the time-dependent equations of an auxiliary, non-interacting system upon condition of V-representability of n:

$$\mathrm{i}\hbar\partial_t \varphi_\alpha(\mathbf{r}, t) = \left[-\frac{\hbar^2}{2m_e}\Delta + V_{\mathrm{K.S.}}[n](\mathbf{r}, t) \right] \varphi_\alpha(\mathbf{r}, t) \; .$$

The auxiliary density equals again the exact one. The exchange-correlation potential $V_{\mathrm{xc}}[n](\mathbf{r}, t)$ is not the same than in the stationary case, since it depends also on the densities at all past times ("memory" effect). To circumvent this difficulty one often uses an adiabatic approximation at this point:

$$V_{\mathrm{xc}}^{\mathrm{ad}}[n](\mathbf{r}, t) = V_{\mathrm{xc}}[n](\mathbf{r})|_{n=n(t)} \; .$$

This is acceptable if the considered processes are slow compared to the correlation effects.

2.3 Summary

Time-dependent density-functional theory augmented by a self-interaction correction provides a versatile tool to describe dynamics of molecules and clusters. The work in hand uses TDDFT at the level of TDLDA with the correlation functional "PW92" improved by ADSIC, all in adiabatic approximation so that memory effects are neglected. The exchange-correlation functional thus remains fully local and decouples the $3N$-dimensional Schrödinger equation into N three-dimensional time-dependent K.S. equations. All functionals are actually used as functionals of spin-densities, so that spin-unpaired systems can be calculated likewise. The set of g.s. single-particle wavefunctions $\varphi_\alpha(t = 0)$ is found by standard iterative techniques [51] on a numerical grid in three-dimensional coordinate space. The time-evolution $\varphi_\alpha(t) \longrightarrow \varphi_\alpha(t+\delta t)$ is performed for sufficiently small time steps δt by splitting the quantum mechanical, exponential propagator (T-V-splitting) [52]. The kinetic energy is evaluated in Fourier space via fast Fourier transformation. The ionic background (nuclei plus core electrons) is either described through the jellium model or through pseudo-potentials. The cluster ions (if explicit ionic background) are frozen which is legitimate for the short time spans used here.

3 Excitation and analysis tools

This chapter provides insight into the numerical tools used and developed in this work. The discussion is focused on the photoemission observables obtained after laser excitation, i.e., the numerical calculation of PES and PAD.

3.1 Gauges and dipole approximation

The classical Hamiltonian of an electron in an electromagnetic field is [53, 54]

$$H = \frac{1}{2m_e}\left(\mathbf{p} - \frac{e}{c}\mathbf{A}\right)^2 + e\Phi\,, \tag{3.1}$$

with $\mathbf{p}$ being the kinetic momentum of the electron. The vector potential $\mathbf{A}(\mathbf{r},t)$ and the scalar potential $\Phi(\mathbf{r},t)$ of the radiation field are defined by:

$$\mathbf{E} = -\frac{1}{c}\frac{\partial \mathbf{A}}{\partial t} - \nabla\Phi\,, \qquad \mathbf{B} = \nabla \times \mathbf{A}\,. \tag{3.2}$$

Electric and magnetic part of the radiation field solve Maxwell's equations in vacuum and the wave equation:

$$\left[\frac{1}{c^2}\frac{\partial^2}{\partial t^2} - \Delta\right]\mathbf{E}(\mathbf{r},t) = 0\,.$$

Assuming a linearly polarized field, $\mathbf{E}$ is then given by $\mathbf{E}(\mathbf{r},t) = \mathbf{e}_{\mathrm{pol}}E_0\sin(\omega_{\mathrm{las}}t - \mathbf{kr})$, where $\mathbf{e}_{\mathrm{pol}}\mathbf{k} = 0$ and $\omega_{\mathrm{las}} = c\cdot k$. $\mathbf{k}$ is the wave vector and $k = |\mathbf{k}|$ the wave number. In first quantization one replaces in Eq. (3.1)

$$\mathbf{p} \longrightarrow \hat{\mathbf{p}} = \frac{\hbar}{\mathrm{i}}\nabla\,, \qquad H \longrightarrow \hat{H} = \mathrm{i}\hbar\partial_t\,,$$

and obtains the Schrödinger equation:

$$\mathrm{i}\hbar\partial_t\Psi(\mathbf{r},t) = \left[\frac{1}{2m_e}\left(\hat{\mathbf{p}} + \frac{e}{c}\mathbf{A}\right)^2 + e\Phi\right]\Psi(\mathbf{r},t)\,.$$

In contrast to the physical observables $\mathbf{E}$ and $\mathbf{B}$, the potentials $\mathbf{A}$ and Φ are not unique in the sense that $\mathbf{E}$ and $\mathbf{B}$ remain unchanged when applying a so-called *gauge transformation* of the following form:

$$\mathbf{A} \longrightarrow \mathbf{A}' = \mathbf{A} + \nabla\chi\,, \qquad \Phi \longrightarrow \Phi' = \Phi - \frac{1}{c}\dot{\chi}\,,$$

where $\chi = \chi(\mathbf{r}, t)$ is an arbitrary scalar potential. In order to retain the form of the Schrödinger equation, the wavefunction transforms simultaneously like

$$\Psi \longrightarrow \Psi' = \exp\left(\frac{\mathrm{i}e}{\hbar c}\chi\right)\Psi \,.$$

The gauge freedom allows to choose certain constraints for $\mathbf{A}$ and Φ. For example in vacuum, one often makes use of the Coulomb gauge $\nabla\mathbf{A}^{(c)} \equiv 0$. The scalar potential $\Phi^{(c)}$ is then given by

$$\Phi^{(c)}(\mathbf{r}, t) = \int d^3r' \, \frac{\rho(\mathbf{r}', t)}{|\mathbf{r} - \mathbf{r}'|}$$

and vanishes because of absence of charges. For charged particles in an electromagnetic field, however, $\Phi^{(c)}$ becomes zero only far away from the particles. In this case, it is better to use other gauges. One suitable gauge is the so-called *velocity gauge*: $\Phi^{(v)} \equiv 0$. Inserting $\Phi^{(v)}$ into Eq. (3.2) determines the vector potential $\mathbf{A}^{(v)}(\mathbf{r}, t)$. Furthermore, if the system is small compared to the wavelength of the radiation light, i.e., $\mathbf{kr} \ll 1$, the electric field can be approximately considered as space-independent: $\mathbf{E}(t) = \mathbf{e}_{\mathrm{pol}} E_0 \sin(\omega_{\mathrm{las}} t)$. $\mathbf{A}^{(v)}$ becomes then a function of time only:

$$\mathbf{A}^{(v)}(t) = -c\mathbf{e}_{\mathrm{pol}} E_0 F(t) \,,$$

with

$$F(t) = \int_{-\infty}^{t} dt' \, f(t') = \int_{-\infty}^{t} dt' \sin(\omega_{\mathrm{las}} t') \,.$$

Another possible gauge is the *length gauge* (also known as *temporal* or *Weyl gauge*). Here the vector potential is set to zero $\mathbf{A}^{(r)} \equiv 0$. Equation (3.2) gives now the scalar potential and interaction term in the dipole approximation:

$$\Phi^{(r)} = -\mathbf{e}_{\mathrm{pol}} E_0 \sin(\omega_{\mathrm{las}} t)\mathbf{r} \quad \text{and} \quad \hat{H}_{\mathrm{int}}^{(r)} = -e\mathbf{e}_{\mathrm{pol}} E_0 \sin(\omega_{\mathrm{las}} t)\mathbf{r} \,.$$

A third, but rarely used gauge is the *acceleration gauge* (*Kramers-Henneberger frame*), for details see Sect. 6.2.2.3. All gauges are fully equivalent. The gauge transformation, e.g., from velocity to length gauge reads as follows:

$$\begin{aligned} & \mathbf{A}^{(v)} = \nabla\chi \quad \Longrightarrow \quad \chi = -cE_0\mathbf{e}_{\mathrm{pol}}\mathbf{r}F(t) \\ \textit{check:} \qquad & \Phi^{(r)} = \frac{1}{c}\dot{\chi} \quad \Longrightarrow \quad \Phi^{(r)} = -E_0\mathbf{e}_{\mathrm{pol}}\mathbf{r}\sin(\omega_{\mathrm{las}}t) \\ & \quad \Longrightarrow \quad \Psi^{(r)} = \Psi^{(v)} e^{\mathrm{i}E_0\mathbf{e}_{\mathrm{pol}}\mathbf{r}F(t)} \end{aligned} \tag{3.3}$$

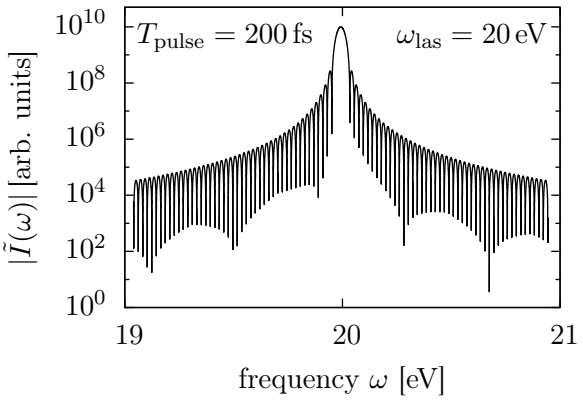

T_{pulse} [fs]	σ_{las} [eV]
10	4.4×10^{-1}
30	1.6×10^{-1}
60	8.3×10^{-2}
75	6.8×10^{-2}
200	2.7×10^{-2}
1000	5.8×10^{-3}

Figure 3.1: Intensity spectrum $|\tilde{I}(\omega)|$ of a laser pulse of the form (3.4) with $\omega_{\text{las}} = 20\,\text{eV}$ and $T_{\text{pulse}} = 200\,\text{fs}$. The resolution σ_{las} for some sample pulse lengths is shown in the right table. There exists an exponential relation between T_{pulse} and σ_{las}. The intensity is given by $I(t) = \frac{c}{8\pi}|\mathbf{E}(t)|^2$.

In the dipole approximation the electric field is active in the whole numerical box. This might lead to problems in the analysis of the kinetic energy of the outgoing electrons since one actually assumes that the electrons are field-free with the Hamiltonian $\hat{H} = \mathbf{p}^2/2m_e$. In length gauge, a simple solution is to apply a radial cut-off of the electric field in coordinate space. However, it is not clear how to choose the cut-off radius. In contrast, in velocity gauge as it is shown in Sect. 3.5, the wavefunction of the outgoing electron moving in the external electromagnetic field basically corresponds to the field-free solution augmented by a simple phase factor. This factor can be easily eliminated in the analysis.

3.2 Pulse profile

As already mentioned above, the electric field $\mathbf{E}(t)$ is described in dipole approximation:

$$\mathbf{E}(t) = \mathbf{e}_{\text{pol}} E_0 \sin(\omega_{\text{las}} t) \cdot g(t)\,, \tag{3.4}$$

with

$$g(t) = \sin^2\left(\frac{t}{T_{\text{pulse}}}\,\pi\right)\Theta(t)\Theta(T_{\text{pulse}} - t)\,. \tag{3.5}$$

The time dependence is augmented by the pulse envelope function $g(t)$. In this work a $\sin^2$-shape is used consistently. The relation between total pulse length T_{pulse} and full width at half maximum (FWHM) is then: $\text{FWHM} = T_{\text{pulse}}/3$.

Figure 3.1 shows the intensity spectrum $|\tilde{I}(\omega)|$ for a sample laser pulse of $T_{\text{pulse}} = 200\,\text{fs}$ and $\omega_{\text{las}} = 20\,\text{eV}$. As it is the case for all finite pulses in time, the frequency content is not a sharp $\delta(\omega - \omega_{\text{las}})$-function, but broadened. The width σ_{las} as a function of ω_{las} is given by,

$$\sigma_{\text{las}}^2 = \int_0^\infty \mathrm{d}\omega\, (\omega - \overline{\omega})^2\, |\tilde{I}(\omega)|\,,$$

with $\overline{\omega}$ being the expectation value for the laser frequency ($\overline{\omega} = \omega_{\text{las}}$). The table in Fig. 3.1 gives the resolution σ_{las} for some pulse lengths at $\omega_{\text{las}} = 20\,\text{eV}$.

3.3 Determination of the emitted density

After excitation of the system, electrons eventually reach the edge of the numerical box. In order to prevent reflection, absorbing boundaries are applied. After each time step from t to $t + \delta t$, $\varphi_\alpha(\mathbf{r}, t) \longrightarrow \tilde{\varphi}_\alpha$, the electronic wavefunctions $\tilde{\varphi}_\alpha$ are multiplied by a mask function $\mathcal{M}(\mathbf{r})$, $\varphi_\alpha(\mathbf{r}, t + \delta t) = \mathcal{M}(\mathbf{r})\tilde{\varphi}_\alpha$. This procedure was found to be equivalent to the addition of an imaginary potential to the time-evolution Hamiltonian. Moreover, it turned out to be an efficient and reliable method for simulating absorbing boundaries [55] and has been extensively tested [24, 56, 57]. A spherical symmetric function of kind

$$\mathcal{M}(r) = \Theta(r_{\text{min}} - r) + \Theta(r - r_{\text{min}})\Theta(r_{\text{max}} - r)\cos^p\left(\frac{\pi}{2} \cdot \frac{r - r_{\text{min}}}{r_{\text{max}} - r_{\text{min}}}\right)$$

is especially suitable for determination of angular distributions, see Fig. 3.2 for illustration. r_{max} is the distance from the origin to the box edge, r_{min} the distance from the origin to the point where absorption starts. Typical values are between $0.0635 - 0.25$ for the power p, and `nabsorb` $\approx 8-12$ for the width of the absorbing layer in units of Δx. The absorbed s.p. densities are accumulated after each time step at each grid point:

$$n_{\text{abso},\alpha}(\mathbf{r}) = \int_0^{T_{\text{end}}} dt\, |\tilde{\varphi}_\alpha(\mathbf{r}, t)|^2 - |\varphi_\alpha(\mathbf{r}, t)|^2\,.$$

Summation over all states gives finally the total emitted density $n_{\text{abso}}(\mathbf{r}) = \sum_\alpha n_{\text{abso},\alpha}$, while integration over the numerical box yields the total number of emitted electrons, $N_{\text{esc}} = \int d^3r\, n_{\text{abso}}$.

The above real-space mask function is a very efficient tool to simulate absorbing boundaries at low computational cost. However, it has also some disadvantages,

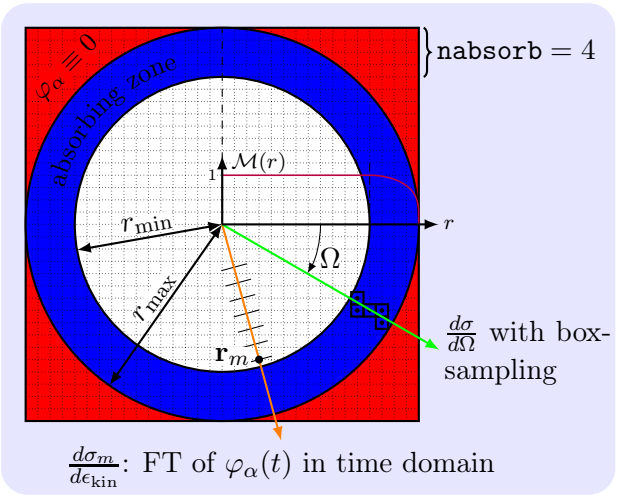

Figure 3.2: Illustration of the spherical absorbing boundaries. The parameter `nabsorb` $= (r_{\max} - r_{\min})/\Delta x$ gives the width of the absorbing layer. The cross-section $d\sigma/d\Omega$ can be calculated through representation of each absorption point with a weight function $\mathcal{W}$ (in the figure box-like). The measuring points $\mathbf{r}_m$ of the PES are just before the boundary starts.

e.g., its energy-dependent absorption: while emitted electrons with high kinetic energy are well absorbed, parts of the low-energy electrons may be reflected. The reason for this is that electrons with low kinetic energy have also a large wavelength. As a consequence, they do not "see" the smooth transition of the mask function from one to zero, but rather an instantaneous step which leads to the reflection of the wave.

Another aspect is that the mask function ensures in any case absorption of electronic density near the edge of the numerical box. However, this is not always a wanted feature. In particular, weakly bound states close to the continuum generally have wavefunctions with long-ranging Coulomb tails. The same applies for electrons excited into a long-ranging bound state or strongly excited clusters with high electronic density close to the numerical edge. Although this electronic density would not be emitted and might, in reality, return to the center of the numerical box, the mask function removes it.

Concluding, for the here considered systems and ionization regimes the use of a real-space mask function is legitimate. In general, however, one should exercise caution when considering less bound systems like negatively charged clusters and/or excitations which are strong or close to the ionization threshold. In these cases, one better uses either very large boxes or other absorbing boundaries which distinguish between bound and continuum states and adapt to the kinetic energy of the emitted electron.

3.4 Determination of photoangular distributions

The spherical absorbing mask gives an accumulated absorbed density $n_{\mathrm{abso}}(\mathbf{r})$ on the three-dimensional Cartesian grid of the numerical box:

$$n_{abc} = n_{\mathrm{abso}}(\mathbf{r}_{abc}) \,,$$
$$\mathbf{r}_{abc} = a \cdot \Delta x\, \mathbf{e}_x + b \cdot \Delta y\, \mathbf{e}_y + c \cdot \Delta z\, \mathbf{e}_z \,, \quad a,b,c = [-L/(2\Delta x), \ldots, L/(2\Delta x)] \,.$$

In order to transform the Cartesian into an angular distribution $d\sigma/d\Omega$, $\Omega = (\vartheta, \varphi)$, one has to define a mapping procedure $\mathcal{M} : n_{\mathrm{abso}}(\mathbf{r}) \longrightarrow d\sigma/d\Omega$. One possibility is to use a weight function $\mathcal{W}$ acting on each grid point $\mathbf{r}_{abc}$:

$$N_{\mathrm{esc}} = \Delta V \sum_{abc} n_{abc} = \Delta V \sum_{abc} n_{abc} \int d^3r\, \mathcal{W}_{abc}(\mathbf{r}) = \Delta V \sum_{abc} n_{abc} \int d^3r\, \mathcal{W}(\mathbf{r}; \mathbf{r}_{abc}) \,,$$

$\Delta V = \Delta x\, \Delta\, y \Delta\, z$. The function $\mathcal{W}(\mathbf{r}; \mathbf{r}_{abc}) = \mathcal{W}(\mathbf{r} - \mathbf{r}_{abc})$ has to be normalized to unity,

$$\int d^3r\, \mathcal{W}(\mathbf{r}) \stackrel{!}{=} 1 \,.$$

Using $N_{\mathrm{esc}} = \int d\Omega\, d\sigma/d\Omega$, the angular distribution becomes:

$$\frac{d\sigma}{d\Omega} = \Delta V \sum_{abc} n_{abc} \int dr\, r^2 \cdot \mathcal{W}(r\mathbf{e}_r - \mathbf{r}_{abc}) \,,$$

where $\mathbf{e}_r = (\sin\vartheta\cos\varphi, \sin\vartheta\sin\varphi, \cos\vartheta)$. It is convenient to use a regular grid in r, ϑ and φ. Several sampling functions are possible, for example:

- δ-function: $\mathcal{W}(\mathbf{r}) = \delta^{(3)}(\mathbf{r})$,
- box-like function:

$$\mathcal{W}(\mathbf{r}) = \frac{1}{\Delta V} \Theta(|x| - \Delta x/2)\Theta(|y| - \Delta y/2)\Theta(|z| - \Delta z/2) \,,$$

- tent-like function:

$$\mathcal{W}(\mathbf{r}) = \frac{1}{(\Delta V)^2} \max(\Delta x - |x|, 0) \max(\Delta y - |y|, 0) \max(\Delta z - |z|, 0) \,,$$

- Gaussian function:

$$\mathcal{W}(\mathbf{r}) = \left(\frac{\lambda}{\pi}\right)^{3/2} e^{-\lambda(x^2+y^2+z^2)} \,.$$

In this work the tent-function is used since it delivers very smooth pictures. In fact, the box-like (see also Fig. 3.2) and tent-like function perform quite similarly in this way. The δ-function is irregular and noisy, briefly not suitable, while the Gaussian function adds isotropic background to the distribution.

Another possibility to determine the angular distribution $d\sigma/d\Omega$ is to expand $n_{\mathrm{abso}}(\mathbf{r})$ into spherical harmonics. The expansion coefficients are then given by:

$$c_{lm} = \int d\Omega\, Y_{lm}(\vartheta\varphi)\frac{d\sigma}{d\Omega} = \Delta V \sum_{abc} n_{abc} \int d^3r\, \frac{\mathcal{Y}_{lm}(\mathbf{r})}{r^l}\mathcal{W}(\mathbf{r}-\mathbf{r}_{abc})\,.$$

In the last expression $Y_{lm}(\vartheta\varphi)$ has been replaced by its corresponding harmonic polynomial $\mathcal{Y}_{lm} = r^l Y_{lm}$ which is a function of Cartesian coordinates. For $\mathcal{W}$ one may choose the δ-function since its delivers already accurate results when integrating over a sufficiently large absorbing layer. This yields the closed expression:

$$c_{lm} = \Delta V \sum_{abc} n_{abc} \frac{\mathcal{Y}_{lm}(\mathbf{r}_{abc})}{\mathbf{r}_{abc}}\,.$$

The summation can be restricted to the absorbing layer excluding the singularity at the origin. Depending on the ionization regime, the spherical expansion may be truncated after a few c_{lm}.

3.5 Determination of photoelectron spectra

Photoelectron spectra are calculated at a measuring point $\mathbf{r}_m$ right before the absorbing boundaries, see Fig. 3.2. The measuring point $\mathbf{r}_m$ is far away from the cluster so that the Kohn-Sham potential is negligible there. Since the laser field is described in dipole approximation, photoelectrons are basically charged particles in an electromagnetic field whose Hamiltonian reads in length gauge:

$$\hat{H}\Psi(\mathbf{r}_m,t) = \left[-\frac{\hbar^2}{2m_e}\Delta - eE_0\,\mathbf{e}_{\mathrm{pol}}\cdot\mathbf{r}_m f(t)\right]\Psi(\mathbf{r}_m,t)\,. \tag{3.6}$$

Assuming that the laser pulse already stops long before photoelectrons reach the measuring point and the boundaries, the second term in Eq. (3.6) vanishes and photoelectrons are purely free particles. For the sake of simplicity, the following considerations are made in one dimension.

A specific solution of the one-dimensional time-dependent Schrödinger equation at z_m is the plane wave, a general solution is then:

$$\Psi(z_m,t) = \int dk\,\Phi_m(k)e^{\mathrm{i}(kz_m-\epsilon_{\mathrm{kin}}t/\hbar)}\,,\quad \epsilon_{\mathrm{kin}} = \frac{(\hbar k)^2}{2m_e}\,.$$

$|\Phi_m(k)|^2$ is the probability to find a particle with wave number k at point z_m, i.e., the cross-section $d\sigma_m/d\epsilon_{\text{kin}} = |\Phi_m(k)|^2$. The exact procedure to find $|\Phi_m(k)|^2$ is a Fourier transformation in space:

$$\int\limits_{|z-z_m|=\delta} dz\, \Psi(z,t)e^{-ikz} = \Phi_m(k)e^{-i\epsilon_{\text{kin}}t/\hbar} \quad \Longrightarrow \quad \Big|\int\limits_{|z-z_m|=\delta} dz\, \Psi(z,t)e^{-\mathrm{i}kz}\Big|^2 = |\Phi_m(k)|^2 \,.$$

The Fourier transformation in space has to be restricted to a volume around z_m where the particle propagates freely so that the spectral decomposition of the wave remains more or less constant[7]. The volume should be large in order to have enough resolution in k-space. In three dimensions, however, even for a small volume around the measuring point it is numerically too expensive to evaluate the PES in this way, since the wavefunction has to be stored for every time step at every needed point. PES are thus calculated by a Fourier transformation in the time domain:

$$\tilde{\Psi}(z_m,\omega) = \int dt\, e^{\mathrm{i}\omega t} \int dk\, \Phi_m(k) e^{\mathrm{i}(kz_m - \epsilon_{\text{kin}}t/\hbar)} = \int dk \underbrace{\delta\left(\omega - \frac{\hbar k^2}{2m_e}\right)}_{=\delta(k-\sqrt{2m_e\omega/\hbar})+\delta(k+\sqrt{2m_e\omega/\hbar})} \Phi_m(k) e^{\mathrm{i}kz_m} \,. \tag{3.7}$$

The second term in the last expression vanishes, if assuming only outgoing waves, $k > 0$. Hence, the transformation yields:

$$|\tilde{\Psi}(z_m,\omega)|^2 = |\Phi_m(k_\omega)e^{\mathrm{i}k_\omega z_m}|^2 = |\Phi_m(k_\omega)|^2 \,,$$

with $\omega = \hbar k_\omega^2/2m_e$. The Hamiltonian is time-independent, thus one can identify $\epsilon_{\text{kin}} = \hbar\omega$, $k = k_\omega$ and $d\sigma_m/\epsilon_{\text{kin}} = |\tilde{\Psi}(z_m,\omega)|^2$. The wavefunction needs so to be stored at one measuring point only in order to get the PES in this direction.

The derivation in three dimension is straightforward. The Fourier transformation in time-domain yields here:

$$\tilde{\Psi}(\mathbf{r}_m,\omega) = \int d\Omega dk\, k^2 \left[\delta(k - \sqrt{2m_e\omega/\hbar}) + \delta(k + \sqrt{2m_e\omega/\hbar})\right] \Phi_m(\mathbf{k}) e^{\mathrm{i}\mathbf{k}\mathbf{r}_m} \,,$$

with $\mathbf{k} = k\mathbf{e}_k$. Since $k > 0$ is positive by definition, the second term vanishes without assumption:

$$\tilde{\Psi}(\mathbf{r}_m,\omega) = k^2 \int d\Omega\, \Phi_m(k\mathbf{e}_k) e^{\mathrm{i}k\mathbf{e}_k\mathbf{r}_m} \,.$$

[7] In order to be defined, the FT has to be evaluated, in fact, at a time t at which the wavefunction has not reached the boundaries of the volume element so that the integration can be truncated to this volume. Otherwise, one has to ensure, e.g., by an exponential decay factor that the wavefunction goes to zero at the boundaries.

Supposing at $\mathbf{r}_m$ only waves with $\mathbf{k} \parallel \mathbf{r}_m$, i.e., $\mathbf{e}_k = \mathbf{e}_m$, yields then:

$$\tilde{\Psi}(\mathbf{r}_m, \omega) = 4\pi k^2 \Phi_m(k\mathbf{e}_m) e^{\mathrm{i}kr_m} \quad \Longrightarrow \quad |\tilde{\Psi}(\mathbf{r}_m, \omega)|^2 \sim |\Phi_m(k\mathbf{e}_m)|^2 = \frac{d\sigma_m}{d\epsilon_{\mathrm{kin}}} ,$$

again with $\hbar\omega = \epsilon_{\mathrm{kin}}$.

The above results are valid under the condition that the laser pulse vanishes before photoelectrons pass the measuring point $\mathbf{r}_m$. However, this is generally not the case. Furthermore, if the laser field is active during measurement, it can be included to the Hamiltonian and to the wavefunction Ψ either in length gauge like in Eq. (3.6) or in velocity gauge. In principle, the result should not depend on the choice of the gauge. Reminding however, that the wavefunction can easily transformed from one gauge into the other by multiplication of the time-dependent factor $\exp(\mathrm{i}E_0 z F(t))$, Eq. (3.3). The evaluation of the PES through Fourier transformation in the time domain, Eq. (3.7), makes the choice of the gauge now a relevant issue. In this aspect, it was found [58, 59] that the velocity gauge is to be preferred as soon as the laser signal overlaps with the flow signal of emitted electrons or when strong laser fields are used. Due to the time-locality of the electric field operator in Eq. (3.6), the wavefunctions φ_α are in practice still propagated in length gauge and for evaluation of the PES transformed into velocity gauge.

3.6 Integrated photoelectron spectra

All wavefunctions φ_α are recorded at several measuring points $\mathbf{r}_m$, $m = 1, \ldots, M$, with angles Ω_m on a sphere with radius $r \leq r_{\mathrm{min}}$ (before the absorbing mask). Each measuring point $\mathbf{r}_m$ represents then one photoelectron spectrum $d\sigma_m/d\epsilon_{\mathrm{kin}}$. In order to obtain an integrated PES independent of any measuring point, all spectra have to be added up while weighting each with a factor:

$$\frac{d\sigma}{d\epsilon_{\mathrm{kin}}} = \sum_{m=1}^{M} \lambda_m \cdot \frac{d\sigma_m}{d\epsilon_{\mathrm{kin}}} , \quad \text{with } \sigma_m \text{ = yield in direction } \mathbf{r}_m .$$

The weight factors λ_m are determined by cutting the surface of the unit sphere into segments $\mathcal{A}_m$ each one belonging to a given $\mathbf{e}_m = \mathbf{r}_m/r_m$. The segment is defined as the collection of points $\mathbf{r}$ on the unit sphere which has – among all measuring (unit) vectors $\mathbf{e}_1, \ldots, \mathbf{e}_M$ – minimum distance to $\mathbf{e}_m$. A measure for the distance is the angle between $\mathbf{r}$ and the measuring point,

$$\mathcal{A}_m = \left\{ \mathbf{r} | \mathbf{r} \cdot \mathbf{e}_m = \max_i (\mathbf{r} \cdot \mathbf{e}_i) \right\} .$$

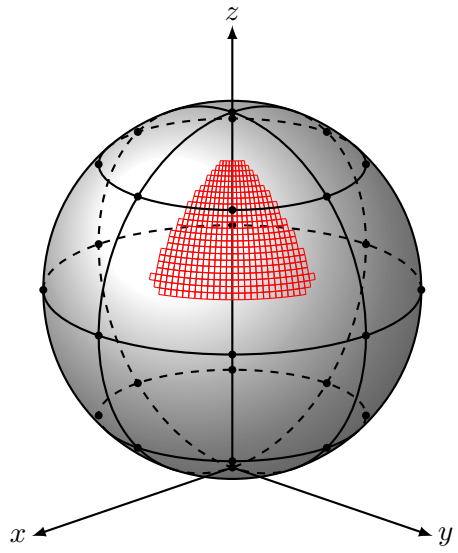

Figure 3.3: Measuring points • for the PES. The PES of all points are added up while using weight factors λ_m, $d\sigma/d\epsilon_{\mathrm{kin}} = \sum_m \lambda_m d\sigma_m/d\epsilon_{\mathrm{kin}}$ which are determined over a fine grid in $\vartheta\varphi$ on the unit sphere. The surface area $\mathcal{A}$ is shown for the measuring point in $(1,1,1)$-direction.

λ_m is then simply given by the surface area covered by $\mathcal{A}_m$:

$$\lambda_m = \int_{\mathcal{A}_m} d\Omega \,.$$

Practically, a very fine mesh is initialized on the sphere, see the red squares in Fig. 3.3, each square representing a point $\mathbf{r}$ with volume $\Delta\Omega_r$. For accurate enough meshes the factors λ_m trivially cover the full unit sphere: $\sum_m \lambda_m = 4\pi$.

3.7 Combined determination of PES and PAD

For a sufficiently large number of measuring points M, it is not only possible to obtain an accurate approximation for the integrated PES, one may even determine an angular-resolved PES. This gives access to a fully combined determination of PAD and PES from the same observables. Like in Sect. 3.4, again two possibilities have been developed:

The first is to sample the unit sphere like in Fig. 3.3 on a regular grid in ϑ and φ and to search for each angle Ω for the nearest measuring point $\mathbf{r}_m$. The PES at angle Ω_r is then given by the cross-section $d\sigma_m/d\epsilon_{\mathrm{kin}}$. This procedure is somewhat similar to the box-like sampling in Sect. 3.4, just on the unit sphere. It is only suitable for very high resolutions, i.e., large numbers M of measuring points (examples: Figs. 5.1, 7.14, 7.17).

For smaller M, the second possibility is to expand the PES into spherical har-

monics:

$$c_{lm}(\epsilon_{\mathrm{kin}}) = \sum_{\mu=1}^{M} \lambda_\mu Y_{lm}^*(\Omega_\mu) \cdot \frac{d\sigma_\mu}{d\epsilon_{\mathrm{kin}}} , \quad \text{with} \quad \frac{d^2\sigma}{d\Omega d\epsilon_{\mathrm{kin}}} = \sum_{lm} c_{lm} Y_{lm}(\Omega) .$$

Depending on the ionization regime, the expansion can again be truncated after a few c_{lm}. This adds some smoothing to the distribution. For example, regarding an ensemble of free, randomly orientated clusters, the sum is independent of m and only even l occur, see next chapter:

$$\frac{d^2\overline{\sigma}}{d\Omega d\epsilon_{\mathrm{kin}}} = \frac{\overline{\sigma}}{4\pi} \left(1 + \mathcal{B}_2(\epsilon_{\mathrm{kin}}) P_2 + \mathcal{B}_4(\epsilon_{\mathrm{kin}}) P_4 + \dots\right) , \tag{7.2a}$$

with

$$\mathcal{B}_l(\epsilon_{\mathrm{kin}}) = \sqrt{2l+1}\, \frac{\mathcal{C}_l(\epsilon_{\mathrm{kin}})}{\mathcal{C}_0(\epsilon_{\mathrm{kin}})} , \tag{7.2c}$$

and P_l being the lth Legendre polynomial (example: Fig. 7.9).

4 Averaging methods

The last chapter presented methods for calculating the TDLDA photoelectron angular distribution $d\sigma/d\Omega$ after laser excitation of a cluster represented on a three-dimensional Cartesian grid. The emission angles $\Omega = (\vartheta, \varphi)$ are measured with respect to the polarization axis of the (linearly polarized) laser pulse. In theory, due to computational limits, one is forced to use small boxes and to simulate one cluster only. At the starting point of the dynamical simulation, the single cluster is considered as fixed in space with a given orientation related to the polarization axis of the electric field. The so determined cross-section $d\sigma/d\Omega$ at the end of the simulation is, in general, a complicated function of the emission angles, more specifically:

$$\frac{d\sigma}{d\Omega} = \sum_{lm} c_{lm} Y_{lm}(\vartheta\varphi) \; .$$

In the experiment the situation is different. Here, most measurements deal with an ensemble of randomly orientated clusters. As a consequence, the orientation-averaged angular distribution (OA-PAD) probably differs from the above expansion. Experiment and theory cannot be compared at this level. The aim of this chapter therefore is to introduce methods for determining the OA-PAD in theory.

4.1 The anisotropy parameter

Starting point for developing an averaging scheme are spherical symmetric systems. In this case, the OA-PAD simply equals the PAD. Moreover, for an excitation with a linearly polarized pulse, say $\mathbf{e}_{\rm pol} = \mathbf{e}_z$ for the sake of simplicity, the angular distribution has to be independent of the polar angle φ ($m = 0$). Spherical symmetric potentials are, of course, used in atomic physics [60], but sometimes also in cluster physics, e.g., for closed-shell metal clusters where one assumes a jellium potential (see Sect. 2.1) for the ionic background.

In perturbation theory, the (orientation-averaged) angular distribution from a state $|i\rangle = |nlm\rangle$ can now be expanded as [61–65]:

$$\begin{aligned} \frac{d\overline{\sigma}^{(i)}}{d\Omega} &= C_0^{(i)} Y_{00} + C_2^{(i)} Y_{20} + C_4^{(i)} Y_{40} + \ldots \\ &= \frac{\overline{\sigma}^{(i)}}{4\pi} \Big(1 + \beta_2^{(i)} P_2 + \beta_4^{(i)} P_4 + \ldots \Big) \; , \end{aligned} \tag{4.1}$$

where P_l are the Legendre polynomials, $\overline{\sigma}^{(i)} = \sqrt{4\pi}\, C_0^{(i)}$ is the ionization from state $|i\rangle$, and the coefficients $\beta_l^{(i)} = \sqrt{2l+1}\, C_l^{(i)}/C_0^{(i)}$ are the so-called anisotropy (or asymmetry) parameters. The kinetic energy of the outgoing electrons becomes asymptotically $\epsilon_{\mathrm{kin}} = (\hbar k)^2/2m_e$ with the wave number $k = |\mathbf{k}|$ and the wave vector $\mathbf{k}$ pointing into the direction of the scattering angles (ϑ, φ). The kinetic energy is given by the relation for photoemission,

$$\epsilon_{\mathrm{kin}} = \epsilon_i + \nu\hbar\omega_{\mathrm{las}}\,, \tag{4.2}$$

where ϵ_i is the binding energy of the initial state. The maximum possible ν corresponds to the order of the photon process. Considering only one-photon processes, the OA-PAD reduces to the very simple form:

$$\frac{d\overline{\sigma}^{(i)}}{d\Omega} = \frac{\overline{\sigma}^{(i)}}{4\pi}\Big(1 + \beta_2^{(i)} P_2(\cos\vartheta)\Big)\,, \tag{4.3}$$

with $P_2(\cos\vartheta) = (3\cos^2\vartheta - 1)/2$. The two remaining quantities $\overline{\sigma}^{(i)}$ and $\beta_2^{(i)}$ are given by the Bethe-Cooper-Zare formula [63, 64] which basically depends on the angular momentum l of the initial states and the transition integral of the radial wavefunctions of initial and final state. Since the final state wavefunction is a function of the kinetic energy, in consequence, the PAD depends also on the chosen laser frequency. The details are discussed later in Chapter 6.

For one-photon processes, the value of the anisotropy ranges in the interval $-1 \le \beta_2^{(i)} \le 2$. The value $\beta_2^{(i)} = 2$ corresponds to a pure $\cos^2\vartheta$-shaped distribution aligned with the laser polarization. The value $\beta_2^{(i)} = -1$ corresponds to a $\sin^2\vartheta$-shape. Accordingly, for positive values the emission maximum is parallel to the laser polarization at $\vartheta = 0$, for negative values at $\vartheta = \pi/2$. For $\beta_2^{(i)} = 0$ the distribution is isotropic and independent of the azimuthal angle ϑ. At first glance, it appears odd that a maximum emission perpendicular to the electric field (i.e., $\beta_2^{(i)} \le 0$) is possible. In reality, these cases arise indeed even though only under certain conditions when destructive interference of outgoing partial waves occurs. This phenomenon is presented also in Chapter 6 extensively. In contrast, a clean s state ($l = 0$) has always $\beta_2^{(s)} = 2$. This can be understood in terms of first-order perturbation theory [53] where the cross-section is derived in form of the transition matrix element:

$$\frac{d\sigma^{(i)}}{d\Omega} = \mathcal{N}|\langle f|\mathbf{e}_{\mathrm{pol}}\cdot\hat{\mathbf{r}}|i\rangle|^2\,, \qquad \mathcal{N} = \frac{4\pi^2 e^2\omega_{\mathrm{las}}}{c}\,. \tag{4.4}$$

Since $\mathbf{e}_{\mathrm{pol}}\cdot\mathbf{r} \propto Y_{10}$ for linearly polarized light, the s state with angular wavefunction $\propto Y_{00}$ transforms through photon absorption into a final state with $l = 1$

while obeying the dipole selection rules. The absolute square in Eq. (4.4) then yields a distribution $\propto (Y_{10})^2 \sim \cos^2\vartheta$. Note, as soon as multiphoton processes or non-perturbative effects come into play, the above mentioned theoretical range $-1 \leq \beta_2^{(i)} \leq 2$ does not apply any more [66].

One aim of this work is to compare different levels of background potentials, from the spherical jellium via a more refined deformed jellium up to local and non-local pseudo-potentials taking explicitly the ionic structure into account. For non-spherical systems, the Bethe-Cooper-Zare formula cannot be used any more. Averaging schemes have to be applied in order to be able to compare theory with experiments. Since an experimental sample with a number of randomly orientated clusters is inherently isotropic, it is expected that the OA-PAD is φ-independent and symmetric around ϑ as long as the excitation is done with a linearly polarized laser. That means, the OA-PAD is supposed to reduce again, independently of the ionization mechanism, to the general form (4.1). It will be shown that in first-order perturbation theory, the OA-PAD of any deformed molecules/clusters is again given by the simple form (4.3) [67–69]. A procedure is developed which determines anisotropy and yield by six independent calculations[8]. Before, some details on the notation and rotation operations are introduced. For a detailed discussion of Euler rotations it shall be referred to [73, 74].

4.2 The analytical averaging scheme

4.2.1 The Euler angles

A rotation of the reference frame K into a new, arbitrary reference frame K''' can be obtained by sequential application of three rotations, see Fig. 4.1:

1. A rotation $\alpha(0 \leq \alpha < 2\pi)$ about the z-axis of K.
2. A rotation $\beta(0 \leq \beta < \pi)$ about the y-axis of K'.
3. A rotation $\gamma(0 \leq \gamma < 2\pi)$ about the z-axis of frame K'''.

Each of the rotations is expressed in terms of the rotation operator $\hat{D}_\xi(\theta)$,

$$\hat{D}_\xi(\theta) = \exp\left(\mathrm{i}\theta\hat{L}_\xi\right) ,$$

where $\hat{L}_\xi$ denotes the projection of the angular momentum $\hat{\mathbf{L}}$ onto the ξ-axis. The above described sequential rotation reads then as follows:

$$\hat{D}_{z''}(\gamma)\hat{D}_{y'}(\beta)\hat{D}_z(\alpha) \equiv \hat{D}_z(\alpha)\hat{D}_y(\beta)\hat{D}_z(\gamma) \coloneqq \hat{D}(\alpha\beta\gamma) ,$$

[8] Parts of the following section have been published in [70–72].

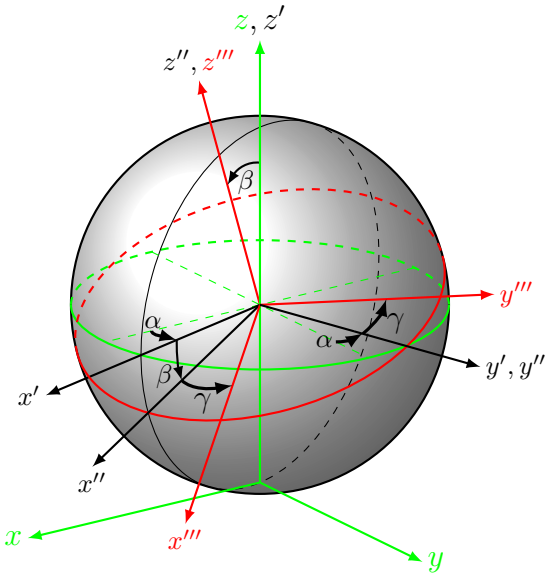

Figure 4.1: Illustration of an Euler rotation $\hat{D}(\alpha\beta\gamma)$. The initial coordinate system K is marked in green, the rotated system K''' in red.

which is equivalent to:

1. A rotation $\gamma(0 \leq \alpha < 2\pi)$ about the z-axis of K.
2. A rotation $\beta(0 \leq \beta < \pi)$ about the y-axis of K.
3. A rotation $\alpha(0 \leq \gamma < 2\pi)$ about the z-axis of frame K.

Hence, the auxiliary frames K' and K'' are actually not needed. In the following, the **laboratory frame of the laser** is denoted as K, whereas K' is the **fixed, intrinsic coordinate system** of the cluster/molecule. Both systems can be transformed into each other by the unitary operator $\hat{D}(\alpha\beta\gamma)$ whose matrix in Cartesian coordinates has the form:

$$\mathbf{D}(\alpha\beta\gamma) = \begin{pmatrix} -\sin\alpha\sin\gamma + \cos\alpha\cos\beta\cos\gamma & -\sin\alpha\cos\gamma - \cos\alpha\cos\beta\sin\gamma & \cos\alpha\sin\beta \\ \cos\alpha\sin\gamma + \sin\alpha\cos\beta\cos\gamma & \cos\alpha\cos\gamma - \sin\alpha\cos\beta\sin\gamma & \sin\alpha\sin\beta \\ -\sin\beta\cos\gamma & \sin\beta\sin\gamma & \cos\beta \end{pmatrix}$$

An alternative description of the three Euler rotations is one single rotation $\xi = |\boldsymbol{\xi}|$ of the coordinate system K about an arbitrary axis $\boldsymbol{\xi}$ with direction $\mathbf{e}_\xi$, for details see Appendix A.1.2.

4.2.2 Notation

Consider now a wavefunction $\varphi_i(x, y, z)$ at point $\mathbf{r} = x\mathbf{e}_x + y\mathbf{e}_y + z\mathbf{e}_z$ in the coordinate system K. In the coordinate system K' which is rotated with respect

to K, the wavefunction at the same point $\mathbf{r} = x'\mathbf{e}'_x + y'\mathbf{e}'_y + z'\mathbf{e}'_z$ has also the same value, but shows in general a new functional dependence. Therefore, the wavefunction in K' is indicated as primed:

$$\varphi_i(x, y, z) = \varphi'_i(x', y', z') \, .$$

In Dirac's notation, the state i is written as $|i\rangle$ in K and as $|i'\rangle$ in K'. Analogously, one can proceed with the scattering state f in K $|f(\vartheta\varphi)\rangle$ and in K' $|f'(\vartheta'\varphi')\rangle$:

$$\Psi_{\vartheta\varphi}(x, y, z) = \Psi'_{\vartheta'\varphi'}(x', y', z') \, .$$

The indices of the function specify the coordinate system to which function and scattering angles are referred. It is obvious that the angles $\vartheta\varphi$ and $\vartheta'\varphi'$ differ, if $K \neq K'$. A rotation of the state i creates now a new state $\alpha\beta\gamma, i$:

$$\begin{aligned} &\text{in } K\text{:} \quad \hat{D}^{-1}(\alpha\beta\gamma)\varphi_i(x, y, z) = \varphi_{\alpha\beta\gamma,i}(x, y, z) \quad \text{or} \quad \hat{D}^{-1}(\alpha\beta\gamma)|i\rangle = |\alpha\beta\gamma, i\rangle \, , \\ &\text{in } K'\text{:} \quad \hat{D}^{-1}(\alpha\beta\gamma)\varphi'_i(x', y', z') = \varphi'_{\alpha\beta\gamma,i}(x', y', z') \quad \text{or} \quad \hat{D}^{-1}(\alpha\beta\gamma)|i'\rangle = |\alpha\beta\gamma, i'\rangle \, , \end{aligned} \tag{4.5}$$

where $\alpha\beta\gamma$ denote the Euler angles. If this rotation is **exactly inverse** compared

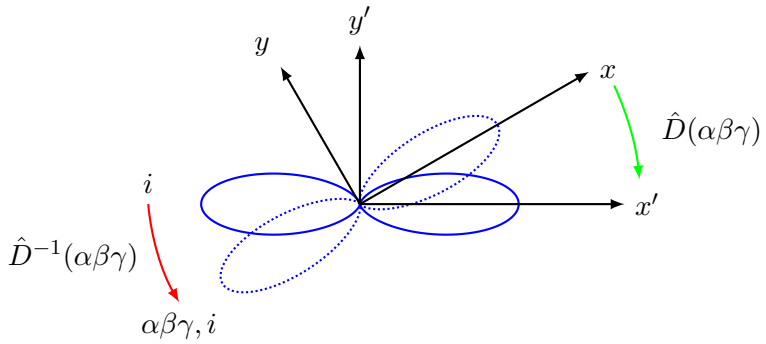

Figure 4.2: Illustration of the rotation from K into K' and from i to $\alpha\beta\gamma, i$. Green arrow: forward rotation; red arrow: backward rotation.

to the one from K to K' (as it is assumed in the upper equations), then the new state $\alpha\beta\gamma, i$ has the same wavefunction in K than the unrotated state i in K', see Fig. 4.2:

$$\varphi_{\alpha\beta\gamma,i}(x, y, z) = \varphi'_i(x, y, z) \quad \text{or} \quad \hat{D}^{-1}(\alpha\beta\gamma)\varphi_i(x, y, z) = \varphi'_i(x, y, z) \, .$$

Note that K' is the intrinsic reference frame. The scattering state f behaves analogously:

$$\hat{D}^{-1}(\alpha\beta\gamma)\Psi_{\vartheta\varphi}(x, y, z) = \Psi'_{\vartheta\varphi}(x, y, z) \quad \text{or} \quad \hat{D}^{-1}(\alpha\beta\gamma)|f(\vartheta\varphi)\rangle = |f'(\vartheta\varphi)\rangle \, . \tag{4.6}$$

4.2.3 Derivation in first-order perturbation theory

In the following, the symbol $\mathscr{A}$ is used as an abbreviation for the cross-section with indices indicating the particular context. The angular distribution of state $\alpha\beta\gamma, i$ reads then in system K $\mathscr{A}^{(i)}(\vartheta\varphi, \alpha\beta\gamma)$ and in system K' $\mathscr{A}'^{(i)}(\vartheta\varphi, \alpha\beta\gamma)$. Here the same angles $\vartheta\varphi$ are used, well knowing that the indices of $\mathscr{A}$ specify again the coordinate system with respect to which these angles are measured. In first-order perturbation theory, $\mathscr{A}^{(i)}$ and $\mathscr{A}'^{(i)}$ are given by:

$$\begin{aligned} \mathscr{A}^{(i)}(\vartheta\varphi, \alpha\beta\gamma) &= \mathcal{N}\,|\langle f(\vartheta\varphi)|\mathbf{e}_{\mathrm{pol}}\cdot\hat{\mathbf{r}}|\alpha\beta\gamma, i\rangle|^2 \quad \text{in system } K, \\ \mathscr{A}'^{(i)}(\vartheta\varphi, \alpha\beta\gamma) &= \mathcal{N}\,|\langle f'(\vartheta\varphi)|\mathbf{e}_{\mathrm{pol}}\cdot\hat{\mathbf{r}}|\alpha\beta\gamma, i'\rangle|^2 \quad \text{in system } K'. \end{aligned} \tag{4.7}$$

The OA-PAD of state i in the laboratory frame becomes then:

$$\overline{\mathscr{A}}^{(i)}(\vartheta\varphi) = \int d^3(\alpha\beta\gamma)\,\mathscr{A}^{(i)}(\vartheta\varphi, \alpha\beta\gamma)\,, \tag{4.8}$$

whereas

$$\int d^3(\alpha\beta\gamma) \equiv \int \frac{d\alpha\, d(\cos\beta)\, d\gamma}{8\pi^2}\,.$$

The derivation proceeds as follows: first, the rotations (4.5) and (4.6) of initial and final state is performed in system K'. Afterwards, the result is transformed into K. Thereby, it must be kept in mind that the operation from K' into K represents a backward rotation $\hat{D}^{-1}(\alpha\beta\gamma)$. So, inserting Eqs. (4.5) and (4.6) into Eq. (4.7) yields:

$$\mathscr{A}'^{(i)}(\vartheta\varphi, \alpha\beta\gamma) = \mathcal{N}\,|\langle f'(\vartheta\varphi)|\mathbf{e}_{\mathrm{pol}}\cdot\hat{\mathbf{r}}|\alpha\beta\gamma, i'\rangle|^2 = \mathcal{N}\,|\langle f(\vartheta\varphi)|\mathbf{e}_{\mathrm{pol}}\cdot\hat{\mathbf{r}}'|i'\rangle|^2\,,$$

where

$$\hat{\mathbf{r}}' = \hat{D}(\alpha\beta\gamma)\hat{\mathbf{r}}\hat{D}^{-1}(\alpha\beta\gamma)\,.$$

In the spherical basis, the position operator $\hat{\mathbf{r}}$ transforms like (Eq. (A.8)):

$$\hat{r}'_\nu = \sum_\mu \hat{r}_\mu \mathcal{D}^{(1)}_{\mu\nu}(\alpha\beta\gamma)\,, \tag{4.9}$$

with $\mu, \mu' = -1, 0, 1$. $|f(\vartheta\varphi)\rangle$ represents here the wavefunction $\Psi_{\vartheta\varphi}(x, y, z)$ from the system K. The $\mathcal{D}^{(1)}_{\mu\nu}$ are the Wigner $\mathcal{D}$-functions, for basic properties see Appendix A. Using Eq. (4.9) further yields:

$$\begin{aligned} \mathscr{A}'^{(i)}(\vartheta\varphi, \alpha\beta\gamma) &= \sum_{\mu\mu'} \mathcal{D}^{(1)}_{\mu 0}(\alpha\beta\gamma)\mathcal{D}^{(1)*}_{\mu' 0}(\alpha\beta\gamma)\,\mathcal{N}\langle f(\vartheta\varphi)|\hat{r}_\mu|i'\rangle\langle f(\vartheta\varphi)|\hat{r}_{\mu'}|i'\rangle^* \\ &\equiv \sum_{\mu\mu'} \mathcal{D}^{(1)}_{\mu 0}(\alpha\beta\gamma)\mathcal{D}^{(1)*}_{\mu' 0}(\alpha\beta\gamma)\mathscr{A}'^{(i)}_{\mu\mu'}(\vartheta\varphi)\,. \end{aligned}$$

The function $\mathscr{A}'^{(i)}_{\mu\mu'}(\vartheta\varphi)$ is now expanded into spherical harmonics,

$$\mathscr{A}'^{(i)}_{\mu\mu'}(\vartheta\varphi) = \sum_{lm'} a^{(i)}_{\mu\mu',lm'} Y_{lm'}(\vartheta\varphi)\,, \tag{4.10}$$

and fully transformed from K' into K (**backward rotation**):

$$\mathscr{A}^{(i)}_{\mu\mu'}(\vartheta\varphi) = \hat{D}^{-1}(\alpha\beta\gamma)\mathscr{A}'^{(i)}_{\mu\mu'}(\vartheta\varphi) \overset{(A.1)}{=} \sum_{lm'} a^{(i)}_{\mu\mu',lm'} \sum_{m} Y_{lm}(\vartheta\varphi)\mathcal{D}^{(l)*}_{m'm}(\alpha\beta\gamma)\,.$$

This results in the distribution $\mathscr{A}^{(i)}(\vartheta\varphi,\alpha\beta\gamma)$ as a function of the orientation $\alpha\beta\gamma$:

$$\begin{aligned}\mathscr{A}^{(i)}(\vartheta\varphi,\alpha\beta\gamma) &= \hat{D}^{-1}(\alpha\beta\gamma)\mathscr{A}'^{(i)}(\vartheta\varphi,\alpha\beta\gamma)\\ &= \sum_{\mu\mu'}\sum_{lmm'} a^{(i)}_{\mu\mu',lm'} Y_{lm}(\vartheta\varphi)\mathcal{D}^{(1)}_{\mu 0}(\alpha\beta\gamma)\mathcal{D}^{(1)*}_{\mu' 0}(\alpha\beta\gamma)\mathcal{D}^{(l)*}_{m'm}(\alpha\beta\gamma)\,.\end{aligned} \tag{4.11}$$

The last expression is finally inserted into the integral (4.8):

$$\begin{aligned}\overline{\mathscr{A}}^{(i)}(\vartheta\varphi) &= \int d^3(\alpha\beta\gamma)\,\mathscr{A}^{(i)}(\vartheta\varphi,\alpha\beta\gamma)\\ &= \sum_{\mu\mu',lmm'} a^{(i)}_{\mu\mu',lm'} Y_{lm}(\vartheta\varphi)\int d^3(\alpha\beta\gamma)\,\mathcal{D}^{(1)}_{\mu 0}\,\mathcal{D}^{(1)*}_{\mu' 0}\,\mathcal{D}^{(l)*}_{m'm}\\ &\overset{(A.4)}{=} \sum_{\mu\mu',lmm'} a^{(i)}_{\mu\mu',lm'} Y_{lm}(\vartheta\varphi)(-1)^{\mu'+m'-m}\begin{pmatrix}1 & 1 & l\\ \mu & -\mu' & -m'\end{pmatrix}\begin{pmatrix}1 & 1 & l\\ 0 & 0 & -m\end{pmatrix}\,.\end{aligned}$$

The Wigner $3j$-symbols are non-vanishing only for $l = 0$ or 2, $m = 0$, and $m' = \mu - \mu'$, see Appendix A.1.1 for a selection of important rules on the $3j$-symbols. This shrinks the summation to a simple final form for the averaged cross-section:

$$\boxed{\begin{aligned}\overline{\mathscr{A}}^{(i)}(\vartheta) &= C^{(i)}_0 Y_{00}(\vartheta) + C^{(i)}_2 Y_{20}(\vartheta)\,,\\ C^{(i)}_0 &= \frac{1}{3}\sum_{\mu} a^{(i)}_{\mu\mu,00}\,,\\ C^{(i)}_2 &= \sum_{\mu\mu'} a^{(i)}_{\mu\mu',2\mu-\mu'}(-1)^{\mu}\begin{pmatrix}1 & 1 & 2\\ -\mu & \mu' & \mu-\mu'\end{pmatrix}\begin{pmatrix}1 & 1 & 2\\ 0 & 0 & 0\end{pmatrix}\,,\\ a^{(i)}_{\mu\mu',lm'} &= \int d\Omega\, Y^*_{lm'}(\vartheta\varphi)\,\mathscr{A}'^{(i)}_{\mu\mu'}(\vartheta\varphi)\,,\\ \mathscr{A}'^{(i)}_{\mu\mu'}(\vartheta\varphi) &= \mathcal{N}\,\langle f(\vartheta\varphi)|\hat{r}_{\mu}|i'\rangle\langle f(\vartheta\varphi)|\hat{r}_{\mu'}|i'\rangle^*\,, \quad \mu,\mu' = -1,0,1\,.\end{aligned}} \tag{4.12}$$

The result appears logical: $\overline{\mathscr{A}}^{(i)}$ depends on coefficients of the (spherical) expansion of $\mathscr{A}'^{(i)}_{\mu\mu'}$ which itself depends on the wavefunctions Ψ_f in K and φ'_i in K'. Ψ_f in K and φ'_i in K' are exactly those wavefunctions which are invariant under rotation of the cluster. Moreover, the OA-PAD depends only on the azimuthal angle ϑ. Reminding that $P_2(\cos\vartheta) = \sqrt{4\pi/5}\,Y_{20}$, the OA-PAD reduces to the form (4.3) introduced at the beginning of this chapter.

The final coefficients $C_0^{(i)}$ and $C_2^{(i)}$ in Eq. (4.12) require information only about a limited number of coefficients $a^{(i)}_{\mu\mu',lm'}$. According to the definition of the function $\mathscr{A}'^{(i)}_{\mu\mu'}$, one can derive the relation:

$$a^{(i)*}_{\mu\mu',2\mu-\mu'} = (-1)^{\mu-\mu'} a^{(i)}_{\mu'\mu,2\mu'-\mu} \,.$$

Thus, the exchange $\mu \leftrightarrow \mu'$ reduces the number of required coefficients, namely three for $C_0^{(i)}$ and six for $C_2^{(i)}$:

$$\begin{aligned} 3\,C_0^{(i)} &= \sum_\mu a^{(i)}_{\mu\mu,00} \,, \\ \frac{\sqrt{120}}{4}\,C_2^{(i)} &= \sum_\mu a^{(i)}_{\mu\mu,20}(-1)^\mu \begin{pmatrix} 1 & 1 & 2 \\ -\mu & \mu & 0 \end{pmatrix} \\ &\quad + \sum_{\mu>\mu'} 2\Re\{a^{(i)}_{\mu\mu',2\mu-\mu'}\}(-1)^\mu \begin{pmatrix} 1 & 1 & 2 \\ -\mu & \mu' & \mu-\mu' \end{pmatrix} . \end{aligned} \tag{4.13}$$

4.2.4 Transformation into Cartesian coordinates

For the derivation of Eq. (4.12) the spherical basis has been used due to its beneficial behaviour under rotation. Unfortunately, it is not suitable for a representation of the wavefunctions on a three-dimensional Cartesian grid with a real dipole field. Moreover, the auxiliary functions $\mathscr{A}'^{(i)}_{\mu\mu'}$ are, in general, not real functions and in consequence no physical quantities. In order to transform into the Cartesian representation, Eq. (4.13) is first written in full form with derived $3j$-symbols, Eqs. (A.5):

$$\begin{aligned} 3\,C_0^{(i)} &= a^{(i)}_{-1-1,00} + a^{(i)}_{00,00} + a^{(i)}_{11,00} \,, \\ 30\,C_2^{(i)} &= -2a^{(i)}_{-1-1,20} + 4a^{(i)}_{00,20} - 2a^{(i)}_{11,20} \\ &\quad -4\sqrt{3}\,\Re\{a^{(i)}_{0-1,21}\} + 4\sqrt{3}\,\Re\{a^{(i)}_{10,21}\} - 4\sqrt{6}\,\Re\{a^{(i)}_{1-1,22}\} \,. \end{aligned}$$

Using the definition of the spherical basis in Cartesian coordinates, Eq. (A.7) in the Appendix, the symbols $\mathscr{A}'$ are then given by:

$$\begin{aligned}
\mathscr{A}'^{(i)}_{+1\pm1} &= \left(-\mathscr{A}'^{(i)}_{xx} + \mathscr{A}'^{(i)}_{yy} \pm \mathrm{i}\mathscr{A}'^{(i)}_{xy} \pm \mathrm{i}\mathscr{A}'^{(i)}_{yx}\right)/2 \\
\mathscr{A}'^{(i)}_{+1\mp1} &= \left(\mathscr{A}'^{(i)}_{xx} + \mathscr{A}'^{(i)}_{yy} \pm \mathrm{i}\mathscr{A}'^{(i)}_{xy} \mp \mathrm{i}\mathscr{A}'^{(i)}_{yx}\right)/2 \\
\mathscr{A}'^{(i)}_{+10} &= \left(\pm\mathscr{A}'^{(i)}_{xz} - \mathrm{i}\mathscr{A}'^{(i)}_{yz}\right)/\sqrt{2} \\
\mathscr{A}'^{(i)}_{0\mp1} &= \left(\pm\mathscr{A}'^{(i)}_{zx} + \mathrm{i}\mathscr{A}'^{(i)}_{zy}\right)/\sqrt{2} \\
\mathscr{A}'^{(i)}_{00} &= \mathscr{A}'^{(i)}_{zz}
\end{aligned}$$

with $\mathscr{A}'^{(i)}_{ab}$ defined similar to Eq. (4.12), but with the positions $a, b \in \{x, y, z\}$ as transition operators. The expansion coefficients $a^{(i)}_{\mu\mu',l\mu-\mu'}$ behave equally and can be replaced by Cartesian coefficients. Moreover, the sums $\mathscr{A}'^{(i)}_{ab} + \mathscr{A}'^{(i)}_{ba} \equiv 2\mathscr{R}'^{(i)}_{ab}$ are now symmetric and real quantities. Finally, it can be written:

$$\begin{aligned}
\frac{d\overline{\sigma}^{(i)}}{d\Omega} &= C_0^{(i)} Y_{00} + C_2^{(i)} Y_{20} \,, \\
3\, C_0^{(i)} &= r^{(i)}_{xx,00} + r^{(i)}_{yy,00} + r^{(i)}_{zz,00} \,, \\
30\, C_2^{(i)} &= -2r^{(i)}_{xx,00} - 2r^{(i)}_{yy,00} + 4r^{(i)}_{zz,00} \,, \\
&\quad -4\sqrt{6}\,\Re\left\{r^{(i)}_{xz,21} + \mathrm{i}r^{(i)}_{yz,21}\right\} - 2\sqrt{6}\,\Re\left\{-r^{(i)}_{xx,22} + r^{(i)}_{yy,22} - 2\mathrm{i}r^{(i)}_{xy,22}\right\} \,, \\
r^{(i)}_{ab,lm} &= \int d\Omega\, Y^*_{lm}(\vartheta\varphi)\, \mathscr{R}'^{(i)}_{ab}(\vartheta\varphi) \,, \\
2\mathscr{R}'^{(i)}_{ab}(\vartheta\varphi) &= \mathcal{N}\langle f(\vartheta\varphi)|\hat{a}|i'\rangle\langle f(\vartheta\varphi)|\hat{b}|i'\rangle^* + \text{c.c.} \,, \quad a, b \in \{x, y, z\} \,.
\end{aligned} \tag{4.14}$$

4.2.5 Procedure

The functions $\mathscr{R}'^{(i)}_{ab}$ represent, in fact, cross-sections which are obtained by transitions induced by dipole operators of *different polarizations in the cluster frame* K'. For example, $\mathscr{R}'^{(i)}_{xz}$ is obtained as an additional term in the cross-section induced by a field polarized along the $(1, 0, 1)$-direction of K':

$$\left.\frac{d\sigma'^{(i)}}{d\Omega}\right|_{(101)} = \mathscr{R}'^{(i)}_{xx} + \mathscr{R}'^{(i)}_{zz} + 2\mathscr{R}'^{(i)}_{xz} \,.$$

So, in order to determine $\mathscr{R}^{(i)}_{xz}$, one needs to calculate the cross-sections $\mathscr{R}'^{(i)}_{xx}$ and $\mathscr{R}'^{(i)}_{zz}$ as well. The coefficient $C_0^{(i)}$ in Eq. (4.14) requires information about

the functions $\mathscr{R}'^{(i)}_{xx}$, $\mathscr{R}'^{(i)}_{yy}$, and $\mathscr{R}'^{(i)}_{zz}$, for $C_2^{(i)}$ the full set of the functions $\mathscr{R}'^{(i)}_{ab}$ is needed. Hence, three linearly independent calculations must be performed in order to determine the orientation-averaged yield $\overline{\sigma}^{(i)} = \sqrt{4\pi}\, C_0^{(i)}$, six[9] for the anisotropy $\beta_2^{(i)} = \sqrt{5}\, C_2^{(i)}/C_0^{(i)}$.

There remains the question how to compute the distributions $\mathscr{R}'_{ab}$? Two analytical procedures have been considered in this work and are directly compared later in Chapter 6:

- Full-perturbative procedure:
  The occupied initial states are computed in a self-consistent manner within static LDA. For the resulting K.S. potential the determination of the final state wavefunction becomes simple only if a spherical background potential, e.g., the jellium model, is used. Both wavefunctions are thus calculated in the same time-independent potential and an averaging scheme is actually not necessary.

  However, if the stationary initial state is calculated with explicit ionic structure, approximate solutions for the final state are used. The wavefunctions are finally inserted into Eq. (4.14) with the dipole operators $\hat{x}$, $\hat{y}$, and $\hat{z}$. This procedure is fully static using the result from first-order perturbation theory.

- Semi-perturbative procedure:
  The distributions $\mathscr{R}'_{ab}$ can also be calculated within full TDLDA through variation of the polarization of the exciting laser. This has the advantage that initial and, in particular, final state, do not have to be determined explicitly. Thus, the procedure can also be used for non-trivial background potentials which arise when the ionic structure is taken into account. Although the scheme is based on the perturbative result, rearrangement of the residual cluster K.S. potential is included in TDLDA. However, the laser parameters have to be well chosen in order to exclude collective or multiphoton processes disturbing the PAD.

4.3 Direct averaging schemes

The above presented averaging scheme is derived analytically on the basis of first-order perturbation theory. Hence, it may fail as soon as the laser excitation takes place in non-perturbative (e.g., when collective effects play a role) or multiphoton

[9] In practice, the following six polarization vectors are used: $\mathbf{e}^{(1)}_{\mathrm{pol}} = (1,0,0)$, $\mathbf{e}^{(2)}_{\mathrm{pol}} = (0,1,0)$, $\mathbf{e}^{(3)}_{\mathrm{pol}} = (0,0,1)$, $\mathbf{e}^{(4)}_{\mathrm{pol}} = (1,1,0)/\sqrt{2}$, $\mathbf{e}^{(5)}_{\mathrm{pol}} = (1,0,1)/\sqrt{2}$, and $\mathbf{e}^{(6)}_{\mathrm{pol}} = (0,1,1)/\sqrt{2}$.

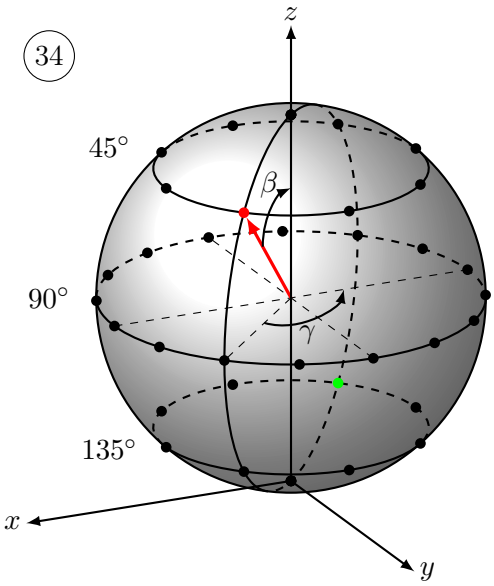

Figure 4.3: Example of a set of orientation points used in the direct averaging scheme. The cluster is first rotated by γ about the z-axis and then by β about the y-axis of the laboratory frame.

regimes. A simpler, more general, but probably also more expensive method is provided by a direct orientation averaging according to Eq. (4.8). Orientation averaging is performed here in the laboratory frame where the laser polarization axis is fixed, $\mathbf{e}_{\mathrm{pol}} = \mathbf{e}_z$. Instead, the whole cluster is rotated and PAD of different orientations, i.e., different combinations of $\alpha(0 \leq \alpha < 2\pi)$, $\beta(0 \leq \beta < \pi)$ and $\gamma(0 \leq \gamma < 2\pi)$ are considered.

Since spherical absorbing boundaries are used, the rotation about $\mathbf{e}_{\mathrm{pol}}$ by the Euler angle α can be done a posteriori and does not require any additional TDLDA runs. This leaves averaging over β and γ. The β-γ integration is approximated by a finite summation. The chosen values for β and γ can be drawn on the unit sphere. As an example, Fig. 4.3 shows a sampling over 34 orientation points. The weight factors for the summation of the points are again determined according to the method described in Sect. 3.6: the surface of the sphere is divided into segments around the sampling directions, the area of each segment corresponds to the weight factor (divided by 4π):

$$\frac{d\overline{\sigma}}{d\Omega} = \sum_{n=1}^{N} \Lambda_n \cdot \left.\frac{d\sigma}{d\Omega}\right|_n , \tag{4.15}$$

with N being the number of sampling points and $\frac{d\sigma}{d\Omega}|_n$ the PAD of the nth orientation representing a combination of β and γ. A proper sampling should cover the sphere homogeneously, i.e., the weight factors should not differ too much.

The sample rotation given in Fig. 4.3 rotates the red point into the z-axis of the laser frame K. Simultaneously, the opposite green point is rotated into

the $-z$-axis. As a consequence, the PAD obtained from the green point is similar the one from the red point just with the replacement $\vartheta \to \pi - \vartheta$ and $\varphi \to \varphi - \pi$. Hence, for a central symmetric sampling only a single hemisphere has to be calculated.

The direct averaging scheme has the advantage that all possible non-perturbative and multiphoton effects are taken into account. However, it is a priori not known how many orientations are needed for convergence of the averaged PAD? The number of necessary calculations might be large and might depend on the investigated system and on the prominent excitation mechanism in the examined regime. This question is discussed in the next chapter in detail for small sodium clusters (Sect. 5.3.2). On the other hand, clusters with highly symmetric ionic configurations allow to reduce the number of actual calculations by using symmetry operations, e.g., in C_{60} a sampling of 182 well chosen orientation points needs only five different calculations due to the high symmetry of this molecule.

5 First results

Ionization mechanisms are often separated into linear and non-linear processes. In general, a process induced by laser excitation is called linear if the impact of the effect scales linearly with the laser intensity, in all other cases it is called non-linear. Linear processes in atoms, molecules and clusters are one-photon ionization and plasmon dominated dynamics. One-photon ionization can be analytically described in first-order perturbation theory. It yields that the total number of emitted electrons, i.e., the cross-section is given by $\sigma \sim I$ as it should be for a linear process.

The two main non-linear photoionization processes in clusters are multiphoton ionization (MPI) and tunneling ionization. The tunneling ionization occurs in strong fields, a typical example is high harmonic generation (HHG). In contrast to HHG, MPI can still be described within lower-order perturbation theory. The relation between the cross-section and the laser intensity depends here also from the order ν of the photon process, $\sigma \sim I^{\nu}$. Thus, one often calls MPI a semi-linear process. In order to distinguish the perturbative and the non-perturbative processes and in order to assess the strength of the laser field, Keldysh [75] introduced the parameter

$$\gamma = \sqrt{\frac{2 \cdot \mathrm{IP} \cdot \omega_{\mathrm{las}}^2}{I}} \,.$$

For strong fields, $\gamma \ll 1$, the photon picture breaks down and the effect does not scale neither linearly nor semi-linearly with the laser intensity. Field dominated processes (optical field ionization) occur, e.g., in HHG with tunneling ionization. For $\gamma \gg 1$, the perturbation is weak and perturbation theory can be used as it is the case in one- and multiphoton ionization, but also in low-order harmonic generation.

5.1 Example: Na_8 spherical jellium

As a typical example for photoionization in the (semi-)linear regime, the simple closed-shell cluster Na_8 is considered, see [76]. The ionic background is approximated by a soft spherical jellium model so that no averaging of the PAD is necessary. In fact, the jellium parameterization is chosen to reproduce the shape of the electronic density of a calculation with explicit ionic background (Wigner-Seitz radius $r_s = 3.65\, a_0$, surface thickness $\sigma_{\mathrm{jel}} = 1\, a_0$). The s.e. energies are then

$\epsilon_{1s} = -0.405\,\mathrm{Ry}$ for the $1s$ state and $\epsilon_{1p} = -0.300\,\mathrm{Ry}$ for the $1p$ shell (three-fold degenerate). Figure 5.1 (left panel) shows the (integrated) PES after excitation with a laser of $T_{\mathrm{pulse}} = 60\,\mathrm{fs}$, $I = 6.9 \cdot 10^{13}\,\mathrm{W/cm^2}$, and $\omega_{\mathrm{las}} = 0.9\,\mathrm{Ry}$ obtained within TDLDA. The laser frequency is far above the plasmon resonance (here at $\omega_{\mathrm{pl}} \approx 0.17\,\mathrm{Ry}$) or any $1ph$ excitation, and is clearly in the one-photon regime for all s.e. states. The total ionization is $N_{\mathrm{esc}} = 0.003$. The (integrated) PES is derived according to the method described in Sects. 3.5 and 3.6. ATI peaks in accordance with the relation $\epsilon_{\mathrm{kin}} = \epsilon_i + \nu\hbar\omega_{\mathrm{las}}$ (4.2) from perturbation theory are nicely visible for $\nu = 1, 2$. However, the two-photon peaks, $\nu = 2$, are strongly suppressed by more than two orders of magnitude and one-photon processes are dominating (note the logarithmic y-scale). The intensity does not seem to be high enough for a crucial emission gain from two-photon processes. The two color maps on the right side show the PAD as a function of the kinetic energy ϵ_{kin}, i.e., the double-differential cross-section zoomed onto the one-photon peaks in the PES. The presented cross-sections are fully combined PES and PAD, both obtained from the Fourier-transformation of the s.e. wavefunctions as described in Sect. 3.7 (first method). Due to the sphericity of the system, the cross-section is just a function of the azimuthal angle ϑ measured with respect to the laser polarization axis. As one can see, $1s$ and $1p$ electrons are mainly emitted in direction to the polarization axis, although there is a slight trend for the $1p$ electrons towards isotropic emission. This can be also seen in the plots below each color map. They represent cuts through the double-differential cross-section at their respective positions where maximum emission occurs (here: $\epsilon_{\mathrm{kin}} = 0.5$ and $0.6\,\mathrm{Ry}$). Both distributions can be nicely fitted to Eq. (4.3). The fit yields $\beta_2^{(1s)} = 2$ as expected for a "clean" $1s$ state and $\beta_2^{(1p)} = 1.6$ for the $1p$ state. This means that the distribution of the $1s$ state is perfectly forward oriented having zero emission in direction $\vartheta = \pi/2$, while the $1p$ state exhibits a small amount of isotropic/sidewards emission.

Figure 5.1 demonstrates a typical example for an ionization in the linear regime. Equations (4.2) (for $\nu = 1$) and (4.3) hold and multiphoton processes are negligible. Accordingly, as long as the laser parameters are properly chosen, perturbation theory can explain the main features of PAD and PES. The following section is focused on ionization processes in a variety of small sodium clusters exactly under such conditions.

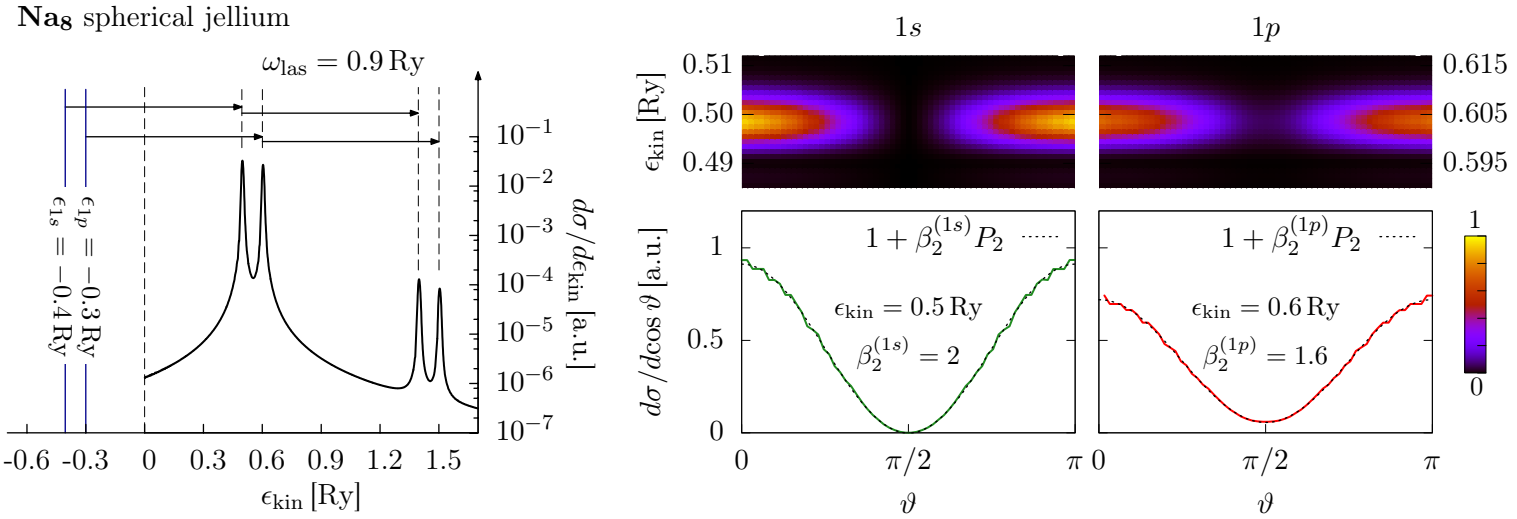

Figure 5.1: Spectrum and angular distributions of photoelectrons in Na_8 spherical jellium ($r_s = 3.65\,a_0$, $\sigma_{\rm jel} = 1\,a_0$, $\epsilon_{1s} = -0.405\,$Ry, $\epsilon_{1p} = -0.300\,$Ry) after excitation with a 60 fs linearly polarized laser pulse of $I = 6.9 \times 10^{13}\,$W/cm^2 and $\omega_{\rm las} = 0.9\,$Ry. The total ionization is $N_{\rm esc} = 0.003$ electrons. The angle ϑ is measured with respect to the laser polarization axis. The s.e. wavefunctions have been stored at a very large number of measuring points, $M = 137$, all along one longitude due to the φ-symmetry. PES and PAD are so determined by Fourier transformation of the same observable.

5.2 One-photon processes in small sodium clusters[10]

In order to reduce calculation costs only positive and neutral clusters have been considered. The laser parameters were chosen so that the excitation stays safely in the perturbative one-photon regime, i.e., the laser frequency ($\omega_{\text{las}} = 0.55\,\text{Ry}$ for neutral and $\omega_{\text{las}} = 0.75\,\text{Ry}$ for positive clusters, $I = 10^{11}\,\text{W/cm}^2$ and FWHM = 60 fs)[11] is above the IP and far away from any collective resonance. The wave-functions are propagated until $t = 120\,\text{fs}$ in order to collect all emitted electrons. The resulting net ionization was very low, $N_{\text{esc}} = 0.0001-0.009$. The analytical, (semi-)perturbative averaging scheme was used as it has been derived for such conditions on the basis of first-order perturbation theory.

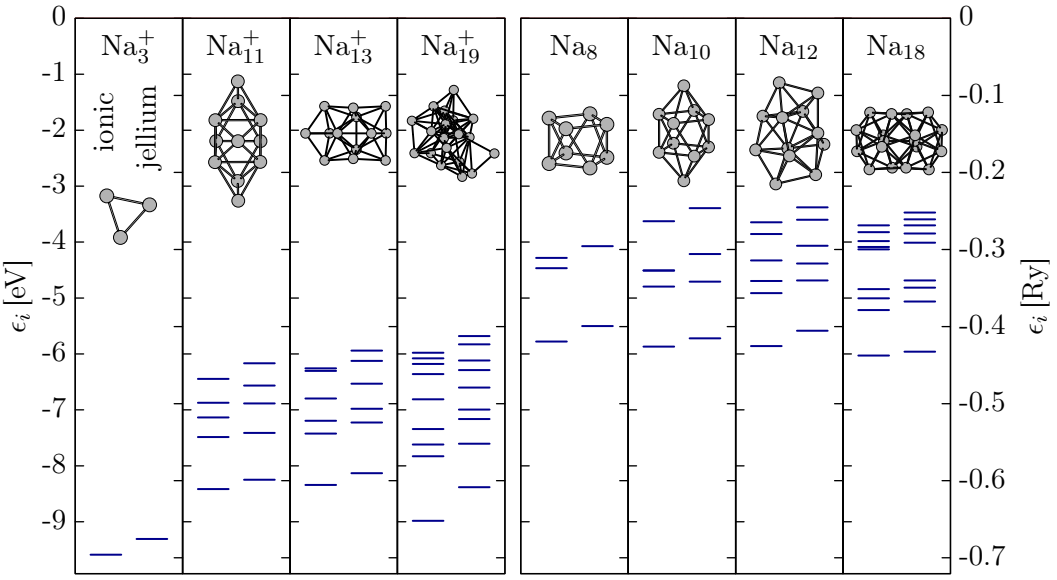

Figure 5.2: Ground-state spectra of occupied s.e. states for the considered clusters. *Left column in each panel:* Spectrum for the electron cloud with detailed ionic background. *Right column:* Spectrum from the equivalent jellium model.

The selection of clusters ranges from closed shell clusters like Na_3^+ and Na_8 with nearly spherical (electronic) shape over weakly axially deformed (Na_{18}, Na_{19}^+) up to triaxial (Na_{12}, Na_{13}^+) and strongly prolate clusters (Na_{10}, Na_{11}^+). Figure 5.2 shows the ground-state spectra of all considered systems. The cluster cations have, of course, an IP much larger than that of the neutral species. In order to see the impact of the ionic structure, the positive background is described

[10] Essential parts of this section have been published in [71, 72].
[11] Exception for Na_3^+: $\omega_{\text{las}} = 0.85\,\text{Ry}$, $I = 3.1 \times 10^{11}\,\text{W/cm}^2$, $T_{\text{pulse}} = 60\,\text{fs}$.

by both, jellium and explicit ionic structure. As was done for Na_8 before, the jellium parameters (Wigner-Seitz radius r_s, surface thickness $\sigma_{\rm jel}$ and deformation parameters α_{20} and α_{22}) are chosen to reproduce the shape of the electronic density of the calculation with ionic background.

Figure 5.3 shows the total anisotropy β_2 (lower panel) and the quadrupole deformation α of the ionic background:

$$\alpha = \sqrt{\sum_{m=-2}^{2} \alpha_{2m}} \,, \quad \alpha_{2m} = 4\pi \overline{r^2 Y_{2m}} / 5 N r_{\rm rms}^2 \,, \tag{5.1}$$

with $r_{\rm rms}$ being the rms radius of the background and N the number of ions (here $N = 8$). The angular distributions and anisotropy parameters are obtained by full TDLDA calculations. The ionic background is non-spherical in any case when using explicit ionic structure, and in most cases for the jellium model (for Na_8 the spherical jellium has been used). The deformation parameter α covers the full possible range from 0 to 0.5. In contrast, β_2 shows only little variation for jellium as well as ionic background. Moreover, the charge seems to play no important role. Nevertheless, a slight decrease of β_2 with cluster size N is seen, especially

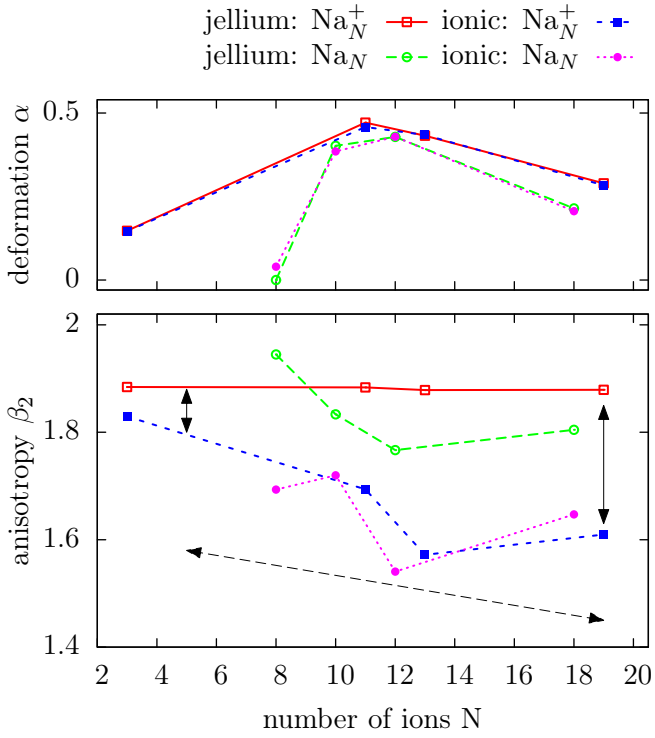

Figure 5.3: β_2 and α as a function of cluster size N, for neutral (squares) and positively charged (circles) species. Open symbols correspond to a jellium background, while the solid ones result from a full ionic background. Trends in β_2 with cluster size are marked with arrows.

for the ionic model as sketched in the plot with a dashed arrow. There might also be a small local minimum in β_2 for strongly deformed clusters. The most prominent feature, however, is the large difference in β_2 between the jellium and the ionic model. The jellium model delivers total anisotropies $\beta_2 \sim 1.9$ near the maximum value of 2, i.e., the maximum of electron emission is parallel to the laser polarization. In comparison, the anisotropies for ionic structure are much lower, $\beta_2 \sim 1.6$. The difference between jellium and ionic model is more striking for large clusters (in the plot marked with solid arrows), especially for cationic clusters. Apparently, additional ions produce more isotropic PAD.

The large difference between jellium and ionic model arises from the fact that the soft pseudo-potentials deform the electronic g.s. density. Figure 5.4 illustrates this issue for the Na_8 cluster. While in the jellium model the electron cloud of Na_8 is trivially spherical, the pseudo-potentials introduce repulsive regions localized around the ions with lacks of density. Also the inner region of the cluster is only weakly populated with electrons.

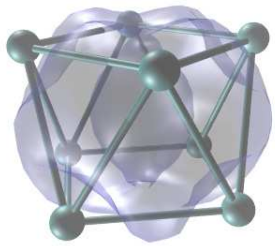

Figure 5.4: Iso-surface plot of the electronic g.s. density in Na_8 with soft pseudo-potentials.

The impact of the pseudo-potentials on the angular distribution is demonstrated in Fig. 5.5, again for Na_8. The left panel shows the PAD for one fixed cluster orientation in space. It is obtained from the absorbed electronic density $n_{\mathrm{abso}}(\mathbf{r})$ by using a "tent"-sampling function, see Sect. 3.4 for details. The angles ϑ and φ of the outgoing electrons are measured with respect to the laser polarization $\mathbf{e}_{\mathrm{pol}} = \mathbf{e}_z$. Pronounced pattern, in particular the four-fold structure of the ionic rings and their relative rotation by 45° is seen. Moreover, the emission maxima are located at $\vartheta \approx \pi/4$ and $3\pi/4$, i.e., sidewards to the laser polarization. After averaging the PAD is by definition φ-independent. However, the sidewards emission introduces an important isotropic component and as a consequence β_2 is lowered.

It is to be noted that ionic structure does not only influence the initial states like it is shown in Fig. 5.4 for the g.s. electronic density, but also modifies the final states. In this sense, outgoing electronic waves seem to be re-scattered by the ionic perturbation.

That deformation plays an important role in electron emission is also supported

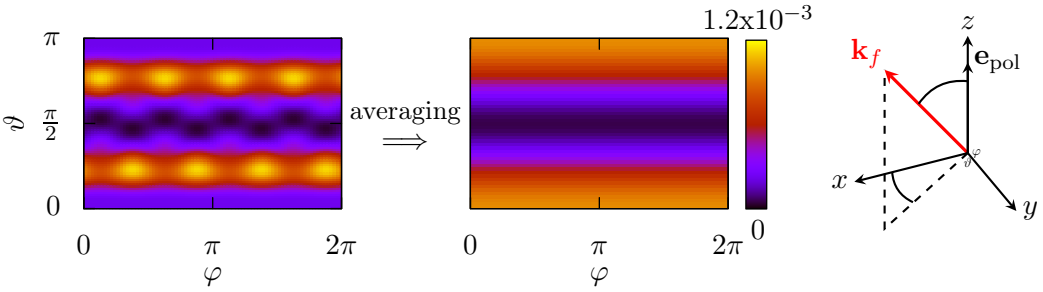

Figure 5.5: PAD for Na_8 with explicit ionic structure for one fixed orientation (*left panel*) and orientation-averaged (*middle panel*). The angles ϑ and φ of photoelectron emitted direction $\mathbf{k}_f$ are measured with respect to the laser polarization $\mathbf{e}_{\mathrm{pol}}$ (*right*).

when resolving the angular distribution state by state. Figure 5.6 shows the s.e. anisotropies $\beta_2^{(i)}$ as a function of the total cluster deformation α for all the considered clusters. The occupied levels are grouped with respect to the main angular momentum component of the s.e. wavefunctions. Except for cationic jellium clusters the trends are clear:

- The results with ionic background are shifted as a whole to lower $\beta_2^{(i)}$ in accordance to the lower total anisotropy β_2 for ionic structure in Fig. 5.3.

- The span between the lowest and highest s.e. anisotropies of a given cluster increases with the cluster deformation α. An overall deformation of the electron cloud seems to lower $\beta_2^{(i)}$. This trend has also already been seen in Fig. 5.3 with a weak local minimum in β_2 for the strongest deformed clusters.

- The span of s.e. anisotropies grows from s over p to the d shell and the larger span extends, of course, to lower $\beta_2^{(i)}$. This is probably caused by the increasingly complex structure of these higher electronic states. The decrease of the s.e. anisotropy with increasing level number corresponds nicely to the weak trend with system size seen in Fig. 5.3 (dashed arrow).

Briefly, it seems that the interplay between complexity of a state (main angular momentum content) *and* deformation (caused by an overall shape modification of the electron cloud as well as by the pseudo-potentials) cooperates to enhance the effect on lowering the anisotropy.

Complementary to the total averaged PAD of Na_8 in Fig. 5.5, a refined analysis on the level of s.e. anisotropies has also the advantage that it is then possible to plot an energy-resolved OA-PAD, see Fig. 5.7. Combining Eqs. (4.2) and (4.3)

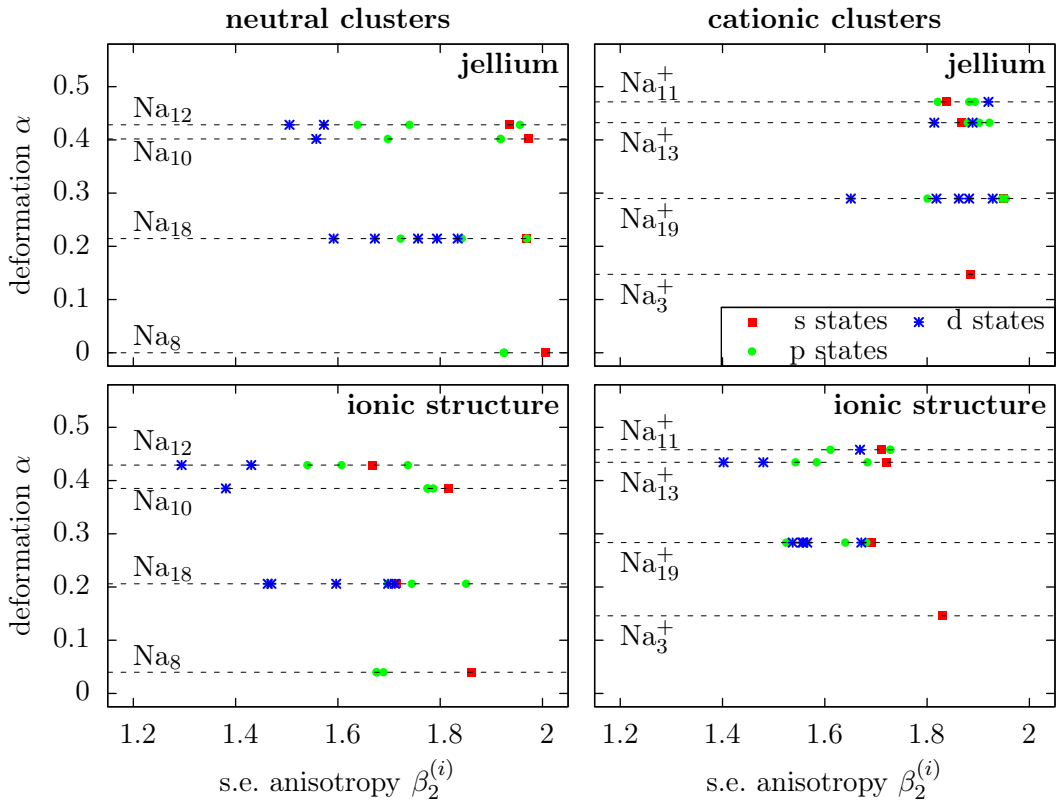

Figure 5.6: State-dependent anisotropies $\beta_2^{(i)}$ for the neutral cluster Na_8, Na_{10}, Na_{12}, and Na_{18} as well as for the positively charged clusters Na_3^+, Na_{11}^+, Na_{13}^+, and Na_{19}^+. For better discrimination, the anisotropies are grouped according to the global quadrupole deformation α. The s.e. states are associated with s, p, and d states of a spherical mean field. *Lower panels:* Results from calculation with full ionic background. *Upper panels:* Jellium results.

yields the double-differential cross-section in the linear one-photon regime:

$$\frac{d^2\overline{\sigma}}{d\Omega\, d\epsilon_{\mathrm{kin}}} = \sum_i \frac{\overline{\sigma}^{(i)}}{4\pi}\Big(1+\beta_2^{(i)}P_2(\cos\vartheta)\Big)\,\delta(\epsilon_{\mathrm{kin}}-\epsilon_i-\hbar\omega_{\mathrm{las}})\,. \tag{5.2}$$

In order to simulate experimental conditions, the δ-function is approximated by a Gaussian function,

$$\mathcal{G}(\epsilon_{\mathrm{kin}}-\epsilon_i-\hbar\omega_{\mathrm{las}}) = \frac{1}{\sigma_{\mathrm{las}}\sqrt{2\pi}}\exp\left(-\frac{1}{2}\frac{(\epsilon_{\mathrm{kin}}-\epsilon_i-\hbar\omega_{\mathrm{las}})^2}{\sigma_{\mathrm{las}}^2}\right)\,. \tag{5.3}$$

The width $\sigma_{\mathrm{las}} \approx 0.006\,\mathrm{Ry}$ is chosen according to the width of the Fourier transformation of the time-dependent pulse profile (see Sect. 3.2), here $T_{\mathrm{pulse}} = 60\,\mathrm{fs}$,

$\omega_{\text{las}} = 0.55\,\text{Ry}$. As one can see in Fig. 5.7, the width is not low enough to resolve the p states. For a better resolution, one has to enhance the frequency or the pulse length.

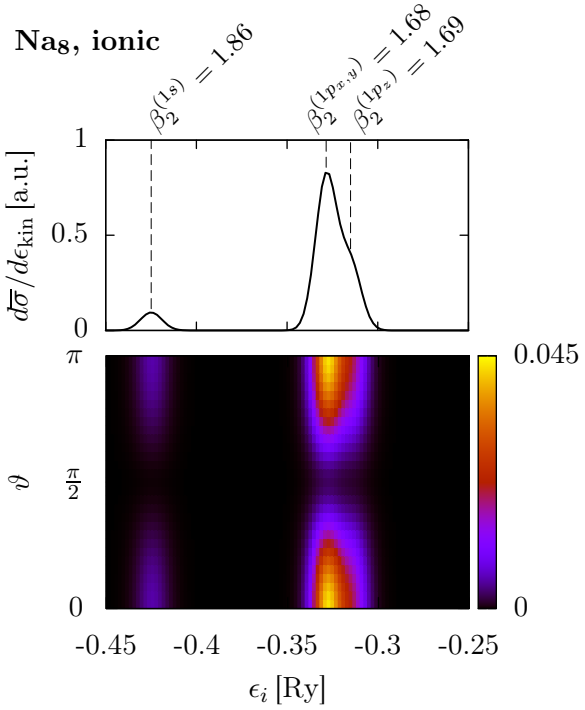

Figure 5.7: "Perturbative" energy-resolved angular distribution of Na_8. *Upper panel:* PES. *Lower panel:* Combined PES and PAD.

In contrast to the combined PES/PAD in Fig. 5.1 for the jellium model, Fig. 5.7 is fully perturbative, i.e, applicable only when multiphoton and collective processes are neglectable. The PES is not a function of the kinetic energy of the outgoing electrons, but of the s.e. energies. Anyway, comparing the combined PES/PAD of jellium and ionic model, the major difference is only seen in the emission yield of the $1s$ state. Of course, there is an overall reduction of the anisotropies when using ionic pseudo-potentials leading to more isotropic emission background, but still for jellium as well as ionic structure the occupied s.e. states emit preferable in direction to the laser polarization. Additionally, the isotropic background of the $1p$ states is in both models larger than that for the $1s$ state.

5.3 Ionization beyond the linear regime

5.3.1 Resonant emission at frequencies below the ionization threshold[12]

Up to present only laser frequencies have been applied which are safely above the one-photon threshold for all occupied s.e. states. An anomalous behaviour has been noticed for frequencies below the IP. The following considerations are restricted to the Na_8 cluster (with explicit ionic structure). However, the effect was also observed for other Na clusters. For the sake of simplicity, the discussion is focused on the $(0, 0, 1)$-orientation of the cluster where the ionic rings are located in the (x, y)-plane.

The cluster is excited by a laser pulse of $\omega_{\text{las}} = 0.08\,\text{Ry}$, $T_{\text{pulse}} = 120\,\text{fs}$, and $I = 3.1 \times 10^{11}\,\text{W/cm}^2$. According to the spectrum of occupied s.e. states ($\epsilon_{1s} = -0.42$, $\epsilon_{1p_{x,y}} = -0.33$, and $\epsilon_{1p_z} = -0.31\,\text{Ry}$) the $1s$ state needs six, the $1p_{x,y}$ states five, and the $1p_z$ state four (which is very close to the threshold) photons to be ionized. The total number of emitted electrons is plotted in Fig. 5.8 as a function of time. Although the laser stops at $t = 120\,\text{fs}$, the cluster surprisingly continues to emit electrons. This is a clear non-perturbative behaviour.

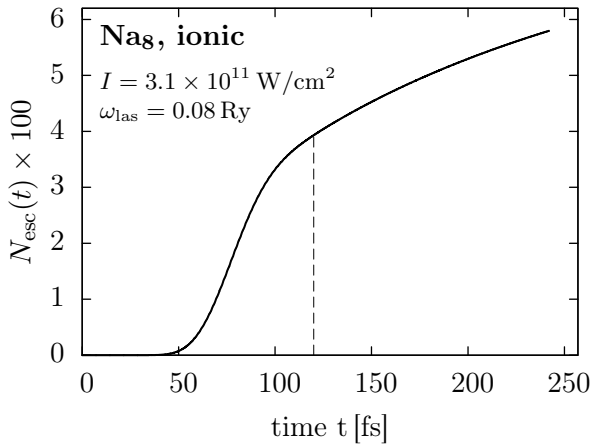

Figure 5.8: Typical emission profile for a laser frequency below the ionization threshold. The laser pulse begins at $t = 0$ and ends at $t = 120\,\text{fs}$. Significant electron emission starts not until $t \approx 50\,\text{fs}$.

A closer look at the dipole signal $D_z(t)$ in the direction of the laser polarization, see the left panel in Fig. 5.9, reveals what happens. For $t < 120\,\text{fs}$, the dipole follows the electric field as expected. For $t > 120\,\text{fs}$, however, the electronic cloud continues to oscillate, but faster than before. Furthermore, the post-pulse oscillations seem to be very "clean", i.e., with one single frequency only. The spectral analysis of the signal from $t = 120 - 250\,\text{fs}$ in the right panel confirms

[12] This section has been submitted for publication in only marginally modified form [77].

that. The electronic cloud oscillates after the pulse with $\omega_r = 0.237\,\mathrm{Ry}$. During the pulse the spectrum is mixed: the main frequency is the laser frequency, but ω_r appears also.

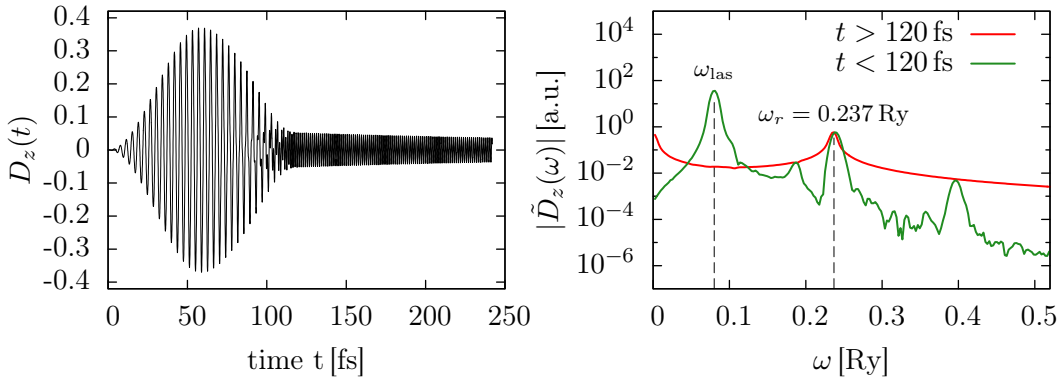

Figure 5.9: *Left:* Dipole signal D_z in the direction of the laser polarization as a function of time. *Right:* Fourier transformation $|\tilde{D}_z(\omega)|$ of the dipole during ($t < 120\,\mathrm{fs}$) and after the pulse ($t > 120\,\mathrm{fs}$).

This analysis provides the following possible explanation to the phenomenon: the laser pulse has excited a dipole resonance of the cluster. The resonance is triggered by absorption of three photons, since $\omega_r \approx 3\,\omega_{\mathrm{las}}$. Figure 5.10 shows the dipole strength $\mathcal{S}_D(\omega) \sim \Im\{\tilde{D}_z(\omega)\}$ of the dipole signal propagated after an initial boost of all s.e. wavefunctions [24, 78],

$$\varphi_\alpha(\mathbf{r}, 0) \longrightarrow e^{\mathrm{i}\mathbf{p}_{\mathrm{boost}}\cdot\mathbf{r}}\,\varphi_\alpha(\mathbf{r}, 0)\,.$$

The strength function is directly related to the photoabsorption cross-section. The predominating excitation mode is, of course, the plasmon at $\omega_{\mathrm{pl}} = 0.187\,\mathrm{Ry}$. However, besides the plasmon, there are plenty of $1ph$ excitations and resonances all of them below the IP. Nevertheless, close to the laser frequency there is only one stronger mode at 0.106 Ry related to $1ph$ excitations from the $1s$ state to the $1p$ states. This mode is too far away for the laser frequency. But the system can still be excited by multiphoton absorption. For laser frequencies below the IP it is therefore very likely to hit a resonance. However, it has to be noted that a dipole resonance can only be induced by an odd number of photons. The present case corresponds to three photons. Apparently, it is also sufficient that the stimulating energy $3\,\omega_{\mathrm{las}}$ lies just in the vicinity of the resonance energy ω_r, an exact matching is not compulsory.

It is interesting to analyze the photoemission observables in more detail. Figure 5.11 shows the PES (in logarithmic scale) for different time spans: during

and after the pulse, and for the full calculated time. The *full* PES (red line on top of the panel) exhibits pronounced peaks with certain distance to each other. At first glance these peaks just resemble MPI peaks. The four-photon peak of the $1p_z$ state should appear closely above the IP, but has not fully passed the threshold. This is due to the positive charge of the residual cluster which shifts the whole spectrum.

More interesting is the shape of the PES *after* the pulse (blue line in the middle of the panel). Because of numerical artifacts of the Fourier transformation it shows more noise. Again, the PES exhibits sharp peaks, but many less. These peaks could finally be identified as *multi-resonance peaks*. Their energy corresponds exactly to the s.e. energy plus multiples of the resonance frequency, here $\epsilon_i + \mu\omega_r$, with $\mu = 2, 3$. The last relation have been marked with black solid, vertical lines. Due to the residual cluster charge, the s.e. spectrum has been shifted about $\delta\epsilon = -0.012\,\mathrm{Ry}$ in order to achieve better match. The first visible peak at $\epsilon_{\mathrm{kin}} = 0.035\,\mathrm{Ry}$ corresponds to the doubly excited ($\mu = 2$) $1s$ state, the following peaks to the $1p_{x,y}$ and $1p_z$ states. The triply excited $1s$ peak disappears behind the noise, but the $1p$ states are still present. No MPI peaks appear in the spectrum *after* the pulse. Hence, the important energy for the post-pulse emission is the resonance energy $\omega_r = 0.237\,\mathrm{Ry}$ and not $\omega_{\mathrm{las}} = 0.08\,\mathrm{Ry}$. The *full* PES, finally, is a superposition of MPI peaks, $\epsilon_i + \nu\omega_{\mathrm{las}}$ (also shifted by $\delta\epsilon$ and marked with black dashed lines), and the multi-resonance peaks. The resonance-enhanced emission already starts *during* the pulse (green line at the bottom of the panel) and continues after the laser excitation has stopped.

Figure 5.12 studies the total number of emitted electrons N_{esc} as a function of the laser intensity in the range $I \sim 10^{10} - 10^{12}\,\mathrm{W/cm^2}$. The frequency $\omega_{\mathrm{las}} = 0.08\,\mathrm{Ry}$ and the pulse length $T_{\mathrm{pulse}} = 120\,\mathrm{fs}$ have been kept constant. All curves

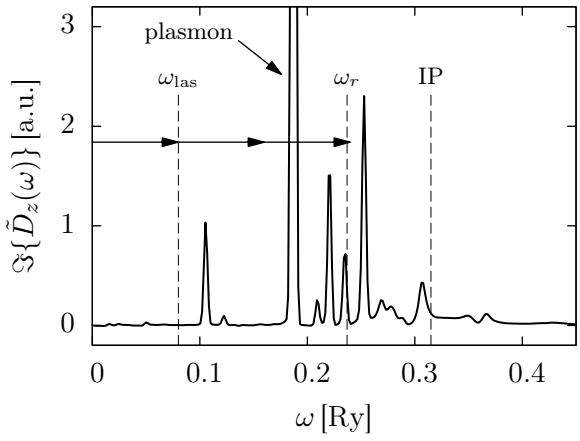

Figure 5.10: Dipole strength function $\mathcal{S}_D \sim \Im\{\tilde{D}_z(\omega)\}$ of Na_8 (ionic background) in the direction of the laser polarization. The plasmon frequency is $\omega_{\mathrm{pl}} = 0.187\,\mathrm{Ry}$, the ionization potential at IP $= 0.315\,\mathrm{Ry}$.

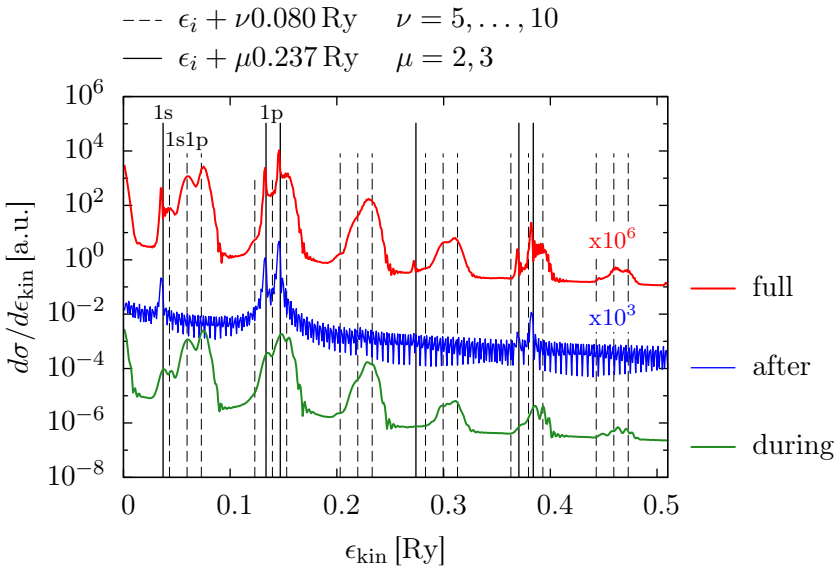

Figure 5.11: PES of Na_8 after excitation with a 120 fs-pulse with $\omega_{\mathrm{las}} = 0.08\,\mathrm{Ry}$ and $I = 3.1 \times 10^{11}\,\mathrm{W/cm^2}$. The PES is evaluated for different time spans: *during* ($t = 0 - 120\,\mathrm{fs}$) and *after* ($t = 120 - 250\,\mathrm{fs}$) the pulse, and for the *full* time span.

are normalized to unity. It seems that the post-pulse emission profile depends sensitively on the intensity: for intensities below $3.1 \times 10^{11}\,\mathrm{W/cm^2}$ all profiles look very similar, typical post-pulse emission occurs. In contrast, for intensities $I \gtrsim 5 \times 10^{11}\,\mathrm{W/cm^2}$ the post-pulse emission becomes weaker and finally disappears. It has to be noted that the ionization is very large for such intensities, $N_{\mathrm{esc}} = 0.2 - 1.4$ for $I \geq 5.6 \times 10^{11}\,\mathrm{W/cm^2}$. The dipole spectrum of Fig. 5.10 then blue-shifts during the emission process and resonances are broadened. Consequently, several resonances can be excited at once, as it is shown in the right panel of Fig. 5.12 for $I = 5.6 \times 10^{11}\,\mathrm{W/cm^2}$. In this specific case, two close frequencies are interfering. However, at large intensities one could also imagine that the blue shift of the spectrum has the consequence that no resonance is induced. Briefly, the emission behaviour becomes unpredictable in this intensity range.

The number of emitted electrons N_{esc} for the different intensities is sketched in Fig. 5.13 in double-logarithmic scale, during (left panel) and after the pulse (right). For a pure multiphoton process one expects that $N_{\mathrm{esc}} \sim I^{\nu}$, where ν is at least the minimum number of photons required for ionization, derived from perturbation theory. Actually, the $1p_z$ state needs four photons to be ionized. However, according to the PES in Fig. 5.11 the four-photon peak has not fully passed the threshold. Moreover, the $1s$ state needs six photons while for the $1p_{x,y}$ states five photons are necessary. Concluding, a value between $6 > \nu > 4$

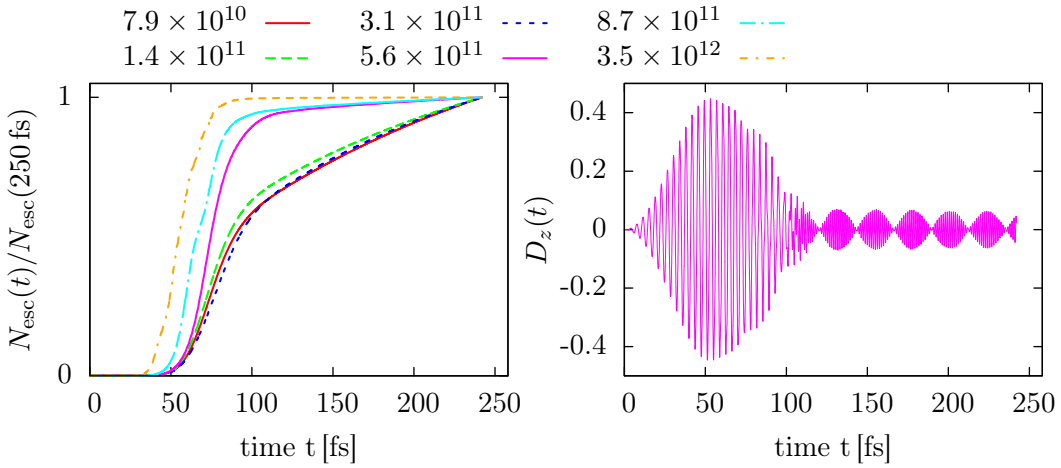

Figure 5.12: *Left panel:* Emission profiles $N_{\mathrm{esc}}(t)$ for different intensities. The lines have been normalized. The final $N_{\mathrm{esc}}(250\,\mathrm{fs})$ ranges from 7×10^{-4} to 1.4 electrons. *Right panel:* Dipole signal $D_z(t)$ for $I = 5.6 \times 10^{11}\,\mathrm{W/cm^2}$. Two close frequencies are interfering after the pulse.

and close to five should be reasonable if emission is dominated by multiphoton processes. According to Fig. 5.11, this is not the case. Instead, the number of emitted electrons is proportional $\sim I^p$, with $p \approx 3$. This applies for the emission during and after the pulse, as long as the laser intensity is weak. For higher intensities, the post-pulse emission disappears and $p \approx 1$.

Apparently, multiphoton processes play only a minor role at weak intensities and the emission is dominated by the resonance at ω_r. Otherwise, one would have expected a much higher power p. Instead, the power corresponds to the number of photons required to induce the resonance. It is interesting that the number μ of resonance energies ω_r needed for ionization is not important, either.

As already mentioned, the presented phenomenon is very sensitive to intensity variation, since for too large intensities the emission could be on- or off-resonant, or several resonances could be hit due to dynamical shifts of the dipole spectrum. Finally, it should be noted, however, that multiple resonances can also be induced by a variation of the laser frequency. The laser frequency could lie next to two or more resonances which may be excited by one photon. One could also imagine a situation where ω_{las} is close to an excitation mode and a multiple of the photon energy as well. In all these cases, several excitation modes interfere, the dipole signal appears "dirtier" and the PES should be more puzzling. Moreover, it becomes difficult to distinguish between multiphoton and multi-resonance ionization. In this respect, the chosen frequency $\omega_{\mathrm{las}} = 0.08\,\mathrm{Ry}$ is a kind of exceptional

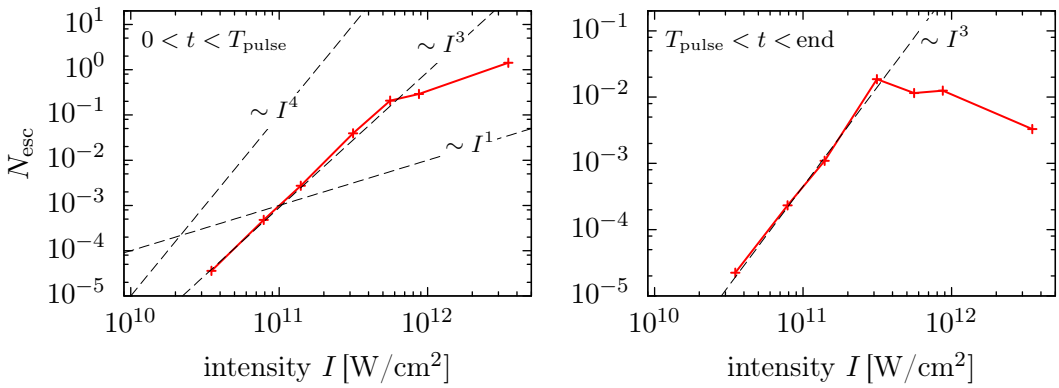

Figure 5.13: Number of emitted electrons as a function of laser intensity during (*left panel*) and after (*right*) the pulse, in double-logarithmic scale. Different power laws are indicated with dashed lines.

case. The first photon energy is below any excitation, the second photon is in the gap between the first 1*ph* excitation and the plasmon, and the third photon hits almost exactly the resonance whose energy is, in turn, different from the photon energy.

5.3.2 Convergence tests of the direct averaging scheme

The analytical averaging scheme derived from first-order perturbation theory is only valid for a limited number of cases. Surely, it is not reliable as soon as multiphoton, collective or resonant processes have an effect on the PAD. Therefore, an alternative method has been described in Sect. 4.3. The remaining question is, how many cluster orientations are needed in order to get a reasonable approximation for the OA-PAD?

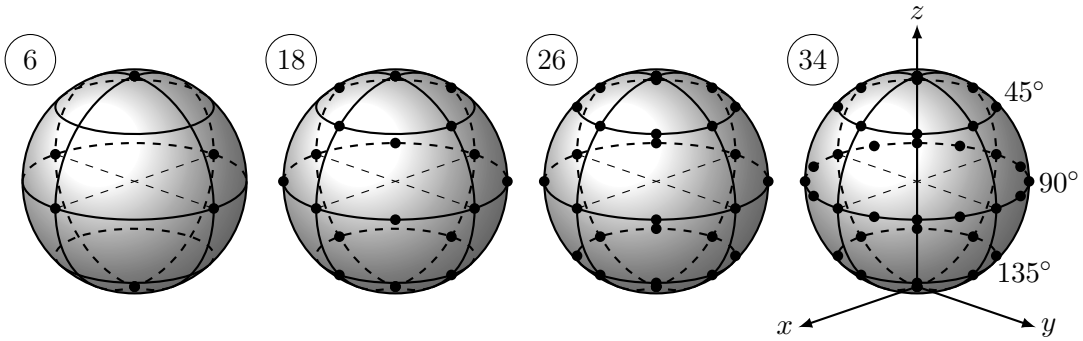

Figure 5.14: Set of orientation points used for the different direct averaging approaches (6, 18, 26, and 34 orientations).

A possible strategy to answer this question is to test first the direct averaging scheme in the linear regime and to compare it with the analytical method. Two levels of refinement for the direct averaging have been considered here, see Fig. 5.14: 6 and 18 cluster orientations. The OA-PAD is calculated for the small clusters Na_3^+ and Na_8. The laser parameters are the same than in the previous section, i.e., in the perturbative one-photon regime. The left panel in Fig. 5.15 shows the results for the Na_3^+ cluster. The analytical scheme yields an anisotropy $\beta_2 = 1.83$, i.e., close to the maximum value of $\beta_2 = 2$ which stands for a $\cos^2$-shaped distribution. As one can see, both direct schemes come very close to the analytical distribution, although the averaging over only 6 orientations exhibit some deviations from the expected distribution shape. In contrast, for Na_8 (right panel) the 6-orientation scheme does not even reproduce the functional dependence and fails totally. Here, only 18 orientations lead to as reliable distribution. The reason for this is that the observed anisotropy of Na_8, $\beta_2 = 1.69$, is much lower than that for Na_3^+. The additional ions in Na_8 allow more re-scattering of outgoing electrons and lower the anisotropy. Furthermore, not only s states, but also p states are occupied. Hence, the number of orientations needed depends on the number of ions (and occupied s.e. states), so on the system itself. The convergence of the direct averaging scheme should be tested therefore actually for each investigated system separately. An evident indicator for a converged result, however, is to get the expected functional dependence of $1 + \beta_2 P_2$ in the linear regime.

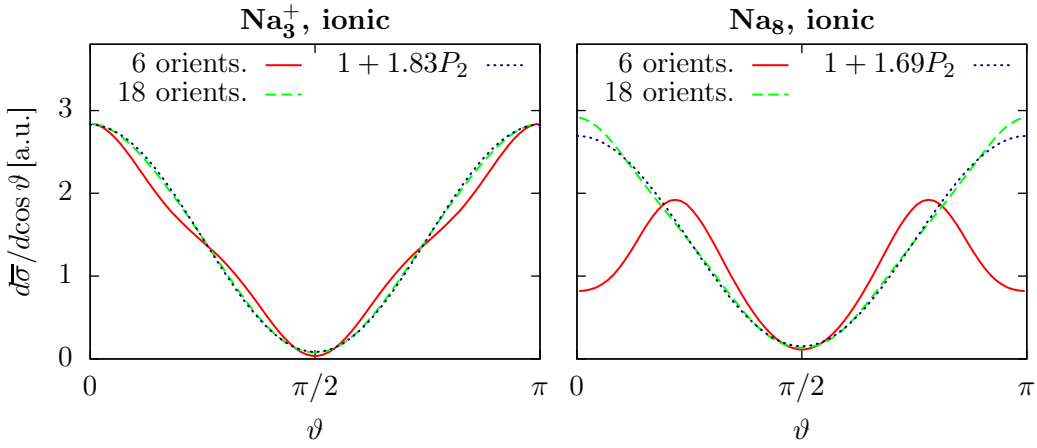

Figure 5.15: OA-PAD along ϑ for Na_3^+ and Na_8 in the linear regime for various averaging schemes: analytical and direct averaging over 6 or 18 orientations (with explicit ionic background).

In the next step, the convergence of the direct averaging scheme has been tested

in the non-linear regime, this time for Na_{12}. In the non-linear regime the functional dependence of the PAD is unknown, in principle. Here, only the trend of the anisotropy as a function of the number of orientations can be taken as a criterion for a converged result. Since this cluster contains even more ions than Na_8, four levels of refinement are investigated here: 6, 18, 26, and 34 orientations (Fig. 5.14).

The cluster is excited by a very strong laser pulse of $T_{\text{pulse}} = 60\,\text{fs}$, $I = 10^{13}\,\text{W/cm}^2$, and $\omega_{\text{las}} = 0.55\,\text{Ry}$. The total number of emitted electrons is $N_{\text{esc}} = 0.82$. The resulting spectrum is shown in Fig. 5.16. The excitation is so strong that the sharp s.p. peaks which can be seen for example for Na_8 (jellium) in Fig. 5.1, disappear. The s.p. energies change during the excitation process, thus the s.p. peaks are smoothed to multiphoton bands. Obviously, the "frozen core" assumption from perturbation theory is no longer valid. The analytical averaging method cannot be applied here. In spite of the high intensity, two- and multiphoton processes are still suppressed by more than two orders of magnitude compared to the one-photon band.

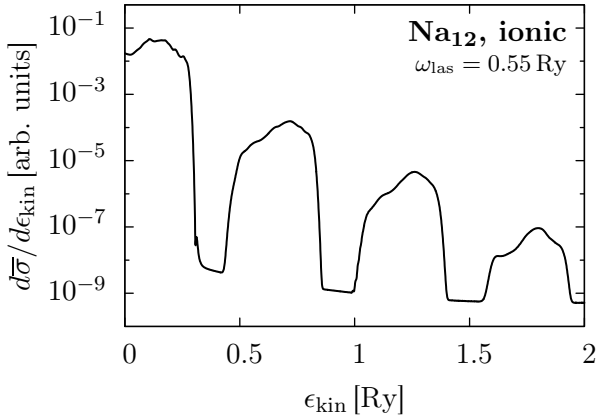

Figure 5.16: PES of Na_{12} after excitation with a strong laser of $T_{\text{pulse}} = 60\,\text{fs}$, $I = 10^{13}\,\text{W/cm}^2$, and $\omega_{\text{las}} = 0.55\,\text{Ry}$. The PES is averaged over 34 orientations.

Although the s.p. states behave dynamically, their anisotropies $\beta_2^{(i)}$ can still be used for a test of the direct averaging, as it is done in Fig. 5.17. The left panel shows the s.e. anisotropies $\beta_2^{(i)}$ for the different levels of precision, the right panel those of the higher momentum $\beta_4^{(i)}$. Again, the averaging over 6 orientations yields unsatisfying values whereas for $\beta_2^{(i)}$ the results seem to be converged after 18 orientations. The situation gets a bit worse regarding the anisotropy $\beta_4^{(i)}$. Obviously, as higher the angular momentum as more averaging points are needed. Anyhow, since the values of 18-orientations scheme are close to those of the 34-orientations scheme, the 18 points still represent a good compromise between expense and precision of the averaging.

The left panel of Fig. 5.17 also quotes the values of the analytical averaging

scheme whose performance seems to range between the 6 and the 18-points averaging. Larger deviations of the analytical result from the direct one can be seen for states which also have a noticeable non-vanishing $\beta_4^{(i)}$ (the green $1p$ and the black $1d$ state). Therefore, the direct scheme should be the preferable choice in the non-linear and multiphoton regime.

5.4 Summary

This chapter presented first results for orientation-averaged PAD and PES calculated for a collection of small, neutral and positively charged sodium clusters. The laser excitation was initially considered in the linear one-photon regime. In this regime, basic properties of the ionization process can be described by first-order perturbation theory and the developed analytical averaging can be applied.

"Deformation" of wavefunctions seems to play a crucial role in determining the PAD. In fact, there are three levels of deformation: 1) an inherent deformation due to the angular momentum of the occupied and final states which trivially increases with system size, 2) the overall cluster deformation which can be quantified by the parameter α, and 3) deformation due to the explicit ionic structure mediated by pseudo-potentials. All three modes were found to grossly influence the PAD and to lower β_2 in the one-photon domain. In this aspect, the pseudo-potentials appear to have the largest effect. This prompts the question whether simple approaches like, e.g., first-order perturbative calculations in a spherical jellium model are also able to resolve the rich details provided by the PAD. This issue is discussed in the next chapter in detail.

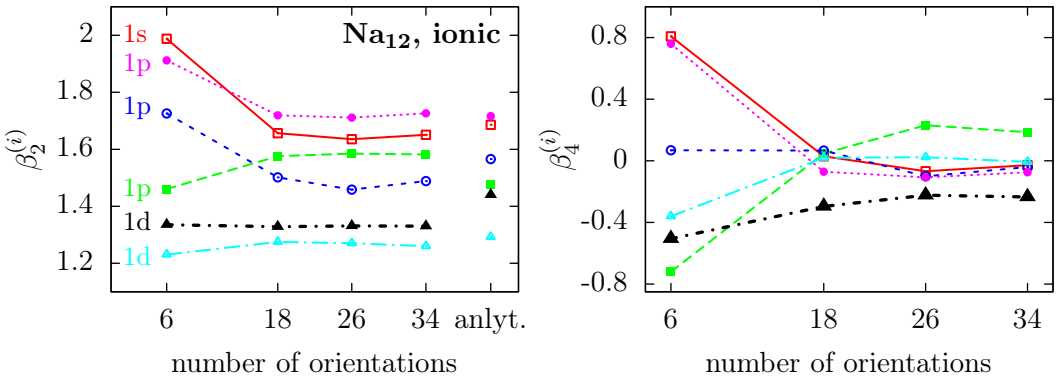

Figure 5.17: Single-electron anisotropies $\beta_2^{(i)}$ (*left*) and $\beta_4^{(i)}$ (*right*) for Na_{12} excited by strong laser pulse in the non-linear regime. Results are drawn as a function of the number of averaging orientations.

The second part of this chapter dealt with excitations beyond the linear regime. Two different cases have been considered here: 1) ionization with frequencies below the IP, and 2) strong ionization with frequencies above IP. In both cases, the analytical averaging scheme developed on the grounds of first-order perturbation theory cannot be used any more. Instead averaging over a finite sum of different cluster orientations has to be applied. Actually, the number of orientations needed for convergence has to be found actually for each system. Among the calculated $Na_N^{(+)}$ clusters, $N = 3 - 19$, the Na_{12} cluster as triaxial system of intermediate size has been considered as representative. Convergence of the first anisotropy parameter β_2 can be achieved for 18 orientations. In order to resolve higher angular momenta, a larger number should be chosen.

An unusual emission behaviour can be observed for laser frequencies below the IP. Contrary to atoms, clusters and among them even small ones exhibit a comparably high spectral density of s.p. and collective excitations, in particular below the IP. Therefore, it is very likely to excite one of these resonances when applying laser frequencies in this domain. In the PES, MPI peaks are then superposed with peaks resulting from resonance-enhanced emission. Furthermore, the post-pulse emission decays only weakly which might be due to neglect of thermalization in the theory. Resonance-enhanced emission emerges later in carbon chains again, see Chapter 8.

6 Frequency dependence of PAD in small sodium clusters

Photoionization cross-sections, photoelectron spectra and angular distributions as a function of photon energy can give insight into electronic structure and dynamics of clusters. Systematic theoretical studies are often based on a perturbative approach, denoted as single-electron, independent-particle or single-active-electron picture in which the "active" electron is excited out of the initial into a final continuum state [79] while the remaining electrons are assumed to be unaffected by the excitation process. Initial and final state are thus calculated within the same effective single-particle potential.

As it was discussed for the Na_8 cluster in the introductory section 5.1 of the last chapter, perturbation theory can indeed describe basic features of the ionization process as long as the laser parameters remain in a regime of linear or weakly non-linear excitations. However, it suffers from the fact that collective and dynamic effects such as dielectric screening, polarization, many-body excitations or rearrangement of the residual cluster, in general, are not included in the model although there exist attempts to consider some of these effects, e.g., by modification of the final state potential or of the transition operator [79, 80] or by time-dependent, perturbative approaches [22, 81].

A crucial point in all perturbative models is the calculation of the final continuum state wavefunction. For bound states the known attractive potential can often be approximated in a first step, e.g., by a harmonic oscillator potential where the basis set of initial wavefunction is more or less finite and well known. The bound state wavefunctions are then calculated in an iterative way. Continuum states above the IP, however, are sensible also against the long-range modification of the attractive potential. The solution of the Schrödinger equation might be possible for atoms and molecules, but definitely gets too involved for larger particles like clusters without any symmetry. One consequently uses approximate solutions for the continuum state [79] or simplified models for the geometrical cluster structure [82], even assumes a spherical jellium model representing the positive ionic background [13, 83, 84].

On the other hand, enough accurate perturbative methods can be used to distinguish single-particle from collective effects, to estimate the impact of these effects on electron dynamics and to understand the importance of a proper de-

scription of the outgoing electronic wave when comparing with full time-dependent many-particle approaches. This chapter therefore is inspired by the above mentioned methods.

The following discussion is focused on one-photon processes in the Na_8 spherical jellium cluster. As can be seen on the dipole response (Fig. 5.10 of Sect. 5.3.1, with ionic background), this cluster has a sharp plasmon resonance at about 0.19 Ry far below the IP. Thus, continuum states do not interfere with a possible collective excitation and should be well described within perturbation theory. For details of the used jellium model it shall be referred to the example section of the last chapter.

Photoionization cross-sections and PAD are first calculated in (static) first-order perturbation theory and are later compared to full time-dependent calculations. Subsequently, the role of deformation in terms of explicit ionic structure is discussed. Finally, results from the negatively charged cluster Na_7^- are presented. It shall be started with an introduction to the used methods.[13]

6.1 Perturbative approaches

6.1.1 Bethe-Cooper-Zare formula

Provided spherical symmetry, the three-dimensional Schrödinger equation of an electron kept in an effective s.p. potential can be simplified to the one-dimensional radial equation

$$\left[-\frac{\hbar^2}{2m_e}\left(\frac{\partial^2}{\partial r^2}+\frac{2}{r}\frac{\partial}{\partial r}\right)+\frac{\hbar^2}{2m_e}\frac{l(l+1)}{r^2}+V(r)-E\right]R_l(r)=0\,, \tag{6.1}$$

with R_l being the radial part of the s.p. wavefunction. Let $|i\rangle$ be the initial bound state with the angular momentum L, M the azimuthal angular momentum, and $E=\epsilon_i<0$,

$$\langle \mathbf{r}|i\rangle = \varphi_i(r\vartheta\varphi) = R_L^{(i)}(r)Y_{LM}(\vartheta\varphi)\,.$$

A general solution for the outgoing wave $|f\rangle$ can be expanded into partial waves,

$$\langle \mathbf{r}|f\rangle = \Psi_{\mathbf{k}}(r\vartheta\varphi) = 4\pi\sum_{lm}\mathrm{i}^l e^{-\mathrm{i}\Delta_l}R_l^{(f)}(r)Y_{lm}^*(\Omega_{\mathbf{k}})Y_{lm}(\Omega_{\mathbf{r}})\,, \tag{6.2}$$

with $E=\epsilon_{\mathrm{kin}}=(\hbar\mathbf{k})^2/2m_e>0$. In spherical potentials, anisotropy and yield can be calculated with the help of the Bethe-Cooper-Zare formula which is derived *in first-order perturbation theory* for one-electron atoms [61], but can also be

[13] Essential parts of the following sections have been published in [76, 85].

applied to many-electron systems provided the wavefunctions are represented by antisymmetrized products of spin orbitals [63]. The independent-particle assumption adopts here its role. The partial cross-section $\sigma^{(i)}$ and the s.e. anisotropy $\beta_2^{(i)}$ are then given by [65, 86]:

$$\sigma^{(i)} = \sigma^{(i)}(\epsilon_{\rm kin}) = \frac{(4\pi)^2\mathcal{N}}{3} \cdot \frac{L\mathcal{R}_-^2 + (L+1)\mathcal{R}_+^2}{(2L+1)}\,, \tag{6.3}$$

$$\beta_2^{(i)} = \beta_2^{(i)}(\epsilon_{\rm kin}) = \frac{L(L-1)\mathcal{R}_-^2 + (L+1)(L+2)\mathcal{R}_+^2 - 6L(L+1)\mathcal{R}_-\mathcal{R}_+\cos\Delta}{(2L+1)[L\mathcal{R}_-^2 + (L+1)\mathcal{R}_+^2]}\,, \tag{6.4}$$

with

$$\mathcal{R}_\pm = \int_0^\infty dr\, r^3 R_{L\pm1}^{(f)}(r) R_L^{(i)}(r) \quad \text{and} \quad \Delta = \Delta_{L+1} - \Delta_{L-1}\,. \tag{6.5}$$

For $L = 0$ the Bethe-Cooper-Zare formula delivers always $\beta_2^{(s)} = 2$. Thus, the angular distribution of the s state is not influenced by the form of the outgoing wave. A spherical symmetric binding potential which modulates the outgoing wave, has consequently no effect on the angular distribution, but still on the yield, as can be seen in Eq. (6.3).

For a given potential $V(r)$ bound and continuum states $R_L^{(i)}$ and $R_{L\pm1}^{(f)}$ are calculated by solving the radial Schrödinger equation (6.1), for details see Appendix B. The phases $\Delta_{L\pm1}$ can be determined by using the asymptotic behaviour:

$$R_l^{(f)}(r) \simeq \frac{\sin\left(kr - \frac{l\pi}{2} - \gamma\ln(2kr) + \Delta_l\right)}{kr} \quad \text{for } r \to \infty\,,$$

with $E = \epsilon_{\rm kin} = (\hbar k)^2/2m_e > 0$ and $\gamma = Z_1 Z_2/(ka_0)$.

6.1.2 Approximations for the outgoing wave

In order to estimate the influence the outgoing wavefunction on the angular distribution, the final state is varied and approximate solutions for $|f\rangle$ are considered. Approximate solutions are furthermore useful as soon as the sphericity is not provided and the three-dimensional Schrödinger equation cannot be decomposed into radial and angular part any more. This is the case, e.g., when explicit ionic structure is included or a deformed jellium model is considered. The Bethe-Cooper-Zare formula is then inapplicable. A possible alternative is given by the analytical, perturbative averaging procedure. The initial wavefunction is still calculated within iterative procedures. For the outgoing waves, the following simple assumptions are made:

Plane wave approximation In the plane wave approximation the outgoing wave becomes

$$\langle \mathbf{r}|f\rangle = \Psi_{\mathbf{k}}^{\text{free}}(r\vartheta\varphi) = e^{\mathrm{i}\mathbf{kr}} = 4\pi \sum_{lm} \mathrm{i}^l j_l(kr) Y_{lm}^*(\Omega_{\mathbf{k}}) Y_{lm}(\Omega_{\mathbf{r}}) \,,$$

i.e., all phases Δ_l in Eq. (6.2) vanish and the functions $R_l^{(f)}$ are given by the spherical Bessel functions.

This approach is the simplest and amounts to the well-known plane wave Born approximation [87]. Plane waves are solutions of the free, three-dimensional Schrödinger equation. Thus, the approximation neglects any effect of the binding potential on the outgoing wave. It is therefore expected, that this assumption is suitable only for weakly bound systems like negatively charged clusters (see Sect. 6.5), or – in case of neutral clusters – for outgoing electrons with very high kinetic energy (Sect. 6.2.2.3).

Continuum waves in a spherical potential well In order to account roughly for the effect of a non-zero potential, the residual binding potential $V(r)$ seen by the continuum waves is approximated by a spherical potential well:

$$V_{\text{s.w.}}(r) = -V_0 \cdot \Theta(r_0 - r) \,, \quad V_0 > 0 \,. \tag{6.6}$$

Continuum states of this short-range potential can still be derived analytically. The radial wavefunction $R_l^{(f)}$ is given by [88]:

$$R_l^{(f)}(r) = \begin{cases} C_l \, j_l(k_0 r) & r < r_0 \,, \\ j_l(kr)\cos(\delta_l) - n_l(kr)\sin(\delta_l) & r > r_0 \,, \end{cases} \tag{6.7}$$

with

$$k_0 = \sqrt{\frac{2m_e}{\hbar^2}(E + V_0)} \,.$$

The unknown quantities C_l and $\Delta_l = \delta_l$ are determined by using the matching conditions,

$$R_l^{(f)}(r_<)\Big|_{r=r_0} = R_l^{(f)}(r_>)\Big|_{r=r_0} \quad \text{and}$$
$$\frac{\partial}{\partial r} R_l^{(f)}(r_<)\Big|_{r=r_0} = \frac{\partial}{\partial r} R_l^{(f)}(r_>)\Big|_{r=r_0} \,.$$

6.2 Static results for Na_8 spherical jellium

6.2.1 Harmonic oscillator model

This section studies the s.e. yield $\sigma^{(i)}(\epsilon_{\rm kin})$ and anisotropy $\beta_2^{(i)}(\epsilon_{\rm kin})$ in Na_8 spherical jellium as a function of the outgoing wave. As a simple analytical example, one may consider at first an electron kept in a spherical harmonic oscillator potential:

$$V_{\rm h.o.}(r) = \frac{1}{2} m_e \Omega_0^2 r^2 - \mathcal{V}_0 \,, \quad \mathcal{V}_0 > 0 \,.$$

This simulates a shell model description instead of a self-consistent one. The radial wavefunctions for the two deepest bound states read [89]:

$$R_0^{(\rm h.o.)}(r) = \mathcal{A} \exp(-\alpha^2 r^2) \,, \qquad L = 0 \,, \tag{6.8a}$$

$$R_1^{(\rm h.o.)}(r) = \mathcal{B}\, r \exp\left(-\alpha^2 r^2\right) \,, \quad L = 1 \,, \tag{6.8b}$$

with

$$\alpha = \sqrt{\frac{m_e \Omega_0}{2\hbar}} \,, \quad \mathcal{A} = \left(\frac{2\alpha^2}{\pi}\right)^{3/4} \cdot \sqrt{4\pi} \,, \quad \mathcal{B} = \sqrt{2}^{5/2} \sqrt{\frac{8}{3}} \frac{\alpha^{3/2}}{\pi^{1/4}} \alpha \,. \tag{6.8c}$$

The eigenvalues for these two states are: $\epsilon_L = \hbar\Omega_0(L + 3/2) - \mathcal{V}_0$. In the plane wave approximation the integrals $\mathcal{R}_-$ and $\mathcal{R}_+$ from Eq. (6.5) can be calculated analytically. For $L = 0$ and $L = 1$ one obtains (see Appendix B.3):

$$\mathcal{R}_+ = \sqrt{\pi}\, \mathcal{A}\, \frac{k}{8\alpha^5} \exp\left(\frac{-k^2}{4\alpha^2}\right) \qquad \text{for } L = 0 \,, \tag{B.7}$$

$$\mathcal{R}_- = \sqrt{\pi}\, \mathcal{B}\, \frac{6\alpha^2 - k^2}{16\alpha^7} \exp\left(\frac{-k^2}{4\alpha^2}\right) \quad \text{for } L = 1 \,, \tag{B.8}$$

$$\mathcal{R}_+ = \sqrt{\pi}\, \mathcal{B}\, \frac{k^2}{16\alpha^7} \exp\left(\frac{-k^2}{4\alpha^2}\right) \qquad \text{for } L = 1 \,. \tag{B.9}$$

Plugging this into Eqs. (6.3) and (6.4) gives yield and anisotropy[14]:

$$\left.\begin{aligned} \sigma^{(1s)} &\sim \epsilon_{\rm kin} \exp\left(\frac{-2\epsilon_{\rm kin}}{\hbar\Omega_0}\right) \\ \beta_2^{(1s)} &= 2 \end{aligned}\right\} \text{for } L = 0 \,, \tag{6.9}$$

[14] Normalization of the plane wave in energy scale is achieved by replacing j_l with $\sqrt{2k/\pi}\, j_l$. This would give an additional prefactor in the order of $\sqrt{\epsilon_{\rm kin}}$ in the yield.

$$\left.\begin{aligned} \sigma^{(1p)} &\sim \left[\left(\frac{3}{2}\hbar\Omega_0 - \epsilon_{\mathrm{kin}}\right)^2 + 2\epsilon_{\mathrm{kin}}^2\right] \exp\left(\frac{-2\epsilon_{\mathrm{kin}}}{\hbar\Omega_0}\right) \\ \beta_2^{(1p)} &= \frac{2k^2(k^2-4\alpha^2)}{k^2(k^2-4\alpha^2)+12\alpha^4} \end{aligned}\right\} \text{for } L = 1\,. \tag{6.10}$$

The self-consistent wavefunctions for the bound $1s$ and $1p$ states in Na_8 spherical jellium are indeed quite similar to the solutions of the harmonic oscillator given in Eq. (6.8). For example, Figure 6.1 (left panel) shows the radial wavefunction of the $1p$ states in Na_8 obtained within static LDA-SIC. The dashed line represents a fit of the harmonic solution to the real wavefunction. As one can see – up to a radius of about $r \sim 10\,a_0$ – the fit matches very well with the self-consistent wavefunction.

The right panel of Fig. 6.1 displays the anisotropy for $L = 1$ obtained by inserting the fitting parameter α^2 into Eq. (6.10). For energies $\epsilon_{\mathrm{kin}} \gtrsim 0.5\,\mathrm{Ry}$ the anisotropy remains at a value close to 2. For smaller kinetic energies the shape of the curve is characteristic for the plane wave approximation: starting from values around 2 for higher energies, it shows a decline first towards $\beta_2^{(1p)} = 1$ at $\epsilon_{\mathrm{kin}} = (6\hbar^2\alpha^2)/(2m_e) = 0.16\,\mathrm{Ry}$ then a zero crossing at $\epsilon_{\mathrm{kin}} = (4\hbar^2\alpha^2)/(2m_e) = 0.11\,\mathrm{Ry}$. Afterwards negative values arise up to the minimum value of $\beta_2^{(1p)} = -1$ at $\epsilon_{\mathrm{kin}} = (2\hbar^2\alpha^2)/(2m_e) = 0.05\,\mathrm{Ry}$. Finally, the anisotropy ends up in $\beta_2^{(1p)} = 0$ at $\epsilon_{\mathrm{kin}} = 0$, since for $k = 0$ the angular distribution

$$\frac{d\sigma^{(i)}}{d\Omega_{\mathbf{k}}} = \mathcal{N}\left|\int d^3r\, z\, \varphi_i(\mathbf{r})\right|^2\,, \quad \text{for } k = 0\,, \tag{6.11}$$

becomes independent in the wave vector $\mathbf{k}$. A detailed explanation of the near-threshold behaviour of $\beta_2^{(1p)}$ is given later in Sect. 6.2.2.2.

6.2.2 Static results with self-consistent wavefunctions

Although the simple harmonic oscillator matches well with the self-consistent calculation, the radial functions $R_L^{(\mathrm{h.o.})}$ do not show the right asymptotic decay. The asymptotic fall off, however, is expected to be an important criterion since the continuum waves definitely are sensitive to the latter. Therefore, the real, self-consistent wavefunctions from the LDA-SIC ground-state of the jellium model are better serving as a starting point in the following. For the outgoing waves $R_l^{(f)}$ $(l = 0, 1, 2)$ the three cases introduced in the last sections have been considered:

(1) A free plane wave.

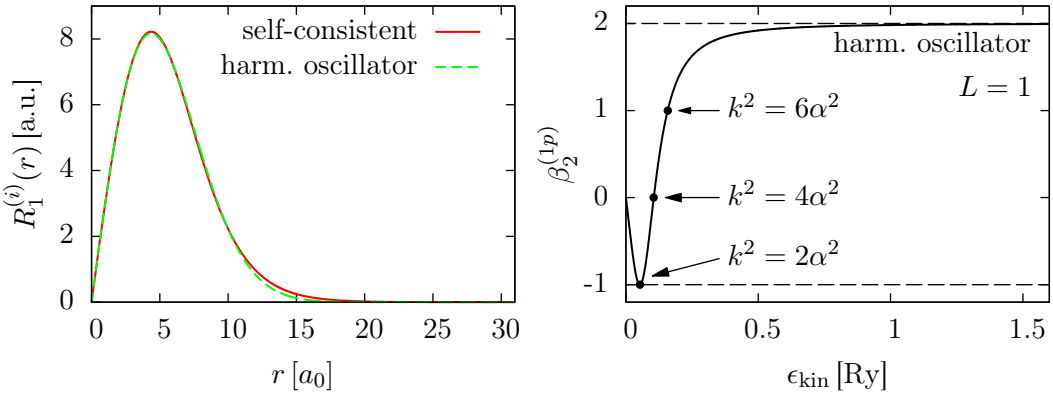

Figure 6.1: *Left panel:* Radial part of the wavefunction in Na_8 spherical jellium for the $1p$ state, calculated self-consistently within static LDA-SIC (red) and fit to the harmonic oscillator (green). The fit yields $\alpha^2 = 0.026\,a_0^{-2}$ ($\Omega_0 = 0.105\,\mathrm{Ry}$). *Right panel:* Anisotropy $\beta_2^{(1p)}$ of the harmonic oscillator fit in the plane wave approximation.

(2) A continuum wave moving in a spherical square-well potential $V_{\rm s.w.}$:
Width r_0 and depth V_0 of the square-well potential were chosen so that its two deepest eigenenergies ϵ_{g0} and ϵ_{g1} with $L = 0$ and $L = 1$ match with the s.e. energies $\epsilon_{1s} = -0.405\,\mathrm{Ry}$ and $\epsilon_{1p} = -0.300\,\mathrm{Ry}$ of the LDA ground-state. The left panel in Fig. 6.2 shows the energy curves $\epsilon_{g0} - \epsilon_{1s} = 0$ and $\epsilon_{g1} - \epsilon_{1p} = 0$ as a function of V_0 and r_0. The two curves intersect at $V_0 = -0.507\,\mathrm{Ry}$ and $r_0 = 8.36\,a_0$.

(3) A continuum wave moving in the self-consistent ground-state Kohn-Sham potential $U_{\rm K.S.}$.

The phases Δ_l are always determined by the asymptotic behaviour. All wavefunctions and phases are finally inserted into Eqs. (6.3) and (6.4). The right panel of Fig. 6.2 summarizes the considered potentials. The harmonic oscillator in plane wave approximation can still serve as a guideline. Its potential ($\hbar\Omega_0 = 0.105\,\mathrm{Ry}$ and $\mathcal{V}_0 = 0.563\,\mathrm{Ry}$) is also sketched.

6.2.2.1 Yield for the 1*s* state

The anisotropy of any state with angular momentum $L = 0$ is always $\beta_2^{(1s)} = 2$, so not worth to consider here. Figure 6.3 (left panel) shows instead the cross-section $\sigma^{(1s)}$ for the three models (1), (2), and (3). For all three curves the main emission takes place below energies $\epsilon_{\rm kin} \lesssim 0.5\,\mathrm{Ry}$. This feature can be explained with the form of the transition integral. For instance, in the plane wave approximation the

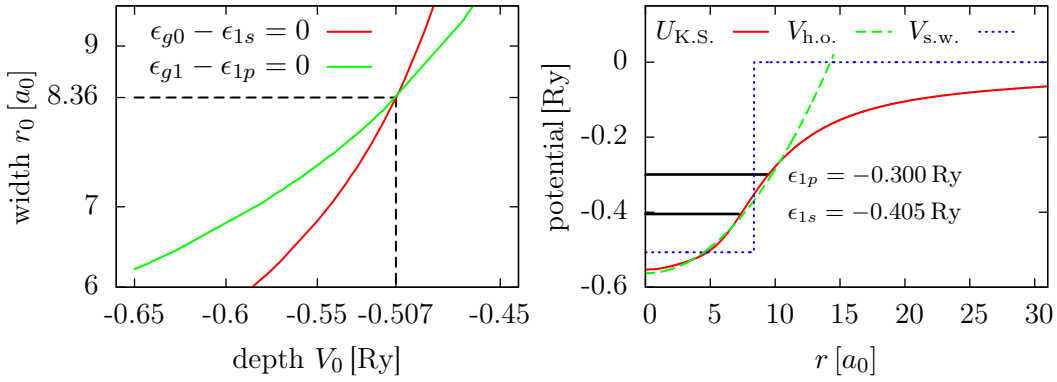

Figure 6.2: *Left panel:* The two deepest eigenenergies ϵ_{g0} and ϵ_{g1} in the square-well potential as a function of its depth V_0 and width r_0. $\epsilon_{g0} = \epsilon_{1s}$ and $\epsilon_{g1} = \epsilon_{1p}$ is fulfilled for $V_0 = -0.507\,\text{Ry}$ and $r_0 = 8.36\,a_0$. *Right panel:* Kohn-Sham potential of the jellium model, square-well potential, and the harmonic oscillator.

transition integral becomes:

$$\langle f|\hat{z}|i\rangle \sim \int d^3r\, e^{-\mathbf{ikr}}\, z\, \varphi_i(\mathbf{r})\,. \tag{6.12}$$

For high kinetic energy, i.e., high wave number k, the plane wave becomes a fast oscillating function in space (in relation to the initial wavefunction), so that the transition integral as well as the cross-section takes negligible values. This reasoning applies also to the distorted (plane or Coulomb) waves of model (2) and (3).

The same argument can be used when comparing the total yields integrated over ϵ_{kin}. The three curves in the left panel have been normalized to the same total emission yield. The normalization factor reveals that emission is strongly suppressed in (2) and (3). This is related to the fact, that the attractive potential modifies the continuum states (right panel). Continuum states with asymptotic wave number k in fact oscillate faster inside the binding potential at small distances r. However, since the main transition takes place also at small distances, the transition integral is suppressed.

6.2.2.2 Anisotropy and yield for the 1*p* state

Figure 6.4 shows anisotropy and cross-section for the $1p$ shell in Na_8 spherical jellium (red line) in the plane wave approximation (1). As a guideline, Eq. (6.10) of the harmonic oscillator model is also drawn (black line). As one can see, below $\epsilon_{\text{kin}} \lesssim 1.0\,\text{Ry}$ it makes practically no difference in anisotropy as well as

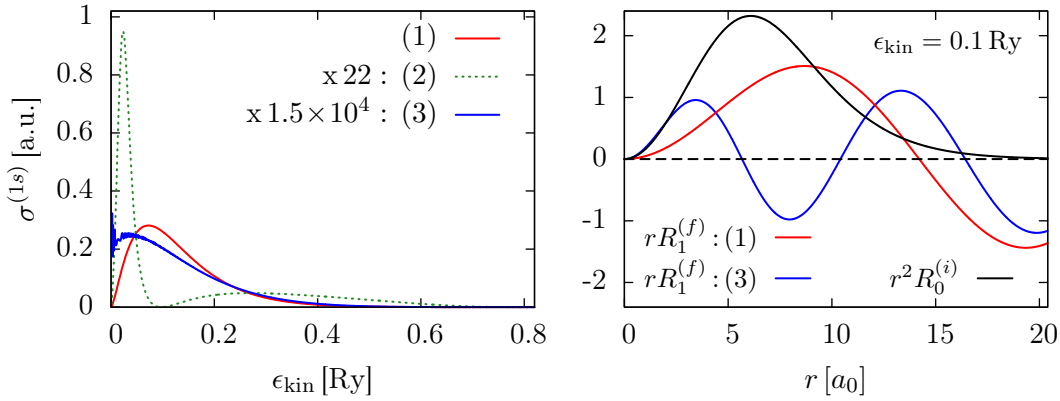

Figure 6.3: *Left panel:* Normalized partial cross-section $\sigma^{(1s)}$ of the $1s$ state in Na_8 spherical jellium for three different continuum state models: (1) plane wave approximation, (2) continuum wave moving in $V_{\text{s.w.}}$, and (3) continuum wave moving in $U_{\text{K.S.}}$. Normalization factors for (2) and (3) are indicated. *Right panel:* Continuum waves $rR_1^{(f)}$ for models (1) and (3) ($\epsilon_{\text{kin}} = 0.1\,\text{Ry}$) and initial radial wavefunction $r^2R_0^{(i)}$.

yield if using the self-consistent wavefunction or the harmonic fit. Note that the initial self-consistent wavefunctions differ only slightly from the (fitted) harmonic oscillator functions (Fig. 6.1, left panel). The modification is mainly located at $r \sim 10\,a_0$. The overall shape of both wavefunctions remains. In **k**-space the picture would be similar. Differences in $\varphi_i(\mathbf{k})$ show up at high wave numbers, and are consequently probed by the transition integral (6.12) only at large kinetic energies.

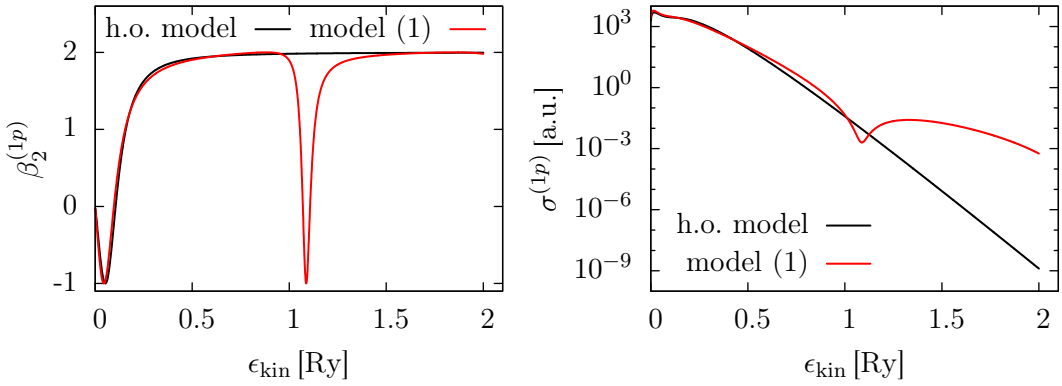

Figure 6.4: Anisotropy (*left*) and cross-section (*right*) of the $1p$ states in Na_8 spherical jellium in plane wave approximation. The initial wavefunction $R_1^{(i)}(r)$ was calculated self-consistently (red). The harmonic oscillator model is also shown (black).

At $\epsilon_{\mathrm{kin}} \approx 1.1\,\mathrm{Ry}$ the two models differ significantly. The anisotropy drops off sharply towards $\beta_2^{(1p)} = -1$ for the self-consistent wavefunction whereas it remains nearly constant at values around $\beta_2^{(1p)} \approx 2$ for the harmonic function. The reason for this sudden decline is the form of the integrals $\mathcal{R}_-$ and $\mathcal{R}_+$:

$$\mathcal{R}_\pm = \int_0^\infty dr\, r^3 R_{L\pm1}^{(f)}(r) R_L^{(i)}(r)\,. \tag{6.5}$$

For the harmonic fit these integrals have been solved analytically in Eqs. (B.8) and (B.9). For the self-consistent wavefunction they were evaluated numerically and are shown in Fig. 6.5 (left panel) as a function of ϵ_{kin}. In the harmonic oscillator model, the integrals $\mathcal{R}_-$ and $\mathcal{R}_+$ have only one root each (at $6\alpha^2 - k^2 = 0$ and at $k = 0$, respectively) at which they change their sign.

In contrast, the self-consistent integrals have several roots in large, irregular intervals of more than 1 Ry. These roots arise since the integrand in $\mathcal{R}_\pm$ consists of the oscillating function $r^2 R_{1\pm1}^{(f)}$ times the smooth function $r R_1^{(i)}$ (see for example Fig. 6.3 for the s state). Hence, the integrals vanish for some kinetic energies. In fact, the harmonic oscillator model is by this view a rather exceptional case.

Another noteworthy aspect is that $\mathcal{R}_+$ and $\mathcal{R}_-$ differ significantly only for $\epsilon_{\mathrm{kin}} \lesssim 0.5\,\mathrm{Ry}$. For higher energies, they are very similar and have their roots almost at the same positions. This is related to the fact that for higher energies the centrifugal term in the radial Schrödinger equation (6.1) plays a minor role. That means $R_{L+1}^{(f)}(r) \approx R_{L-1}^{(f)}(r)$ for radii r with $\hbar^2/2m_e \times L(L+1)/r^2 \ll \epsilon_{\mathrm{kin}}$. As higher ϵ_{kin} as closer this radius comes to zero and the integrals $\mathcal{R}_\pm$ become more and more aligned.

The roots of $\mathcal{R}_\pm$, however, play now a major role in determining the PAD. When writing down the Bethe-Cooper-Zare formula for $L = 1$ in the plane wave approximation,

$$\beta_2^{(1p)} = \frac{2\mathcal{R}_+^2 - 4\mathcal{R}_-\mathcal{R}_+}{\mathcal{R}_-^2 + 2\mathcal{R}_+^2} = \begin{cases} 2\,, & \text{for } \mathcal{R}_- = -\mathcal{R}_+ \\ 1\,, & \text{for } \mathcal{R}_-(\mathcal{R}_- + 4\mathcal{R}_+) = 0 \\ 0\,, & \text{for } \mathcal{R}_+(\mathcal{R}_+ - 2\mathcal{R}_-) = 0 \\ -1\,, & \text{for } 2\mathcal{R}_+ = \mathcal{R}_- \end{cases} \tag{6.13}$$

one observes that for $\beta_2^{(1p)} = 2$, $\mathcal{R}_-$ and $\mathcal{R}_+$ have opposite, for $\beta_2^{(1p)} = -1$ the same sign. Since $\mathcal{R}_-$ can change its sign only at $\beta_2^{(1p)} = 1$ and $\mathcal{R}_+$ only at $\beta_2^{(1p)} = 0$, $\mathcal{R}_-$ and $\mathcal{R}_+$ also have same sign for $\beta_2^{(1p)} < 0$ and opposite sign for $\beta_2^{(1p)} > 1$. The right panel in Fig. 6.5 illustrates these considerations. The dip in $\beta_2^{(1p)}$ is so sharp because the roots of $\mathcal{R}_-$ and $\mathcal{R}_+$ are located very close to each other.

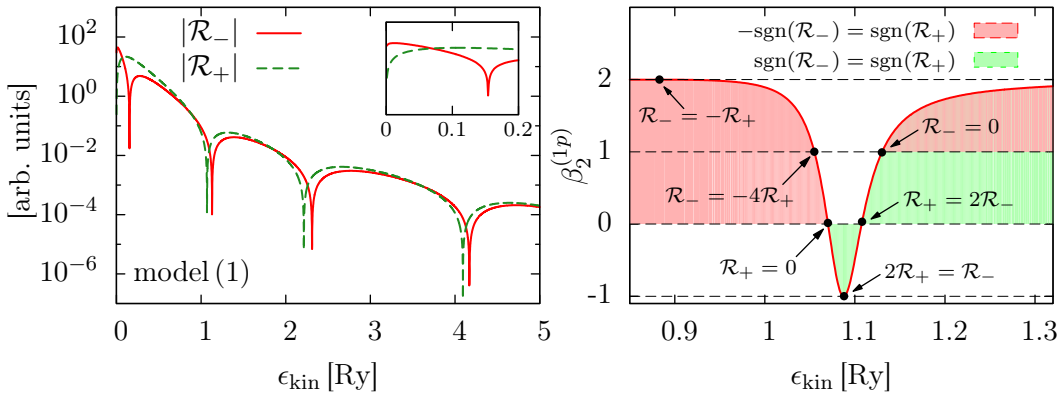

Figure 6.5: *Left panel:* Absolute value of the integrals $\mathcal{R}_\pm$ as a function of $\epsilon_{\rm kin}$ for Na_8 spherical jellium in plane wave approximation. *Right panel:* Anisotropy $\beta_2^{(1p)}$ (see also red line in Fig. 6.4). Interesting points are indicated. In the red region $\mathcal{R}_\pm$ have opposite, in the green region same sign.

The minimum of $\beta_2^{(1p)}$ around $\epsilon_{\rm kin} \approx 1.1\,\mathrm{Ry}$ correlates with a drop in the cross-section, Fig. 6.4 right panel. Since both integrals $\mathcal{R}_\pm$ change their sign in this region, they consequently take small values and the cross-section

$$\sigma^{(1p)} = \frac{(4\pi)^2\mathcal{N}}{9} \cdot \left(\mathcal{R}_-^2 + 2\mathcal{R}_+^2\right)$$

decreases, too.

Returning now to the threshold behaviour of $\beta_2^{(1p)}$. As already mentioned, the decline first to negative $\beta_2^{(1p)}$ then towards zero is typical for the plane wave approximation. Having a closer look at the left panel of Fig. 6.5, one notices that at $\epsilon_{\rm kin} \lesssim 0.5\,\mathrm{Ry}$ the two integrals $\mathcal{R}_\pm$ differ more strongly with $|\mathcal{R}_-| \gg |\mathcal{R}_+|$ for $\epsilon_{\rm kin} \to 0$ (see inset). This can again be attributed to the centrifugal term in the Schrödinger equation: for $L(L+1) \gg (kr^*)^2$, the centrifugal term dominates the form of the radial wavefunctions.[15] Within the extension r^* the wavefunctions $R_{L\pm1}^{(f)}$ differ then substantially and so do the integrals $\mathcal{R}_\pm$.

Figure 6.5 shows only the absolute values of $\mathcal{R}_\pm$ (due to the logarithmic scale). In fact, near threshold both integrals are positive since the spherical Bessel functions behave like

$$j_l(kr^*) = \frac{(kr^*)^l}{(2l+1)!!}\,, \quad k \to 0\,.$$

over the whole extension of the bound state wavefunction. Moreover, because

[15] The parameter r^* denotes roughly the radius at which the integration in Eq. (6.5) has converged sufficiently accurate, here $r^* \approx 20\,a_0$.

of the larger repulsive centrifugal term, the outgoing wave with $L+1$ is more pushed away from the inner bound region than the $L-1$ wave. In consequence, $\mathcal{R}_- \gg \mathcal{R}_+$ for $\epsilon_{\text{kin}} \to 0$ and $\beta_2^{(1p)}$ vanishes, Eq. (6.13).

The starting point for the anisotropy near threshold corresponds to the point $\mathcal{R}_+ = 0$ in the right panel of Fig. 6.5. Since both integrals are positive and have same sign, negative values for $\beta_2^{(1p)}$ follow. With further increasing of ϵ_{kin} the oscillations of the j_l approach the binding zone and the integrals $\mathcal{R}_\pm$ diminish. The root of $\mathcal{R}_-$ arises first since the oscillations approach earlier due to the lower repulsive centrifugal term for $L-1$.

Having understood the trend of β_2 in the plane wave approximation, it is also interesting to compare different continuum wave models. Figure 6.6 plots the results for the models (1), (2), and (3). In contrast to the plane wave, the phases Δ_2 and Δ_0 must be considered in model (2) and (3). All three curves for $\beta_2^{(1p)}$ in the left panel vary between -1 and 2 and exhibit sharp minima at certain frequencies. The minima in anisotropy are also correlated with minima in the cross-section. The position of the minima, however, dramatically depends on the chosen form of the continuum wavefunction. The discrepancy between the continuum models becomes even more striking for small kinetic energies. This is reasonable because for outgoing waves with low kinetic energy the depth of the scattering potentials becomes more important.

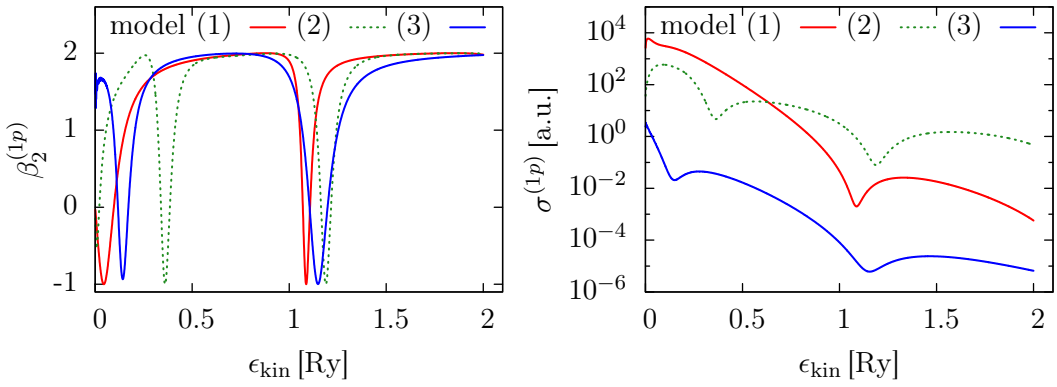

Figure 6.6: Anisotropy $\beta_2^{(1p)}$ and cross-section $\sigma^{(1p)}$ of the $1p$ shell in Na_8 spherical jellium within the three presented models.

In case of a non-zero potential $V(r)$ for the continuum states, the detailed threshold behaviour is less predictable. For $l(l+1) \gg (kr^*)^2$ the kinetic term is still negligible in the radial Schrödinger equation, but not so $V(r)$[16]. While the

[16] $V(r)$ is only negligible for $r \to 0$, but this is not the here considered case!

centrifugal term is repulsive, the short-range component of $V(r)$ attracts again the oscillating continuum waves into the binding zone. Thus, the von-Neumann functions n_l also contribute to the continuum wave which additionally gets a phase shift. All in all, the roots of the integrals $\mathcal{R}_\pm$ arise at different positions compared to the plane wave approximation. In contrast, high kinetic energies overrule both, centrifugal term and short range component of $V(r)$ and $R^{(f)}_{L+1} \approx R^{(f)}_{L-1}$ should align as already discussed. Additionally, the phases Δ_0 and Δ_2 approach each other and $\Delta \to 0$. This amounts then again to the plane wave approximation. The detailed behaviour of $\sigma^{(1p)}$ and $\beta_2^{(1p)}$ at high energies is discussed the next section.

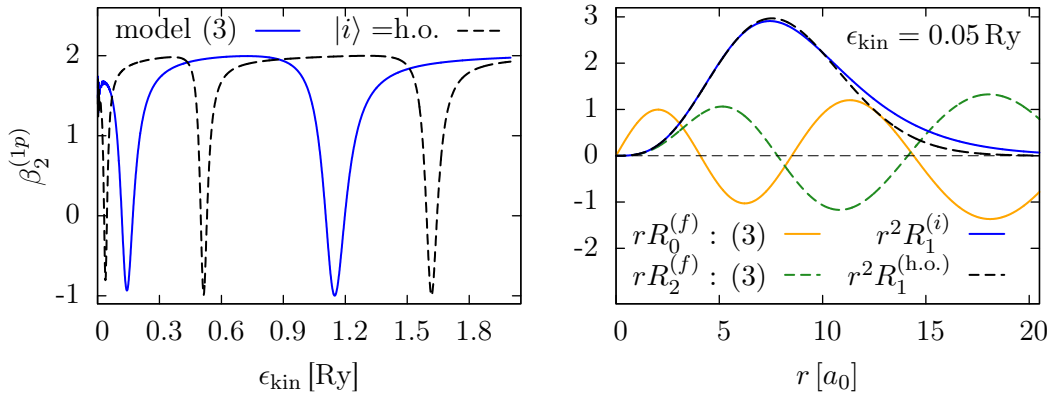

Figure 6.7: *Left panel:* Anisotropy of the $1p$ shell in Na_8 spherical jellium within model (3) (blue line). Replacing the initial self-consistent state by the harmonic fit yields the black, dashed line. *Right panel:* Continuum waves $rR_0^{(f)}$ and $rR_2^{(f)}$ within model (3) at energy $\epsilon_{\rm kin} = 0.05\,$Ry, initial self-consistent wavefunction $r^2R_1^{(i)}$, and harmonic fit function $r^2R_1^{(\rm h.o.)}$.

Another interesting aspect can be derived when replacing the initial self-consistent wavefunction in model (3) with the harmonic fit function, but keeping the continuum wave of the self-consistent K.S. potential. This is similar to a slight modification of the initial bound wavefunction as already done in Fig. 6.4. The original and the modified model are compared in the left panel of Fig. 6.7. In contrast to Fig. 6.4, original and modified model differ here already for small kinetic energies. A possible explanation is that the continuum waves with asymptotic wave number k are inside the binding region continuously compressed towards shorter wavelengths due to the attractive potential $U_{\rm K.S.}$, as was already discussed previously (right panel of Fig. 6.7). They are thus also sensitive to small variations in $|i\rangle$ and accordingly filter this in the transition integral.

6.2.2.3 Photoionization oscillations at high frequencies

Frank and Rost [90] have found that the partial photoionization cross-sections of Na_{40} and C_{60} spherical jellium oscillate at high laser frequencies like they are typically used at the synchrotron. These oscillations are genuine for all spherical (non-Coulomb) potentials. The frequencies of the oscillations are related to the diameter of the electronic cloud. As an example, Figure 6.8 shows anisotropy and cross-section of the $1p$ shell in Na_8 spherical jellium (same jellium parameterization as above) for the three considered continuum wave models at high kinetic energies. The quantities are plotted versus the wave number $k = \sqrt{2m_e/\hbar^2\epsilon_{\rm kin}}$ divided by the oscillation period.

The oscillations can be understood when considering initial and final states in the spherical square-well potential [90], e.g.:

$$\hat{H}\varphi_i(\mathbf{r}) = \left[\frac{\hat{\mathbf{p}}^2}{2m_e} + V_{\rm s.w.}(\mathbf{r})\right]\varphi_i(\mathbf{r}) = \epsilon_i\varphi_i(\mathbf{r})\,.$$

The matrix element for the transition from state $|i\rangle$ to $|f\rangle$ in velocity gauge is proportional to $\langle i|\mathbf{e}_{\rm pol}\cdot\hat{\mathbf{p}}|f\rangle$. From there one can transform into the so-called *acceleration gauge* [91]:

$$\left[\hat{\mathbf{p}},\hat{H}\right] = \frac{\hbar}{\mathrm{i}}\nabla V_{\rm s.w.}(\mathbf{r}) \quad\Longrightarrow\quad \langle i|\hat{\mathbf{p}}|f\rangle(\epsilon_f-\epsilon_i) = \langle i|\left[\hat{\mathbf{p}},\hat{H}\right]|f\rangle\,.$$

The derivative of the spherical square-well potential $V_{\rm s.w.}$ gives a delta-function,

$$\nabla V_{\rm s.w.}(\mathbf{r}) = V_0\mathbf{e}_r\,\delta(r_0-r)\,,$$

thus the transition integral reads ($\mathbf{e}_{\rm pol}=\mathbf{e}_z$):

$$\langle i|\mathbf{e}_{\rm pol}\cdot\hat{\mathbf{p}}|f\rangle \sim \langle i|\delta(r_0-r)\,Y_{10}|f\rangle \sim R_L^{(i)}(r_0)R_l^{(f)}(r_0)\,,$$

upon condition that the dipole selection rule $|L-l|=1$ is fulfilled. The exact solution of $R_l^{(f)}$ (inside the square-well), given in Eq. (6.7),

$$R_l^{(f)}(r_0) = C_l j_l(k_0 r_0)\,, \tag{6.7}$$

where $k_0^2 = \frac{2m_e}{\hbar^2}(\epsilon_f-\epsilon_i)$, is a spherical Bessel function which goes for $k_0r_0 \gg 1$ like:

$$R_l^{(f)}(r_0) \sim \sin\left(k_0r_0 - \frac{l\pi}{2}\right)\,.$$

In the limit of high kinetic energies $\epsilon_f = \epsilon_{\mathrm{kin}}$, one can neglect the binding energy ϵ_i and the wave number k_0 is approximately $k_0^2 \approx \frac{2m_e}{\hbar^2}\epsilon_{\mathrm{kin}} = k^2$. Hence, for high kinetic energies the partial cross-section

$$\sigma^{(if)} \sim \sin^2\left(kr_0 - \frac{l\pi}{2}\right) = \frac{1}{2} - \frac{1}{2}\cos(2kr_0 - l\pi) \tag{6.14}$$

oscillates with a frequency of $2r_0$ in k. The initial state $|i\rangle$ with angular momentum L couples to final states with $l_1 = L + 1$ and $l_2 = L - 1$. Since $l_1 - l_2 = 2$, the partial cross-sections for both final states oscillate in phase. Finally, both partial cross-sections have to be added up to the cross-section $\sigma^{(i)}$ out of state $|i\rangle$ which oscillates then with the same frequency.

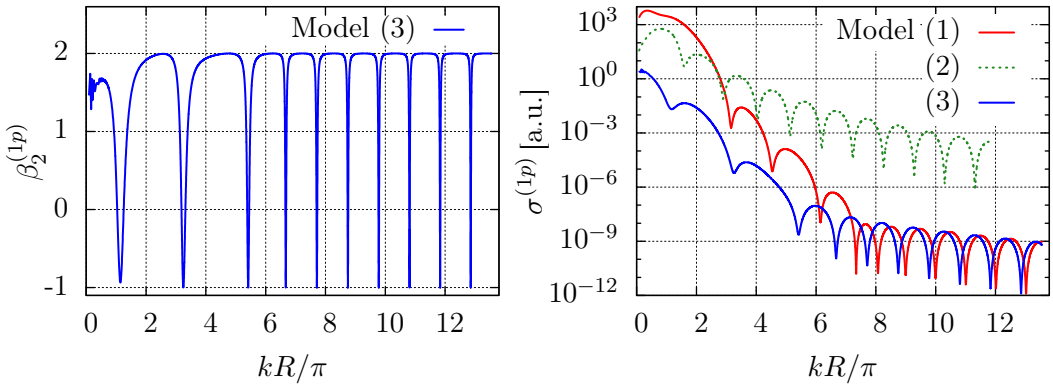

Figure 6.8: Anisotropy and cross-section for the $1p$ shell in Na_8 spherical jellium as a function of kR/π ($\epsilon_{\mathrm{kin}} = 0 - 20\,\mathrm{Ry}$) with the oscillation period $R_1 = R_3 = 9.52\,a_0$ for models (1) and (3) and $R_2 = r_0 = 8.36\,a_0$ ($r_0 =$ width of the square-well potential) for model (2).

Cross-section and anisotropy in Fig. 6.8 are shown as a function of kR/π. The radius R is obtained by a fit of the high frequency behaviour to Eq. (6.14). Thereby, $R = 9.52\,a_0$ is obtained for model (1) and (3) and $R_2 = 8.36\,a_0$ for model (2). Thus, model (2) behaves exactly as described above, i.e., in the limit of high kinetic energies the radius R_3 corresponds to the width of the square-well, $R_3 = r_0$. In contrast, cross-section and anisotropy for model (1) and (3) oscillate slightly faster ($R = 9.52\,a_0$). The binding potential here is not a sharp edge like the square-well potential. Hence, the derivative is not a δ-function. However, the softened potential edge has still a peaked derivative around $R = 9.52\,a_0$ which preserves the diffraction effect. Furthermore, model (1) and (3) oscillate at high energies within the same period, since the influence of the (soft) binding potentials on the continuum waves in model (3) can be neglected in this range and the plane wave becomes a legitimate approximation.

6.3 Time-dependent spherical jellium calculations

The above results confirm that the continuum wavefunction is an essential ingredient for a correct description of the angular distribution. The high sensitivity indicates, however, that the independent-particle picture might be a questionable assumption. Important dynamical effects in the course of the photoionization process, like polarization, rearrangement of the residual cluster, or many-body excitations are not included in the model, even if initial bound and final continuum states are calculated in the same self-consistent potential [13]. It is therefore interesting to lie time-dependent calculations next to the static results [85]. This is demonstrated in the left panel of Fig. 6.9 which compares a fully dynamical TDLDA calculation to a TDLDA calculation in which the electrons are propagated, but the ground-state K.S. potential is kept frozen during evolution. A frozen K.S. potential, in turn, suppresses all dynamical polarization and rearrangement effects and should correspond to a perturbative treatment.

The jellium parameters have been the same as previously used ($r_s = 3.65\,a_0$, $\sigma_{\mathrm{jel}} = 1\,a_0$). The laser pulse length was $T_{\mathrm{pulse}} = 60\,\mathrm{fs}$. The intensity $I = 10^{13}\,\mathrm{W/cm^2} \times \omega_{\mathrm{las}}/\mathrm{Ry}$ was scaled with the frequency in order to keep ionization in a perturbative range of $N_{\mathrm{esc}} = 10^{-4} - 10^{-1}$. The case with frozen $U_{\mathrm{K.S.}}$ restores the result obtained from first-order perturbation theory in Fig. 6.7 for the anisotropy $\beta_2^{(1p)}$ (for better comparison of time-dependent and static calculation, the left panel in Fig. 6.9 is plotted versus the kinetic energy $\epsilon_{\mathrm{kin}} = \omega_{\mathrm{las}} - 0.3\,\mathrm{Ry}$). The full TDLDA calculation, however, yields a totally different pattern. Dynamic effects as the interaction of the outgoing electrons with the residual cluster have apparently a significant influence on the angular distribution.

The right panel of Fig. 6.9 displays the anisotropy for two different jellium parameterizations, now both fully time-dependent. Jellium 1 is the original one. Jellium 2 uses slightly different parameters ($r_s = 3.9\,a_0$, $\sigma_{\mathrm{jel}} = 0.7\,a_0$). Again, one can observe the great sensitivity of the angular distribution to small variations of the underlying potential. While the ionization potential of both models differ only marginally ($\mathrm{IP}_1 = 0.30\,\mathrm{Ry}$, $\mathrm{IP}_2 = 0.31\,\mathrm{Ry}$), the frequency shift between the two minima amounts to more than 0.1 Ry.

6.4 Role of deformation

6.4.1 Trends in static plane wave approximation

From the above observed sensitivity of PAD, one expects that the treatment of the ionic background is also very important. As a simple improvement of the spherical jellium model, one occasionally makes use of a deformed jellium model,

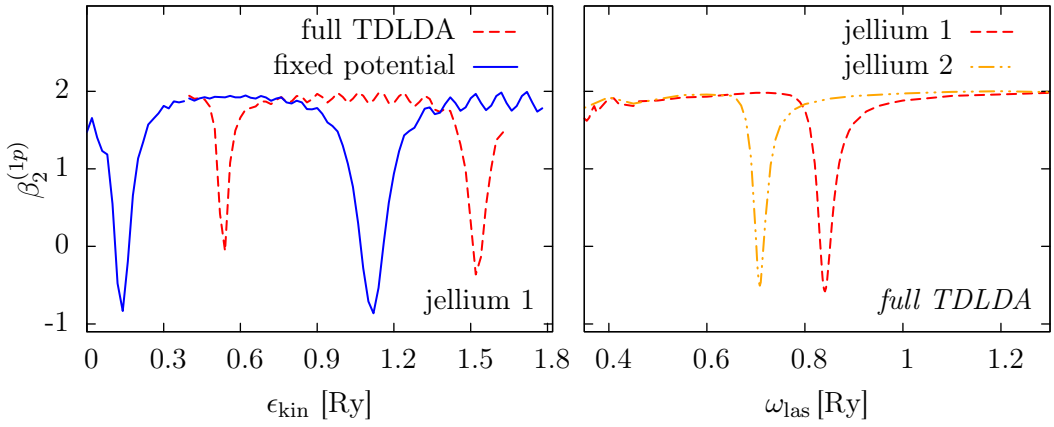

Figure 6.9: *Left panel:* Anisotropy $\beta_2^{(1p)}$ of the $1p$ shell in Na_8 spherical jellium as a function of the kinetic energy $\epsilon_{\rm kin} = \epsilon_{1p} + \omega_{\rm las}$ (with $\epsilon_{1p} = -0.3\,$Ry). Compared are results obtained by full TDLDA and by TDLDA with fixed K.S. potential. *Right panel:* $\beta_2^{(1p)}$ vs. $\omega_{\rm las}$ for the two different jellium models (jellium 1: $r_s = 3.65\,a_0$, $\sigma_{\rm jel} = 1\,a_0$; jellium 2: $r_s = 3.9\,a_0$, $\sigma_{\rm jel} = 0.7\,a_0$).

here quadrupole deformed. The strength of the deformation is then given by the dimensionless moment α defined in Eq. (5.1). Since spherical symmetry is no longer conserved, the Bethe-Cooper-Zare formulae (6.3) and (6.4) cannot be used here. Consequently, one has to apply averaging schemes in order to obtain $\beta_2^{(i)}$ and $\sigma^{(i)}$. As a preliminary step, the following basic trends are obtained in static first-order perturbation using the methods stressed above.

Figure 6.10 (upper left panel) shows the angular distribution depending on the deformation parameter α for Na_8 jellium[17]. The deformation takes place along the z-axis of the cluster frame and stretches the cluster into a prolate shape. The deformation splits the $1p$ shell into two non-degenerate states "$1p_{x,y}$" and "$1p_z$". The self-consistent $1p_z$ state which is axial symmetric ($m = 0$), was considered here as initial bound state. The continuum states were assumed to be plane waves. The averaging was done by application of the analytical scheme (full-perturbative scheme according to Sect. 4.2.5). The red line indicates the spherical ($\alpha = 0$) result (Fig. 6.4). As one can see, already a very small deformation wipes out the characteristic sharp $\beta_2^{(1p_z)}$-minimum of the spherical model. The same applies for the cross-section $\sigma^{(1p_z)}$ (upper right panel). A possible explanation is, that the deformation adds further angular momentum components to the initial state, for instance, for a quadrupole deformation the deformed initial state can

[17] The original jellium parameterization is used again (jellium 1).

be approximately[18] written as follows:

$$\varphi_i(r\vartheta\varphi) = R_1^{(i)}(r)Y_{10}(\vartheta\varphi) + \eta R_2^{(i)}(r)Y_{20}\,,$$

where $\eta \propto \alpha$. Theses components open new channels for the transition of the

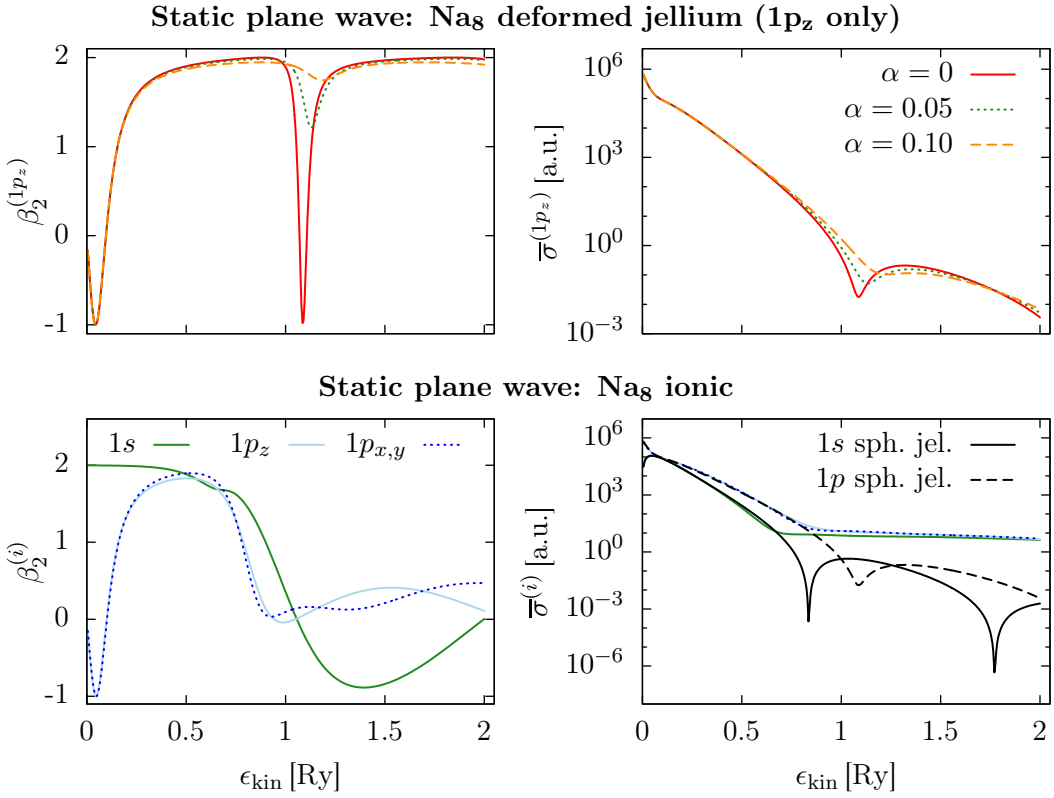

Figure 6.10: Anisotropy and cross-section in static plane wave approximation, as a function of kinetic energy. *Upper panels:* $1p_z$ state in Na_8 deformed jellium model with different degrees of deformation α ($\alpha = 0$ is spherical). *Lower panels:* Static model for Na_8 with explicit ionic structure. For comparison, the corresponding cross-sections of Na_8 spherical jellium are also plotted in the lower right panel.

electron into a continuum state. The behaviour of $\beta_2^{(i)}$ as a function of ϵ_{kin} becomes now less predictable since the favorite emission direction of the new channels is unknown, in principle. In order to observe sharp minima in the cross-section $\sigma^{(i)}$, not only the transition integral $\mathcal{R}_0$ and $\mathcal{R}_2$, but also $\mathcal{R}_3$ and $\mathcal{R}_1$ must take negligible values, each at similar frequency. This event is much more improbable and great fluctuations are smoothed out. The additional channels also lead to

[18] "Approximately" because the functions $R^{(i)}$ depend actually also on $\vartheta\varphi$.

a higher cross-section as seen in the lower right panel when compared to the spherical jellium results.

A more realistic and detailed description of the ionic background is provided by pseudo-potentials. Pseudo-potentials do not change only the overall form of the electronic density, but constitute a strong, located modification of the initial wavefunctions corresponding to high angular momentum. Analogously to the previous perturbative approach, the initial wavefunction of the $1p_z$ state was extracted now from a calculation using explicit ionic background. The final state is still a plane wave, the averaging was performed again with the help of the analytical scheme. Same procedure was followed for the $1s$ and $1p_{x,y}$ states in Na_8.

The result is plotted in the lower panels of Fig. 6.10. Below $\epsilon_{\mathrm{kin}} \lesssim 0.5\,\mathrm{Ry}$ all curves follow the expected behaviour: for the p states, there is a decline in $\beta_2^{(1p)}$ towards negative values, for the s state $\beta_2^{(1s)} \approx 2$. The pattern totally differs for high kinetic energies. The anisotropy for the p state dramatically falls off towards values around zero, the one for the s state even takes negative values. The strong, located modification of the initial wavefunctions in **r**-space represents in **k**-space in fact deviations at the level of higher wavenumbers k. These deviations are filtered out at high kinetic energies in the transition integral (6.12). Furthermore, in spherical coordinates the modified initial state constitutes a mixture of states with different angular momentum, i.e., $\varphi_i = R_1^{(i)} Y_{10} + \sum_{lm} R_{lm}^{(i)} Y_{lm}$. An interesting aspect is that the additional angular momentum content prefer to emit isotropic or even transverse to the laser polarization.

6.4.2 Time-dependent calculations

This section presents exclusively full time-dependent calculations. In analogy to the last section, anisotropy and yield have been calculated in Na_8 with deformed jellium as well as with explicit ionic structure. The results are drawn in Fig. 6.11 (upper panels: jellium; lower panels: ionic background). The deformation parameter $\alpha = 0.05$ of the jellium calculation is chosen such that the quadrupole moment (of the electronic density) matches the one computed with full ionic background. The intensity of the 60 fs laser pulse was again scaled in order to keep ionization in a perturbative range of one-photon processes so that the analytical averaging (semi-perturbative scheme) can be applied. According to the previous section, the perturbation theory predicts for the jellium model a smoothing of the anisotropy as soon as deformation comes into play. The corresponding full time-dependent calculation in the upper panels of Fig. 6.11 confirms that. The deformation adds further angular momentum components to initial and continuum state which prevent anisotropy and yield from dropping into a sharp minimum.

Using even stronger deformation like explicit ionic structure (lower panels), seems now to completely wipe out the minimum. The anisotropy remains here quite constant. The detailed ionic structure reduces the maximum anisotropies of $\beta_2 \sim 1.6$ for the p states around 25% [72] when compared with the spherical jellium result.

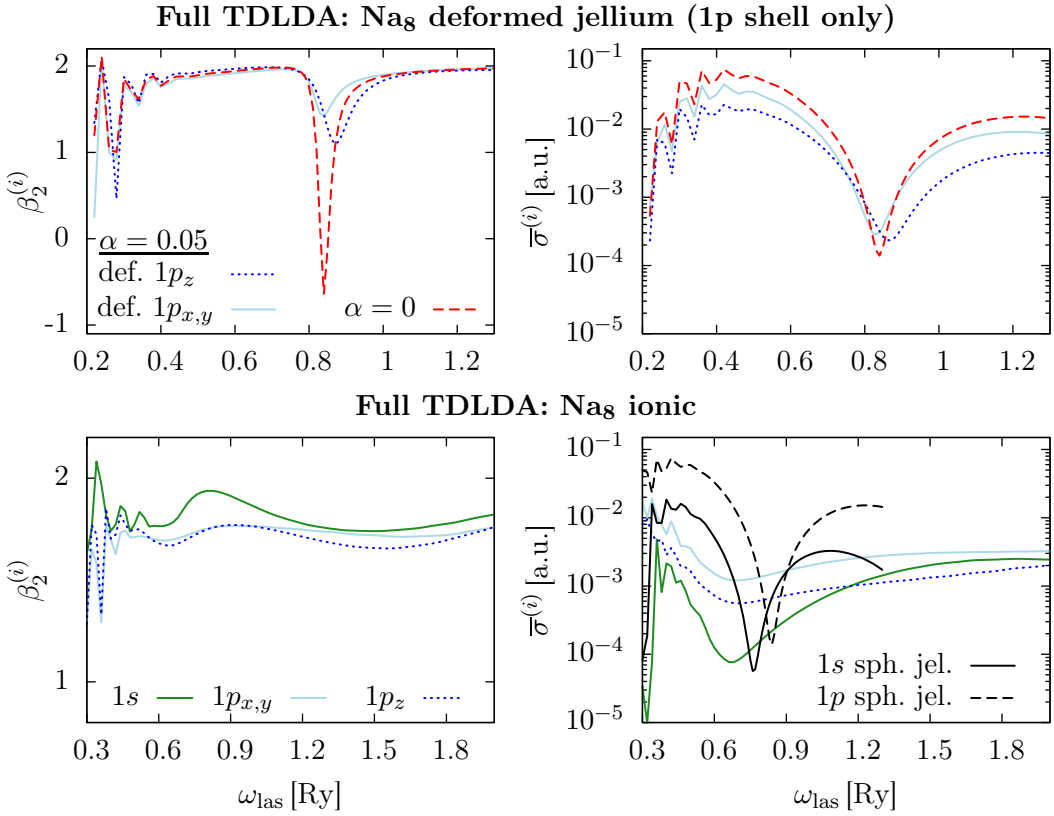

Figure 6.11: Anisotropy and cross-section of the occupied states in Na_8 within full TDLDA. *Upper panels:* $1p$ states in Na_8 spherical and deformed ($\alpha = 0.05$) jellium. *Lower panels:* Result for explicit ionic structure. For comparison, the spherical jellium result is also plotted in the lower right panel. The laser intensity is scaled with the frequency according to $I = 10^{14}\,\mathrm{W/cm^2} \times (\omega_{las}/\mathrm{Ry})^8$ for jellium and $I = 10^{12}\,\mathrm{W/cm^2} \times (\omega_{las}/\mathrm{Ry})^4$ for ionic background. Overall pulse length was $T_{pulse} = 60\,\mathrm{fs}$.

The discrepancy between the background models can be attributed to the local modification of the continuum state at small distances r (in the region of the cluster potential). Following the discussion in 6.2.2.1, the continuum state is then not a simple plane wave being sensitive for a single frequency only, but becomes a distorted (Coulomb) wave, contains rather a continuum of frequencies and is distributed over a great variety of large momentum components. Thus,

the transition integral filters deformations of the initial state already at small kinetic energies. The chances for occasional coincidence of nodal lines of the transition integral are even less than for the quadrupole deformed jellium. Hence, anisotropy as well as yield remain quite constant. The mix of angular momentum contains always some pieces with isotropic or transverse scattering which have the effect of lowering $\beta_2^{(i)}$, as discussed in the previous section (for the plane wave approximation).

A final word on the state dependent ionization shown in the lower right panel of Fig. 6.11. Comparing the $1s$ depletion with the $1p$ depletions, one notices that for low frequency the laser removes electrons preferentially from the upper bound p states, whereas for high frequency electrons are extracted about equally from all states. This trend is a general feature and appears also in other Na as well as organic clusters [26]. The trend does not seem to hold for the jellium background.

6.5 Static and time-dependent results for Na_7^-

As a final example, this section discusses results from the negatively charged cluster Na_7^-. This cluster is of particular interest since there are systematic measurements available [92]. Figure 6.12 shows the obtained g.s. spectra of the occupied s.e. states with ionic and spherical jellium background, respectively. The jellium parameterization ($r_s = 3.6\,a_0$ and $\sigma_{\rm jel} = 0.4\,a_0$) differs slightly from the usual one in order to better reproduce the experimental ionization potential of $\mathrm{IP}_{\rm exp} = 0.099\,\mathrm{Ry}$ which is, of course, much lower than in neutral clusters.

Due to the extensive spread of the electronic cloud in Na_7^-, calculations have been performed in huge numerical boxes: for ionic background in a three-dimensional cubic box of $(160{\cdot}0.8\,a_0)^3$, and for the spherical jellium in a two-dimensional cylindrical box of radius $(300 \cdot 0.2\,a_0)$ and height $(900 \cdot 0.2\,a_0)$.

Static calculations In order to get a first idea, anisotropy and yield are again calculated in the static plane wave approximation, see Fig. 6.13. Similar to Fig. 6.10, initial wavefunctions from explicit ionic structure have been used. Comparing the static plane wave model for Na_7^- with that for Na_8 in Fig. 6.10, only small differences appear. The trend of the s.e. anisotropies is in both clusters similar. The s.e. anisotropies of the p states show again the typical behaviour near the ionization threshold whereas the $1s$ state anisotropy converges to $\beta_2^{(1s)} \approx 2$ in the limit of small kinetic energies. The following decline towards zero starts for the negative cluster already at smaller kinetic energies. This is due to the differences in the IP and the strength of the binding potential.

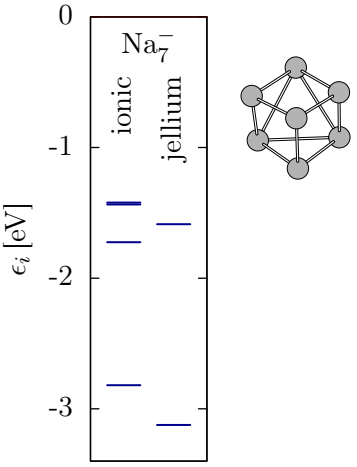

Figure 6.12: Ground-state spectra of occupied s.e. states for Na_7^-. *Left column:* detailed ionic background. *Right column:* Jellium model. The calculated s.e. energies are $\epsilon_1 = -2.82\,\text{eV}$, $\epsilon_2 = -1.72\,\text{eV}$, and almost degenerate $\epsilon_{3,4} = -1.42\,\text{eV}$ for ionic background, and $\epsilon_1 = -3.12\,\text{eV}$ and three-fold degenerate $\epsilon_2 = -1.59\,\text{eV}$ for the jellium model. The ionization potentials are $\text{IP}_{\text{ion}} = 0.104\,\text{Ry}$ and $\text{IP}_{\text{jel}} = 0.117\,\text{Ry}$. For comparison, the s.e. binding energies obtained from experiment [92] are $\epsilon_A = -1.35\,\text{eV}$, $\epsilon_B = -1.57\,\text{eV}$, $\epsilon_C = -1.73\,\text{eV}$ for the $1p$ states. The ionization potential is then $\text{IP}_{\text{exp}} = 0.099\,\text{Ry}$.

Time-dependent calculations In the second step, TDLDA calculations have been performed for explicit ionic background as well as for the spherical jellium model. The laser intensity is again scaled to maintain similar ionization for all frequencies. The laser frequency ranges from 1.5 to 18 eV ($T_{\text{pulse}} = 60\,\text{fs}$). The result is plotted in Fig. 6.14. It shows the s.e. anisotropy $\beta_2^{(1p)}$ of the p shell in jellium and ionic model on the left panel, and the total ionization N_{esc} in the jellium model on the right.

Close to the ionization threshold, both models show negative values and are, in fact, very similar. Apparently, the long outgoing waves do not resolve the details of the initial state. Additionally, the anisotropy exhibits the characteristic decline near the threshold. Due to the weak ionic background, the influence of

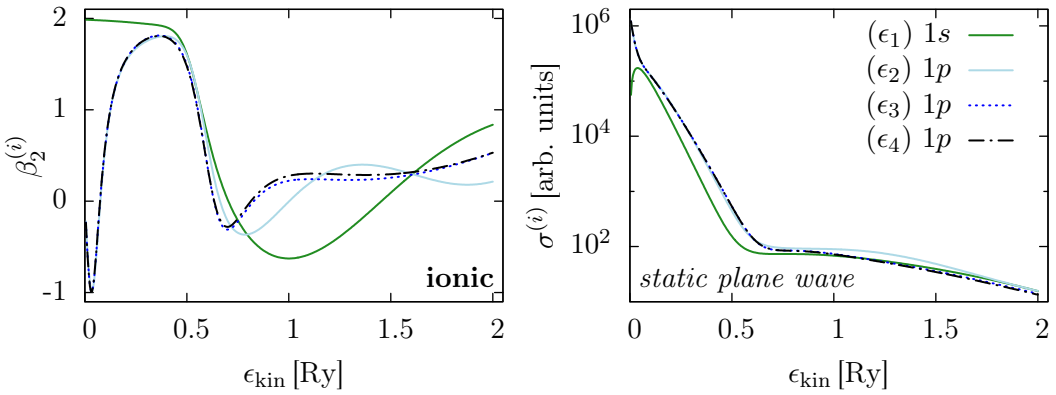

Figure 6.13: Anisotropy and cross-section for the occupied s.e. states in Na_7^- with explicit ionic structure in plane wave approximation, as a function of kinetic energy.

the binding potential on the outgoing continuum wave can be neglected. Thus, the plane wave for the final state seems to be a reasonable approximation for the continuum wave.

At higher energies the known difference between jellium and ionic background establishes. The jellium model produces values near two and occasional deep dips. In contrast, again nearly constant values around 1.5 for $\beta_2^{(1p)}$ appear for ionic structure, similar to Na_8. The outgoing waves resolve here the details of the initial states, i.e., the located modifications due to the pseudo-potentials and do also "feel" themselves the effect of the pseudo-potentials. The remaining isotropic component at higher ω_{las} is the typical result for ionic structure.

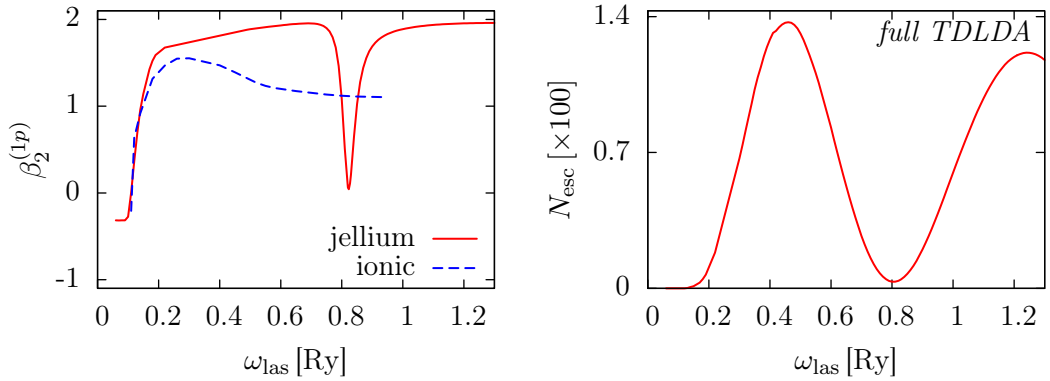

Figure 6.14: Anisotropy for the p states in Na_7^- with explicit ionic structure as well as jellium model and total emitted density (jellium model), calculated in full TDLDA, as a function of laser frequency.

The right panel in Fig. 6.13 shows the total emitted density as a function of ω_{las} for the jellium model. As one can see, it shows again nicely the photoionization oscillations also observed in Sect. 6.2.2.3, but here already at small energies, probably because of the negative charge of the cluster.

Fig. 6.15 finally shows again the (most realistic) ionic TDLDA result near the IP and compares it with experimental data available in this energy range. As predicted by the calculation, the measurement exhibits negative values close above the IP and values around $\beta_2^{(1p)} \approx 1.5$ for higher frequencies. Calculation and experiment match very well in this case.

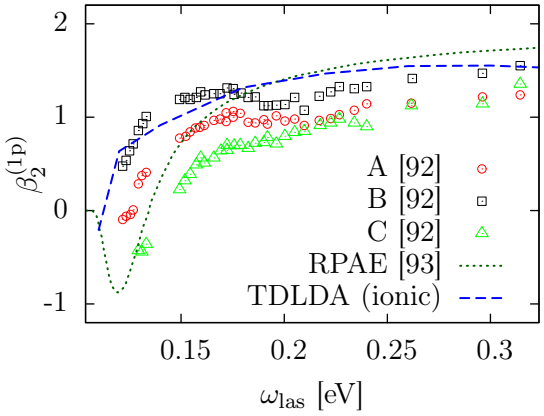

Figure 6.15: Anisotropy for the p states in Na_7^- near the ionization threshold. Experimental results show the s.e. anisotropy $\beta_2^{(1p)}$ where A, B, and C denote the different measured p states [92]. Theoretical results are average $1p$ anisotropy $\beta_2^{(1p)}$ for TDLDA and for calculations within the random-phase approximation with exact exchange (RPAE) using spherical jellium background [93].

6.6 Summary

This section presented static, perturbative methods for calculating PAD in small sodium clusters and compared them with full time-dependent calculations. As an important question appears whether the final state wavefunction can be approximated by a plane wave. A crucial point here is the considered kinetic energies of the outgoing electrons.

Long outgoing waves do not "see" the fine structure of the binding potential of the residual cluster. Hence, it does not matter if pseudo-potentials or jellium model are used. What first counts is the rough shape and mean depth of the potential. The negative charge of Na_7^-, e.g., strongly weakens the mean binding potential which in consequence can be neglected for waves close above the ionization threshold, and *long plane* waves become a good approximation for the final state. Moreover, all angular components are equally distributed in the final plane wavefunction. In other words, what is dominating in the angular distribution is the main angular momentum of the initial state! As a consequence, pseudo-potentials and jellium model behave similar near the IP.

In contrast, in the neutral Na_8 cluster, the potential depth is neglectable only at high kinetic energies. Hence, for short outgoing waves the remaining fine structure of the binding potential plays the major role. Ionic and soft jellium background strongly mismatch. In the ionic model, the plane wave approximation definitely fails. Final state as well as angular distribution are more complex. A good knowledge of the final state is required just as it is for the initial state. An analytical description seems to be hardly possible all the more so as dynamic effects in the coarse of the emission process come into play.

Briefly, the best chances in order to filter the main angular content of the initial states are given by performing a laser frequency scan in (strongly) negative

systems close to the ionization threshold. In this case, the angular distribution is a finger print of the initial wavefunction. In any case, static models, including the Bethe-Cooper-Zare formula, have to be handled with care since they do not account for dynamic effects such as rearrangement which, however, have considerable influence on ionization of clusters.

7 Buckminsterfullerene

Since its discovery by Kroto *et al.* [94] in 1985 which was awarded with the Nobel Prize[19], the buckminsterfullerene C_{60} attracts more and more interest among scientists. This is all the more so as methods for extraction of macroscopic quantities have been developed over the years [96] paving the way for various experiments and findings on this remarkable molecule. Up to now, C_{60} shows a bunch of outstanding properties in theory as well as experiment:

C_{60} is extremely stable for a cluster of such a size. Together with C_{50} and C_{70}, it is clearly favored during the formation process in comparison with other even clusters [97, 98] which suggests that it has a closed-shell electronic structure. Ionization potential and HOMO-LUMO gap are very high. Moreover, the low electron affinity (EA = 2.65 eV [99]) makes it resistant to chemical attack. The ionic "football configuration" which also resembles the geodesic domes designed by Buckminster Fuller, is highly symmetric. This necessarily effects the electronic structure. Photoelectron spectra show sharp, well-defined, molecular-like features which is related to the fact that several orbitals are degenerate or close in energy [3, 4, 100–102]. Additionally, continuum wavefunctions are in spite of the cluster size still dominated by a small selection of angular momentum components. Hence, selection rules and forbidden transitions come into play. Benning *et al.* [3] first observed also an oscillating behaviour of the partial cross-sections of the highest occupied molecular orbitals at large photon energies ($\sim 20-100$ eV). These energy-dependent intensity oscillations in particular of the HOMO and the HOMO-1 were explained later by the geometrical properties of the cage structure and the distribution of the delocalized electron cloud [90, 103, 104].

Another noteworthy property is the "giant plasmon resonance" predicted in 1991 by Bertsch *et al.* [105] and experimentally verified a few months later by Hertel *et al.* [106]. This very broad, collective resonance is centered around 20 eV. An additional, not so prominent resonance near 40 eV was also reported [107]. Both resonances are well above the ionization potential so that an important decay mechanism is the emission of electrons.

Concerning ionization mechanisms C_{60} differs essentially from Na clusters in the occurrence of delayed ionization [5, 108, 109] which starts on a nanosecond to microsecond time scale after excitation with ns pulses. In fact, depending on the excitation duration four basic ionization mechanisms can be observed in

[19] 1996 Nobel Prize in Chemistry for H. Kroto, R. Curl, and R. Smalley [95].

clusters: 1) direct/above-threshold ionization, 2) tunnel ionization, 3) thermal electron emission, and 4) thermionic emission. Processes 1 and 2 dominate after excitation with very short fs laser pulses. Depending on the intensity (and the Keldysh parameter) either ATI or tunnel ionization occur. The PES measured in this domain reflects the single-particle and excited-state spectrum. The PAD depends on the angular momentum coupling of initial and final state and is, in general, anisotropic. For longer pulses ($\sim 100\,\mathrm{fs}$), the electronic subsystem gets more and more heated while the ions remain unaffected (vibrationally cold). Through electron-electron collisions the electronic degrees of freedom are equilibrated. Thus, possible emission of electrons becomes statistical at this stage and decays Boltzmann-like, the PAD becomes isotropic (Process 3). Within pico- or hundreds of femtoseconds the hot electronic subsystem couples then to the ionic degrees of freedom. After transfer of the energy to the ions and cooling of the electronic system, electron emission firstly collapses. At this stage, both electrons and ions are in perfect thermal equilibrium. Subsequently, weakly bound systems like sodium clusters usually cool down by evaporation of atoms or fragments [11, 110, 111] since their dissociation energy is far below the ionization potential. In contrast, in C_{60} and systems where the dissociation energy is larger than the IP, delayed ionization as a second type of thermal, statistical electron emission may occur (Process 4).

All these remarkable properties have lead to more and more sophisticated experimental setups and detailed studies on C_{60}. For example, starting with PES [3, 4, 100] and PAD [8] experiments separately, both are nowadays measured in combination [14, 15, 112]. There exist also recent, theoretical studies on photoabsorption and photoemission using a time-dependent approach [80, 104, 113]. Most of them are based on the jellium model [27]. As already mentioned in Chapter 2, the ions are in this case thought of smeared out over a spherical shell with outer and inner radius. This type of jellium model does not deliver the right sequence of "magic" numbers. For example, for the C_{60} cluster the nearest closed electronic shell is located at $N_{\mathrm{val}} = 250$ electrons. According to the previous results on small Na clusters, it is, however, highly recommended to account for the explicit ionic structure in order to get a detailed insight into photoionization processes. This is all the more so, since the number of ions in C_{60} is much larger than that of the studied Na clusters.

The following sections are dedicated to the results obtained for C_{60}. Among all the approaches presented in the previous chapters, the most detailed using TDLDA including explicit ionic structure through non-local Goedecker potentials has been applied. Direct averaging is performed for calculation of orientation-averaged PAD and PES (Sect. 7.2). Systematic studies in both one- and multi-photon regime are presented (Sects. 7.3 and 7.4, respectively). It shall be started

with an introduction to the basic properties found within this approach.

7.1 Basic properties

7.1.1 Ionic structure

The 60 atoms in C_{60} constitute an ionic configuration which can be described as a *truncated icosahedron*, see Fig. 7.1. This truncated icosahedron consists of 20

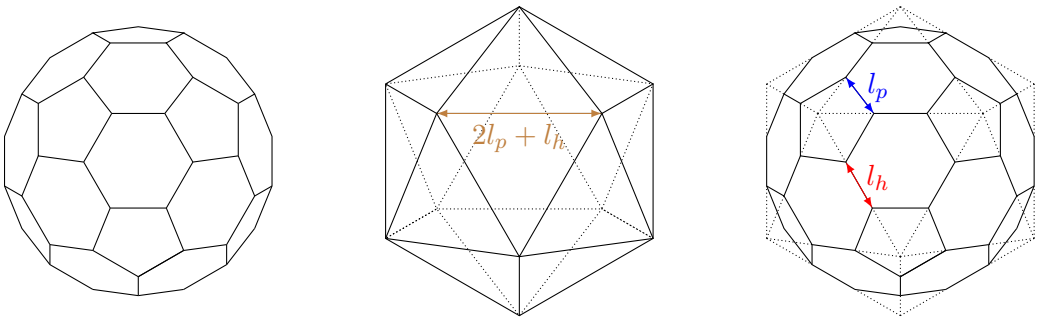

system	R_s [a_0]	l_p [a_0]	l_s [a_0]	reference
condensed C_{60}	—	2.750	2.629	[114]
free C_{60}	6.721	2.755	2.648	[115]
	6.441	2.650	2.508	*used in this work*

Figure 7.1: Ionic configuration (*top left*) constructed from a truncated icosahedron and bond lengths of C_{60}.

hexagons and 12 pentagons. Each pentagon is surrounded by hexagons. The 12 pentagons form 6 pairs of opposite faces, the 20 hexagons form 10 pairs of opposite faces [116]. All atoms lie on a sphere of radius R_s. The icosahedron ($\widehat{=}$ 20 regular triangles) is truncated in such a way that the resulting pentagons are regular with side length l_p and the hexagons are irregular with side lengths l_p and l_h. The table in Fig. 7.1 shows experimental values for R_s, l_p and l_h. The configuration used in the calculations differs slightly, but still retains the full symmetry. Moreover, it is expected that small changes of ionic configuration and bond lengths do not significantly effect the electron dynamics.

7.1.2 Electronic structure, ionization potential, and gaps

Figure 7.2 shows an iso-surface plot of the calculated electronic density in C_{60} (left) and the electronic density in the plane of a hexagon (right). Like in all calculations for C_{60}, non-local Goedecker potentials (see Sect. 2.1) have been used. As one can

see, the pseudo-potentials concentrate the electronic density well around the ions and leave a large void in the middle of the ball. This is somewhat inconsistent with the pseudo-potential calculations on Na clusters (Fig. 5.4) where the electrons are kept away from the cores. Apparently, the attractive force predominates the Pauli repulsion more strongly.

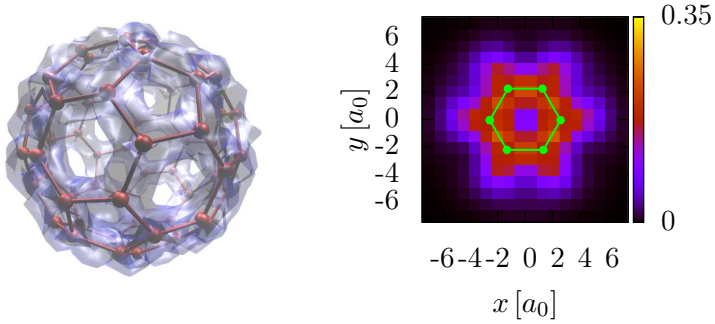

Figure 7.2: *Left:* Iso-surface plot of the calculated electronic density. *Right:* Electronic density in the plane of a hexagon.

The exceptional electronic setting places particularly high computational demands. On the one hand, the large diameter of the molecule desires a large numerical box, i.e., a large grid spacing. On the other hand, the electronic density is distributed on a small surface and exhibits rich structure there which a small grid spacing would be optimal for. The calculation on a grid of size 96^3 with spacing $dx = 0.82\,a_0$ represents a compromise leading to reasonable values for the obtained s.p. energies.

According to photoemission experiments [3, 4, 100] and pseudo-potential local-density calculations [101, 102] it is possible to group the 240 valence electrons into 60 π and 180 σ electrons. The radial wavefunctions of the π electrons have one node ($n = 2$) each around the radius of the cage, while the σ wavefunctions exhibit none ($n = 1$). All radial wavefunctions with same n are nearly the same. Moreover, in spite of the ionic structure each wavefunction has a single dominating angular momentum component. The bound wavefunctions can thus be labeled as π_l or σ_l, respectively. It has been also shown that orbitals of the same type are close in energy. The bottom of the valence band is made of σ state, the top of π states. Orbitals with increasing l have increasing energy [102].

The effect of the ionic configuration on the electron structure has been studied by others in detail with local-density calculations using "soft" pseudo-potentials [101, 102]. The non-spherical components of these pseudo-potentials, split all π_l and σ_l bands with main angular component $l \geq 3$ and $l \geq 5$, respectively. As a consequence, the π_5 and σ_9 subbands which actually could occupy in total

22 and 38 electrons, are then only partly filled. In contrast to the spherical jellium shell with a closed electronic shell at $N_{\text{val}} = 250$, new "magic" numbers therefore arise ($N_{\text{val}} = 240$) as soon as the icosahedral symmetry of the cluster is taken into account. The two highest occupied molecular orbitals, the HOMO and HOMO-1, are both of π character. The HOMO is a subband of the π_5 shell (odd l: ungerade symmetry) filled with 10 electrons. The next deeper lying shell π_4 is also of π character, but has now gerade symmetry and is fully filled. All π_4 subbands are very close and represent the 18-fold degenerate HOMO-1.

Figure 7.3 shows the spectrum of occupied s.e. energies (spin up & down) calculated with Goedecker potentials in a 96^3 grid as mentioned above. The first few unoccupied states are also sketched. As expected, the 120 different occupied levels

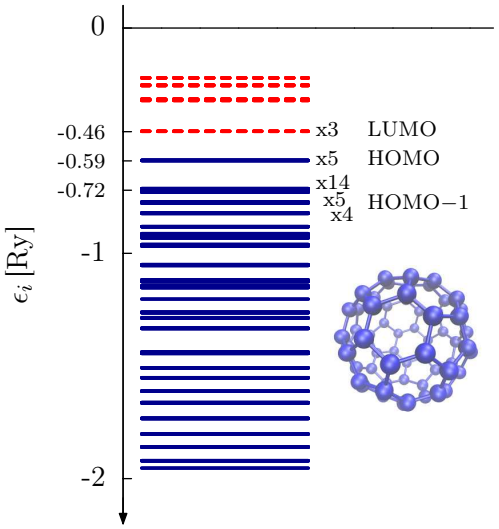

Figure 7.3: Spectrum of s.e. energies in C_{60}. Solid blue lines: occupied; dashed red lines: unoccupied states. The HOMO is occupied by 10 electrons, whereas the HOMO-1 by 28 electrons.

are reduced to a significant lower number of bands. Moreover, there is a huge span of about 1.5 Ry between HOMO and the lowest occupied state. The degeneracy of these bands is also given. The HOMO is five-fold degenerate and well separated from the rest of the occupied and unoccupied states which is in good agreement with other work presented above. Thanks to the pseudo-potentials there is also no conflict concerning shell closings, the 240 electrons build a closed electronic structure. Also the binding energy, i.e., the ionization potential of IP = 0.59 Ry which is comparable to Na clusters, matches very well with other experimental data, see Table 7.1. However, the second highest occupied shell, the HOMO-1 which should be nine-fold degenerate, splits into several subbands with different degeneracy. This may be a deficiency of the sparse grid and/or pseudo-potentials. Unfortunately, the π_l and σ_l character of the occupied states has not (yet) been

examined. It is possible that the 14-fold degenerate subband of the HOMO-1 is of σ character and that its bound energy is underestimated. Nevertheless, the gap between HOMO and HOMO-1 amounts to $\Delta_{\mathrm{HH}-1} = 0.13\,\mathrm{Ry}$, the one between HOMO and LUMO is $\Delta_{\mathrm{HL}} = 0.13\,\mathrm{Ry}$. Both values are in acceptable agreement with experiments.

system	Δ_{HL} [eV]	$\Delta_{\mathrm{HH}-1}$ [eV]	IP [eV]	reference
C_{60} fullerite	1.9	1.4	7.3	Weaver *et al.* [100]
	1.6			Skumanich [117]
			7.6	Lichtenberger *et al.* [118]
C_{60}^{-} free	$1.5 - 2.0$			Yang *et al.* [97]
C_{60} free	2.14	1.8		Sattler [119]: pp. 45-5, 27-11
			7.61	Lichtenberger *et al.* [120]
			7.61	Zimmerman *et al.* [98]
			7.58	de Vries *et al.* [121]
		1.6		Liebsch *et al.* [8]
	1.77	**1.8**	**8.0**	*this work*
	(0.130)	**(0.133)**	**(0.588 Ry)**	

Table 7.1: Experimental values for HOMO-LUMO gap Δ_{HL}, gap between HOMO and HOMO-1 $\Delta_{\mathrm{HH}-1}$, and ionization potential compared with theoretical results of this work.

7.1.3 Dipole response

Theoretical [105] and experimental work [106, 107] predict a "giant surface plasmon resonance" at around 20 eV in the photoabsorption cross-section. This value matches surprisingly well with predictions of the classical Mie theory: for a solid, homogeneously charged sphere the (multi-pole) plasmon frequency is given by:

$$\omega_l^2 = \frac{4\pi\rho e^2}{3m} \cdot \frac{3l}{2l+1} = \frac{4N_{\mathrm{val}}}{R^3} \cdot \frac{3l}{2l+1}\,\mathrm{Ry}^2\,a_0^3\,,$$

with N_{val} being the number of valence electrons, R the radius of the sphere, and $\rho = 3N_{\mathrm{val}}/(4\pi R^3)$ the charge density. Setting $l = 1$ for the dipole resonance yields the well known Mie formula. In contrast, for a spherical, infinitely thin electronic shell with $\rho = N_{\mathrm{val}}/(4\pi R^2)$ which is rather similar to the electronic density supposed in C_{60}, the frequency is [122, 123]:

$$\omega_l^2 = \frac{4N_{\mathrm{val}}}{R^3} \cdot \frac{l(l+1)}{2l+1}\,\mathrm{Ry}^2\,a_0^3\,.$$

Inserting now $N_{\mathrm{val}} = 240$, $R = 6.683\, a_0$ (which accounts roughly for the extensions of the electronic cloud) and $l = 1$, yields $\omega_1 = 1.46\,\mathrm{Ry} \approx 20\,\mathrm{eV}$.

Besides the giant resonance, several sharp excitations below $\sim 8\,\mathrm{eV}$ have been found theoretically [124–126] and experimentally in solid [127, 128] and in gas phase C_{60} [129]. Moreover, a broad volume-like plasmon at around 40 eV [107, 130] has been reported. The appearance of more than one collective mode is in contradiction to the photoabsorption cross-sections of Na clusters. The ionic structure of C_{60}, however, causes the electrons moving in a narrow shell far away from the center of the cage. The sharp edges of the shell divides the valence electrons according to their radial wavefunctions into two types, the π and σ electrons. It appears therefore logical that the photoabsorption cross-section differs substantially from that of Na clusters [104].

The photoabsorption cross-section was calculated through an instantaneous boost of all s.p. wavefunctions, similar to Sect. 5.3.1 for Na_8. The result is plotted in Fig. 7.4. It shows the dipole strength function $\mathcal{S}_D(\omega)$ in linear (left panel) and logarithmic scale (right). The boost ionizes the system only weakly, $N_{\mathrm{esc}} = 0.04$. As a consequence of the (almost) spherical symmetry of the electronic system, the strength is identical along all three directions. Below the ionization potential of IP = 8 eV, the dipole response exhibits several excitations. The excitation at 6.0 eV is very prominent. Above the IP the response is dominated by a broad resonance of width $\sim 10\,\mathrm{eV}$ with peak position at 19.6 eV, superimposed with $1ph$ excitations and strongly fragmented. No feature is visible at energies above $\sim 30\,\mathrm{eV}$.

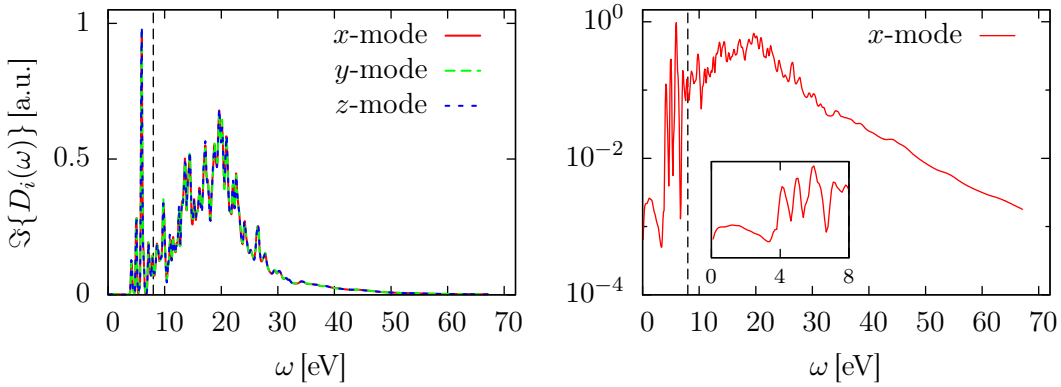

Figure 7.4: Dipole response of C_{60} obtained through an instantaneous boost in x-, y-, and z-direction. The IP is indicated with a dashed, vertical line.

As already mentioned, the s.p. wavefunctions have not been examined with respect to their radial behaviour. Thus, only the total photoabsorption cross-

section can be presented here. With the current state of research, the lower excitations correspond to excitations of the highest occupied levels and have a $\pi - \pi^*$ character (below $\lesssim 14\,\mathrm{eV}$), while at higher energies transitions also from the σ subsystem contribute. The giant resonance at 20 eV can be ascribed to a plasmon of all valence electrons ($\pi + \sigma$ plasmon). The width of the plasmon is due to the high density of $1ph$ excitations triggering Landau damping (Landau width). Moreover, in contrast to simple metal clusters, the energy of the plasmon is far in the continuum. Hence, it can decay fast through electron emission, possesses a short lifetime and is even broader in energy scale (decay width). The prominent excitation at 6.0 eV could be related to a collective resonance of the π electron system (π plasmon). Its position agrees well with other TDLDA calculations [125] and measurements [129]. The two modes of the surface plasmon are purely dynamical and cannot be seen in static calculations based on the independent-particle assumption [104]. The lowest excitation peak of about 4.1 eV is larger than the HOMO-LUMO gap which suggests that both states have the same angular momentum ($l = 5$) and that transitions between HOMO and LUMO are optically forbidden.

Experiments [107, 130] also reported a second giant resonance which is not present in Fig. 7.4. This resonance, however, is even further in the continuum than the one at 20 eV. As a consequence, it is much broader and only visible in the experimental data as a small hump at about 40 eV.

The resonance at 20 eV is strongly fragmented. This is only partly due to $1ph$ excitations lying in the vicinity of the plasmon, but also artificial as the finite numerical box discretizes the continuum.[20] One can overcome this problem through smoothing of the dipole response by hand. This can be achieved by multiplication of the dipole momentum in the time-domain with a cut-off function, e.g., $\cos^{N_{\mathrm{filt}}}(t\pi/2T_{\mathrm{fin}})$, before applying the Fourier transformation. In fact, this is always necessary in small boxes since the dipole signal never dies out and the Fourier transformation of the sheer signal gives rise to artifacts. The smoothing can be tuned through the power N_{filt}. In practice, the extra width in the

[20] Supposing a hard, numerical grid without absorbing boundaries. The small box sizes as they are used here, effect that reflection of emitted electrons crucially influence the result. Standings waves can set up and artificially discretize the spectrum similar to a spherical potential well. The discretization can be approximated through the echo time $T_{\mathrm{echo}} = L/v$ of a reflected wave, where L is the dimension of the box and v the velocity of the emitted electron [55]. Taking as kinetic energy the energy of the giant plasmon, $E_{\mathrm{kin}} = 20\,\mathrm{eV}$, and $L = 96 \cdot 0.82\,a_0$ yields velocity and echo time of $v \sim 50\,a_0/\mathrm{fs}$ and $T_{\mathrm{echo}} \sim 1.55\,\mathrm{fs}$, respectively. The corresponding box level spacing is then $\Delta_\epsilon = \hbar\pi/T_{\mathrm{echo}} \sim 0.1\,\mathrm{Ry}$. Switching on the absorbing layer, of course, smoothes the spectrum, i.e, reflection of continuum waves of certain wavelengths at the boundaries is suppressed, but not fully wiped out which in turn still could leave a partly fragmented spectrum.

spectrum obtained by the filtering should be larger than the box level spacing. The spectrum in Fig. 7.4 was obtained with a very small filtering, $N_{\text{filt}} = 4$. Increasing the filtering to $N_{\text{filt}} = 100$ yields the response as it is shown in Fig. 7.5 (red line). The response appears now much smoother, but still exhibits some

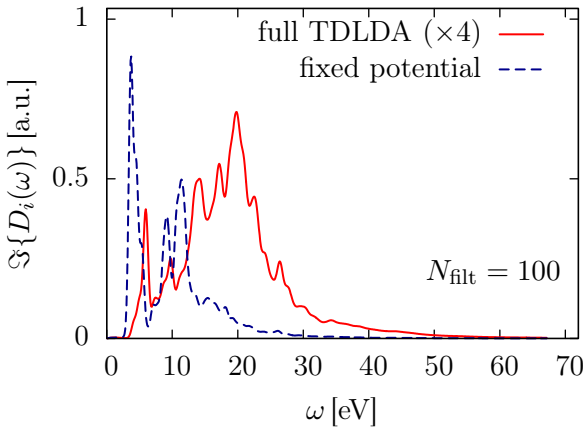

Figure 7.5: Smoothed dipole responses of C_{60} of a full TDLDA calculation and a TDLDA calculation with frozen g.s. Kohn-Sham potential (x-mode only).

structure. In contrast, all experimental results show a rather homogeneous photoabsorption cross-section. The remaining difference may be attributed to several issues. First, electron-electron collisions in the form of $2ph$, multi-electron excitations and thermalization of the electronic subsystem are not considered in TDLDA. These collisions might have a blurring effect on excitations as well as plasmon resonances. Second, in experiments, some part of the deposited energy is always transferred to ionic motion, in other words, the experimental sample usually has a finite temperature. This induces fluctuations of the cluster shape which, in turn, might also broaden the electronic excitations.

Figure 7.5 also displays the response obtained when keeping the K.S. potential fix. This should then deliver only $1ph$ excitations. As can be seen, the plasmon at 20 eV disappears which demonstrates its collective nature. Moreover, $1ph$ excitations are present up to about 1.5 Ry.

Finally, as a side note, the artificial discretization of the continuum is not only visible in the dipole response as a function of oscillation frequency, but also in the total number of emitted electrons N_{esc} as a function of ω_{las} after excitation with a laser. The smooth trend seen, e.g., in Fig. 6.11 for the Na_8 cluster in a $(96{\cdot}0.8\,a_0)^3$ box with `nabsorb` $= 8$ suggests, however, that the size of the box and the width of the absorbing layer have been well chosen in this case.

7.2 Averaging and integration scheme

Before presenting PAD and PES of C_{60} after laser excitation, the procedure used for determination of the orientation-averaged observables shall be introduced. As already mentioned, for all calculations on C_{60} non-local Goedecker potentials accounting for the explicit ionic structure have been used. According to Fig. 7.2 the resulting electronic setup of C_{60} is clearly non-spherical. Averaging is consequently necessary, in particular, for determination of the anisotropy β_2. In order to perform calculations in one- and multiphoton regime while keeping consistency in the applied methods, the *direct* averaging scheme is chosen (see Sect. 4.3). Although direct averaging needs generally a lot of calculations, one can exploit here the symmetry of the cluster. Five different orientations have been considered. They are indicated as follows:

(■)	the center of a hexagon is oriented along the laser polarization	20	$\Lambda_1 = 2.30$
(□)	center of a pentagon	12	$\Lambda_2 = 0.92$
(▲)	edge of two hexagons (in the middle of two vertices)	30	$\Lambda_4 = 2.15$
(△)	edge of a hexagon and a pentagon (in the middle of two vertices)	60	$\Lambda_5 = 4.03$
(•)	vertex (ionic positions) in direction of the laser	60	$\Lambda_3 = 3.16$
		182	4π

The weight factors Λ_i are again determined through division of the unit sphere into segments:

$$\frac{d\overline{\sigma}}{d\Omega} = \sum_{n=1}^{5} \Lambda_n \left.\frac{d\sigma}{d\Omega}\right|_n = C_0 Y_{00} + C_2 Y_{20} + C_4 Y_{40} + \ldots \tag{7.1}$$

Due to the symmetry of the cluster, this averaging is effectively a 182-point central symmetric averaging, see Fig. 7.6. For comparison, for sodium clusters already 18 orientations had converged. Hence, it can be safely assumed that the current sampling is sufficiently fine.

The averaging was done on PAD *and* PES. For the integration of the PES $M = 308$ measuring points have been initialized:

$$\frac{d\sigma}{d\epsilon_{\mathrm{kin}}} = \sum_{m=1}^{308} \lambda_m \frac{d\sigma_m}{d\epsilon_{\mathrm{kin}}}\,, \qquad \frac{d\overline{\sigma}}{d\epsilon_{\mathrm{kin}}} = \sum_{m=1}^{308}\sum_{n=1}^{5} \lambda_m \Lambda_n \left.\frac{d\sigma_m}{d\epsilon_{\mathrm{kin}}}\right|_n .$$

The total anisotropy parameters are, in general, extracted from the PAD, Eq. (7.1): $\beta_l = \sqrt{2l+1}C_l/C_0$. But also the combined PES/PAD can serve for

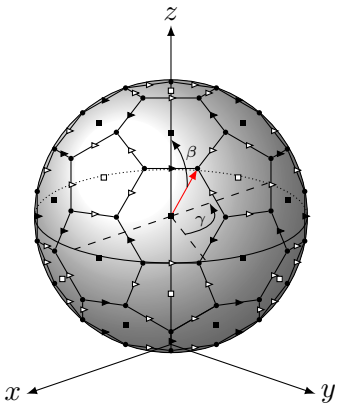

Figure 7.6: Orientation points used for calculation of averaged PES and PAD. Due to the cluster symmetry, all points can be reduced to 5 orthogonal orientations indicated with (■), (□), (▲), (△), and (•). The orientation points were rotated into the z-axis of the laboratory frame, by a first rotation $\gamma(0 \leq \gamma < 2\pi)$ about the z-axis (of the laboratory frame) and a second rotation $\beta(0 \leq \beta < \pi)$ about the y-axis.

determination of an energy-resolved anisotropy:

$$\frac{d^2\overline{\sigma}}{d\Omega\, d\epsilon_{\mathrm{kin}}} = \mathcal{C}_0 Y_{00} + \mathcal{C}_2 Y_{20} + \mathcal{C}_4 Y_{40} + \dots \,, \tag{7.2a}$$

with

$$\mathcal{C}_l(\epsilon_{\mathrm{kin}}) = \sum_{\mu=1}^{M} \sum_{n=1}^{5} \lambda_\mu \Lambda_n Y_{l0}(\Omega_\mu) \cdot \left.\frac{d\sigma_\mu}{d\epsilon_{\mathrm{kin}}}\right|_n \,, \tag{7.2b}$$

and

$$\mathcal{B}_l(\epsilon_{\mathrm{kin}}) = \sqrt{2l+1}\, \frac{\mathcal{C}_l(\epsilon_{\mathrm{kin}})}{\mathcal{C}_0(\epsilon_{\mathrm{kin}})} \,. \tag{7.2c}$$

In principle, the energy-resolved anisotropies integrated over ϵ_{kin} should agree with the β_l:

$$\beta_l \stackrel{!}{=} \sqrt{2l+1}\, \frac{\int d\epsilon_{\mathrm{kin}}\, \mathcal{C}_l}{\int d\epsilon_{\mathrm{kin}}\, \mathcal{C}_0} \,.$$

7.3 Photoemission in one-photon domain

7.3.1 First results – Velocity maps

At first, PES and PAD were calculated at the frequency $\omega_{\mathrm{las}} = 2.5\,\mathrm{Ry}$ for two different intensities $I_1 = 10^{10}$ and $I_2 = 10^{12}\,\mathrm{W/cm^2}$. The lower intensity yields an ionization in the perturbative range, $\overline{\sigma}_1 = 0.006$ electrons, whereas the cluster is strongly ionized for I_2, $\overline{\sigma}_2 = 0.57$. At the chosen frequency the whole s.p. spectrum is within the range of possible one-photon processes. The pulse length of $T_{\mathrm{pulse}} = 30\,\mathrm{fs}$ ranges for both calculations in the short fs regime where direct emission is expected to be the dominant ionization mechanism according to experimental results. In this way, the theory which does not account for thermalization

of the electronic subsystem can be better compared to experiments performed on the same time scale.

Figure 7.7 shows an example of a PAD for one fixed cluster orientation (orientation •). The PAD shows rich structure and reflects the ionic configuration. This is related to the fact that the binding potential seen by the outgoing waves cannot be neglected as it is perhaps the case for the small, negative Na_7^- cluster. Quite the contrary, the deformation of the initial and final wavefunctions is supposed to be large due to the high number of ions/scattering centers and also just due to the high occupied angular momentum components. This deformation is, of course, reflected in the PAD. Orientation averaging is thus needed for determination of anisotropy parameters. The latter are expected to be smaller when compared to small Na clusters since deformation and complexity of the wavefunctions add more isotropic content to the one-photon PAD as stressed in Chapter 5.

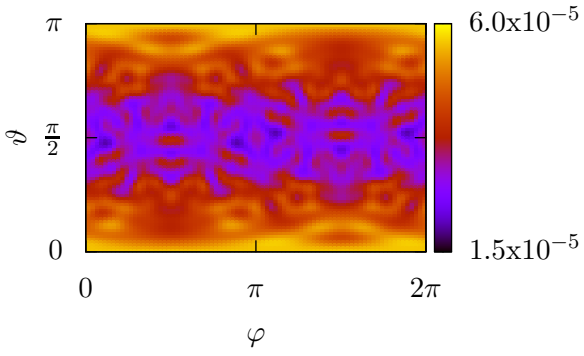

Figure 7.7: PAD for configuration (•). Laser parameters: $\omega_{\text{las}} = 2.5\,\text{Ry}$, $I_2 = 10^{12}\,\text{W/cm}^2$, $T_{\text{pulse}} = 30\,\text{fs}$. The total ionization was $N_{\text{esc}} = 0.56$.

The next figure displays orientation-averaged PAD (left column) and OA-PES (right column) for both intensities. The PAD at weak intensity (upper left panel) exhibits considerable spurious ionization at $\vartheta = 0, \pi/2, \pi$. Subtraction of the background yields then a distribution which clearly follows $1 + \beta_2 P_2$. The PAD at higher intensity (lower left panel) differs insofar that the emission signal due to the laser field exceeds the spurious background. The extracted anisotropy parameter of $\beta_2 = 0.38$ is for both distributions identical. The anisotropy thus seems to be very robust to intensity variation. The reason for this is that due to the relatively high laser frequency photoelectrons from two- or multiphoton processes have already such a high kinetic energy that their transition probability becomes negligible. Multiphoton processes are thus strongly suppressed and the PAD remains dominated by one-photon processes.

The value of $\beta_2 = 0.38$ is very low when compared to sodium clusters. This is again due to the influence of the ionic structure. For sodium it was observed that the ionic structure decreases the anisotropy about $\approx 25\%$. This effect should be even stronger in C_{60}, since the number of ions is much higher than for the

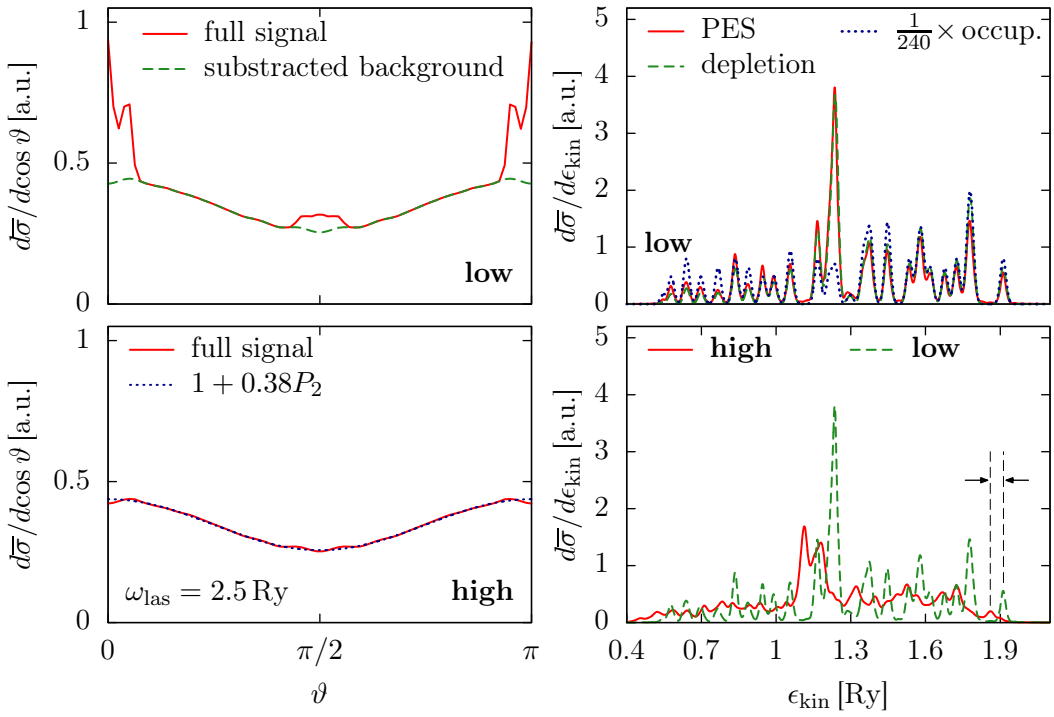

Figure 7.8: OA-PAD and PES for the two intensities, $I_1 = 10^{10}$ (*low*) and $I_2 = 10^{12}\,\mathrm{W/cm^2}$ (*high*) at $\omega_{las} = 2.5\,\mathrm{Ry}$ ($T_{pulse} = 30\,\mathrm{fs}$). The low intensity yielded $\overline{\sigma}_1 = 0.006$, the high one $\overline{\sigma}_2 = 0.57$ ionized electrons.

considered sodium clusters with $N = 3-19$. Additionally, for carbon clusters the coupling of the electrons to the ions may be even stronger than for simple metal clusters.

In the upper right panel, the PES for the perturbative case (I_1) is compared to the level depletion:

$$\frac{d\overline{\sigma}}{d\epsilon_{kin}} = \sum_i \overline{\sigma}^{(i)} \mathcal{G}_i(\epsilon_{kin}) \,,$$

assuming that $\epsilon_{kin} = \epsilon_i + \hbar\omega_{las}$ ($\nu = 1$). The Gaussian functions are defined in Eq. (5.3). Again, the width $\sigma_{las} \approx 0.012\,\mathrm{Ry}$ has been chosen according to the resolution of the pulse ($T_{pulse} = 30\,\mathrm{fs}$, $\omega_{las} = 2.5\,\mathrm{Ry}$). Each function is weighted with the corresponding (averaged) s.p. depletion $\overline{\sigma}^{(i)}$. For comparison, the blue, dotted line represents the occupation, i.e., a theoretical uniform depletion with $\overline{\sigma}^{(i)} = \overline{\sigma}/240$.

Depletion and PES match perfectly which again underlines that ionization is in the linear one-photon regime for this frequency and intensity. The PES is characterized by a dominant peak in the middle of the spectrum at around

1.25 Ry = 17 eV and exhibits rich details highly resolved down to the deepest s.p. states. Some states are so closely that they appear just as one peak which is related to the high symmetry and level degeneracy. A comparison of the PES to the occupation suggests that almost all states are equally depleted. A striking exception is the dominant peak in the middle of the spectrum which might be a special property of the spatial matrix elements of the states contributing in this region.

The lower right panel finally shows the PES for both intensities. In contrast to the PAD, the PES significantly changes when going to higher laser intensities. The sharp peaks which occur at low ionization, disappear. The s.e. energies change during the ionization process and peaks are broadened. The PES is consequently smoothed. Furthermore, the whole spectrum is shifted to lower kinetic energies (Coulomb shift) due to the higher charge of the residual cluster. However, the prominent feature in the middle of the spectrum and the more or less uniform depletion of the other s.p. states remain.

The expansion of the PAD into spherical harmonics according to Eq. (7.1) yields the anisotropy $\beta_2 = 0.38$. This is (almost) similar to the value obtained by expansion of the averaged PES, Eq. (7.2),

$$\sqrt{5}\,\frac{\int d\epsilon_{\mathrm{kin}}\,\mathcal{C}_2}{\int d\epsilon_{\mathrm{kin}}\,\mathcal{C}_0} = 0.40\,.$$

In addition to the PES $\propto \mathcal{C}_0(\epsilon_{\mathrm{kin}})$, the sampling of measuring points ($M = 308$) seems so to resolve even higher orders of angular momentum. Taking the anisotropy $\mathcal{B}_2(\epsilon_{\mathrm{kin}})$, it is thus possible to plot the (one-photon) velocity map

$$\frac{d\overline{\sigma}}{d\cos\vartheta\,dv} = m_e v \frac{\overline{\sigma}}{2\pi}(1 + \mathcal{B}_2(v)P_2)\,,$$

i.e., a double-differential cross-section with $\epsilon_{\mathrm{kin}} = m_e v^2/2$. The angle-resolved PES for $\omega_{\mathrm{las}} = 2.5\,\mathrm{Ry}$ and the two different intensities are shown in Fig. 7.9 (left and middle). As expected, both distributions are symmetric, $\vartheta \longleftrightarrow \pi - \vartheta$. In both cases, most of the outer and inner shells prefer to emit parallel to the laser polarization, even though only very slightly. The trend to parallel emission seems to emerge for stronger intensities. The emission out of the dominant peak in the middle of the spectrum, however, remains more or less isotropic.

The next step was to modify the laser frequency. Figure 7.9 also displays the map for $\omega_{\mathrm{las}} = 1.5\,\mathrm{Ry}$ (close to the plasmon), $I \sim 10^8\,\mathrm{W/cm^2}$, and $T_{\mathrm{pulse}} = 60\,\mathrm{fs}$. These parameters yielded an overall ionization of $\overline{\sigma} = 0.0058$. The middle of the spectrum is now even more dominant and the velocity-map appears more isotropic than previously. Hence, it is expected that β_2 is even closer to zero. It

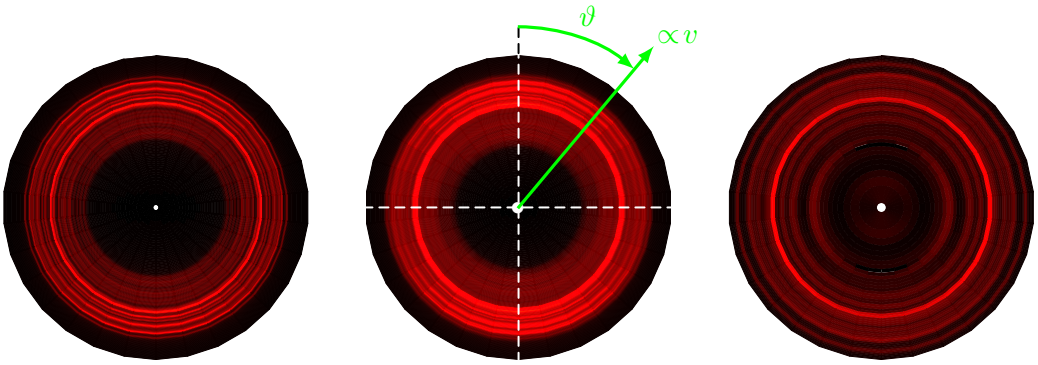

Figure 7.9: Velocity-maps at $\omega_{\text{las}} = 2.5\,\text{Ry}$ and $T_{\text{pulse}} = 30\,\text{fs}$ (*left* and *middle*). The intensity is $I_1 = 10^{10}$ (*left*), and $I_2 = 10^{12}\,\text{W/cm}^2$ (*middle*). *Right map*: $\omega_{\text{las}} = 1.5\,\text{Ry}$, $I = 5 \times 10^8\,\text{W/cm}^2$, and $T_{\text{pulse}} = 60\,\text{fs}$.

is to be noted that the dominant shells differ for both laser frequencies $\omega_{\text{las}} = 1.5$ and $\omega_{\text{las}} = 2.5\,\text{Ry}$. Figure 7.10 finally shows the calculated OA-PAD/PES. The s.p. spectrum which is shown in the right panel (shifted about ω_{las}) is not fully excited by one photon at this frequency. Whereas $\omega_{\text{las}} = 2.5\,\text{Ry}$ produces $\beta_2 = 0.39$, the anisotropy results indeed in the smaller value of $\beta_2 = 0.29$ at $\omega_{\text{las}} = 1.5\,\text{Ry}$.

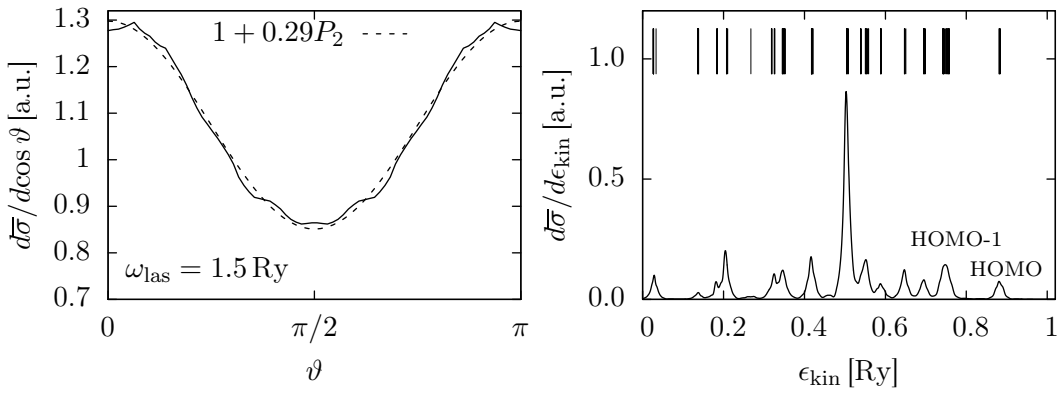

Figure 7.10: OA-PAD and PES for $\omega_{\text{las}} = 1.5\,\text{Ry}$, $I = 5 \times 10^8\,\text{W/cm}^2$, $T_{\text{pulse}} = 60\,\text{fs}$. The total (averaged) number of escaped electrons was $\overline{\sigma} = 0.0058$. An expansion of the PAD in spherical harmonics yields $\beta_2 = 0.29$. The right panel shows the PES together with the s.p. spectrum shifted about ω_{las}.

In summary of the first results, all PAD for the frequencies $\omega_{\text{las}} = 2.5$ as well as 1.5 Ry follow the expected one-photon law $1 + \beta_2 P_2$. Hence, one-photon velocity-maps with a dominant feature in the middle of the spectrum are generated. For 2.5 Ry two intensities have been tested. The PAD shows no variation with the intensity, but with the frequency. In contrast, the PES depends on the intensity. At sufficiently weak ionization, the depletion matches very well with the PES and can serve as a tool in order to determine the nature/order of the ionization. At higher ionization, the sharp peaks are broadened, the PES gets smoothed and shifted due to the residual cluster charge. All in all, the values of calculated anisotropies are very small when compared to sodium clusters.

7.3.2 Systematics with frequency

As observed previously, the anisotropy β_2 differs for the two frequencies $\omega_{\text{las}} = 2.5$ and 1.5 Ry while it shows little variation with the laser intensity. Therefore, the behaviour of β_2 as a function of ω_{las} has been investigated in a more systematic way. More specifically: the laser frequency has been varied in the range from 14 to 28 eV while keeping the intensity constant, $I = 7.8 \times 10^9\,\text{W/cm}^2$.

Figure 7.11 shows total β_2 and $\overline{\sigma}$ as a function of ω_{las}. The total ionization of $0.02 - 0.11$ shows its maximum at about 21 eV. This corresponds well with the maximum of the dipole response which is displayed in dotted lines. Anyway, the shape of the ionization follows nicely the dipole response. Reminding that the dipole response is dominated at this energy by the giant plasmon as well as $1ph$ excitations. Hence, both effects may play a role for emission at this laser frequencies.

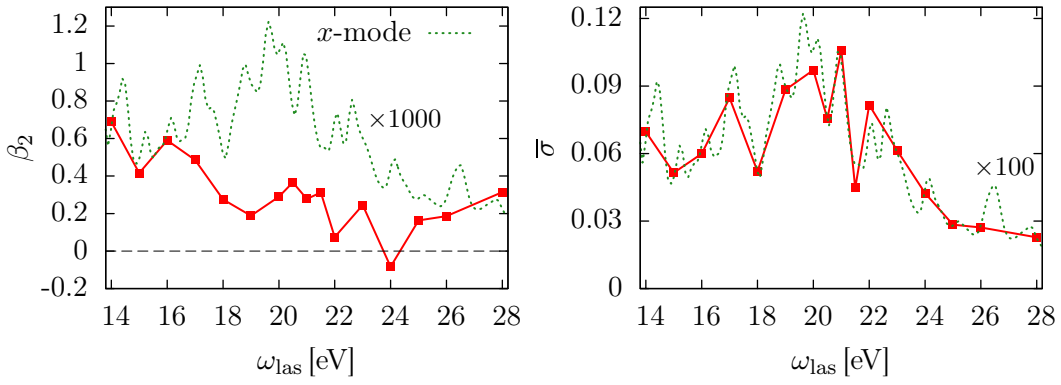

Figure 7.11: Total anisotropy β_2 and total yield $\overline{\sigma}$ as a function of laser frequency ω_{las} around the plasmon. The (scaled) dipole response from Fig. 7.4 is indicated with dotted lines.

The total anisotropy also varies as a function of ω_{las} and takes even a negative value at $\omega_{\text{las}} = 24\,\text{eV}$. This is in contrast to the result obtained in Na clusters (with explicit ionic structure), where β_2 is rather stable. On the other hand, C_{60} has a lot of $1ph$ excitations above the IP plus the 20 eV-plasmon. These excitations might have an influence on β_2. Two-dimensional jellium calculations (not shown) have yielded that the trend of the anisotropy complies in the frequency range of 14 to 28 eV with the three-dimensional result of Fig. 7.11, but even more variation of β_2 can be seen in the range below 1 Ry. A full frequency scan is thus needed in order to correctly interpret the behaviour of β_2 as a function of ω_{las} and the influence of the plasmon on the latter. It could be further helpful to explore the state-dependent $\beta_2^{(i)}$ in more detail, as the total β_2 is an observables integrated over a large number of states which might mask existing effects.

7.4 Multiphoton domain

In analogy to the discussion on one-photon processes, it shall be started with an example of a PAD for the orientation ($\bullet$), see Fig. 7.12. The laser frequency of $\omega_{\text{las}} = 0.11\,\text{Ry}$ is far below the ionization potential of IP $= 0.59\,\text{Ry}$. The intensity of the pulse has been chosen in order to obtain an ionization of $N_{\text{esc}} = 0.60$ similar to the one in Fig. 7.7 for the one-photon regime. Compared to Fig. 7.7, the PAD is here strongly aligned along the laser polarization and much less structured, in particular in direction sidewards to the laser. The outgoing waves are close to the threshold and have low kinetic energy. In consequence, they cannot resolve the details of the ionic structure. The strong alignment is probably due to the fact that the multiphoton processes populate scattering states with high angular momentum. At first glance already, the multiphoton domain differs considerably from the one-photon domain.

Extensive studies have thus been performed with laser frequencies below the IP. In order to have a better resolution, the pulse length is enhanced, $T_{\text{pulse}} = 75\,\text{fs}$. Variation of both, laser intensity and frequency shall be discussed. The intensity varies from the perturbative to the non-perturbative regime.

7.4.1 Systematics with intensity

Systematic studies of PAD and PES as a function of intensity were performed at $\omega_{\text{las}} = 0.11\,\text{Ry}$ with laser intensities[21] ranging within $1.25 - 3 \times 10^{13}\,\text{W/cm}^2$. This resulted in ionization[22] between $\overline{\sigma} = 0.03 - 0.60$. The laser frequency is

[21] $I_1 = 1.25 \times 10^{13}$, $I_2 = 1.5 \times 10^{13}$, $I_3 = 1.75 \times 10^{13}$, $I_4 = 2.4 \times 10^{13}$, and $I_5 = 3 \times 10^{13}\,\text{W/cm}^2$.
[22] $\overline{\sigma}_1 = 0.03$, $\overline{\sigma}_2 = 0.06$, $\overline{\sigma}_3 = 0.12$, $\overline{\sigma}_4 = 0.31$, and $\overline{\sigma}_5 = 0.60$.

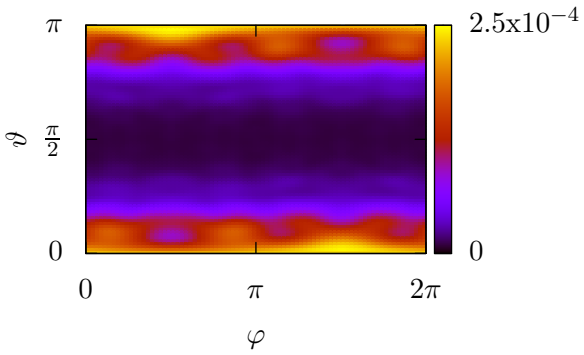

Figure 7.12: PAD for configuration (•). Laser parameters: $\omega_{\text{las}} = 0.1139\,\text{Ry}$, $I = 3 \times 10^{13}\,\text{W/cm}^2$, $T_{\text{pulse}} = 75\,\text{fs}$. The total ionization was $N_{\text{esc}} = 0.60$.

far below the IP $= 0.59\,\text{Ry}$, six and seven photons are at minimum needed for ionization out of the HOMO and HOMO-1, respectively. Figure 7.13 shows the OA-PAD and PES for this frequency. All PES (right panel) show a clear repeated sequence of peaks separated by ω_{las}. The sequences are visible up to a very high photon order. For small ionization, the amplitude of the repeated oscillations is at first glance surprisingly high. Due to the s.p. spectrum spanning a huge range of 1.5 Ry one would have rather expected a smooth, continuous trend. In addition, a double peak structure seems to appear (see the inset, especially for the black line, $\overline{\sigma}_2 = 0.06$) on the maximum amplitudes. The large oscillations and the double peak pattern are smoothed out at higher ionization, but the repetition is still visible.

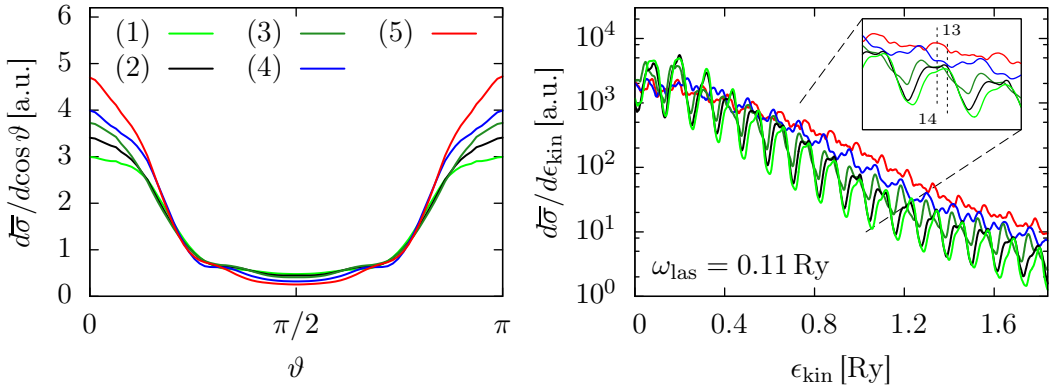

Figure 7.13: OA-PAD and PES for different laser intensities/ionization at $\omega_{\text{las}} = 0.1139\,\text{Ry}$. The inset shows a zoom into the range $\epsilon_{\text{kin}} = 10, \ldots, 14\,\text{eV}$. The expected kinetic energies for 13- and 14-photon processes out of HOMO and HOMO-1 are indicated ($\epsilon_{\text{HOMO}} + 13\omega_{\text{las}}$ and $\epsilon_{\text{HOMO-1}} + 14\omega_{\text{las}}$).

The left panel shows the OA-PAD. They all have basically the same form. The PAD gets more and more focused around $\vartheta = 0\,, \pi$ with increasing intensity. This

is in contrast to the one-photon domain where the PAD remains stable with laser intensity! Due to the low laser frequency in the present case the order of the prominent multiphoton processes depends significantly on the laser intensity. With increasing intensity, higher orders of multiphoton processes become more and more probable. The angular distribution

$$\frac{d\overline{\sigma}}{d\Omega} \sim 1 + \beta_2 P_2 + \beta_4 P_4 + \beta_6 P_6 + \dots$$

extends then also to higher orders of anisotropy parameters. The following table lists the values of β_2, β_4 and β_6 for the different intensities:

intensity $[10^{13}\,\mathrm{W/cm^2}]$	ionization	β_2	β_4	β_6
$I_1 = 1.25$	$\overline{\sigma}_1 = 0.03$	1.55	0.79	-0.07
$I_2 = 1.50$	$\overline{\sigma}_2 = 0.06$	1.61	0.88	0.15
$I_3 = 1.75$	$\overline{\sigma}_3 = 0.12$	1.66	0.92	0.30
$I_4 = 2.40$	$\overline{\sigma}_4 = 0.31$	1.97	1.09	0.19
$I_5 = 3.00$	$\overline{\sigma}_5 = 0.60$	2.19	1.24	0.38

Obviously, the higher the intensity the more parameters take non-vanishing values. In turn, the higher the order l of non-vanishing β_{2l}, the stronger the distribution is peaked along the laser. This can be demonstrated with the completeness of the Legendre polynomials:

$$\sum_l \frac{2l+1}{2} P_l(x) P_l(x) = \sum_{2l} c_{2l} P_{2l} = \delta(0)\,.$$

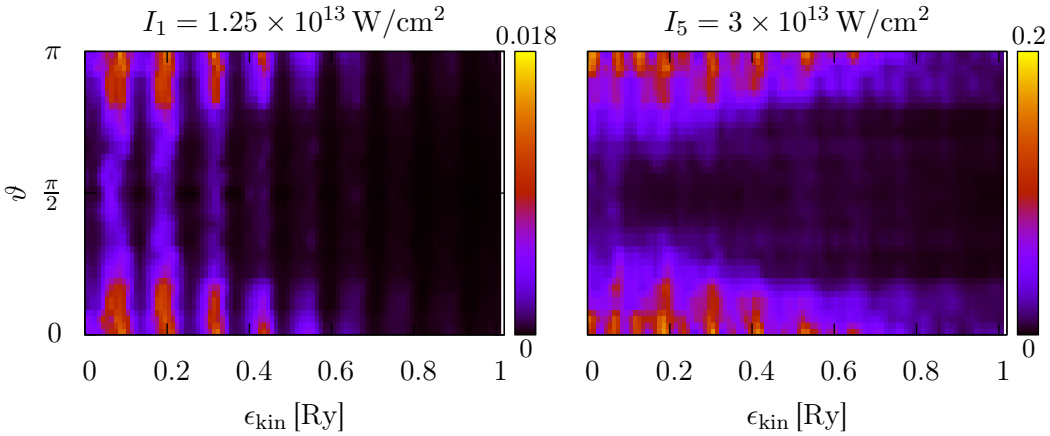

Figure 7.14: Combined PES and PAD for the lowest chosen intensity (*left*; $\overline{\sigma}_1 = 0.03$) and the highest one (*right*; $\overline{\sigma}_5 = 0.6$).

Moreover, it can be noticed also in the combined PES/PAD, Fig. 7.14 (left: lowest intensity; right: highest intensity). Both distributions exhibit a cone-like structure. For the low frequency, ionization above $\approx 0.6\,\mathrm{Ry}$ is only weakly visible. At higher intensity, the photoelectrons also reach higher kinetic energies and the cone gains visibility.

The double peak pattern can be understood when having a closer look on the level depletion $d\overline{\sigma}/d\epsilon_i = \sum_i \overline{\sigma}^{(i)}\mathcal{G}_i$, see Fig. 7.15. As already observed in the one-photon domain, the depletion can serve as a tool in order to determine the ionization origin. In this case, the depletion is plotted as a function of the s.e. energies ϵ_i since multiphoton processes occur and ν takes several, possible values in $\epsilon_{\mathrm{kin}} = \epsilon_i + \nu\hbar\omega_{\mathrm{las}}$. Additionally, only the upper bound levels are displayed. The width of the Gaussians was again properly chosen according the pulse length.

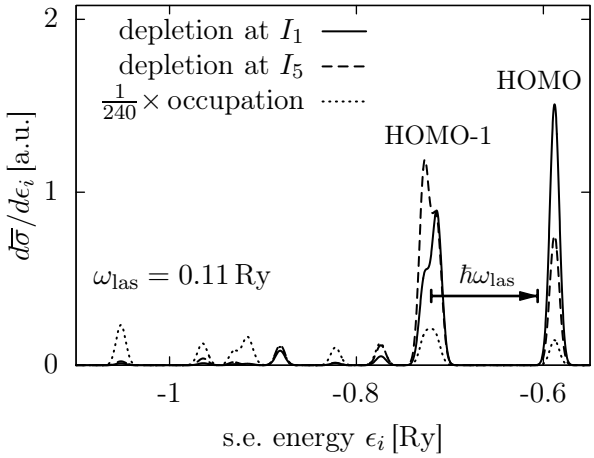

Figure 7.15: Depletion of the higher s.e. states at $\omega_{\mathrm{las}} = 0.1139\,\mathrm{Ry}$ for different intensities. The depletions are normalized to unity and compared to a uniformly distributed depletion.

In contrast to the one-photon domain where all s.e. states are more or less equally depleted, the main electron emission stems here from the two levels HOMO and HOMO-1. The ionization of deeper bound states is negligible. Also the PES emission pattern is then, of course, composed from these two s.p. states only. This explains the large amplitude of the oscillations which allow to resolve the multiphoton steps. Thereby, the HOMO level is excited by N photons and the HOMO-1 by $N+1$ photons. For example, the inset of Fig. 7.13 shows the expected peak positions of the two levels with $\nu = 13$ for the HOMO and $\nu = 14$ for the HOMO-1. At the maximum of each oscillation, two peaks occur very close to each other, since the photon frequency does not match exactly with the gap energy between HOMO and HOMO-1. For higher ionization, double peak pattern as well as large amplitude are smoothed out. This smoothing is again related to the gradual Coulomb down-shift of the spectra during ionization as

already observed above.

In Fig. 7.15, one encounters also a transition in the depletion of HOMO and HOMO-1. Whereas for low intensity, the HOMO depletion is larger, the reverse situation occurs for higher intensity. Note, this transition is also weakly visible in the PES.

7.4.2 Systematics with frequency

The double peak structure observed at low intensities invites to play with the laser frequency. Besides $\omega_{\rm las} = 0.11\,{\rm Ry}$, four further frequencies have been analyzed. They are all connected to the gap energy between HOMO and HOMO-1, $\Delta_{\rm HH-1} = 0.133\,{\rm Ry}$:

$\omega_{\rm las}$ [Ry]		intensity $[10^{13}\,{\rm W/cm^2}]$	ionization	$\nu_{\rm min}$ HOMO	$\nu_{\rm min}$ HOMO-1
0.067	$\approx \Delta_{\rm HH-1}/2$	$I_6 = 1.75$	$\overline{\sigma}_6 = 0.05$	9	11
0.100	$\approx 3\Delta_{\rm HH-1}/4$	$I_7 = 1.75$	$\overline{\sigma}_7 = 0.09$	6	8
0.133	$\approx \Delta_{\rm HH-1}$	$I_8 = 1.25$	$\overline{\sigma}_8 = 0.05$	5	6
0.266	$\approx 2\Delta_{\rm HH-1}$	$I_9 = 0.50$	$\overline{\sigma}_9 = 0.02$	3	3

The intensity is chosen so that ionization remains again in the perturbative regime and so that the gradual down-shift is neglectable.

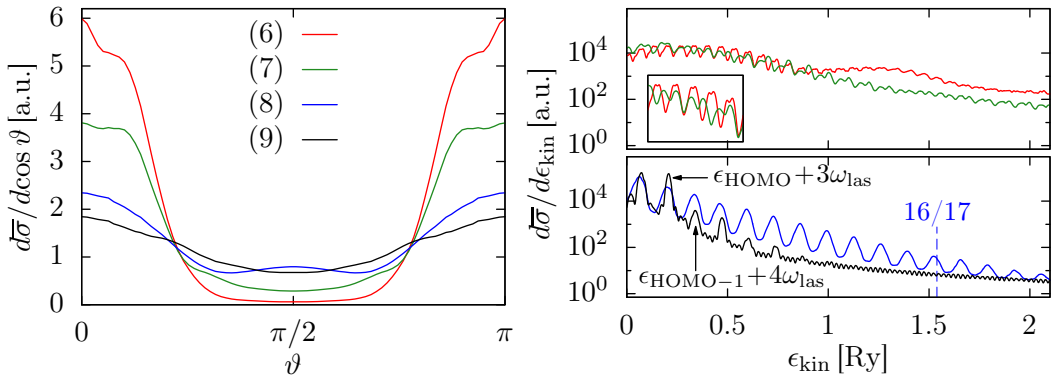

Figure 7.16: OA-PAD and PES for different laser frequencies according to the table in the text. For $\omega_{\rm las} = 0.2659\,{\rm Ry}$ (black line in the lower right panel), 3- and 4-photon peaks of the HOMO and the HOMO-1 are indicated with arrows. For $\omega_{\rm las} = 0.1329\,{\rm Ry}$ (blue line in the lower right panel) 16- and 17-photon processes are indicated as well. The inset in the upper right panel displays the PES in the range $\epsilon_{\rm kin} = 0.3, \ldots, 0.65\,{\rm Ry}$.

Figure 7.16 displays OA-PAD and PES for the different laser frequencies. For the lowest frequency $\omega_{\rm las}^{(6)}$ (red line) double peak pattern still occurs in the PES

(see the inset in the upper right panel). Apparently, the half of the gap energy was not hit exactly which is not surprising at this small frequency. Furthermore, wide oscillations appear in this case. In contrast, the frequency $\omega_{\text{las}}^{(8)}$ (blue line) was well chosen since double peak pattern disappears here completely. Oscillations are in this case visible up to a very high photon order. The expected position of 16-photon and 17-photon processes out of HOMO and HOMO-1, respectively, are marked in blue and match very well with the maximum amplitude. The frequency $\omega_{\text{las}}^{(9)}$ (black line) differs in this aspect. Multiphoton peaks are here clearly separated, but noticeable only up to an order of about five photons.

The PAD is the more focused around $\vartheta = 0\,, \pi$, the lower the laser frequencies. This is in agreement with the intensity dependence of the PAD observed in the last section. The larger the influence of higher orders of photon processes, the more focuses the PAD (see also Fig. 7.17). In the present case, with decreasing laser frequency, the minimum number needed for ionization trivially increases and so do the order of non-vanishing anisotropy parameters β_{2l} in the PAD.

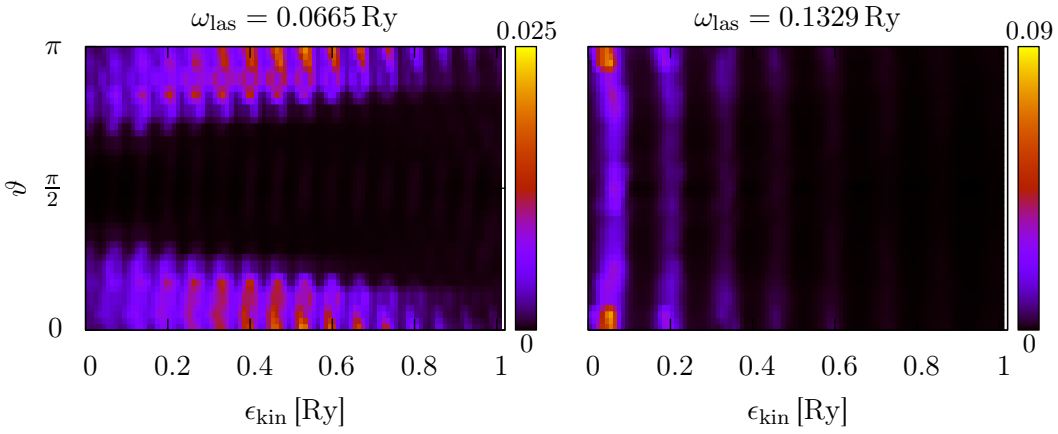

Figure 7.17: Combined PES and PAD for $\omega_{\text{las}} = 0.0665\,\text{Ry} \approx \Delta_{\text{HH}-1}/2$ (*left*) and for $\omega_{\text{las}} = 0.1329\,\text{Ry} \approx \Delta_{\text{HH}-1}$ (*right*).

7.5 Comparison with experiment

Thanks to the group in Lyon, France,[23] who provided results of measurements on C_{60}, a direct comparison of theory and experiment is possible.

Figure 7.18 compares the theoretical PES (from Fig. 7.10) in the one-photon domain with the experimental one obtained at the synchrotron ($T_{\text{pulse}} \sim 100\,\text{ps}$

[23] Contact: Franck Lépine, Institut Lumière Matière, Université de Lyon

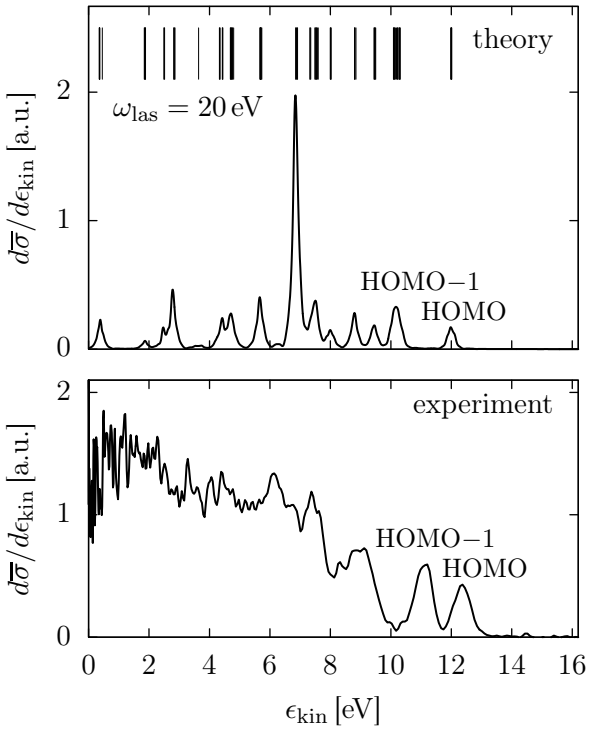

Figure 7.18: *Upper panel:* Theoretical OA-PES at $\omega_{\rm las} = 20\,{\rm eV}$, taken from Fig. 7.10, together with the s.p. spectrum shifted about $\omega_{\rm las}$. *Lower panel:* Experimental PES measured at the synchrotron for $\omega_{\rm las} = 20\,{\rm eV}$ and $T_{\rm pulse} \sim 100\,{\rm ps}$.

and $\omega_{\rm las} = 20\,{\rm eV}$). As one can see, the experimental PES strongly differs from the theory at low kinetic energies. This can be attributed to a structureless, isotropic and exponential background from thermal emission which effects the measured PAD and PES at pulse durations used in the experiment. The theory, in contrast, misses electron-electron collisions. The energy deposited into the system can thus only decay through $1ph$ or plasmon excitations and direct emission.

A comparison can be drawn at higher kinetic energies where the thermal background is negligible. Here, the experimental data show immediately more structure. HOMO and HOMO-1 are nicely visible. Their peak positions are in reasonable agreement with the theoretical prediction.

Experiments have been also performed in the multiphoton domain, see Fig. 7.19. Again, the experimental PES matches well with the theory. The laser parameters in the experiment are: $T_{\rm pulse} \sim 40\,{\rm fs}$, $\omega_{\rm las} = 0.11\,{\rm Ry}$, $I \sim 10^{13}\,{\rm W/cm^2}$. Theoretical as well as experimental PES exhibit the repeated structure stemming from sequences of multiphoton processes, up to a very high order. However, the oscillations are less pronounced in the measurement which might be again due to a thermal, structureless background. The trend with laser intensity seen in the PAD reaffirms that. While the theoretical PAD gets more focused around $\vartheta = 0, \pi$ with increasing intensity, the opposite is found in the experiment. This suggests that a

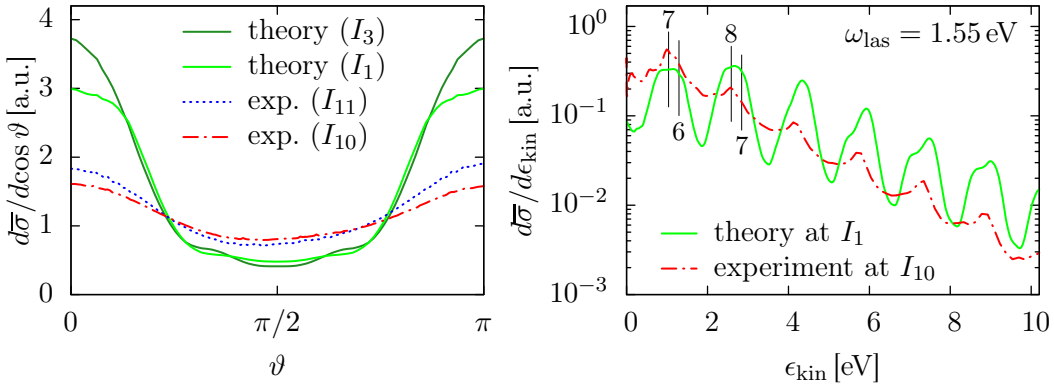

Figure 7.19: Experimental and theoretical (taken from Fig. 7.13) PAD and PES. The laser intensities used in the experiment are $I_{10} = 4.3 \times 10^{13}$ and $I_{11} = 3.4 \times 10^{13}\,\mathrm{W/cm^2}$.

thermal effect is involved which gets more important for higher laser intensities.

7.6 Summary

Systematic TDLDA studies have been performed on the buckminsterfullerene C_{60}. Concerning the g.s. calculation it pays off that the ionic structure is taken into consideration. The electronic structure form then a closed shell. In addition, IP, HOMO-LUMO gap and gap between HOMO and HOMO-1 match well with experimental values. There is a doubt on the level degeneracy of the HOMO-1. An analysis of the character of the s.p. wavefunction could clarify this issue.

The broad resonance of the dipole response around 20 eV can be reproduced (although fragmented artificially and by $1ph$ excitations) and identified as a dynamical effect. There is also a prominent feature below the IP which could be associated with the so-called π-plasmon.

The special geometry of the cluster facilitates the development of an efficient averaging scheme. This allows determination of averaged PAD and PES in one- and multiphoton domain. It turns out, that these two regimes differ significantly.

In the one-photon domain all PAD follow the expected behaviour, $1 + \beta_2 P_2$ with very small values for β_2 when compared to sodium clusters. β_2 also shows little variation with intensity, but with frequency which is again in contrast to Na clusters. The PES is particularly rich in detail in this regime with some peaks very close in energy due to the high symmetry. Depletion of the s.p. states is about uniform, with one exception in the middle of the spectra.

In the multiphoton domain PAD and PES are composed of many non-vanishing anisotropies $\beta_2, \ldots, \beta_{2l}$ and sequences of multiphoton processes up to an increas-

ingly high order with increasing laser intensity and/or decreasing frequency. The two levels HOMO and HOMO-1 are predominating the depletion which leads to large oscillations in the PES. Accordingly, low frequencies detach electrons exclusively from the vicinity of the Fermi surface while high frequencies deplete all levels about equally strong. This trend has been already found previously in Na_8 (Fig. 6.11) and other clusters [26].

Comparison with experiments suggests that the TDLDA approach misses an important effect: electron-electron collisions. Dynamical correlations, however, have implications on energy transfer and ionization observables [131] and are grossly visible in the experiment. Nevertheless, very good agreement with experiment was found in both, one- and multiphoton regime at high energies where the thermal background is negligible.

8 Carbon chains

Small carbon molecules appear in a variety of chemical reactions involving hydrocarbons, in sooting flames and even in certain astrophysical environments like interstellar clouds, carbon stars, comets, etc. [132]. Microscopic numbers of small carbon molecules can be produced in laboratory by thermal/laser vaporization of graphite or by electron impact induced fragmentation of hydrocarbons [133, 134]. Among all physical properties, their structure has been debated most controversially since long. Electron affinities measured by photoelectron spectroscopy as well as abundances show an even-odd alternation for $n < 10$ [132, 135, 136]. This supports the assumption that linear chains are the predominant structure at this size: C_{2n+1} chains have closed-shell while C_{2n} chains have open-shell ground-states. In fact, the situation is not that clear for the even-numbered species. In general, the linear (open-shell) chain is the favored geometry, but also planar, monocyclic structures with energy close to the linear one coexist. A typical example is C_4 which has two almost isoenergetic structural isomers [132], a rhombic and a linear form. Also the charge state seems to have an influence on the ground-state configuration, in particular, for small molecules [137].

The higher the number of atoms the more preferred are cyclic structures. At first, monocyclic structures occur, later on even bi- or polycyclic forms may exist. The transition from linear to monocyclic configurations takes place at around $n = 10$, can be nicely seen in photoelectron spectra [6, 135, 136] and is more or less understood: the small linear chains have unsaturated bonds at their ends which can be avoided by bending to a ring. Therefore, the energy gained by formation of an additional bond has to be larger than the destabilization created by the ring strain. This is the case for $n \geq 10$. The even-odd alternation then switches with a special stability attributed to the aromatic rings with $4n + 2$ atoms (Hückel's rule). But still, to some extent, there may coexist linear chains up to 20 atoms [137].

A second transition has been observed at $n = 30$ where three-dimensional structures start to appear. In contrast to the transition from chains to cyclic structures, the growth of fullerene-like structures is still not well understood and so far several mechanisms have been proposed for their formation [119].

Although photoelectron spectroscopy has been mainly applied on carbon clusters in order to determine the structure of the size-selected species, the method also helps to elucidate the different competing decay processes after excitation,

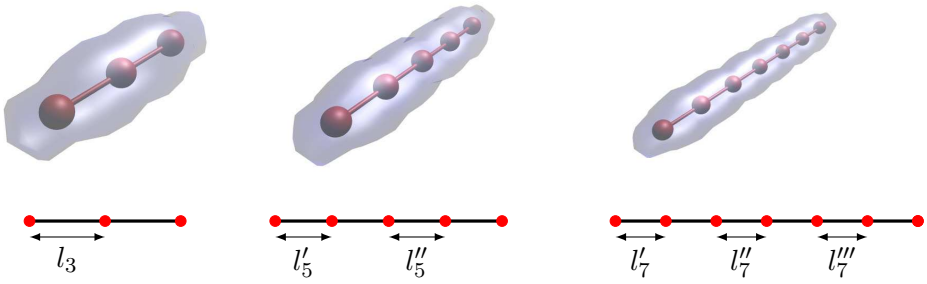

system	*this work* $[a_0]$	others [138–142]
C_3	$l_3 = 2.414$	$2.415 - 2.485$
C_5	$l'_5 = 2.422$; $l''_5 = 2.414$	$2.402 - 2.500$; $2.409 - 2.517$
C_7	$l'_7 = 2.405$; $l''_7 = 2.414$;	$2.400 - 2.459$, $2.389 - 2.457$;
	$l'''_7 = 2.422$	$2.419 - 2.513$

Figure 8.1: Ionic configurations (with iso-surface of the electronic cloud) and bond lengths of the small linear chains C_3, C_5, and C_7, compared to measured bond lengths.

in particular when applied time-resolved [16]. This chapter briefly addresses a photoemission process which was observed in the calculations on small carbon chains and which can be seen in the PES. The mechanism is most likely related to the resonance process presented in Sect. 5.3.1. For the sake of simplicity, the discussion remains restricted to the small linear chains C_3, C_5, and C_7.

8.1 Ionic and electronic structure

Figure 8.1 illustrates the ionic configurations of the selected carbon molecules. As previously mentioned, these small odd-numbered molecules have a linear ground-state configuration. The used bond lengths are close to (theoretical) results obtained by others, however, it is expected that small deviations do not have a large effect on electron dynamics. For small, linear chains, there is general agreement that the cumulenic electronic configuration (:C=C···C=C:) with electron pairs located at the end of the chains and rather equivalent bonds is preferred over the acetylenic (·C≡C−C···C≡C·) one with alternating bond lengths [143].

Figure 8.2 shows the obtained s.p. spectrum of the considered chains. The IP of about 10 eV slightly decreases with increasing cluster size. Comparing the values with other theoretical results, Table 8.1, it seems that the IP is generally weakly underestimated in this work. The experimental values are still varying in literature not to mention the bound energies of occupied states. The spread of the s.p.

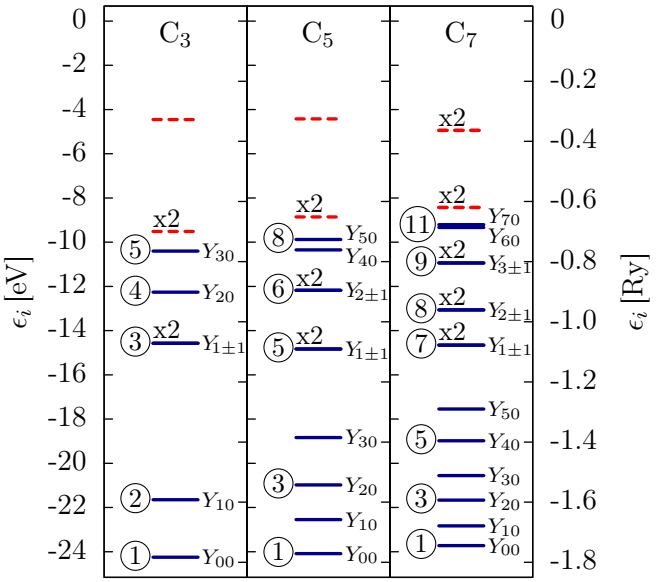

Figure 8.2: Ground-state spectra of the linear carbon chains C_3, C_5, and C_7. Solid blue lines: occupied; dashed red lines: unoccupied states. The occupied states are labelled with circled numbers, some of them are doubly degenerate, hence occupied with four electrons (spin up & down).

energies amounts in the calculations to around 1 Ry which is large in comparison with small sodium clusters. The s.p. states are labelled with circled numbers. For C_3 there is large gap between state ② and the first doubly degenerate state ③. This gap tends to close for the longer chains while the number of degenerate states enhances.

Although the binding potential is non-spherical, spherical harmonics can still be attributed to the s.p. wavefunctions in all cases. The s.p. states with $m \neq 0$ are always less bound then the corresponding states with $m = 0$ but similar l, since the states with $m \neq 0$ exhibit a node completely along the z-axis. Their

		theory				*experiment*			
		TW	[144]	[145]		[143]	[146]	[147]	
IP [eV]	C_3	**10.4**	12.0	12.0		11.6	13.0	12.1	
	C_5	**9.9**	11.6	11.3		9.9	12.3	11.4	
	C_7	**9.2**	9.5	10.0		10.1			
		TW	[148]	[149]	[150]	[151]	[152]	[153]	[154]
ω_{pl} [eV]	C_3	**8.4**	8.1	8.1		7.3/7.8	6.6		
	C_5	**6.5**	6.4	6.4	6.8			5.3	
	C_7	**5.4**	5.3	5.5					4.9

Table 8.1: Experimental and theoretical values for the ionization potential and for the (longitudinal) plasmon resonance for C_3, C_5, and C_7.

electronic s.p. density is therefore shifted with respect to the z-axis and pushed into a region of lower binding potential which is energetically unfavourable. In contrast, states with $m = 0$ have their density exactly along the z-axis eventually with only occasional nodes corresponding to the angular momentum l. The upper boundary of the gap in the occupied s.p. spectrum is in all three chains built up by $Y_{1\pm1}$-state. Two more C atoms (from C_3 to C_5, and from C_5 to C_7) add always two states with $m = 0$ and one doubly degenerate state with $m = \pm 1$.

8.2 Dipole response

Similar to the previous chapters, dipole responses are calculated through an instantaneous boost. For better comparison, the chains have been boosted equivalently, at once in all three directions: $\mathbf{p}_{\text{boost}} = (p, p, p)$, with $p = 0.01\, a_0^{-1}$. The strength p of the boost is chosen so that ionization remains weak, $N_{\text{esc}} \sim 10^{-3}$. The chains are aligned along the z-axis. The resulting dipole responses are plotted in Fig. 8.3.

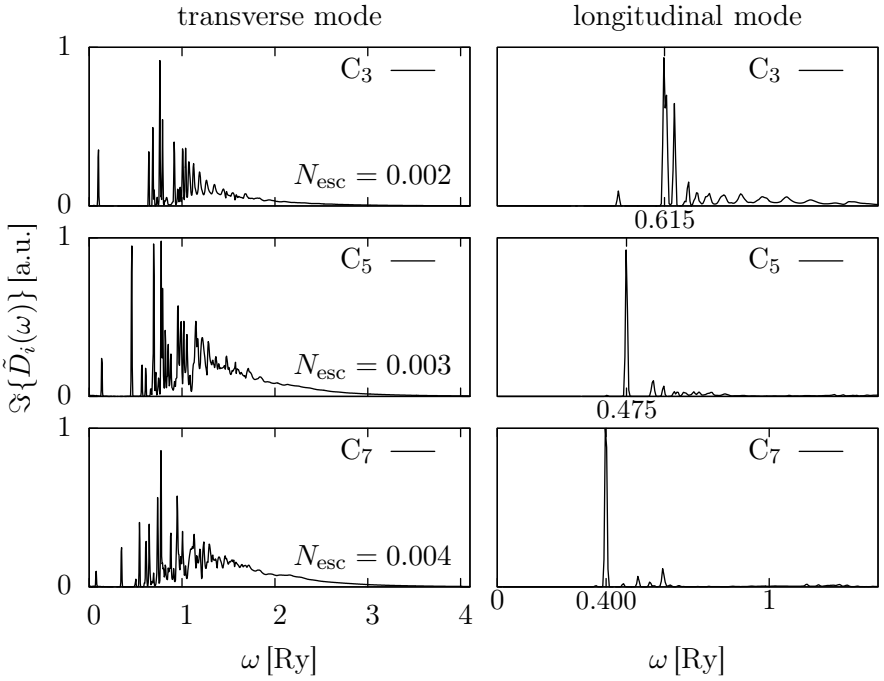

Figure 8.3: Dipole responses of the considered chains after instantaneous excitation with a slight boost in all directions, $p_x = p_y = p_z = 0.01\, a_0^{-1}$. The longitudinal resonance frequencies are $\omega_{\text{pl}} = 0.615$, 0.475, and 0.400 Ry for C_3, C_5, and C_7, respectively.

As much as the ionic configuration, the dipole responses of the chains are strongly anisotropic, in contrast to the optical absorption of C_{60}. In longitudinal direction, the spectra of all three systems are very clean and dominated by one single, strong and sharp resonance emerging at longer wavelengths the longer the wire. In theory, this absorption resonance is assigned to a $\pi \to \pi^*$ transition ($^1\Sigma_u^+ \leftarrow X\,^1\Sigma_g^+$) and moves progressively to the red as the chain grows [148, 154]. The calculated values for the plasmon frequency match better with other TDLDA and CI calculations than with experiments (see Table 8.1), are much higher located than the ones for sodium clusters (e.g., Na_8: $\omega_{\rm pl} \approx 0.19\,{\rm Ry}$), but stay below the ionization potential. On the other hand, the transverse spectrum is fragmented and broadly spread over several Ry, but substantially suppressed by $1-2$ orders of magnitude compared to the longitudinal one.

8.3 Plasmon-enhanced photoemission

Excitation of the chains with stronger instantaneous boosts leads to a significant ionization. This simulates a collision of the considered cluster with a fast ion.

The boost is chosen exclusively in direction parallel to the chain in order to excite the strong, collective, longitudinal mode. Thus, it is expected that the latter mode is predominant and that other excitations are negligible. In order to resolve slow photoelectrons (long wavelength), calculations have been carried out up to $T_{\rm end} = 64\,{\rm fs}$ after the boost. The chains are again aligned along the z-axis, photoelectron spectra are recorded at $M = 121$ measuring points. Due to the axial symmetry there is no need for a uniform coverage of the unit sphere with measuring points. Hence, the measuring points are located on a single longitude of the absorbing sphere so that each point corresponds to an azimuthal scattering angle ϑ, with $\vartheta = 0$ pointing in direction of the boost $\mathbf{p}_{\rm boost} = (0, 0, p)$.

The two upper panels in Fig. 8.4 show the obtained PES of the boosted C_3 chain ($p = 0.1\,a_0^{-1}$, $N_{\rm esc} = 0.07$) in linear (upper left) and logarithmic scale. The red line indicates the full PES (integrated over ϑ) of all occupied s.p. states. Although the boost represents an excitation containing usually a broad spectrum of frequencies, the PES exhibits distinct features at certain kinetic energies, in particular at around $\epsilon_{\rm kin} = 0.14$, 0.31, and 0.45 Ry. The upper panels also display the PES of the three upper most occupied s.e. states indicated as states ③, ④, and ⑤ in Fig. 8.2[24]. The determination of state-dependent PES is possible since all s.p. wavefunctions $\varphi_\alpha(t)$ are stored at the measuring points. Especially in the

[24] The deep lying states ① and ② do not significantly contribute to the PES. The total depletions are: $\sigma^{(1)} = 0.001$, $\sigma^{(2)} = 0.006$, $\sigma^{(3)} = 0.010$, $\sigma^{(4)} = 0.015$, and $\sigma^{(5)} = 0.045$ for $N_{\rm esc} = 0.067$.

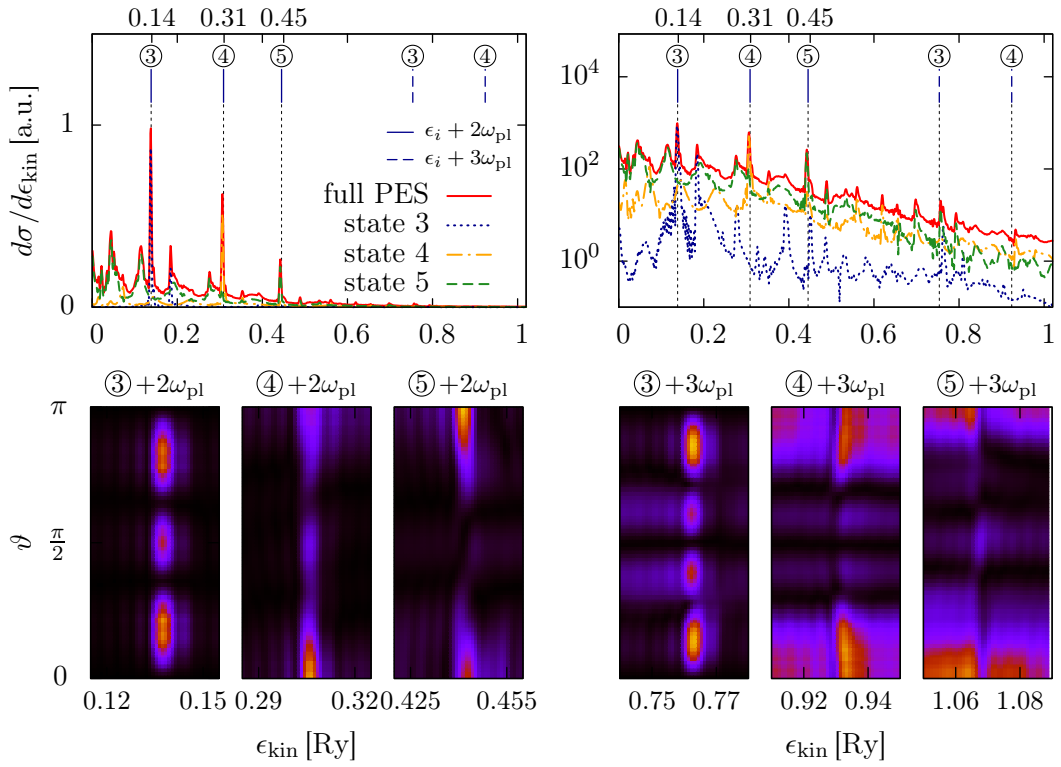

Figure 8.4: *Upper panels:* PES of all occupied states in C_3 (full PES) and of the states ③, ④, and ⑤ after boost along the chain ($p_z = 0.1\, a_0^{-1}$, $N_{\mathrm{esc}} = 0.07$), in linear (left) and logarithmic scale. The contribution of the lowest occupied states ① and ② is negligible. The resonance frequency is $\omega_{\mathrm{pl}} = 0.615\,\mathrm{Ry}$. The blue, vertical lines indicate the doubly and triply excited s.p. spectrum $\epsilon_i + \delta\epsilon + \mu\omega_{\mathrm{pl}}$ ($\mu = 2$: solid; $\mu = 3$: dashed). Due to the residual cluster charge, all s.e. energies have been equally shifted about $\delta\epsilon = -0.02\,\mathrm{Ry}$. *Lower panels:* Combined PES/PAD zoomed onto the doubly and triply excited states ③, ④, and ⑤.

logarithmic PES one can see that the three peaks in question can be assigned to the three states ③, ④, and ⑤, respectively. In consequence, there is a clear relation between the PES obtained after instantaneous boost and the s.e. energies of the system.

There remains the question about the ionization mechanism resulting in the so found connection. The two upper panels also show the shifted s.p. spectrum $\epsilon_i + \mu\omega_{\mathrm{pl}}$ (only states ③, ④, and ⑤) for $\mu = 2$ (blue solid, vertical lines) and $\mu = 3$ (blue dashed). The peak positions correspond exactly to the shifted spectrum. Similar to the resonance effect observed in Na_8 at laser frequencies below the ionization potential (Sect. 5.3.1), it is again a resonance of the system, here the

dominating plasmon which mediates electron emission. Apparently, the energy given by the boost to the system is at first mainly stored in the collective plasmon and then from time to time transferred to single electrons. Since the plasmon frequency is below the ionization threshold, two or more modes are needed in order to ionize the system. In the logarithmic plot one may even catch the triply excited spectrum.

Of course, since excitation is done through the boost, the PES in Fig. 8.4 does not exhibit the ATI peaks which have been observed in Na_8 after laser excitation (Fig. 5.11). However, one may also detect some smaller signals which are most likely images of the s.p. spectrum, too, but for different resonance frequencies. In contrast to a frequency-selective laser pulse, the boost excites here all possible modes. Due to the strength of the excitation, there might be also some cross-talk to the transverse modes. It is therefore expected that the present phenomenon can only be seen in systems with a rather "clean" dipole response characterized by a sharp plasmon resonance.

The lower panels in Fig. 8.4 display the full combined PES/PAD zoomed onto the features corresponding to the doubly (left) and triply excited states ③, ④, and ⑤. Although, chain and longitudinal mode are aligned along the z-axis, electrons are not exclusively emitted in this direction, quite opposite, e.g., for state ③: for $\mu = 2$ (three left panels), maxima of emission do not occur at $\vartheta = 0, \pi$ at all, but at around $\vartheta = \pi/6$, $5\pi/6$, and $\pi/2$. State ④ emits along the z-axis in direction of the boost ($\vartheta = 0$) as well as slightly perpendicular and in the opposite direction at $\vartheta = \pi$, while state ⑤ emits along the chain with preference for $\vartheta = \pi$.

Absorption of an additional mode ($\mu = 3$, right panels) adds further angular momentum to the distributions. This can be clearly seen for state ③. While for $\mu = 2$ emission exhibits three maxima, there can be found four for $\mu = 3$. Similar pictures are obtained for state ④, although already less clear ones. The triply excited peak of ⑤ cannot be resolved any more. In addition to the PES, one may thus conclude also in the PAD that it is the plasmon mode with $l = 1$ and $m = 0$ which triggers the photoemission. Furthermore, the emission behaviour of the s.p. states can be related to the form of the wavefunction. State ③ has angular momentum $m = \pm 1$ according to the spectrum of occupied s.p. states in Fig. 8.2. Absorption of two plasmon modes ends up in a final state also with $m = \pm 1$ with a node completely along the z-axis. Therefore, emission does occur at $\vartheta = 0, \pi$. In contrast, states ④ and ⑤ both with $m = 0$ exhibit emission maximum at $\vartheta = 0, \pi$.

Plasmon-enhanced emission can also be observed for the larger chains C_5 and to a lesser extent also in C_7, see Fig. 8.5. At longer chain length, the system gains collectivity, the dipole response clears up and the plasmon aligns even stronger with increasing chain length, but the s.p. spectrum gets more and more compli-

cated. In consequence, also the PES gets more involved: more s.p. states are contributing and the images of the shifted s.p. spectra may overlap for different process orders μ.

Finally, it is to be noted that the present phenomenon has only been observed within a certain range of excitation strength. For too weak excitations, the plasmon is not strongly enough excited and the continuum background discretized due to the finite numerical simulation box, becomes relevant. For too strong excitations the PES is smeared out as a consequence of the gradual downshift of the s.p. spectrum.

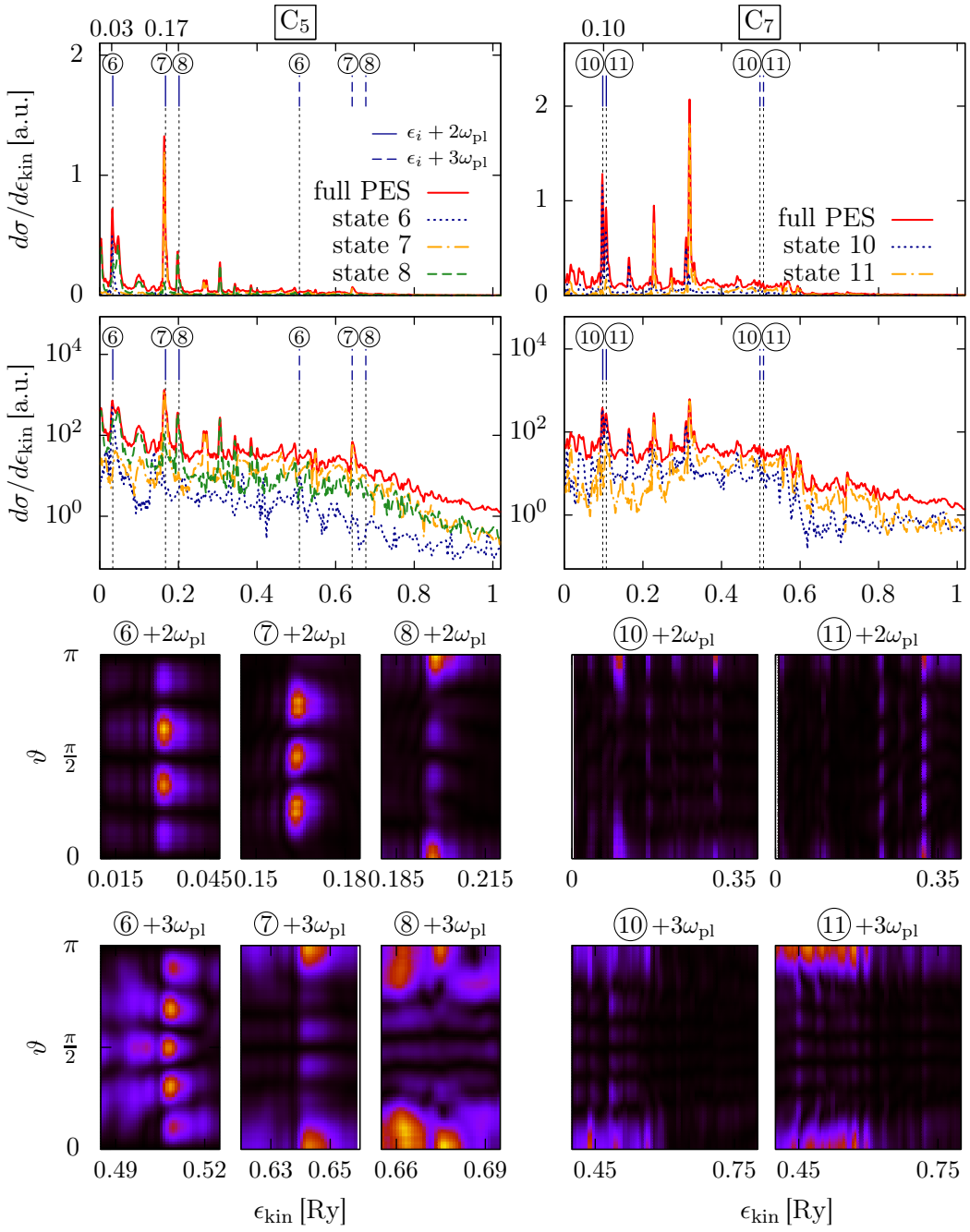

Figure 8.5: *Upper panels:* PES of C_5 (left) and C_7 in linear and logarithmic scale. *Lower panels:* Combined PES/PAD zoomed onto selected doubly (left) and triply excited states.

9 Conclusion

The first part of this work presented and reviewed the theoretical approach and the numerical methods used throughout. The theoretical framework based on time-dependent density-functional theory (local-density approximation with self-interaction correction) provides a suitable, efficient tool to describe ground-state as well as dynamical properties of finite many-body systems. Within this approach, electron dynamics of small sodium clusters, carbon chains, and the buckminsterfullerene C_{60} have been studied, with particular focus on photoangular distributions (PAD) and spectra (PES) of electrons emitted from the considered systems after excitation by linearly polarized femtosecond laser pulses or by instantaneous boosts. Absorbing boundary conditions and measuring points allow to determine the PAD and PES.

While in theory the single cluster/molecule is fixed in space (in the numerical simulation box) with a given orientation with respect to the laser polarization axis, experiments rather deal with an ensemble of randomly orientated clusters. It turns out that the orientation-averaged PAD (OA-PAD) reduces in spherical coordinates to a very simple form $\sim 1+\beta_2 P_2(\cos\vartheta)+\beta_4 P_4(\cos\vartheta)+\ldots$, with P_{2l} being the Legendre polynomials, ϑ the scattering angle of the emitted electrons measured with respect to the laser polarization axis, and β_{2l} the so-called anisotropy parameters. The highest order of a possible non-vanishing β_{2l} is related to the order of the photon process. In the one-photon regime, only a single anisotropy parameter remains to describe the OA-PAD: $d\overline{\sigma}/d\Omega = \overline{\sigma}/(4\pi)(1+\beta_2 P_2)$, with β_2 ranging between -1 and 2. For $\beta_2 = 2$, the OA-PAD exhibits so an anisotropic $\cos^2\vartheta$-shaped dependence, while for $\beta_2 = -1$ a $\sin^2\vartheta$-dependence is observed. For $\beta_2 = 0$ the distribution is isotropic. The value of β_2 is not only related to the order of the photon process, but also to the angular momentum of initial and final state. For perfectly spherical symmetric initial s states, e.g., β_2 equals always to two.

In order to overcome the discrepancy between experiment and theory, procedures for calculating the OA-PAD have been developed. The first averaging scheme is based on first-order perturbation theory and was derived through Euler rotations. Here three linearly independent calculations are needed to determine the orientation-averaged yield $\overline{\sigma}$ and six for the anisotropy β_2. In practice, the cluster remains fixed in the simulation box, but the laser polarization is varied. In contrast, the second scheme rotates the cluster orientation, but fixes the polarization axis. The OA-PAD is thus calculated by summation over a finite set of

different orientations. This conceptually simpler procedure is more general since it can be applied also in multiphoton and non-linear regimes. However, the number of different cluster orientations needed for convergence is not known, in principle, to the possible detriment of higher computational cost.

In the second part of this work, the developed schemes were first applied to a selection of small neutral and positively charged $Na_N^{(+)}$ clusters with $N = 3 - 19$. Thereby, different models for the description of the ionic background have been compared: local pseudo-potentials and the widely used spherical/deformed jellium model. The first model explicitly accounts for the ionic structure of the cluster while in the second one the ionic cores are thought of smeared out. The differences in the OA-PAD of these two models are striking. While the jellium model yields for most of the clusters anisotropy parameters close to the maximum possible value of two, the ionic background reduces these substantially. The deformation of initial and final state wavefunctions imposed by the pseudo-potentials, introduces a mix of high angular momentum components which always contains some pieces with sidewards scattering.

Detailed analysis have been performed for a better understanding of the dependence of β_2 on laser parameters, in particular, on the laser frequency ω_{las}. A spherical jellium model for Na_8 served here as a starting point. Within this model, a direct comparison of stationary perturbation theory and results from time-dependent density-functional theory is possible. In the stationary model several assumptions for initial as well as final states have been proposed and inserted into the Bethe-Cooper-Zare formula. In any case, the resulting single-particle anisotropy $\beta_2^{(i)}(\omega_{\text{las}})$ depends on the angular momentum content of the considered initial state i and becomes as such a finger print of i. For example, the plane wave model shows a characteristic decline in the anisotropy of the p state near the ionization potential. Sharp dips towards negative values which are related to zero-crossings of transition matrix elements, follow at larger kinetic energies. However, small variations of both wavefunctions have generally enormous effects on $\beta_2^{(i)}(\omega_{\text{las}})$ in accordance with the previous comparison of explicit ionic background and jellium model. Hence, introducing explicit ionic background seems to reshuffle the cards. The trends of the anisotropy as a function of the laser frequency become now very smooth with emission preferably along the laser polarization plus some isotropic background. An exception seem to represent negatively charged clusters, here Na_7^-, where the plane wave assumption for the outgoing wave holds due to the weak binding potential so that the generic tendency to sidewards emission prevails for frequencies near the threshold. Nevertheless, static models can never fully describe the ionization process since they do not account for dynamical effects in the course of the ionization process such as polarization and rearrangement of the residual cluster.

The results on sodium cluster have shown that the angular distribution is very sensitive to all details of the modeling. This requires a theoretical description without compromises. Thus, the full time-dependent approach using non-local Goedecker potential for the ionic background was employed for the buckminsterfullerene C_{60} and the linear carbon chains C_3, C_5, and C_7. For C_{60}, application of pseudo-potentials is all the more important since a spherical jellium shell does not even deliver the correct ground-state with a shell-closing after 240 valence electrons. Using pseudo-potentials, however, breaks the sphericity, implements the icosahedral symmetry of the molecule, and a shell-closing is obtained for $N_{\mathrm{val}} = 240$. The spectrum of occupied single-particle states reduces to a significantly lower number of bands which is related to the high symmetry and level degeneracy. The symmetry of the cluster also helps to find an appropriate direct averaging scheme in order to determine the anisotropy parameters $\beta_2, \beta_4, \ldots$ Thereby different regimes were considered: the one-photon regime employing laser frequencies like they are typically used at the synchrotron, and the multiphoton regime with frequencies far below the ionization threshold. It is found that these two regimes deliver completely different PAD and PES. In the one-photon regime, the PES reflects the molecular-like single-particle spectrum and the PAD follows the expected $1 + \beta_2 P_2$ dependence. In contrast in the multiphoton domain, the PES exhibits an exponential decay superimposed with large oscillations and the PAD yields non-vanishing anisotropies β_{2l} of higher orders. The two different behaviours particularly of the PES are found to be related to the depletion of the single-particle spectrum.

The work was concluded by a brief study of the small, linear carbon chains C_3, C_5, and C_7. In contrast to C_{60}, these small molecules exhibit a distinct, longitudinal plasmon which can be excited by a strong instantaneous boost simulating a fast ion passing by the cluster. The deposited energy is first stored in the plasmon and later transferred to single particles. Since the plasmon frequency is lower than the ionization potential, two or more modes have to be absorbed in order to ionize the system. The PES so reflects the doubly and triply excited single-particle spectrum. The angular momentum components of the PAD always increases by one unit when absorbing an additional dipole mode.

The present work leaves some open questions and perspectives. From the numerical point of view it would be desirable to enhance the angular resolution of the combined PES/PAD. The limiting factor here is, in particular, the number of measuring points at which all single-particle wavefunctions have to be stored as a function of time in order to evaluate the Fourier transformation afterwards. An alternative procedure is to calculate the Fourier transformation $\varphi_\alpha(\omega)$ on-the-fly for a given, limited frequency range. Thus, one is able to increase the number of measuring points. Another aspect concerning the PES is

that the present evaluation scheme assumes freely propagating electrons which reduces the range of possible applications. A generalized scheme which accounts for non-vanishing electromagnetic fields during the measuring time, has been already proposed in [59]. This allows to consider also strong laser intensities, long laser pulses and pump-and-probe scenarios where the electron flow is known to interfere with the electromagnetic field.

The absorbing real-space mask function is a very efficient way to evaluate photoangular distributions. However, it has also some deficiencies, e.g., when considering less bound systems like negatively charged clusters, strong laser fields leading to high electronic densities near the boundaries, or very slow electrons which are still reflected. Moreover, performance of the absorbing mask crucially depends on the chosen number of absorbing points. A possible, more flexible solution is to implement the absorption as an operator depending on time and kinetic energy of the outgoing wavefunction.

A critical analysis of the calculated single-particle spectrum of C_{60} reveals that although the ionization potential matches very well with experimental data, the degeneracy in particular of the HOMO-1 does not. This may be a deficiency of the sparse grid and/or the pseudo-potential parameterization. The non-local pseudopotentials with a large grid spacing used in this work are actually a modification of the original ones proposed by Goedecker *et al.* [29] using a much smaller spacing. Hence, coarser grids may be unavoidable. Moreover, the used ionic configuration differs slightly from experiments which measure a larger radius of the cage. Studies on the sensitivity of single-particle spectrum and dipole response to the cage radius are under way. Theoretical work by others [101, 102] also suggests that all single-particle wavefunctions can be grouped according to their nodal behaviour into 60 π and 180 σ electrons. Therefore, a more detailed analysis of the wavefunctions can additionally help to improve the modeling. After optimization of the ground-state properties one could explore some more dynamical features of C_{60}, e.g., the often mentioned oscillations of the partial cross-sections of HOMO and HOMO-1.

The plasmon-enhanced photoemission effect observed in carbon chains suggests a tool for determining plasmon frequency and single-particle spectrum at once. An open question is whether the effect can also be measured in experiments. If yes, it could in addition used for size-selection or size-specification of carbon chains through photoelectron spectroscopy after ion collision. An interesting question is also how the effect scales with system size and geometry. According to the calculations, the clearest results have been found for C_3. With increasing chain length, the effect seems to disappears although the plasmon is getting sharper and more dominant. One may therefore explore, at first, other small systems like diatomic molecules such as C_2, N_2, CO, etc. and later investigate the transition to larger systems, e.g., C_{60}. In the latter case, preliminary attempts, however,

could not identify such an effect, perhaps due to the large width of the plasmon at 20 eV. Also geometrical aspects, i.e., different behaviour for one-, two- and three-dimensional ionic structures, might have an influence.

The results on Na_8 indicate that an excited resonance breaks the relation $N_{esc} \sim I^{\nu}$ known from perturbation theory. Post-pulse emission occurs and characteristic photoelectron spectra after the pulse show up. Tests have shown that this holds already for very small system sizes like Na_3^+ when laser frequencies below the ionization threshold are applied. This behaviour could be explored also for the carbon materials, in particular C_{60}, in order to estimate the impact of the "giant resonance" on the ionization.

Post-pulse emission and direct comparison of the theoretical results with measurements show that the theory lacks to describe electron thermalization observed, for example, as isotropic and exponential background in experimental PAD and PES on C_{60}, in particular when longer pulses are applied. Hence, an important decay mechanism is still missing in the modeling. The inclusion of electron-electron collisions into the TDLDA approach remains as a further open task.

Appendix

A Angular momentum and rotations

A.1 Euler angles and rotation operators

The rotation operator $\hat{D}$ is a unitary operator,

$$\hat{D}^{-1}(\alpha\beta\gamma) = \hat{D}^{*}(\alpha\beta\gamma)\,.$$

In spherical coordinates, the spherical harmonics as eigenfunctions of the angular momentum operator $\hat{\mathbf{L}}^2$ transform under forward rotation like:

$$\hat{D}(\alpha\beta\gamma)Y_{lm}(\vartheta\varphi) = \sum_{m'} Y_{lm'}(\vartheta\varphi)\langle lm'|\hat{D}(\alpha\beta\gamma|lm\rangle = \sum_{m'} Y_{lm'}(\vartheta\varphi)\mathcal{D}^{(l)}_{m'm}(\alpha\beta\gamma)\,.$$

The backward rotation, $\hat{D}^{-1}(\alpha\beta\gamma) = \hat{D}^{*}(\alpha\beta\gamma) = \hat{D}(-\gamma-\beta-\alpha)$, behaves like a forward rotation with Euler angles $-\gamma$, $-\beta$, and $-\alpha$:

$$\hat{D}^{-1}(\alpha\beta\gamma)Y_{lm}(\vartheta\varphi) = \sum_{m'} Y_{lm'}(\vartheta\varphi)\langle lm|\hat{D}(\alpha\beta\gamma)|lm'\rangle^{*} = \sum_{m'} Y_{lm'}(\vartheta\varphi)\mathcal{D}^{(l)*}_{mm'}(\alpha\beta\gamma)\,. \tag{A.1}$$

The matrix elements $\mathcal{D}^{(l)}_{m'm}$ are the so-called Wigner $\mathcal{D}$-functions. An important property of the $\mathcal{D}$-functions is the relation between forward and backward rotation:

$$\mathcal{D}^{(l)*}_{mm'}(\alpha\beta\gamma) = (-1)^{m-m'}\mathcal{D}^{(l)}_{-m-m'}(\alpha\beta\gamma) = \mathcal{D}^{(l)}_{m'm}(-\gamma-\beta-\alpha)\,. \tag{A.2}$$

Integrals over two or three $\mathcal{D}$-functions yield:

$$\int d^3(\alpha\beta\gamma)\,\mathcal{D}^{(j_1)*}_{m_1'm_1}(\alpha\beta\gamma)\mathcal{D}^{(j_2)}_{m_2'm_2}(\alpha\beta\gamma) = \delta_{m_1'm_2'}\delta_{m_1m_2}\delta_{j_1j_2}\cdot\frac{1}{2j_1+1}\,, \tag{A.3}$$

$$\begin{aligned}&\int d^3(\alpha\beta\gamma)\,\mathcal{D}^{(j_1)}_{m_1'm_1}(\alpha\beta\gamma)\mathcal{D}^{(j_2)}_{m_2'm_2}(\alpha\beta\gamma)\mathcal{D}^{(j_3)}_{m_3'm_3}(\alpha\beta\gamma)\\ &\quad= \begin{pmatrix} j_1 & j_2 & j_3\\ m_1' & m_2' & m_3'\end{pmatrix}\begin{pmatrix} j_1 & j_2 & j_3\\ m_1 & m_2 & m_3\end{pmatrix}\,.\end{aligned} \tag{A.4}$$

The large brackets denote the Wigner $3j$-symbols.

A.1.1 Wigner 3j-symbols

The Wigner 3j-symbols are defined in terms of Clebsch-Gordan coefficients as

$$\begin{pmatrix} j_1 & j_2 & j_3 \\ m_1 & m_2 & m_3 \end{pmatrix} = (-1)^{j_1-j_2-m_2}(2j_3+1)^{-\frac{1}{2}}(j_1\, m_1\, j_2\, j_2\, m_2|j_1\, j_2\, j_3\, -m_3)\,.$$

A permutation of *gerade* symmetry does not change the value of the symbol, whereas the symbol is multiplied by $(-1)^{j_1+j_2+j_3}$ after an *ungerade* permutation:

$$\begin{pmatrix} j_1 & j_2 & j_3 \\ m_1 & m_2 & m_3 \end{pmatrix} = \begin{pmatrix} j_2 & j_3 & j_1 \\ m_2 & m_3 & m_1 \end{pmatrix} = \begin{pmatrix} j_3 & j_1 & j_2 \\ m_3 & m_1 & m_2 \end{pmatrix} \quad \textit{gerade}$$

$$\begin{pmatrix} j_1 & j_2 & j_3 \\ m_1 & m_2 & m_3 \end{pmatrix} = (-1)^{j_1+j_2+j_3}\begin{pmatrix} j_1 & j_3 & j_2 \\ m_1 & m_3 & m_2 \end{pmatrix} \quad \textit{ungerade}$$

Special rules for the 3j-symbols are:

$$\begin{pmatrix} j & j & 0 \\ m & -m & 0 \end{pmatrix} = (-1)^{j-m}(2j+1)^{-1/2}$$

$$\begin{pmatrix} j_1 & j_2 & j_3 \\ 0 & 0 & 0 \end{pmatrix} = 0\,, \quad \text{for odd } j_1+j_2+j_3$$

$$\begin{pmatrix} j_1 & j_2 & j_3 \\ m_1 & m_2 & m_3 \end{pmatrix} = (-1)^{j_1+j_2+j_3}\begin{pmatrix} j_1 & j_2 & j_3 \\ -m_1 & -m_2 & -m_3 \end{pmatrix}$$

$$\begin{pmatrix} j & j & 2 \\ m & -m & 0 \end{pmatrix} = (-1)^{j-m}\frac{6m^2-2j(j+1)}{[(2j+3)(2j+2)(2j+1)2j(2j-1)]^{1/2}}$$

$$\begin{pmatrix} j & j & 2 \\ m & -m-1 & 1 \end{pmatrix} = (-1)^{j-m}(1+2m)\left[\frac{6(j+m+1)(j-m)}{(2j+3)(2j+2)(2j+1)2j(2j-1)}\right]^{\frac{1}{2}}$$

$$\begin{pmatrix} j & j & 2 \\ m & -m & 2 \end{pmatrix} = (-1)^{j-m}\left[\frac{6(j-m-1)(j-m)(j+m+1)(j+m+2)}{(2j+3)(2j+2)(2j+1)2j(2j-1)}\right]^{\frac{1}{2}}$$

With these rules one obtains the following 3j-symbols explicitely:

$$\begin{aligned}
\begin{pmatrix} 1 & 1 & 0 \\ 0 & 0 & 0 \end{pmatrix} &= -\frac{1}{\sqrt{3}}, & \begin{pmatrix} 1 & 1 & 0 \\ 1 & -1 & 0 \end{pmatrix} &= \frac{1}{\sqrt{3}}, \\
\begin{pmatrix} 1 & 1 & 2 \\ 0 & 0 & 0 \end{pmatrix} &= \frac{4}{\sqrt{120}}, & \begin{pmatrix} 1 & 1 & 2 \\ 1 & -1 & 0 \end{pmatrix} &= \frac{2}{\sqrt{120}}, \\
\begin{pmatrix} 1 & 1 & 2 \\ -1 & 0 & 1 \end{pmatrix} &= -\sqrt{\frac{12}{120}}, & \begin{pmatrix} 1 & 1 & 2 \\ 1 & 0 & -1 \end{pmatrix} &= -\sqrt{\frac{12}{120}}, \\
\begin{pmatrix} 1 & 1 & 2 \\ -1 & -1 & 2 \end{pmatrix} &= \sqrt{\frac{24}{120}}, & \begin{pmatrix} 1 & 1 & 2 \\ 1 & 1 & -2 \end{pmatrix} &= \sqrt{\frac{24}{120}}.
\end{aligned} \tag{A.5}$$

Furthermore, the angular part of a general transition matrix elements, i.e.,

$$(lm|LM|l'm') = \int d\Omega\, Y^*_{lm}(\Omega) Y_{LM}(\Omega) Y_{l'm'}(\Omega),$$

can be expressed with Wigner $3j$-symbols in the following simple form:

$$\begin{aligned}(lm|LM|l'm') = (-1)^m \sqrt{\frac{(2l+1)(2L+1)(2l'+1)}{4\pi}} \\ \times \begin{pmatrix} l & L & l' \\ -m & M & m' \end{pmatrix} \begin{pmatrix} l & L & l' \\ 0 & 0 & 0 \end{pmatrix}\end{aligned} \tag{A.6}$$

Explicitely, one obtains with the last relation:

$$\begin{aligned}(lm|00|lm) &= \frac{1}{\sqrt{4\pi}}\,, \\ (l+1\,m|10|lm) &= \sqrt{\frac{3}{4\pi}} \sqrt{\frac{(l+m+1)(l-m+1)}{(2l+1)(2l+3)}}\,, \\ (l+1\,m+1|11|lm) &= \sqrt{\frac{3}{8\pi}} \sqrt{\frac{(l+m+1)(l+m+2)}{(2l+1)(2l+3)}}\,, \\ (l-1\,m+1|11|lm) &= -\sqrt{\frac{3}{8\pi}} \sqrt{\frac{(l-m)(l-m-1)}{(2l-1)(2l+1)}}\,.\end{aligned}$$

A.1.2 Transformation of 1st-order tensors

A finite rotation of any reference frame about the origin can be considered as transformation of the coordinates, but also as a unitary transformation of all operators. For any operator one may thus write:

$$\hat{Q} \longrightarrow \hat{Q}' = \hat{D}(\alpha\beta\gamma) \hat{Q} \hat{D}^{-1}(\alpha\beta\gamma)\,.$$

As an example, consider the position operator $\hat{\mathbf{r}}$ of the laboratory frame K in the so-called spherical basis:

$$\begin{aligned} r_{-1} &= \frac{1}{\sqrt{2}}(x - \mathrm{i}y)\,, \\ r_0 &= z\,, \\ r_1 &= \frac{1}{\sqrt{2}}(-x - \mathrm{i}y)\,. \end{aligned} \tag{A.7}$$

In this basis, the position operator represents a first-order spherical tensor which transforms like:

$$\hat{r}'_\nu = \sum_\mu \hat{r}_\mu \mathcal{D}^{(1)}_{\mu\nu}(\alpha\beta\gamma)\,. \tag{A.8}$$

An alternate means to describe an Euler rotation is a rotation of the coordinate system K about a given axis $\boldsymbol{\xi}$ with direction $\mathbf{e}_\xi$ and about the angle $\xi = |\boldsymbol{\xi}|$. The position operator $\hat{\mathbf{r}}$ in Cartesian basis transforms then like:

$$\hat{\mathbf{r}}' = \exp\left(\mathrm{i}\boldsymbol{\xi}\cdot\hat{\mathbf{L}}\right)\hat{\mathbf{r}}\,\exp\left(-\mathrm{i}\boldsymbol{\xi}\cdot\hat{\mathbf{L}}\right), \tag{A.9}$$

where $\hat{\mathbf{L}}$ is again the angular momentum operator. The three rotations α, β and γ about the coordinate axis of the laboratory frame K are thus replaced by one single rotation about an arbritrary vector in K. Using the relations

$$\exp(\hat{A})\hat{B}\exp(-\hat{A}) = \sum_{n=0}^{\infty}\frac{1}{n!}[\hat{A},\hat{B}]_{(n)}\,, \qquad [\hat{A},\hat{B}]_{(0)} \equiv \hat{B}\,,$$
$$[\hat{A},\hat{B}]_{(n+1)} \equiv [\hat{A},[\hat{A},\hat{B}]_{(n)}]\,, \qquad \left[\mathrm{i}\boldsymbol{\xi}\cdot\hat{\mathbf{L}},\mathbf{r}\right] = \boldsymbol{\xi}\times\mathbf{r}\,,$$

expression (A.9) can be expanded as:

$$\begin{aligned}\mathbf{r}' &= \mathbf{r} + \mathrm{i}[\boldsymbol{\xi}\cdot\hat{\mathbf{L}},\mathbf{r}] - \frac{1}{2}[\boldsymbol{\xi}\cdot\hat{\mathbf{L}},[\boldsymbol{\xi}\cdot\hat{\mathbf{L}},\mathbf{r}]] \pm \dots \\ &= \mathbf{r} + \boldsymbol{\xi}\times\mathbf{r} + \frac{1}{2}\boldsymbol{\xi}\times(\boldsymbol{\xi}\times\mathbf{r}) + \dots = \sum_n \frac{1}{n!}\underbrace{\boldsymbol{\xi}\times(\dots(\boldsymbol{\xi}\times}_{n\text{-fold}}\mathbf{r}))\dots)\,.\end{aligned}$$

The n-fold vector product can be further simplified[25]. The series expansion becomes then:

$$\mathbf{r}' = \mathbf{r}\left(1 - \frac{1}{2}\xi^2 \pm \dots\right) + (\boldsymbol{\xi}\times\mathbf{r})\left(1 - \frac{1}{3!}\xi^2 \pm \dots\right) - \boldsymbol{\xi}\,(\boldsymbol{\xi}\cdot\mathbf{r})\left(-\frac{1}{2} + \frac{1}{4!\xi^2} \pm \dots\right)$$

which can be summed up to the closed expression

$$\mathbf{r}' = \mathbf{r}\cos(\xi) + \frac{\boldsymbol{\xi}\times\mathbf{r}}{\xi}\sin(\xi) - \boldsymbol{\xi}\frac{\boldsymbol{\xi}\cdot\mathbf{r}}{\xi^2}\left(\cos(\xi) - 1\right)\,. \tag{A.10}$$

[25] The sequence

$$\boldsymbol{\xi}\times(\boldsymbol{\xi}\times\mathbf{r}) = -\xi^2\mathbf{r} + \boldsymbol{\xi}\,(\boldsymbol{\xi}\cdot\mathbf{r})\,, \quad \boldsymbol{\xi}\times(\boldsymbol{\xi}\times(\boldsymbol{\xi}\times\mathbf{r})) = -\xi^2\boldsymbol{\xi}\times\mathbf{r}\,,$$

repeats itself for higher orders of interlaced vector products.

One seeks now to write this transformation as a 3×3 matrix operation $\mathbf{r}' = \hat{T}\mathbf{r}$ like in Eq. (A.8) for the Euler rotation. Identifying

$$\boldsymbol{\xi} \times \mathbf{r} = \begin{pmatrix} 0 & -\xi_z & \xi_y \\ \xi_z & 0 & -\xi_x \\ -\xi_y & \xi_x & 0 \end{pmatrix} \mathbf{r}\,, \quad \boldsymbol{\xi}\,(\boldsymbol{\xi}\cdot\mathbf{r})\cos(\xi) = \begin{pmatrix} \xi_x\xi_x & \xi_x\xi_y & \xi_x\xi_z \\ \xi_y\xi_x & \xi_y\xi_y & \xi_y\xi_z \\ \xi_z\xi_x & \xi_z\xi_y & \xi_z\xi_z \end{pmatrix} \mathbf{r}\,,$$

and inserting that into Eq. (A.10) yields the wanted rotation matrix

$$\mathbf{r}' = \begin{pmatrix} c - \frac{\xi_x^2}{\xi^2}c_2 & -\frac{\xi_z}{\xi}s - \frac{\xi_x\xi_y}{\xi^2}c_2 & \frac{\xi_y}{\xi}s - \frac{\xi_x\xi_z}{\xi^2}c_2 \\ \frac{\xi_z}{\xi}s - \frac{\xi_y\xi_x}{\xi^2}c_2 & c - \frac{\xi_y^2}{\xi^2}c_2 & -\frac{\xi_x}{\xi}s - \frac{\xi_y\xi_z}{\xi^2}c_2 \\ -\frac{\xi_y}{\xi}s - \frac{\xi_z\xi_x}{\xi^2}c_2 & \frac{\xi_x}{\xi}s - \frac{\xi_z\xi_y}{\xi^2}c_2 & c - \frac{\xi_z^2}{\xi^2}c_2 \end{pmatrix} \mathbf{r}\,, \tag{A.11}$$

with

$$c = \cos(\xi)\,, \quad s = \sin(\xi)\,, \quad c_2 = \cos(\xi) - 1\,.$$

A.2 Legendre polynomials and spherical harmonics

Y_{00}	$\frac{1}{\sqrt{4\pi}}$	1	P_0
Y_{10}	$\sqrt{\frac{3}{4\pi}}\cos\vartheta$	$\cos\vartheta$	P_1
$Y_{1\pm1}$	$\mp\sqrt{\frac{3}{8\pi}}\sin\vartheta e^{\pm i\varphi}$		
Y_{20}	$\sqrt{\frac{5}{16\pi}}(3\cos^2\vartheta - 1)$	$\frac{1}{2}(3\cos^2\vartheta - 1)$	P_2
$Y_{2\pm1}$	$\mp\sqrt{\frac{15}{8\pi}}\sin\vartheta\cos\vartheta e^{\pm i\varphi}$		
$Y_{2\pm2}$	$\sqrt{\frac{15}{32\pi}}\sin^2\vartheta e^{\pm 2i\varphi}$		
Y_{40}	$\frac{1}{8}\sqrt{\frac{9}{4\pi}}(35\cos^4\vartheta - 30\cos^2\vartheta + 3)$	$\frac{1}{8}(35\cos^4\vartheta - 30\cos^2\vartheta + 3)$	P_4
$Y_{l0}(\vartheta,\varphi) = \sqrt{\frac{2l+1}{4\pi}}\,P_l(\cos\vartheta)$			

Table A.1: Spherical harmonics and Legendre polynomials.

Addition theorem of the spherical harmonics:

$$P_l(\cos\vartheta) = \frac{4\pi}{2l+1}\sum_{m=-l}^{l} Y_{lm}^*(\Omega_{\mathbf{k}})Y_{lm}(\Omega_{\mathbf{r}})$$

Harmonic polynomials and spherical harmonics:

$$\mathcal{Y}_{lm}(x,y,z) = r^l\,Y_{lm}(\vartheta,\varphi)$$

Relation to Wigner $\mathcal{D}$-functions:

$$\mathcal{D}^{(l)}_{0m}(\alpha\beta\gamma) = \left(\frac{4\pi}{2l+1}\right)^{1/2} Y_{lm}(\vartheta,\varphi) \qquad \text{and} \qquad \mathcal{D}^{(l)}_{00}(\alpha\beta\gamma) = P_l(\cos\beta)$$

Relation to Cartesian and spherical basis:

$$\begin{aligned}
x &= r\sin\vartheta\cos\varphi = r\sqrt{\frac{2\pi}{3}}(Y_{1-1} - Y_{11}) = \frac{\sqrt{2}}{2}(r_{-1} - r_1) \\
y &= \mathrm{i}r\sqrt{\frac{2\pi}{3}}(Y_{1-1} + Y_{11}) = \mathrm{i}\frac{\sqrt{2}}{2}(r_{-1} + r_1) \\
z &= r\sqrt{\frac{4\pi}{3}}Y_{10} = r_0
\end{aligned}$$

B Radial Schrödinger equation

This section gives a brief introduction to analytical and numerical methods for the solution of the Schrödinger equation in spherical potentials. For a detailed overview, see standard textbooks on quantum mechanics [88, 155].

B.1 Introduction

Using the separation ansatz $\Psi(r\vartheta\varphi) = R_l(r)Y_{lm}(\vartheta\varphi)$ the three-dimensional Schrödinger equation in spherical coordinates can be simplified to the one-dimensional radial equation:

$$\left[-\frac{\hbar^2}{2m_e}\left(\frac{d^2}{dr^2}+\frac{2}{r}\frac{d}{dr}\right)+\frac{\hbar^2}{2m_e}\frac{l(l+1)}{r^2}+V(r)-E\right]R_l(r)=0\,. \tag{6.1}$$

The radial part $R_l(r)$ of the wavefunction Ψ has to be normalized to unity, i.e., for bound states

$$\int_0^\infty dr\, r^2 R_l(r)^2 = 1\,.$$

The continuum states are normalized in energy scale, see Sect. B.2.3. Moreover, $R_l(r)$ must satisfy the asymptotic conditions

$$R_l(0)=0 \quad \text{for all } l\,, \quad \text{and} \quad R_l(r)\sim r^l \quad \text{for } r\to 0 \tag{B.1}$$

(for potentials $V(r) < 1/r^2$ for $r \to 0$).

Reduced radial equation Equation (6.1) can be further simplified. Inserting the ansatz $R_l(r) = u_l(r)/r$ gives the homogeneous second-order differential equation

$$\left[\frac{\hbar^2}{2m_e}\frac{d^2}{dr^2}-\frac{\hbar^2}{2m_e}\frac{l(l+1)}{r^2}-V(r)+E\right]u_l(r)=0 \tag{B.2}$$

which can be used for numerical computations.

B.2 Continuum solutions

B.2.1 Free solution

The spherical Bessel and Neumann functions j_l and n_l, see Sect. B.4.1, analytically solve the free radial Schrödinger equation (6.1) for $E > 0$ and $V = 0$,

$$\left[\frac{d^2}{dr^2} + \frac{2}{r}\frac{d}{dr} - \frac{l(l+1)}{r^2} + k^2\right] R_l(r) = 0 \,,$$

where $E = (\hbar k)^2/2m_e > 0$ and $R_l = j_l$ or $R_l = n_l$.

In three dimensions, the general solution of the free Schrödinger equation is the plane wave $e^{\mathrm{i}\mathbf{kr}}$. The angular part of the plane wave can be expressed in spherical harmonics, the radial part in spherical Bessel functions:

$$\Psi_{\mathbf{k}}^{\text{free}}(r\vartheta\varphi) = e^{\mathrm{i}\mathbf{kr}} = 4\pi \sum_{lm} \mathrm{i}^l j_l(kr) Y_{lm}^*(\Omega_{\mathbf{k}}) Y_{lm}(\Omega_{\mathbf{r}}) \,.$$

Since the spherical Neumann functions diverge for $r = 0$ and the solution has to be normalizable, they do not contribute to the expansion.

B.2.2 Solution in short-range potentials

For potentials $V \neq 0$ the general solution of the three-dimensional Schrödinger equation can be expanded into partial waves,[26]

$$\Psi_{\mathbf{k}}(r\vartheta\varphi) = 4\pi \sum_{lm} \mathrm{i}^l e^{-\mathrm{i}\Delta_l} R_l(r) Y_{lm}^*(\Omega_{\mathbf{k}}) Y_{lm}(\Omega_{\mathbf{r}}) \,. \tag{6.2}$$

In order to derive the asymptotic behaviour $R_l(r \to \infty)$ and the phase Δ_l, one has to distinguish between potentials which go with $V(r) \leq 1/r$ (long-range potential) and those with $V(r) < 1/r^2$ (short-range potential) at large distances $r \to \infty$. It is therefore useful to separate the phase $\Delta_l = \sigma_l + \delta_l$ into a Coulomb phase σ_l and a non-Coulomb phase δ_l [54, 91].

Let V be a pure short-range (s.r.) potential, i.e., $\sigma_l = 0$. The ansatz of Sect. B.2.1 can then be adopted by including the Neumann functions into the expansion. The *asymptotic* form of the radial part of the wavefunction can thus be written as a *distorted plane wave*, i.e., a plane wave plus an incoming wave [61, 156]:

$$R_l^{\text{s.r.}}(r) = j_l(kr)\cos(\delta_l) - n_l(kr)\sin(\delta_l) \simeq \frac{\sin(kr - \frac{l\pi}{2} + \delta_l)}{kr} \,, \qquad \text{for } r \to \infty \,. \tag{B.3}$$

[26] The separation of the factor $e^{-\mathrm{i}\Delta_l}$ out of the function R_l is convention. In this case R_l is a real function.

B.2.3 Solution in long-range potentials

Supposing the potential V is a pure Coulomb potential,

$$V(r) = \frac{Z_1 Z_2 e^2}{r} = \frac{\hbar^2}{m}\frac{k\gamma}{r} ,$$

with Z_1, Z_2 being the asymptotic charges and $\gamma = \frac{Z_1 Z_2}{k a_0}$ the so-called Coulomb parameter [155]. The analytical solutions of Eq. (6.1) are then given in terms of regular and irregular spherical Coulomb functions F_l and G_l, see Sect. B.5. Since the irregular solution G_l does not vanish at $r = 0$, it has to be excluded from the expansion:

$$\Psi_{\mathbf{k}}^{\text{Coul.}}(r\vartheta\varphi) = 4\pi \sum_{lm} i^l e^{-\mathrm{i}\sigma_l} \frac{F_l(\gamma; kr)}{kr} Y_{lm}^*(\Omega_{\mathbf{k}}) Y_{lm}(\Omega_{\mathbf{r}}) . \tag{B.4}$$

The phase δ_l vanishes for a pure Coulomb potential.

In most cases, however, one deals with long-range (l.r.) potentials which asymptotically behave like a Coulomb potential, but which are modified in the short-range region. In this case, one has to allow both, regular and irregular Coulomb functions at large distances:

$$\begin{aligned} R_l^{\text{l.r.}}(r) &= \frac{F_l(\gamma; kr)}{kr}\cos(\delta_l) + \frac{G_l(\gamma; kr)}{kr}\sin(\delta_l) \\ &\simeq \frac{\sin(kr - \frac{l\pi}{2} - \gamma\ln(2kr) + \Delta_l)}{kr} \end{aligned} \qquad \text{for } r \to \infty . \tag{B.5}$$

As one can see, the full phase of the sin in the last equation $\Gamma_l(r) \equiv -l\pi/2 - \gamma\ln(2kr) + \Delta_l$ evolves with the radius r even at large distances due to the logarithmic term $\gamma\ln(kr)$. This term, however, is independent of the angular momentum l. As a consequence, phase shifts $\Gamma_l(r) - \Gamma_{l'}(r)$ of different angular momenta l and l' remain constant at large distances.[27] The reason for this is that the only l-dependent term in Eq. (6.1) is the short-ranged centrifugal term. Phase shifts are so produced in the short-range region of any given potential $V(r)$.

The distorted plane wave (B.3) can be derived from the last equation by setting $\gamma = 0$ and $\sigma_l = 0$ and using relation (B.13) between the functions F_l, G_l and j_l, n_l.

Normalization Independent of the scattering potential, the continuum states are normalized in energy scale,

$$\int d^3\mathbf{r}\, \Psi_{\mathbf{k}}^*(\mathbf{r})\Psi_{\mathbf{k}'}(\mathbf{r}) = \delta(E - E') ,$$

[27] Phase shifts become important in interference of partial waves.

which is equivalent to an asymptotic amplitude of $\sqrt{2/(\pi k)}$ for the the radial partial [91], e.g., for the Coulomb wave[28]:

$$R_l(r) \simeq \sqrt{\frac{2}{\pi k}}\frac{1}{r}\sin\left(kr - \frac{l\pi}{2} - \gamma\ln(2kr) + \Delta_l\right) \quad \text{for } r \to \infty\,.$$

B.3 Integrals for the harmonic oscillator model

For the solution of the radial overlap integral

$$\mathcal{R}_\pm = \int_0^\infty dr\, r^3 R^{(f)}_{L\pm1}(r) R^{(i)}_L(r) \tag{6.5}$$

with initial radial wavefunctions of the harmonic oscillator,

$$R^{(i)}_0(r) = \mathcal{A}\exp(-\alpha^2 r^2)\,, \qquad L = 0\,, \tag{6.8a}$$
$$R^{(i)}_1(r) = \mathcal{B}\, r\exp\left(-\alpha^2 r^2\right)\,, \quad L = 1\,, \tag{6.8b}$$

and a plane wave as the final state wavefunction, $R^{(f)}_{L\pm1}(r) = j_L(kr)$, the following relations are neeeded:

$$\int_0^\infty dx\, \cos(ax)\exp(-b^2x^2) = \frac{\sqrt{\pi}}{2b}\exp\left(\frac{-a^2}{4b^2}\right)\,,$$
$$\int_0^\infty dx\, x^2\cos(ax)\exp(-b^2x^2) = \frac{\sqrt{\pi}\,(2b^2-a^2)}{8b^5}\exp\left(\frac{-a^2}{4b^2}\right)\,,$$
$$\int_0^\infty dx\, x\sin(ax)\exp(-b^2x^2) = \frac{\sqrt{\pi}a}{4b^3}\exp\left(\frac{-a^2}{4b^2}\right)\,,$$
$$\int_0^\infty dx\, x^3\sin(ax)\exp(-b^2x^2) = \frac{\sqrt{\pi}a\,(6b^2-a^2)}{16b^7}\exp\left(\frac{-a^2}{4b^2}\right)\,.$$

[28] Since the normalization is independent of the angular momentum l, it has also no effect on the angular distribution of outgoing partial waves.

Using this and the definition of the spherical Bessel function j_0, j_1, and j_2 (Table B.1), the final integration becomes simple. For $L = 0$:

$$\begin{aligned}\mathcal{R}_+ &= \int dr\, r^3 j_1(kr) R_0^{(i)}(r) \\ &= \frac{\mathcal{A}}{k} \underbrace{\int dr\, r \left\{ \frac{\sin(kr)}{k} - r\cos(kr) \right\} \exp(-\alpha^2 r^2)}_{= \frac{\sqrt{\pi}k^2}{8\alpha^5} \exp\left(\frac{-k^2}{4\alpha^2}\right)} \\ &= \sqrt{\pi}\, \mathcal{A}\, \frac{k}{8\alpha^5} \exp\left(\frac{-k^2}{4\alpha^2}\right) ,\end{aligned} \tag{B.7}$$

and for $L = 1$:

$$\begin{aligned}\mathcal{R}_- &= \int dr\, r^3 j_0(kr) R_1^{(i)}(r) = \frac{\mathcal{B}}{k} \int dr\, r^3 \sin(kr) \exp(-\alpha^2 r^2) \\ &= \sqrt{\pi}\, \mathcal{B}\, \frac{6\alpha^2 - k^2}{16\alpha^7} \exp\left(\frac{-k^2}{4\alpha^2}\right) ,\end{aligned} \tag{B.8}$$

$$\begin{aligned}\mathcal{R}_+ &= \int dr\, r^3 j_2(k_f r) R_1^{(i)}(r) \\ &= -\mathcal{R}_- + \frac{3\mathcal{B}}{k^2} \int dr\, r \left\{ \frac{\sin(kr)}{k} - r\cos(kr) \right\} \exp(-\alpha^2 r^2) \\ &= -\mathcal{R}_- + \frac{3\sqrt{\pi}\mathcal{B}}{8\alpha^5} \exp\left(\frac{-k^2}{4\alpha^2}\right) = \sqrt{\pi}\, \mathcal{B}\, \frac{k^2}{16\alpha^7} \exp\left(\frac{-k^2}{4\alpha^2}\right) .\end{aligned} \tag{B.9}$$

B.4 Spherical Bessel and Coulomb functions

B.4.1 Spherical Bessel and Neumann functions

The spherical Bessel and Neumann functions are given by:

$$j_l(x) = (-x)^l \left(\frac{1}{x}\frac{d}{dx}\right)^l \frac{\sin x}{x} , \quad n_l(x) = -(-x)^l \left(\frac{1}{x}\frac{d}{dx}\right)^l \frac{\cos x}{x} . \tag{B.10}$$

The asymptotic behaviour of these functions for small and large x reads as follows:

$$\begin{aligned} j_l(x) &= \frac{x^l}{(2l+1)!!} \quad x \to 0 , & n_l(x) &= \frac{(2l-1)!!}{x^{l+1}} \quad x \to 0 , \\ j_l(x) &\simeq \frac{\sin\left(x - \frac{l\pi}{2}\right)}{x} \quad x \to \infty , & n_l(x) &\simeq -\frac{\cos\left(x - \frac{l\pi}{2}\right)}{x} \quad x \to \infty . \end{aligned} \tag{B.11}$$

The Neumann functions n_l are irregular and have a singularity at $x = 0$.

j_0	$\frac{\sin(x)}{x}$
j_1	$\frac{\sin(x)}{x^2} - \frac{\cos(x)}{x}$
j_2	$\left(\frac{3}{x^2} - 1\right)\frac{\sin(x)}{x} - \frac{3\cos(x)}{x^2} = -j_0 + \frac{3}{x}j_1$
n_0	$-\frac{\cos(x)}{x}$
n_1	$-\frac{\cos(x)}{x^2} - \frac{\sin(x)}{x}$
n_2	$\left(-\frac{3}{x^2} + 1\right)\frac{\cos(x)}{x} - \frac{3\sin(x)}{x^2}$

Table B.1: Spherical Bessel and Neumann functions.

B.5 Spherical Coulomb functions

Asymptotic behaviour of the Coulomb functions for small and large x:

$$\begin{aligned} F_l(\gamma;x) &\simeq c_l x^{l+1} \quad x \to 0\,, \qquad G_l \simeq \frac{1}{(2l+1)c_l x^l}\,, \quad x \to 0\,, \\ F_l(\gamma;x) &\simeq \sin\left(x - \frac{l\pi}{2} - \gamma\ln(2x) + \sigma_l\right) \quad x \to \infty\,, \\ G_l(\gamma;x) &\simeq \cos\left(x - \frac{l\pi}{2} - \gamma\ln(2x) + \sigma_l\right) \quad x \to \infty \end{aligned} \tag{B.12}$$

with $\sigma_l = \arg\Gamma(l+1+\mathrm{i}\gamma)$ for the Coulomb phase shift and c_l being a positive coefficient depending on l. The Bessel functions can be expressed in Coulomb functions:

$$j_l(x) = \frac{F_l(0;x)}{x} \quad \text{and} \quad n_l(x) = -\frac{G_l(0;x)}{x}\,. \tag{B.13}$$

B.6 Numerical solution

B.6.1 The Numerov algorithm

The Numerov algorithm is an efficient tool for solving second-order differential equations of the form

$$\frac{d^2y}{dx^2} - W(x)\cdot y = U(x)\,. \tag{B.14}$$

Supposing that $W(x)$ is given on an equidistant grid with spacing h, the function $y(x)$ can be calculated iteratively with

$$y_{n+1} = \frac{2y_n - y_{n-1} + \frac{h^2}{12}\left(U_{n+1} + 10F_n + F_{n-1}\right)}{\left(1 - \frac{W_{n+1}h^2}{12}\right)} + \mathcal{O}(h^6), \tag{B.15}$$

where $y_n = y(x_n)$, $x_n = n\cdot h$, and

$$F(x) = U(x) + W(x)\cdot y\,.$$

The forward relation (B.15) needs the two initial values y_0 and y_1. If the value y_1 is not known, but the gradient y_0', y_1 can be obtained by using a Taylor expansion [157]. Resolution of Eq. (B.15) according y_{n-1} yields the backward relation

$$y_{n-1} = \frac{2y_n - y_{n+1} + \frac{h^2}{12}\left(U_{n-1} + 10F_n + F_{n+1}\right)}{\left(1 - \frac{h^2}{12}W_{n-1}\right)} \,. \tag{B.16}$$

Again, two values are needed to start the iteration.

B.6.2 Application of the Numerov algorithm

By setting $U(r) = 0$ and

$$W(r) = V(r) + \frac{\hbar^2}{2m_e}\frac{l(l+1)}{r^2} - E \,,$$

with $x = r$ in Eq. (B.14), the Numerov algorithm can also be used in order to solve the reduced radial equation (B.2) and to determine the solution $u_l(r)$ for given E. For bound and continuum states, the forward iteration (B.15) is initiated by using $y_0 = 0$ and $y_0 = \text{const.}$ which corresponds to the asymptotic behaviour of $u_l(r)$ for $r \to 0$.

Bound states For larger r, the treatment of bound and continuum states differ. For bound states, the forward iteration which starts at $r = 0$ with $E - V(0) > 0$ and $E < 0$, reaches the classical turning point at $r = r_{\text{cl}}$ with $E - V(r_{\text{cl}}) = 0$, see Fig. B.1 for the potential well. In the classically forbidden region, however, the function $u_l(r)$ decays exponentially. The forward iteration cannot deliver this behaviour. Thus, a common procedure is to start a backward iteration at a point $r_{\max}$ far away from the classical turning point and match backward and forward iteration as well as their derivatives at $r = r_{\text{cl}}$. The backward iteration is initiated with $y_{N_{\max}} = 0$ and $y_{N_{\max}-1} = \text{const.}$, the energy eigenvalue E is changed stepwise. A bound state is found as soon as the error

$$\text{error} = \frac{y'_{\text{forward}}(r_{\text{cl}})}{y_{\text{forward}}(r_{\text{cl}})} - \frac{y'_{\text{backward}}(r_{\text{cl}})}{y_{\text{backward}}(r_{\text{cl}})}$$

changes its sign. A root-finding algorithm, e.g., the bisection method, can in a next step determine the eigenvalue E with more accuracy.

Continuum states For continuum states the forward iteration delivers in principle already the solution $u_l(r)$ which has the asymptotic behaviour

$$u_l(r) \sim \sin(kr - \frac{l\pi}{2} + \delta_l) \quad \text{for } r \to \infty \,, \tag{B.17}$$

in the (s.r.) square-well potential. In order to calculated the phase δ_l, a backward iteration with $V = 0$ is started from $r = r_{\max}$ with initial values provided by the forward iteration. The phase is then determined from the value $y_{\text{backward}}(0)$ at the origin.

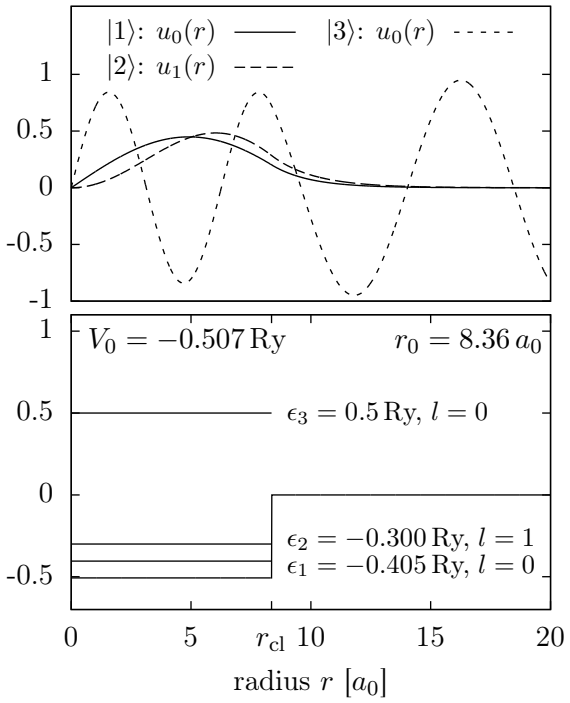

Figure B.1: *Lower panel:* Calculated bound states $|1\rangle$ and $|2\rangle$ for $l = 0$ and $l = 1$ (lowest bound states) and continuum state $|3\rangle$ at ϵ_3 ($l = 0$) in the potential well of depth $V_0 = -0.507\,\text{Ry}$ and width $r_0 = r_{\text{cl}} = 8.36\,a_0$. *Upper panel:* Corresponding radial part $u_l(r)$ of the wavefunctions. The bound states are normalized to unity, the amplitude of the continuum state is $\sqrt{2/(\pi k)}$ at large distances.

Bibliography

[1] D. G. Leopold and W. C. Lineberger, *A study of the low-lying electronic states of* Fe_2 *and* Co_2 *by negative ion photoelectron spectroscopy*, J. Chem. Phys. **85**, 51 (1986).

[2] K. M. McHugh *et al.*, *Photoelectron spectra of the alkali metal cluster anions:* $Na^-_{n=2-5}$, $K^-_{n=2-7}$, $Rb^-_{n=2-3}$, *and* $Cs^-_{n=2-3}$, J. Chem. Phys. **91**, 3792 (1989).

[3] P. J. Benning *et al.*, *Electronic states of solid* C_{60}*: Symmetries and photoionization cross sections*, Phys. Rev. B **44**, 1962 (1991).

[4] M. B. Jost *et al.*, *Band dispersion and empty electronic states in solid* C_{60}*: Inverse photoemission and theory*, Phys. Rev. B **44**, 1966 (1991).

[5] E. E. B. Campbell *et al.*, *From Above Threshold Ionization to Statistical Electron Emission: The Laser Pulse-Duration Dependence of* C_{60} *Photoelectron Spectra*, Phys. Rev. Lett. **84**, 2128 (2000).

[6] H. Handschuh *et al.*, *Stable Configurations of Carbon Clusters: Chains, Rings, and Fullerenes*, Phys. Rev. Lett. **74**, 1095 (1995).

[7] O. Kostko *et al.*, *Structure Determination of Medium-Sized Sodium Clusters*, Phys. Rev. Lett. **98**, 043401 (2007).

[8] T. Liebsch *et al.*, *Angle-resolved photoelectron spectroscopy of* C_{60}, Phys. Rev. A **52**, 457 (1995).

[9] A. T. J. B. Eppink and D. H. Parker, *Velocity map imaging of ions and electrons using electrostatic lenses: Application in photoelectron and photofragmentation ion imaging of molecular oxygen*, Rev. Sci. Inst. **68** (1997).

[10] J. C. Pinaré *et al.*, *Photoelectron Imaging Spectroscopy of Small Clusters: Evidence for Non-Boltzmannian Kinetic-Energy Distribution in Thermionic Emission*, Phys. Rev. Lett. **81**, 2225 (1998).

[11] J. C. Pinaré *et al.*, *Angular distributions in photoelectron spectroscopy of small tungsten clusters: competition between direct and thermionic emission*, Euro. Phys. J. D **9**, 21 (1999).

[12] O. Kostko *et al.*, *Photoelectron spectroscopy of the structure and dynamics of free size selected sodium clusters*, JPCS **88**, 012034 (2007).

[13] C. Bartels *et al.*, *Probing the Angular Momentum Character of the Valence Orbitals of Free Sodium Nanoclusters*, Science **323**, 1323 (2009).

[14] M. Kjellberg *et al.*, *Momentum-map-imaging photoelectron spectroscopy of fullerenes with femtosecond laser pulses*, Phys. Rev. A **81**, 023202 (2010).

[15] J. O. Johansson *et al.*, *Angular-resolved Photoelectron Spectroscopy of Superatom Orbitals of Fullerenes*, Phys. Rev. Lett. **108**, 173401 (2012).

[16] F. Pagliarulo *et al.*, *Study of competing decay processes in small carbon clusters using time-resolved photoelectron imaging*, Int. J. Mass Spectrom. **252**, 100 (2006).

[17] T. Brabec and F. Krausz, *Intense few-cycle laser fields: Frontiers of nonlinear optics*, Rev. Mod. Phys. **72**, 545 (2000).

[18] P. Agostini and L. F. DiMauro, *The physics of attosecond light pulses*, Rep. Prog. Phys. **67**, 813 (2004).

[19] F. Krausz and M. Ivanov, *Attosecond physics*, Rev. Mod. Phys. **81**, 163 (2009).

[20] W. A. de Heer, *The physics of simple metal clusters: experimental aspects and simple models*, Rev. Mod. Phys. **65**, 611 (1993).

[21] M. Brack, *The physics of simple metal clusters: self-consistent jellium model and semiclassical approaches*, Rev. Mod. Phys. **65**, 677 (1993).

[22] T. Seideman, *Time-resolved photoelectron angular distributions: Concepts, Applications and Directions*, Annu. Rev. Phys. Chem. **53**, 41 (2002).

[23] P.-G. Reinhard and E. Suraud, *Introduction to Cluster Dynamics* (Wiley-VCH Verlag, Weinheim, 2004).

[24] F. Calvayrac *et al.*, *Nonlinear electron dynamics in metal clusters*, Phys. Rep. **337**, 493 (2000).

[25] P. Hohenberg and W. Kohn, *Inhomogeneous Electron Gas*, Phys. Rev. **136**, B 864 (1964).

[26] S. Vidal *et al.*, *Frequency dependence of level depletion in* Na *clusters and* C_2H_4, J. Phys. B: At. Mol. Opt. Phys. **43**, 165102 (2010).

[27] D. Bauer *et al.*, C_{60} *in intense femtosecond laser pulses: Nonlinear dipole response and ionization*, Phys. Rev. A **64** (2001).

[28] S. Kümmel, M. Brack, and P.-G. Reinhard, *Ionic and electronic structure of sodium up to* $N = 59$, Phys. Rev. B **62**, 7602 (2000).

[29] S. Goedecker, M. Teter, and J. Hutter, *Separable dual-space Gaussian pseudopotentials*, Phys. Rev. B **54**, 1703 (1996).

[30] W. Kohn, *Nobel Lecture: Electronic structure of matter—wave functions and density functionals*, Rev. Mod. Phys. **71**, 1253 (1999).

[31] R. M. Dreizler and E. K. U. Gross, *Density Functional Theory* (Springer-Verlag, Berlin, 1990).

[32] H. Eschrig, *The fundamentals of density functional theory* (Teubner, 1996).

[33] M. A. L. Marques and E. K. U. Gross, *Time-Dependent Density Functional Theory*, in C. Fiolhais, F. Nogueira, and M. Marques (Editors), *A Primer in Density Functional Theory*, volume 620 of *Lecture Notes in Physics*, pp. 145–186 (Springer, Berlin, 2003).

[34] T. L. Gilbert, *Hohenberg-Kohn theorem for nonlocal external potentials*, Phys. Rev. B **12**, 2111 (1975).

[35] W. Kohn and L. J. Sham, *Self-Consistent Equations Including Exchange and Correlation Effects*, Phys. Rev. **140**, A 1133 (1965).

[36] T. Koopmans, *Über die Zuordnung von Wellenfunktionen und Eigenwerten zu den Einzelnen Elektronen Eines Atoms*, Physica **1**, 104 (1934).

[37] M. Levy, J. P. Perdew, and V. Sahni, *Exact differential equation for the density and ionization energy of a many-particle system*, Phys. Rev. A **30**, 2745 (1984).

[38] C.-O. Almbladh and U. von Barth, *Exact results for the charge and spin densities, exchange-correlation potentials, and density-functional eigenvalues*, Phys. Rev. B **31**, 3231 (1985).

[39] D. P. Chong, O. V. Gritsenko, and E. J. Baerends, *Interpretation of the Kohn–Sham orbital energies as approximate vertical ionization potentials*, J. Chem. Phys. **116**, 1760 (2002).

[40] O. V. Gritsenko and E. J. Baerends, *The analog of Koopmans' theorem in spin-density functional theory*, J. Chem. Phys. **117**, 9154 (2002).

[41] M. Mundt *et al.*, *Photoelectron spectra of sodium clusters: The problem of interpreting Kohn-Sham eigenvalues*, Phys. Rev. B **73**, 205407 (2006).

[42] J. P. Perdew *et al.*, *Density-Functional Theory for Fractional Particle Number: Derivative Discontinuities of the Energy*, Phys. Rev. Lett. **49**, 1691 (1982).

[43] P. A. M. Dirac, *Note on Exchange Phenomena in the Thomas Atom*, Math. Proc. Camb. Philos. Soc. **26**, 376 (1930).

[44] J. C. Slater, *A Simplification of the Hartree-Fock Method*, Phys. Rev. **81**, 385 (1951).

[45] J. P. Perdew and Y. Wang, *Accurate and simple analytic representation of the electron-gas correlation energy*, Phys. Rev. B **45**, 13244 (1992).

[46] J. P. Perdew and A. Zunger, *Self-interaction correction to density-functional approximations for many-electron systems*, Phys. Rev. B **23**, 5048 (1981).

[47] J. G. Harrison, R. A. Heaton, and C. C. Lin, *Self-interaction correction to the local density Hartree-Fock atomic calculations of excited and ground states*, J. Phys. B: At. Mol. Phys. **16**, 2079 (1983).

[48] E. Fermi and E. Amaldi, *Le orbite [infinito] s degli elementi*, Roma: Reale Accademia d'Italia **6**, 119 (1934).

[49] C. Legrand, E. Suraud, and P.-G. Reinhard, *Comparison of self-interaction–corrections for metal clusters*, J. Phys. B: At. Mol. Opt. Phys. **35**, 1115 (2002).

[50] E. Runge and E. K. U. Gross, *Density-Functional Theory for Time-Dependent Systems*, Phys. Rev. Lett. **52**, 997 (1984).

[51] V. Blum *et al.*, *Comparison of Coordinate-Space Techniques in Nuclear Mean-Field Calculations*, J. Comput. Phys. **100**, 364 (1992).

[52] M. D. Feit, J. A. F. jr., and A. Steiger, *Solution of the Schrödinger Equation by a Spectral Method*, J. Comput. Phys. **47**, 412 (1982).

[53] F. Faisal, *Theory of multiphoton processes* (Plenum Press, New York, 1987).

[54] H. Friedrich, *Theoretical atomic physics* (Springer-Verlag, Berlin, 1991).

[55] P.-G. Reinhard *et al.*, *Role of boundary conditions in dynamic studies of nuclear giant resonances and collisions*, Phys. Rev. E **73**, 036709 (2006).

[56] A. Pohl, *Der doppelt differentielle Wirkungsquerschnitt für Photoionisation von Metallclustern*, Ph.D. thesis, Friedrich-Alexander-Universität Erlangen-Nürnberg (2003).

[57] M. Bär, *Non-Linear Dynamics of Metal Clusters on Insulating Substrates*, Ph.D. thesis, Friedrich-Alexander-Universität Erlangen-Nürnberg (2008).

[58] P.-G. Reinhard *et al.*, *personal communation* (2011).

[59] P. M. Dinh *et al.*, *A critical analysis of the theoretical scheme to evaluate photoelectron spectra*, arXiv:1206.3918 (2012).

[60] P. Ghosh, *Introduction to photoelectron spectroscopy* (John Wiley and Sons, New York, 1983).

[61] H. Bethe, *Handbuch der Physik*, volume 24/1 (Springer-Verlag, Berlin, 1933).

[62] C. Yang, *On the Angular Distribution in Nuclear Reactions and Coincidence Measurements*, Phys. Rev. **74**, 764 (1948).

[63] J. Cooper and R. N. Zare, *Angular Distribution of Photoelectrons*, J. Chem. Phys. **48**, 942 (1968).

[64] J. Cooper and R. N. Zare, *Erratum: Angular Distribution of Photoelectrons*, J. Chem. Phys. **49**, 4252 (1968).

[65] J. Cooper and R. N. Zare, *Photoelectron Angular Distribution*, in S. Geltman, K. Mahanthappa, and W. Brittin (Editors), *Lectures in Theoretical Physics: Atom Collision Processes*, volume 11 (Gordon and Breach, New York, 1969).

[66] M. S. Child, *Limits on the asymmetry parameters for two- and three-photon fragmentation*, Phys. Chem. Chem. Phys. **10**, 6169 (2008).

[67] J. C. Tully, R. S. Berry, and B. J. Dalton, *Angular Distribution of Molecular Photoelectrons*, Phys. Rev. **176**, 95 (1968).

[68] M. Y. Amusia, N. A. Cherepkov, and L. V. Chernysheva, *Angular Distribution of Photoelectrons With Many-Electron Correlations*, Phys. Lett. **40A**, 15 (1972).

[69] R. R. Lucchese, G. Raseev, and V. McKoy, *Studies of differential and total photoionization cross sections of molecular nitrogen*, Phys. Rev. A **25**, 2572 (1982).

[70] P. Wopperer, *Winkelverteilungen von Photoelektronen aus Metallclustern*, Diplomarbeit, Friedrich-Alexander-Universität Erlangen-Nürnberg (2009).

[71] P. Wopperer *et al.*, *Orientation averaged angular distributions of photo-electrons from free Na clusters*, Phys. Lett. A **375**, 39 (2010).

[72] P. Wopperer *et al.*, *Angular distributions of photoelectrons from free Na clusters*, Phys. Rev. A **82**, 063416 (2010).

[73] A. R. Edmonds, *Drehimpulse in der Quantenmechanik* (Hochschultaschenbücher-Verlag, Mannheim, 1960).

[74] M. E. Rose, *Elementary Theory of Angular Momentum* (John Wiley and Sons, New York, 1963).

[75] L. V. Keldysh, *Ionization in the field of a strong electromagnetic wave*, Soviet Physics, JETP **20**, 1307 (1965).

[76] P. Wopperer, P.-G. Reinhard, and E. Suraud, *On photo-electron angular distributions from clusters*, published online in Ann. Phys. (Berlin), DOI: 10.1002/andp.201200280 (2013).

[77] P. Wopperer *et al.*, *On the role of resonances in photoionization of metal clusters* (2013), submitted to JPCS.

[78] F. Calvayrac, P.-G. Reinhard, and E. Suraud, *Spectral Signals from Electronic Dynamics in Sodium Clusters*, Ann. Phys. **255**, 125 (1997).

[79] I. Wilhelmy *et al.*, *Molecular photoionization cross sections by the Lobatto technique. I. Valence photoionization*, J. Chem. Phys. **100**, 2808 (1994).

[80] E. Maurat, P.-A. Hervieux, and F. Lépine, *Surface Plasmon resonance in* C_{60} *revealed by photoelectron imaging spectroscopy*, J. Phys. B: At. Mol. Opt. Phys. **42**, 165105 (2009).

[81] T. Seideman, *Time-resolved photoelectron angular distributions: A nonperturbative theory*, J. Chem. Phys. **107**, 7859 (1997).

[82] B. Wästberg and A. Rosén, *Calculation of photoionization cross sections of* Na_{2-8} *and* K_{2-8} *clusters*, Z. Phys. D: At., Mol. Clusters **18**, 267 (1991).

[83] K. Jänkälä, M.-H. Mikkelä, and M. Huttula, *Valence photoionization of free, neutral, and size-varied alkali metal clusters*, J. Phys. B: At. Mol. Opt. Phys. **44**, 105101 (2011).

[84] M. Koskinen and M. Manninen, *Photoionization of metal clusters*, Phys. Rev. B **54**, 14796 (1996).

[85] P. Wopperer *et al.*, *Frequency dependence of photoelectron angular distributions in small* Na *clusters*, Phys. Rev. A **85**, 015402 (2012).

[86] A. D. Buckingham, B. J. Orr, and J. M. Sichel, *Angular Distribution and Intensity in Molecular Photoelectron Spectroscopy I. General Theory for Diatomic Molecules*, Philos. Trans. R. Soc. London A, Math. Phys. Sci. **268**, 147 (1970).

[87] Y. Wu and T. Omura, *Quantum Theory of Scattering* (Prentice-Hall Inc., N.Y., 1962).

[88] F. Schwabl, *Quantenmechanik (QM I)*, volume 1 (Springer-Verlag, Berlin, 2005).

[89] C. Cohen-Tannoudji *et al.*, *Quantenmechanik*, volume 2 (De Gruyter, Berlin, 2010).

[90] O. Frank and J. M. Rost, *Diffraction effects in the photoionization of clusters*, Chem. Phys. Lett. **271**, 367 (1997).

[91] G. W. Drake, *Springer handbook of atomic, molecular, and optical physics*, volume 1 (Springer New York, 2005).

[92] C. Bartels, *Angular distributions of photoelectrons from cold, size-selected sodium cluster anions*, Ph.D. thesis, Albert-Ludwigs-Universität Freiburg (2008).

[93] A. V. Solov'yov, R. G. Polozkov, and V. K. Ivanov, *Angle-resolved photoelectron spectra of metal cluster anions within a many-body-theory approach*, Phys. Rev. A **81**, 021202(R) (2010).

[94] H. W. Kroto *et al.*, C_{60}*: Buckminsterfullerene*, Nature **318**, 162 (1985).

[95] H. Kroto, *Symmetry, space, stars and* C_{60}, Rev. Mod. Phys. **69**, 703 (1997).

[96] W. Krätschmer *et al.*, *Solid* C_{60}*: a new form of carbon*, Nature **347**, 354 (1990).

[97] S. H. Yang *et al.*, *UPS of Buckminsterfullerene and other large clusters of carbon*, Chem. Phys. Lett. **139**, 233 (1987).

[98] J. A. Zimmerman *et al.*, *"Magic number" carbon clusters: Ionization potentials and selective reactivity*, J. Chem. Phys. **94**, 3556 (1991).

[99] L.-S. Wang *et al.*, *Threshold photodetachment of cold* C_{60}^-, Chem. Phys. Lett. **182**, 5 (1991).

[100] J. H. Weaver *et al.*, *Electronic Structure of Solid* C_{60}*: Experiment and Theory*, Phys. Rev. Lett. **66**, 1741 (1991).

[101] J. L. Martins, N. Troullier, and J. H. Weaver, *Analysis of occupied and empty electronic states of* C_{60}, Chem. Phys. Lett. **180**, 457 (1991).

[102] N. Troullier and J. L. Martins, *Structural and electronic properties of* C_{60}, Phys. Rev. B **46**, 1754 (1992).

[103] A. Rüdel *et al.*, *Imaging Delocalized Electron Clouds: Photoionization of* C_{60} *in Fourier Reciprocal Space*, Phys. Rev. Lett. **89**, 125503 (2002).

[104] M. E. Madjet *et al.*, *Photoionization of* C_{60}*: a model study*, J. Phys. B: At. Mol. Opt. Phys. **41**, 105101 (2008).

[105] G. F. Bertsch *et al.*, *Collective Plasmon Excitation in* C_{60} *Clusters*, Phys. Rev. Lett. **67** (1991).

[106] I. V. Hertel *et al.*, *Giant Plasmon Excitation in Free* C_{60} *and* C_{70} *Molecules Studied by Photoionization*, Phys. Rev. Lett. **68** (1992).

[107] S. W. J. Scully *et al.*, *Photoexcitation of a Volume Plasmon in* C_{60} *Ions*, Phys. Rev. Lett. **94**, 065503 (2005).

[108] E. E. B. Campbell, G. Ulmer, and I. V. Hertel, *Delayed Ionization of* C_{60} *and* C_{70}, Phys. Rev. Lett. **67**, 1986 (1991).

[109] K. Hansen, K. Hoffmann, and E. E. B. Campbell, *Thermal electron emission from the hot electronic subsystem of vibrationally cold* C_{60}, J. Chem. Phys. **119**, 2513 (2003).

[110] R. Schlipper *et al.*, *Thermal emission of electrons from highly excited sodium clusters*, Appl. Phys. A **72**, 255 (2001).

[111] M. Maier, M. A. Hoffmann, and B. von Issendorff, *Thermal emission of electrons from highly excited* Na_{16}^+ *to* Na_{250}^+, New J. Phys. **5**, 3.1 (2003).

[112] S. Korica *et al.*, *Partial cross sections and angular distributions of resonant and nonresonant valence photoemission of* C_{60}, Phys. Rev. A **71**, 013203 (2005).

[113] A. K. Belyaev *et al.*, *Photoabsorption of the fullerene* C_{60} *and its positive ions*, Phys. Scr. **80**, 048121 (2009).

[114] W. I. F. David *et al.*, *Crystal structure and bonding of ordered* C_{60}, Nature **353**, 147 (1991).

[115] K. Hedberg *et al.*, *Bond Lengths in Free Molecules of Buckminsterfullerene,* C_{60}*, from Gas-Phase Electron Diffraction*, Science **254** (1991).

[116] H. Fripertinger, *The Cycle Index of the Symmetry Group of the Fullerene* C_{60}, match **33** (1996).

[117] A. Skumanich, *Optical absorption spectra of carbon 60 thin films from 0.4 to 6.2 eV*, Chem. Phys. Lett. **182**, 486 (1991).

[118] D. L. Lichtenberger, K. W. Nebesny, and C. D. Ray, *Valence and core photoelectron spectroscopy of* C_{60}*, buckminsterfullerene*, Chem. Phys. Lett. **176** (1991).

[119] K. Sattler, *Handbook of Nanophysics: Clusters and Fullerenes*, Handbook of Nanophysics (CRC Press, 2010).

[120] D. L. Lichtenberger *et al.*, *The Ionizations of* C_{60} *in the Gas Phase and in Thin Solid Films*, Mater. Res. Soc. Symp. Proc. **206** (1991).

[121] J. de Vries *et al.*, *Single-photon ionization of* C_{60}*- and* C_{70}*-fullerene with synchrotron radiation: determination of the ionization potential of* C_{60}, Chem. Phys. Lett. **188**, 159 (1992).

[122] G. Barton and C. Eberlein, *Plasma spectroscopy proposed for* C_{60} *and* C_{70}, J. Chem. Phys. **95**, 1512 (1991).

[123] D. Gorokhov, R. Suris, and V. Cheianov, *Electron-energy-loss spectroscopy of the* C_{60} *molecule*, Phys. Lett. A **223**, 116 (1996).

[124] F. Alasia *et al.*, *Single-particle and collective degrees of freedom in* C_{60}, J. Phys. B: At. Mol. Opt. Phys. **27**, 643 (1994).

[125] K. Yabana and G. F. Bertsch, *Time-dependent local-density approximation in real time*, Phys. Rev. B **54**, 4484 (1996).

[126] D. Östling, P. Apell, and A. Rosén, *Theory for Collective Resonances of the* C_{60} *Molecule.*, Europhys. Lett. **21**, 539 (1993).

[127] G. Gensterblum *et al.*, *High-Resolution Electron-Energy-Loss Spectroscopy of Thin Films of* C_{60} *on* Si(100), Phys. Rev. Lett. **67**, 2171 (1991).

[128] E. Sohmen, J. Fink, and W. Krätschmer, *Electron energy-loss spectroscopy studies on* C_{60} *and* C_{70} *fullerite*, Z. Phys. B: Condens. Matter **86**, 87 (1992).

[129] J. W. Keller and M. A. Coplan, *Electron energy loss spectroscopy of* C_{60}, Chem. Phys. Lett. **193**, 89 (1992).

[130] A. Reinköster *et al.*, *The photoionization and fragmentation of* C_{60} *in the energy range* $26 - 130\,eV$, J. Chem. Phys. **37**, 2135 (2004).

[131] E. Giglio, P.-G. Reinhard, and E. Suraud, *Influence of the dynamical correlations on the ionization of irradiated metal clusters*, Nucl. Instrum. Methods Phys. Res., Sect. B **205**, 350 (2003).

[132] W. Weltner, Jr. and R. J. Van Zee, *Carbon Molecules, Ions, and Clusters*, Chem. Rev. **89**, 1713 (1989).

[133] E. A. Rohlfing, D. M. Cox, and A. Kaldor, *Production and characterization of supersonic carbon cluster beams*, J. Chem. Phys. **81**, 3322 (1984).

[134] C. Lifshitz, *Carbon clusters*, Int. J. Mass Spectrom. **200**, 423 (2000).

[135] D. W. Arnold *et al.*, *Vibrationally resolved spectra of* C_2 - C_{11} *by anion photoelectron spectroscopy*, J. Chem. Phys. **95**, 8753 (1991).

[136] S. Yang *et al.*, *UPS of 2-30-atom carbon clusters: chains and rings*, Chem. Phys. Lett. **144**, 431 (1988).

[137] G. von Helden *et al.*, *Isomers of Small Carbon Cluster Anions: Linear Chains with up to 20 atoms*, Science **259**, 1300 (1993).

[138] D. P. Kosimov, A. A. Dzhurakhalov, and F. M. Peeters, *Theoretical study of the stable states of small carbon clusters* C_n *(*$n = 2 - 10$*)*, Phys. Rev. B **78**, 235433 (2008).

[139] C. Zhang *et al.*, *Geometry optimization of* C_n *(*$n = 2 - 30$*) with genetic algorithm*, Chem. Phys. Lett. **364**, 213 (2002).

[140] M. Menon, K. R. Subbaswamy, and M. Sawtarie, *First-principles molecular-dynamics study of carbon clusters*, Phys. Rev. B **48**, 8398 (1993).

[141] C. H. Xu *et al.*, *A transferable tight-binding potential for carbon*, J. Phys.: Condens. Matter **4**, 6047 (1992).

[142] K. Raghavachari and J. S. Binkley, *Structure, stability, and fragmentation of small carbon clusters*, J. Chem. Phys. **87**, 2191 (1987).

[143] L. Belau *et al.*, *Ionization Thresholds of Small Carbon Clusters: Tunable VUV Experiments and Theory*, J. Am. Chem. Soc. **129**, 10229 (2007).

[144] S. Díaz-Tendero, F. Martín, and M. Alcamí, *Structure, Dissociation Energies, and Harmonic Frequencies of Small Doubly Charged Carbon Clusters* C_n^{2+} *(*$n = 3 - 9$*)*, J. Phys. Chem. A **106**, 10782 (2002).

[145] X. Liang *et al.*, *Comparative study on the structure and properties of small* C_n *and* NaC_n *clusters*, Euro. Phys. J. D **46**, 93 (2008).

[146] R. Ramanathan, J. A. Zimmerman, and J. R. Eyler, *Ionization potentials of small carbon clusters*, J. Chem. Phys. **98**, 7838 (1993).

[147] J. Benedikt *et al.*, *Threshold ionization mass spectrometry of reactive species in remote* Ar/C_2H_2 *expanding thermal plasma*, J. Vac. Sci. Technol., A **23**, 1400 (2005).

[148] K. Yabana and G. F. Bertsch, *Optical response of small carbon clusters*, Z. Phys. D: At., Mol. Clusters **42**, 219 (1997).

[149] M. Kolbuszewski, *Ab initio study of the optical spectra of* C_3*,* C_5*, and* C_7 *chains*, J. Chem. Phys. **102**, 3679 (1995).

[150] G. Pacchioni and J. Koutecký, *Ab initio MRD CI investigation of the optical spectra of* C_4 *and* C_5 *clusters*, J. Chem. Phys. **88**, 1066 (1988).

[151] G. Monninger *et al.*, *Vacuum Ultraviolet Spectroscopy of the Carbon Molecule* C_3 *in Matrix Isolated State: Experiment and Theory*, J. Phys. Chem. A **106**, 5779 (2002).

[152] K. W. Chang and W. R. M. Graham, *Vacuum UV spectrum of* C_3 *trapped in argon at 8 K*, J. Chem. Phys. **77**, 4300 (1982).

[153] A. E. Boguslavskiy and J. P. Maier, *Gas phase electronic spectra of the carbon chains* C_5*,* C_6*,* C_8*, and* C_9, J. Chem. Phys. **125**, 094308 (2006).

[154] D. Forney *et al.*, *Electronic absorption spectra of linear carbon chains in neon matrices. IV.* C_{2n+1} $n = 2 - 7$, J. Chem. Phys. **104**, 4954 (1996).

[155] A. Messiah, *Quantum Mechanics*, volume 1 (North Holland, Amsterdam and Interscience, New York, 1961).

[156] G. Breit and H. A. Bethe, *Ingoing Waves in Final State of Scattering Problems*, Phys. Rev. **93**, 888 (1954).

[157] J. L. M. Q. González and D. Thompson, *Getting started with Numerov's method*, Computers in Physics **11** (1997).

Title: Electron photoemission from sodium and carbon clusters

---

Abstract:

Photoangular distributions (PAD) and spectra (PES) of electrons emitted from clusters after excitation with linearly polarized femtosecond laser pulses or with instantaneous boost are calculated theoretically in the framework of time-dependent density-functional theory. The studied finite systems are small sodium clusters, carbon chains C_N ($N = 3, 5, 7$), and the famous buckminsterfullerene C_{60}. The behaviour of emission observables is explored as a function of size, shape, electronic and ionic structure of the considered systems and as a function of laser parameters. Moreover, schemes for determination of the PAD of an ensemble of randomly orientated molecules and clusters are elaborated. The TDDFT results are compared to stationary models and experimental data. Ionization mechanisms are studied in one- as well as multiphoton regime.

Keywords: time-dependent density-functional theory, angle-resolved photoelectron spectroscopy, electronic properties of sodium and carbon clusters, ionization mechanisms.

Titel: Photoemission von Elektronen aus Natrium- und Kohlenstoffclustern

---

Zusammenfassung:

Winkelverteilungen (PAD) und Spektren (PES) von Photoelektronen aus Clustern werden mit Hilfe zeitabhängiger Dichtefunktionaltheorie berechnet. Als Systeme werden kleine Natriumcluster, Kohlenstoffketten C_N ($N = 3, 5, 7$) sowie das berühmte Buckminster-Fulleren C_{60} betrachtet und mit linear polarisierten Femtosekunden-Laserpulsen oder instantanen Boosts angeregt. Anschließend wird das Verhalten der Emissionsobservablen als Funktion der Größe, der Form, der Elektronen- und Ionenstruktur sowie der Einfluss von Laserparametern untersucht. Die Ergebnisse aus TDDFT werden weiterhin mit stationären Modellen und experimentellen Werten verglichen. Die Ionisationsmechanismen werden sowohl im Ein- als auch im Multiphotonenregime studiert.

Schlagwörter: Zeitabhängige Dichtefunktionaltheorie, winkelaufgelöste Photoelektronenspektrospie, elektronische Eigenschaften von Natrium- und Kohlenstoffclustern, Ionisationsmechanismen.

Auteur : Philipp Wopperer

Titre : Emission de photoélectrons dans des agrégats de sodium et de carbone

Directeurs de thèse : Paul-Gerhard REINHARD/Eric SURAUD

Lieu et date de soutenance : Université Toulouse III, le 7 juin 2013

Résumé :
Des distributions angulaires (PAD) et des spectres (PES) de photoélectrons émis par des agrégats sous l'action des lasers à impulsions femtosecondes linéairement polarisées ou d'une impulsion instantanée sont calculés théoriquement dans un modèle basé sur la théorie de la fonctionnelle de la densité dépendante du temps (TDDFT). Les systèmes finis étudiés sont de petits agrégats de sodium, des chaînes de carbone C_N ($N = 3, 5, 7$), et le célèbre buckminsterfullerène C_{60}. Le comportement de l'émission éléctronique est exploré en fonction de la taille, la forme, la structure électronique et ionique ainsi qu'en fonction des paramètres du laser. En outre, des procédures de détermination de la PAD d'un ensemble de molécules ou d'agrégats orientés de façon aléatoire, sont élaborées. Les résultats de la TDDFT sont de plus comparés aux modèles stationnaires et aux données expérimentales. Les méchanismes d'ionisation sont étudiés dans le régime à un photon et à multi-photon.

Mots-clés : Théorie de la fonctionnelle de la densité dépendante du temps, spectroscopie de photoélectrons résolue en angle, propriétés électroniques d'agrégats de sodium et de carbone, méchanismes d'ionisation.

Discipline administrative : Physique de la matière

Unité de recherche :
Laboratoire de Physique Théorique de Toulouse (IRSAMC)
Université Toulouse III – Paul Sabatier
118 route de Narbonne
F-31062 Toulouse Cedex 4, France